THE UNIVERSITY *of* EDINBURGH

COMPARATIVE ANATOMY
OF THE
HUMAN NEUROMUSCULAR JUNCTION

Ross Alexander Jones

A thesis submitted for the degree of
Doctor of Philosophy

The University of Edinburgh
2017

Declaration

(a) that the thesis has been composed by the student, and
(b) either that the work is the student's own, or, if the student has been a member of a research group, that the student has made a substantial contribution to the work, such contribution being clearly indicated, and
(c) that the work has not been submitted for any other degree or professional qualification except as specified, and
(d) that any included publications are the student's own work, except where indicated throughout the thesis and summarized and clearly identified on the declarations page of the thesis.

Signature ……

Date ……

Abstract

The neuromuscular junction (NMJ), the synapse formed between lower motor neuron and skeletal muscle fibre, is known to be a target in a number of neurodegenerative conditions, including motor neuron disease (MND). Located in an accessible part of the peripheral nervous system, the NMJ can be used as a 'model synapse' in the context of 'connectomics' – the study of synaptic connectivity throughout the nervous system as a whole. Although the NMJ has been studied in a number of species, relatively little is known about its structure in humans, complicating the translation of animal models of disease to the human condition.

Described here is the first detailed cellular and molecular characterization of the human NMJ. A standardized methodology for comparative morphometric analysis of NMJs was developed and validated ('NMJ-morph'). NMJ-morph was used to generate baseline data for 2160 NMJs from a single litter of wild type mice, representing 9 distinct muscles across 3 body regions.

Principal components analysis (PCA) revealed synaptic size and fragmentation to be the key determinants of synaptic variability. Correlation data revealed the pre-synaptic cell (motor neuron) to be a stronger predictor of synaptic morphology than the post-synaptic cell (muscle fibre). Other factors influencing synaptic variability were in a clear hierarchy: muscle identity accounted for more variation in synaptic form than animal identity, with side having no effect.

Human tissue was obtained from 20 patients (aged 34 to 92 years) undergoing lower limb amputation, primarily for the complications of peripheral vascular disease (PVD). Muscle samples were harvested from non-pathological regions of the surgical discard tissue. 2860 human NMJs were analyzed from 4 distinct muscles (*extensor digitorum longus*, *soleus*, *peroneus longus* and *peroneus brevis*), and compared with equivalent NMJs from wild type mice.

Human NMJs displayed unique morphological characteristics, including small size, thin axons, rudimentary nerve terminals and distinctive 'nummular' endplates, all of which distinguished them from equivalent mouse NMJs. The previous notion of partial occupancy in human NMJs was disproved. As in mice, the pre-synaptic cell was shown to correlate more strongly with NMJ morphology; in contrast to mice, the human NMJ was found to be relatively stable throughout its 90+ year lifespan. In support of the tissue harvesting procedure, patient co-morbidities (diabetes mellitus and vascular disease) did not significantly impact NMJ morphology.

Super-resolution imaging of the NMJ revealed significant differences in the functional architecture of human and mouse active zones. Despite the smaller synaptic size in humans, the total quantity of active zone material was conserved between the species, suggesting a homeostatic mechanism to preserve effective neurotransmission. Parallel proteomic profiling demonstrated further species-specific differences in the broader molecular composition of the NMJ.

The cellular and molecular anatomy of the human NMJ is fundamentally different to that of other mammalian species. These differences must be taken into account when translating animal models of disease to the human condition.

Lay summary

The neuromuscular junction (NMJ) is the point of contact between nerve and muscle, and is essential for the control of movement. The NMJ is known to break down in a number of conditions including motor neuron disease (MND). Studies to find treatments for such conditions are mainly based on animals with disease, assuming that the findings can be applied to humans. Although NMJs in various animals have been studied previously, relatively little is known about the human NMJ.

The aim of this project was to provide the first detailed description of the structure of the human NMJ. The ability to compare human NMJs with those of other animals will allow researchers to understand how the results of animal studies can be applied to the treatment of human disease.

The first part of the project describes the development and testing of a new method for measuring NMJs ('NMJ-morph'), to allow NMJs from different species to be compared in a consistent manner. NMJ-morph was then used to study NMJs from a range of muscles in mice. This identified the 2 key features that distinguish NMJs from one another: their overall size, and the number of smaller pieces that contribute to the whole.

To see how this data compared with humans, muscle samples were then obtained from patients (aged from 34 to 92 years) undergoing leg amputation. NMJs were analyzed from parts of the leg without disease. In comparison with mice, human NMJs were smaller and divided into more pieces. Also in contrast to mice, the human NMJ maintained a stable structure throughout its lifetime.

Cutting edge techniques (super resolution imaging and tandem mass spectrometry) were then used to study the molecular make-up of the human NMJ. Again, compared to mice, these results revealed clear differences in the proteins that make up the human NMJ, and how they are arranged to form the 'active zones' that send signals from nerve to muscle to control movement.

In summary, this project provides the first detailed description of the structure of the human NMJ, and shows it to be fundamentally different to the mouse NMJ. In future research, these findings will help to guide the interpretation of animal based studies and treatments in relation to human disease.

Acknowledgements

First and foremost, I would like to thank the great man, Professor Thomas Gillingwater, for inspiration and vision. It is an honour and a pleasure to work together – we did it!

I also wish to sincerely thank everyone who has offered help and guidance:

My other supervisors for their unwavering support: Prof Gordon Findlater, Dr Fanney Kristmundsdottir and Prof Hamish Simpson. ***The Vascular and Orthopaedic teams at the Royal Infirmary of Edinburgh, especially:*** Mr Roderick Chalmers, Mr Andy Tambyraja, Dan Ablett, Rachael Forsythe and Olivia McBride. ***For their significant contributions to key aspects of the project, special thanks to:*** Martin Simmen (for statistical expertise); Carl Harrison and Christian Soeller (for the super-resolution work); Samantha Eaton, Maica Llavero Hurtado, Laura Graham, Douglas Lamont and Thomas Wishart (for the proteomic work). ***For close collaboration on other aspects of the project, special thanks also to:*** Kosala Dissanayake, Richard Ribchester, Richard Skipworth and Scott Pirie. ***And for technical expertise, many thanks to:*** Trudi Gillespie (confocal microscopy); Vivian Allison and Louise Dunn (histology); Derek Thomson (all round knowledge!); and Susan Bond and Iain Campbell (anatomy). ***All of the PhD, MSc and Honours students who have made valuable contributions to this work:*** Ines Böhm, Caitlan Reich, Leena Alkhammash, Oladayo Oladiran, Andy Gale, Randa Alamer, Rosie Weston, Gavin Minty and Michael Johnston. ***All of my colleagues in the Gillingwater, Murray and Paxton labs (past and present) with particular help (and understanding!) from:*** Ewout Groen, Hannah Shorrock, Penelope Boyd, Fiona Lane, Ines Amorim, Rachael Powis, Nikky Huang, Helen Newbery, Eilidh Somers, Sarah Roche and Gillian Hunter.

I also wish to gratefully acknowledge all of the patients who contributed to this work.

Acknowledgements

And of course, to my family:

Mum, Dad, Anna, Grandma and Grandpa; all of my family in Malaysia; and my best man Jeremy Mortimer. I would also like to thank Jacqueline Cockcroft and Shirley Newsham for their inspirational teaching in earlier times; it feels like only yesterday!

Last but not least, the indefatigable Bubo… all my love.

All of the imaging in this thesis was undertaken at night. For inspiration during the small hours, I would like to acknowledge the work of: JS Bach, Glenn Gould, Jean-Michel Jarre, Sting, Steve Austin, Dave Edwardson, Scott Kelly, Noah Landis, Jason Roeder, Steve von Till, JK Broadrick, GC Green, James Hetfield, Lars Ulrich, Kirk Hammett, Cliff Burton, Jason Newsted, Robert Trujillo, Glenn Danzig, Ian 'Lemmy' Kilmister, Rob Halford, Glenn Tipton, KK Downing, Ian Hill, Scott Travis, JB, Fox, Ludwig, Seb, Trisse and Magnus Pelander. Thank you for the music.

This work is dedicated to

E. B. Jamieson, MD
Formerly Senior Demonstrator and Lecturer on Anatomy
The University of Edinburgh

who bequeathed the funds that made this work possible

and

D. W. Sinclair, FRCS Ed
Professor of Anatomy
The Royal College of Surgeons of Edinburgh

for inspirational teaching and guidance

In memory of

Doris and Cedric Eastwood
(Grandma and Grandpa)

Contents

Figures

Tables

"…I am got [sic] extremely interested in tabulating, according to mere size of genera, the species having any varieties marked by Greek letters or otherwise: the result (as far as I have yet gone) seems to me one of the most important arguments I have yet met with, that varieties are only small species–or species only strongly marked varieties. The subject is in many ways so very important for me; I wish much you would think of any well-worked Floras with from 1000-2000 species, with the varieties marked. It is good to have hair-splitters and lumpers. (Those who make many species are the "splitters," and those who make few are the "lumpers.")…"

Letter to J. D. Hooker, 1857

"…I am convinced that the most experienced naturalist would be surprised at the number of the cases of variability, even in important parts of structure, which he could collect on good authority, as I have collected, during a course of years. It should be remembered that systematists are far from being pleased at finding variability in important characters, and that there are not many men who will laboriously examine internal and important organs, and compare them in many specimens of the same species…"

Variation under Nature: Individual Differences, On the Origin of Species, 1859

Charles Darwin
(1809–1882)

"…When you are studying any matter, or considering any philosophy, ask yourself only what are the facts and what is the truth that the facts bear out. Never let yourself be diverted either by what you wish to believe, or by what you think would have beneficent social effects if it were believed. But look only, and solely, at what are the facts…"

Interview, Face to Face, BBC, 1959

Bertrand Russell
(1872–1970)

Chapter 1

General Introduction

1.1 Chapter summary

This opening chapter will review our current understanding of the human neuromuscular junction (NMJ) and outline the aims of the project. By highlighting aspects of human NMJ form and function where knowledge is presently lacking, and examining the implications for translational research, this review aims to set the context and scope of the project.

1.2 Background: The human NMJ in context

The NMJ is the synapse formed between lower motor neuron and skeletal muscle fibre. The basic structure of the NMJ is well established (Engel, 2008), with the synapse being specially adapted to facilitate rapid neurotransmission with a high 'safety factor' (Wood and Slater, 2001). The basic architecture of the NMJ comprises a core 'triad' of cellular components – motor axon, muscle fibre and terminal Schwann cell – to which a putative 4th cell type, the NMJ-capping cell or 'kranocyte' (Court et al, 2008) might now be included (Figure 1.1). In addition to being the largest and most effective synapse in the body, the NMJ is also one of the most abundant; approximately 40% of the body weight comprises skeletal muscle, with each muscle fibre possessing at least one NMJ.

Historically, many of the most important breakthroughs in synaptic biology have been derived from the study of NMJs, including the quantal nature of transmitter release (Fatt and Katz, 1952), the demonstration of synaptic vesicles by electron microscopy (Couteaux and Pécot-Dechavassine, 1970) and the identification and role of agrin (Nitkin et al, 1987). These fundamental insights into synaptic biology highlight the major contribution of the NMJ to the basic sciences, and underpin many of the various forms of NMJ dysfunction.

Clinically, the NMJ is a known pathological target in a number of neuromuscular disorders, including myasthenia gravis (Sommer et al, 2008), the Lambert-Eaton and congenital myasthenic syndromes (Nagel et al, 1988; Beeson et al, 2008) and 'limb-girdle myasthenia' (Slater et al, 2006). In addition, there is an increasing body of evidence to support the

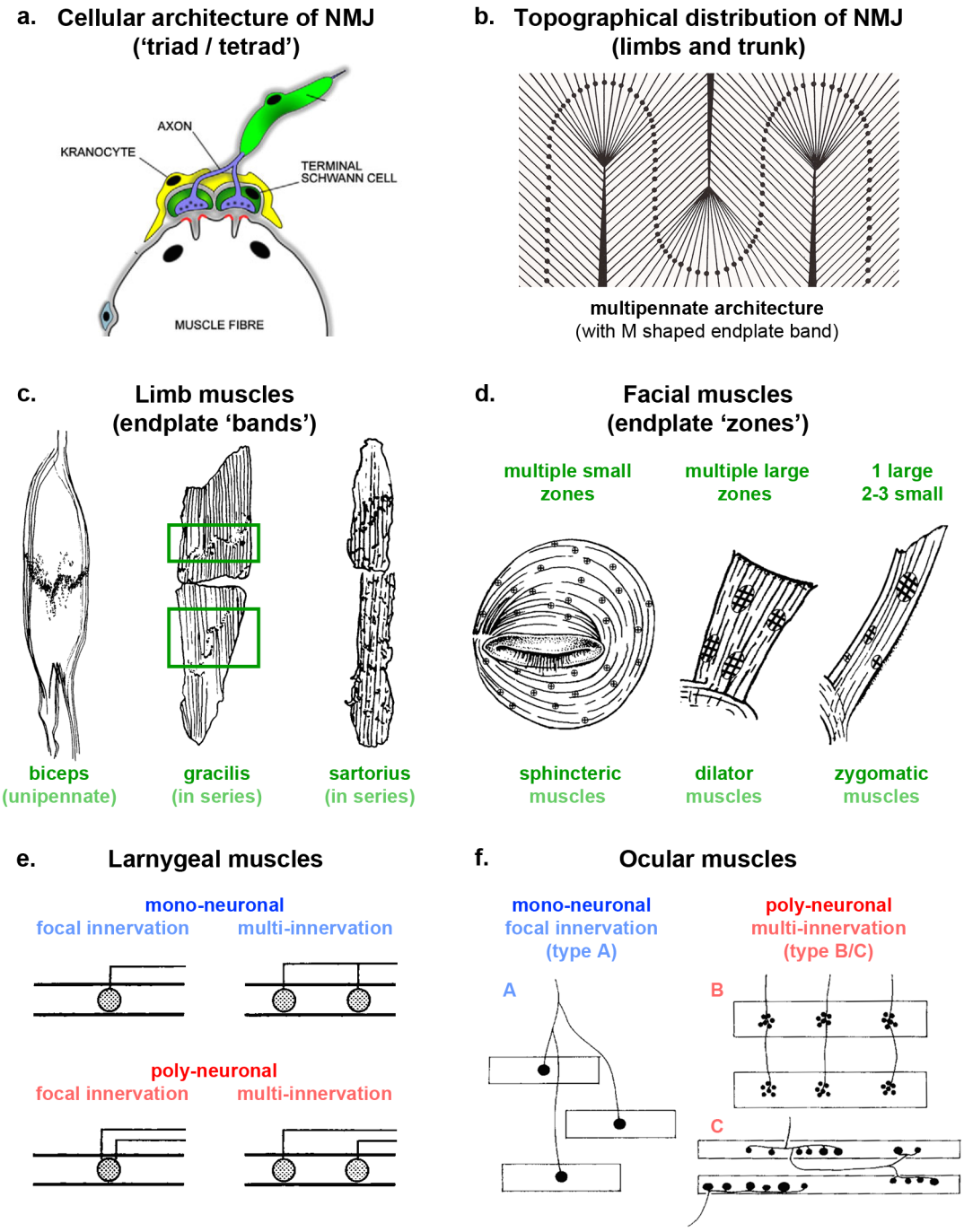

Figure 1.1 | Topographical distribution of human NMJs

a. Schematic of the cellular 'triad/tetrad' of the NMJ: motor neuron, muscle fibre, terminal Schwann cell and 'kranocyte' (the putative 4th cell type; from Court et al, 2008). **b.** Topographical distribution of NMJs located at midpoint of each fibre (black dots) in 1:1 ratio, with shape of endplate band determined by overall muscle architecture (from Coërs and Woolf, 1959). **c.** Endplate 'bands' of limb muscles. Biceps brachii is unipennate, with a single endplate band across the middle of the muscle belly (from Aquilonius et al, 1982). Exceptions include gracilis (2 endplate bands) and sartorius (disseminated endplates) due to their 'in series' architecture (Christensen, 1959). **d.** Endplate 'zones' of facial muscles, with 3 patterns described: multiple small zones (or isolated endplates), multiple large zones (2 to 4) or a single large zone (and 2-3 smaller zones). The patterns are explained by multi-innervation (≈ 25% of fibres) and eccentric endplate location (Happak et al, 1997). **e.** Laryngeal muscles also display multi-innervation (≈ 21% of fibres) by a single axon (mono-neuronal) (blue). The 2 forms of poly-neuronal innervation (red) are only present in the fetus (Périé et al, 1999). **f.** Ocular muscles display both multi- and poly-neuronal innervation. 3 patterns are described: type A (plaque-like), type B (grape-like) and type C (bead-like). Types B/C (≈ 33% of fibres) receive multi- and poly-neuronal innervation by axons and/or branches running either perpendicular (B) or parallel (C) to the muscle fibres (Oda, 1986).

vulnerability of NMJs in different forms of motor neuron disease, including amyotrophic lateral sclerosis and spinal muscular atrophy (Murray et al, 2010). The NMJ is also a target of external agents in botulism (Johnson and Montecucco, 2008) and organophosphate and carbamate poisoning (De Bleecker, 2008).

As a research tool, the simplicity of the NMJ as a three/four-cell synapse, combined with its accessible location in the peripheral nervous system, makes it an ideal 'model synapse' for studying underlying principles of synaptic biology. In this context, the NMJ has been used to uncover molecular mechanisms of synaptic maturation and maintenance (Shi et al, 2012), activity-dependent plasticity (Newman et al, 2017) and age-related degeneration (Liu et al, 2017). Many of these basic principles are intimately linked with the ongoing 'connectomic' effort – the attempt to map the total synaptic connectivity of the nervous system (Morgan and Lichtman, 2013). The only complete connectome to date is that of the nematode *C. elegans* (White et al, 1986), but there are ongoing projects in other species including *Drosophila* (Meinertzhagen, 2016) and mice (Oh et al, 2104; Jiang et al, 2105). Given the complexity inherent in even a small volume of mouse cortex (1,500 μm^3 contains some 1,700 synaptic connections; Kasthuri et al, 2105), the challenges of mapping the human connectome are formidable. On a smaller scale however, individual muscle connectomes have been successfully mapped in various muscles of the mouse (e.g. *interscutularis*, Lu et al, 2009; *4th deep lumbrical* muscle, Hirst and Ribchester, 2013), where the final pattern of connectivity is determined (critically) by postnatal synapse elimination at the NMJ.

Historically then, although many of the most important breakthroughs in synaptic biology have derived from studies of the NMJ, the NMJs themselves have generally been of mammalian or lower vertebrate and invertebrate origin, with relatively infrequent focus given to the human NMJ. An understanding of the comparative anatomy of the NMJ is of crucial importance therefore to the translation of these findings to the human NMJ.

1.2.1 Comparative anatomy of the NMJ

NMJs have been studied in numerous species across the whole of the animal kingdom (Slater, 2008), with many of the most primitive animals (e.g. *Drosophila*) possessing discrete NMJs with discernable synaptic boutons. Nematodes (e.g. *C. elegans*) are the exception,

wherein each longitudinal muscle fibre of the body wall sends out multiple 'muscle arms' to contact several longitudinal motor axons (Slater, 2015).

Aside from nematodes, recognizable NMJs have been studied in the following groups, subgroups and species: invertebrates, e.g. insects (*Drosophila*, Campbell and Ganetzky, 2012), molluscs (*snail*, Elekes et al, 2000), crustaceans (*crayfish*, King et al, 1996) and arachnids (*funnel weaver*, Moon, 1996); 'lower' vertebrates, e.g. fish (*zebrafish*, Helmprobst et al, 2015), amphibians (*frog*, Torri-Tarelli et al, 1990; *toad*, Everett et al, 2002), reptiles (*snake*, Wilkinson and Teng, 2003; *lizard*, Walrond and Reese, 1985) and birds (*zebra finch*, Desaki and Uehara, 1981) and 'higher' vertebrates (i.e. mammals), e.g. *mouse, rat, rabbit, cat, dog, monkey* and (albeit to a relatively limited degree) *humans* (Coërs and Woolf, 1959; Fahim et al, 1984; Slater et al, 1992) (Figure 1.2).

When reviewed in totality, there is great morphological diversity in NMJs (on both sides of the synapse) within and between species. Similarly, although there appears to be a general trend toward smaller NMJs in larger animals (Figure 1.2), this relationship has not been quantitatively established and is by no means absolute; nor is the size of the NMJ determined by (or necessarily correlated with) the size of the muscle fibre it innervates (though positive correlations between endplate size and fibre diameter have been demonstrated in certain species and muscles, e.g. frog *sartorius*, Kuno et al, 1971; mouse *diaphragm*, *EDL* and *soleus*, Harris and Ribchester, 1979).

The comparative anatomy of NMJ ultrastructure in relation to active zones is discussed in Chapter 5 (Section 5.2.1).

1.2.2 Topographical distribution of the human NMJ

The topography of terminal motor innervation in humans varies considerably between the skeletal muscle of the limbs and trunk (somatic origin), and that of the head and neck (with both somatic and branchial origins; Last, 1984).

1.2.2.1 Limb and trunk muscles

In striated muscle of the limbs and trunk, NMJs are located at the midpoint of individual muscle fibres, in a 1:1 ratio (1 NMJ per muscle fibre) (Christensen, 1959). In a simple

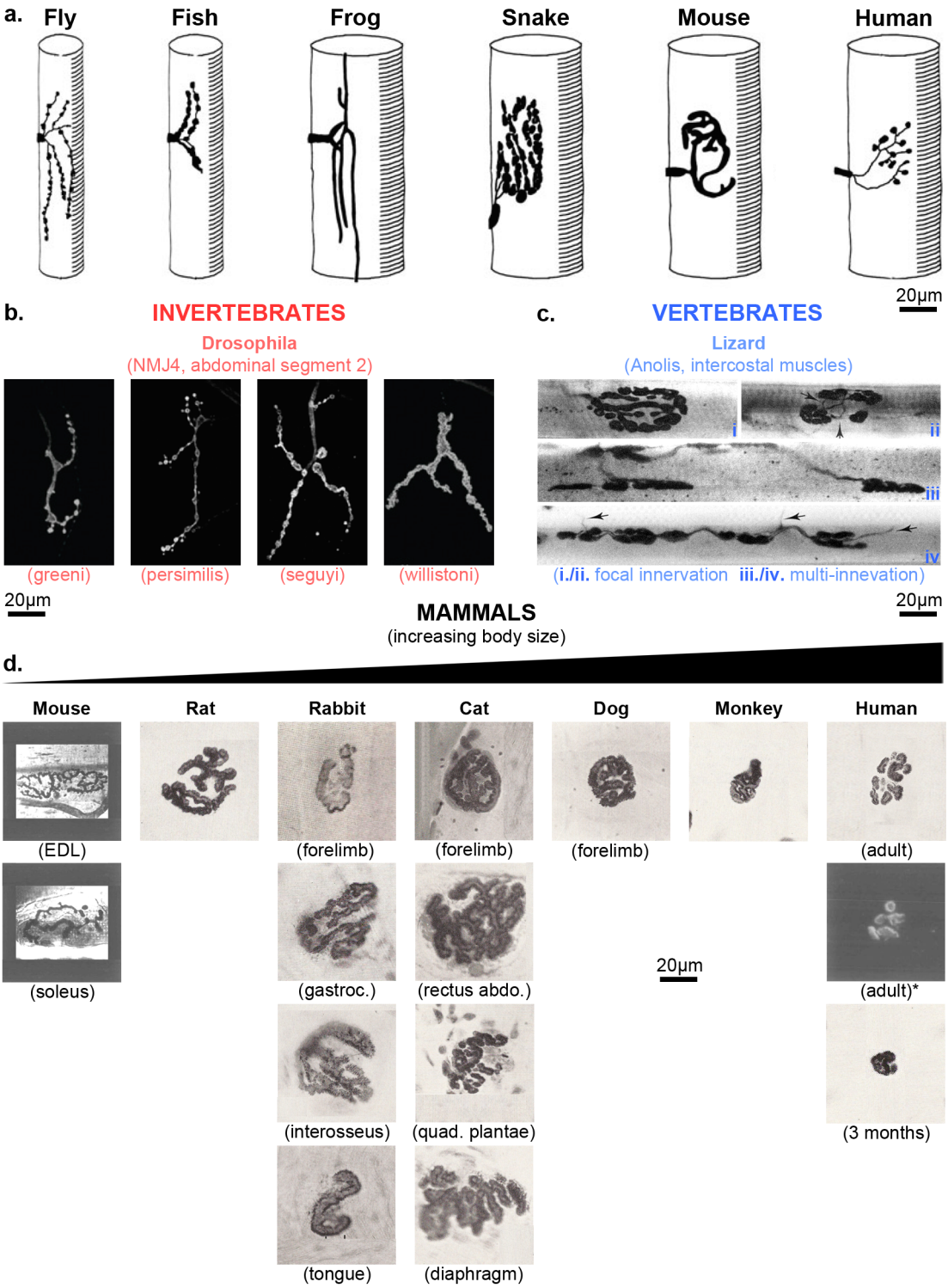

Figure 1.2 | Comparative anatomy of the NMJ
All images and illustrations of NMJs are at the same magnification for ease of comparison. Scale bars = 20μm. **a.** Schematic of NMJ morphology in different species. Comparative anatomy of the NMJ is less well understood than the illustration implies, particularly in humans (from Slater, 2008). **b.** Invertebrate NMJs from 4 species of *Drospohila* (NMJ4 of abdominal segment 2), showing substantial variation in NMJ morphology (nerve terminal labeling w/ anti-HRP; from Campbell & Ganetzky, 2012). **c.** Vertebrate NMJs from *Anolis* lizard (intercostal muscles). Examples of focal (i/ii) and multi-innervation (iii/iv) shown. The multi-innervated NMJs may also be poly-neuronal (nerve terminal staining w/ zinc iodide; from Walrond & Reese, 1985). **d.** Mammalian NMJs from 7 species arranged according to size of animal (smallest to largest). NMJ morphology varies substantially between different species and muscles. Although there appears to be a general trend toward smaller NMJs in larger animals, this is by no means absolute (e.g. cat cf. rabbit). These early images of the human NMJ are very different from those of other mammals, including Rhesus monkeys. Sources: mouse, Fahim et al, 1984 (nerve terminal staining w/ zinc iodide); human (adult)*, Slater et al 1992 (endplate AChRs labeled w/ αBTX); all others, Coërs & Woolf, 1959 (endplate ChE, Koelle's method).

unipennate muscle (eg, *biceps brachii*), NMJs are therefore located in a relatively tight 'band' running across the midpoint of the muscle belly. In muscles with a more complex architecture (bipennate, multipennate), the overall shape of the 'motor endplate band' (MEP band) conforms to the gross arrangement of the individual fibres within the muscle (or part thereof, if the muscle has multiple heads or bellies) but always with NMJs located mid-fibre (Christensen, 1959; Coërs and Woolf, 1959) (Figure 1.1).

In the first extensive study of NMJ topography, Christensen (1959) mapped the MEP bands for 16 different muscles (mainly from the upper and lower limbs) obtained from stillborn infants using a cholinesterase method (Table 1.1 and Figure 1.1). The only exceptions to the rule of a single endplate band per muscle were in *gracilis* (2 endplate bands) and *sartorius* (disseminated endplates), where the spurious 'multiple innervation' of individual muscle fibres is thought to be due to the development of these muscles from chains of myoblasts lying in series.

[Electron microscopy has since shown that the exact nature of this 'in series' architecture varies considerably, with several types of 'myo-tendinous' and 'myo-myous' junctions described (Torigoe and Nakamura, 1987). In relation to these different types of muscle architecture, multi-innervation has also been demonstrated in various animal muscles, e.g. *sternomastoid* (guinea pig, Duxson and Sheard, 1995; guinea pig, rabbit, Paul, 2001), *sternocephalicus* (horse; Zenker et al, 1990), *latissimus dorsi* (rat; Zenker et al, 1990), *semitendinosus* (mouse, guinea pig, rabbit, monkey, human; Paul, 2001) and *gracilis* (rat, Zenker et al, 1990; mouse, guinea pig, rabbit, monkey, human, Paul, 2001).]

Over the course of several studies, Coërs and Woolf (1959) confirmed the findings of Christensen (1959) in adult muscles (14 in total; Table 1.1) using the technique of 'motor point biopsy'. Clinically, the 'motor point' refers to the point on the skin/muscle where an electrical stimulus (of minimal strength) will produces a twitch of the underlying muscle; anatomically, it is defined as the point(s) at which a motor nerve(s) enters the muscle belly. The position of endplate bands has also been documented in *whole* adult muscles by means of heavy cryostat microtome (for *biceps brachii*, *tibialis anterior* and *sartorius*; Aquilonius et al, 1982, 1984).

muscle	localization by histochemistry	localization by electromyography
upper limb		
arm		
pectoralis major		Masuda et al, 1987
latissimus dorsi		Masuda et al, 1987
deltoid	Christensen, 1959	Masuda et al, 1987
	Coërs and Woolf, 1959	Saitou et al, 2000
biceps brachii	Christensen, 1959	Masuda et al, 1983a
		'83b '85 '86 '87 '88 '91
	Coërs and Woolf, 1959	Saitou et al, 2000
	Aquilonius et al, 1982; 1984	Moon et al, 2012
triceps brachii	Christensen, 1959	Masuda et al, 1987
		Saitou et al, 2000
forearm		
brachioradialis	Christensen, 1959	Masuda et al, 1987
	Coërs and Woolf, 1959	Saitou et al, 2000
		Lateva et al, 2010
pronator teres		Masuda et al, 1987
		Saitou et al, 2000
flexor carpi radialis	Coërs and Woolf, 1959	Saitou et al, 2000
flexor carpi ulnaris		Masuda et al, 1987
		Saitou et al, 2000
flexor digitorum superficialis	Coërs and Woolf, 1959	Masuda et al, 1987
palmaris longus	Coërs and Woolf, 1959	Saitou et al, 2000
extensor carpi radialis longus		Saitou et al, 2000
extensor carpi radialis brevis		Saitou et al, 2000
extensor carpi ulnaris		Saitou et al, 2000
extensor digitorum		Masuda et al, 1987
		Saitou et al, 2000
'outcropping' muscles of thumb		Saitou et al, 2000
hand		
thenar muscle group		Saitou et al, 2000
hypothenar muscle group		Saitou et al, 2000
abductor pollicis brevis		Masuda et al, 1987
abductor digiti minimi		Masuda et al, 1987
opponens pollicis	Christensen, 1959	
opponens digiti minimi	Christensen, 1959	
first dorsal interosseous		Saitou et al, 2000

muscle	localization by histochemistry	localization by electromyography
lower limb		
thigh		
tensor fasciae latae		Saitou et al, 2000
rectus femoris	Christensen, 1959	Masuda et al, 1987
		Saitou et al, 2000
vastus lateralis		Masuda et al, 1987
		Saitou et al, 2000
vastus medialis	Coërs and Woolf, 1959	Masuda et al, 1987
		Saitou et al, 2000
sartorius	Christensen, 1959	Saitou et al, 2000
	Aquilonius et al, 1984	Harris et al, 2005
gracilis	Christensen, 1959	
semitendinosus	Christensen, 1959	Masuda et al, 1987
		Saitou et al, 2000
biceps femoris (long head)		Saitou et al, 2000
leg		
gastrocnemius	Christensen, 1959	Masuda et al, 1987
	Coërs and Woolf, 1959	Saitou et al, 2000
soleus		Masuda et al, 1987
		Saitou et al, 2000
peroneus longus	Coërs and Woolf, 1959	Saitou et al, 2000
peroneus brevis	Coërs and Woolf, 1959	Saitou et al, 2000
extensor digitorum longus	Coërs and Woolf, 1959	
extensor hallucis longus	Coërs and Woolf, 1959	
tibialis anterior	Christensen, 1959	Masuda et al, 1987
	Coërs and Woolf, 1959	Saitou et al, 2000
	Aquilonius et al, 1984	
foot		
extensor digitorum brevis	Christensen, 1959	Saitou et al, 2000
abductor hallucis		Saitou et al, 2000
abductor digiti minimi		Saitou et al, 2000

muscle	localization by histochemistry	localization by electromyography
trunk		
scalenus anterior		Falla et al, 2002
rectus abdominis	Woodley et al, 2007	
external oblique	Woodley et al, 2007	
internal oblique	Woodley et al, 2007	
transversus abdominis	Woodley et al, 2007	
erector spinae muscle group		Masuda et al, 1987
transversospinalis muscle group	Cornwall et al, 2011	
external anal sphincter		Enck et al, 2004; 2005

muscle	localization by histochemistry	localization by electromyography
head and neck		
extra-ocular muscles		
rectus superior	Christensen, 1959	
muscles of mastication		
temporalis		Tokunaga et al, 1998
		Castroflorio et al, 2005
masseter		Masuda et al, 1987
		Tokunaga et al, 1998
		Castroflorio et al, 2005
		Toshifumi, 2005
muscles of facial expression		
frontalis		Masuda et al, 1987
orbicularis oculi	Happak et al, 1997	Masuda et al, 1987
orbicularis oris	Happak et al, 1997	Masuda et al, 1987
		Lapatki et al, 2006
zygomaticus major	Happak et al, 1997	
zygomaticus minor	Happak et al, 1997	
levator labii superioris	Happak et al, 1997	
depressor labii inferioris	Happak et al, 1997	Lapatki et al, 2006
levator anguli oris	Happak et al, 1997	
depressor anguli oris	Happak et al, 1997	Lapatki et al, 2006
lev. lab. sup. alaeque nasi	Happak et al, 1997	
buccinator	Happak et al, 1997	
mentalis		Lapatki et al, 2006
larynx		
cricothyroid	Christensen, 1959	
	Rossi and Cortesina, 1965b	
	De Vito et al, 1985	
	Périé et al, 1997	
vocalis	Christensen, 1959	
	Rossi and Cortesina, 1965a,b	
thyroarytenoid	Konig and Leden, 1961	
	Rosen et al, 1983	
	Périé et al, 1997	
	Sheppert et al, 2003	
posterior cricoarytenoid	Gambino et al, 1985	
	Rossi and Cortesina, 1965b	
	Périé et al, 1997	
lateral cricoarytenoid	Freije et al, 1986	
	Rossi and Cortesina, 1965b	
interarytenoid	Freije et al, 1987	
	Périé et al, 1997	
ventricular/vestibular muscle	Guida and Zorzetto, 2007	
neck		
trapezius		Masuda et al, 1987
sternocleidomastoid	Coërs and Woolf, 1959	Masuda et al, 1987
		Falla et al, 2002
tongue		
superior longitudinal muscle	Slaughter et al, 2005	

Table 1.1 | Studies documenting NMJ location in human muscles by histochemistry and EMG
Lists of muscles are arranged by anatomical region (limbs, trunk, head & neck) and grouped by structure/function (eg, position in limb, cranial nerve supply, etc).

In the trunk, endplate bands have been confirmed for *rectus abdominis*, *external oblique*, *internal oblique* and *transversus abdominis* (Woodley et al, 2007); multiple endplate bands were noted in some regions of all 4 muscles, due to the in series development of individual muscle fibres (as noted above). In the back, endplates have been labeled in the *transversospinal* group of paravertebral muscles (Cornwall et al, 2011).

Endplate bands have since been documented for a large number of human muscles, both by staining and electromyography (EMG) (Table 1.1). The non-invasive nature of surface EMG confers a clear advantage over motor point biopsy in terms of endplate localization, and has found a wide range of clinical and research applications including the study of muscle fatigue, motor neuron disease, neuropathies and myopathies (Hogrel, 2005; Drost et al, 2006). Although *biceps brachii* has been extensively studied in this regard, surface EMG has been used to map a wide range of other muscles (Table 1.1).

Micro-dissection has also been used to establish the terminal motor innervation of several muscles, including *psoas major* (Van Campenhout et al, 2010), *triceps surae* (Parratte et al, 2002) and the *flexors/extensors* of the forearm (El-Din Safwat and Abdel-Meguid, 2007); however, in the absence of confirmation by immunohistochemical labeling, these studies provide only an estimate of endplate location.

In the head and neck, NMJs demonstrate a number of unusual features, and are reviewed separately in the following sections.

1.2.2.2 Laryngeal muscles

The location of NMJs in the laryngeal muscles have been particularly studied in regard to reinnervation procedures following paralysis or transplantation (Gambino et al, 1985) and the use of botulinum toxin to treat spastic dysphonia (De Vito et al, 1985). Using AChE labeling in post-mortem specimens, the shape and location of endplate bands have been documented for the key laryngeal muscles: *posterior cricoarytenoid* (Gambino et al, 1985; loose arc), *lateral cricoarytenoid* (Freije et al, 1986; tight band), *interarytenoid* (*transverse arytenoid*) (Freije et al, 1987; inverted 'Y' distribution), *cricothyroid* (De Vito et al, 1985; middle two thirds), *thyroarytenoid* (*vocalis*) (Konig and Leden, 1961; Rosen et al, 1983; Sheppert et al, 2003 – middle third, using synaptophysin labeling). Endplates bands have also been documented

for the poorly understood *'ventricular/vestibular'* muscle, located in the false vocal cords (Guida and Zorzetto, 2007).

Several of these studies also supported earlier reports (Rossi and Cortesina, 1965; twice) of apparent 'multi-innervation' of laryngeal muscle fibres (> 1 NMJ per muscle fibre). More detailed study of adult NMJs in 4 muscles (*cricothyroid, thyroarytenoid, interarytenoid* and *posterior cricoarytenoid*) by Périé et al, 1997, confirmed genuine multi-innervation (> 1 NMJ per muscle fibre) in up to 21% of muscle fibres; all of these fibres were (nevertheless) mono-innervated by a single axon/motor neuron (not poly-innervated from different axons/motor neurons). The spacing of multiple endplates was highly variable, ranging from circumferential positions opposite one another, to longitudinal distances of up to 150μm apart. In contrast to earlier studies, NMJs were not confined to discrete bands, but scattered throughout the muscles.

1.2.2.3 Facial muscles

Similar to the laryngeal muscles, a key feature of the facial muscles is the presence of individual fibres with multiple endplates. In an extensive study, Happak et al (1997) documented the endplate locations for 10 different facial muscles (Figure 1.1, Table 1.1).

Endplates were found in 'zones' rather than 'bands', with 3 patterns described: multiple small 'zones' (or isolated endplates, e.g. the circumferential, sphincteric muscles), a single large 'zone' (and 2-3 smaller zones, e.g. the *zygomatic* muscles) and multiple large 'zones' (2-4 in number, e.g. the dilator muscles of the lips). Furthermore, none of the muscles had a gross 'in series' architecture (i.e. all fibres ran from origin to insertion without interruption), suggesting multi-innervation in at least a proportion of the muscle fibres.

Single fibre preparations confirmed both the presence of multiple endplates and their eccentric position (i.e. endplates were *not* located at the midpoint of the fibres). Multiple endplates were found in ≈ 25% of fibres (≈ 20% with 2 NMJs, ≈ 5% with ≥ 3 NMJs), whilst the distance between multiple endplates varied from < 50μm (≈ 45%) to > 200μm (≈ 5%).

The distribution of endplates in distinct clusters and eccentric locations has been confirmed using surface EMG for several other facial muscles (Masuda et al, 1987; Lapatki et al, 2006;

Table 1.1). Similar localization using surface EMG has also been performed for other muscle groups of the head and neck, including the muscles of mastication (Tokunaga et al, 1998; Castroflorio et al; 2005), *sternocleidomastoid* and *trapezius* (respectively, Falla et al, 2002; Masuda et al, 1987). Multiple endplates per muscle fibre have also been demonstrated histochemically in the tongue (for *superior longitudinalis*; Slaughter et al, 2005).

1.2.2.4 Ocular muscles

Given the unique nature and special function of the extra-ocular muscles (Porter et al, 1995), it is hardly surprising that the neuromuscular innervation is neither simple nor fully understood. These difficulties are further compounded by confusing nomenclature and conflicted findings of different studies. As with other muscles of the head and neck (preceding sections), extra-ocular muscles contain fibres displaying multiple endplates (Kupfer, 1960), but the individual innervation patterns also appear to be more complex.

Oda (1986) defined 3 types of innervation (see Figure 1.1). Type A innervation (≈ 66% of fibres) described a single large (plaque-like) endplate on a large diameter fibre (≈ 30μm) (i.e. mono-neuronal, focal innervation). Type B innervation (≈ 5% of fibres) described multiple fragmented (grape-like) endplates on an intermediate diameter fibre (≈ 20μm), with endplates spaced ≤ 500μm apart (i.e. multi-innervation, and possibly poly-neuronal). Type C innervation (≈ 33% of fibres) described multiple small (bead-like) endplates on a small diameter fibre (≈ 10μm), with endplates spaced ≤ 50μm apart (i.e. multi-innervation, and possibly poly-neuronal)

Sadeh and Stern (1984) simply defined 'en plaque' endplates on *felderstruktur* fibres* and 'en grappe' endplates on *fibrillenstruktur* fibres*, reflecting focal and multi-innervation patterns, respectively (*the fibre structures relate simply to the myofibril arrangement; Kruger, 1949). Rather confusingly however, the 'grape-like' fibres of Sadeh and Stern were synonymous with the 'bead-like' fibres of Oda (Type C, above), whereas the 'grape-like' fibres of Oda (Type B, above) represented a third, previously undescribed group (perhaps a reflection of their scarcity, in only 5% of the total fibres). In addition, Sadeh and Stern (1984) did not note any evidence of poly-neuronal innervation of either single or multiple endplates. Earlier work by Dietert (1965) also recognized two endplate types (en plaque/en grappe) and two

fibres types (*felderstruktur/fibrillenstruktur*) but the pairings were reversed cf. Sadeh and Stern (1984) (i.e. en plaque w/ *fibrillenstruktur* fibres, en grappe w/ *felderstruktur* fibres).

Ruskell (1984; twice) described a small percentage of muscle fibres (≈ 5%) with unusual 'spiral nerve endings' innervating multiple circumferential 'dapple' (fragmented) endplates, two-thirds of which were ensheathed by extensions from perineural epithelial cells. These fibres were postulated to be responsible for the exceptional speed of contraction of the extra-ocular muscles. In retrospect, although these fibres were not referred to as such at the time, it is possible that they might represent the Type B fibres described by Oda in 1986, based on their similar prevalence (≈ 5%) and morphology (multiple, fragmented).

Overall, the complexity of the innervation patterns described along with the possibility of poly-neuronal innervation of some fibre types (which is usually only associated with fetal innervation before synapse elimination) points to a very different functional organization of the extra-ocular muscles. Compared with the skeletal muscles of the limbs and trunk, the structural and functional differences exhibited by the extra-ocular muscles might explain (at least in part) their selective vulnerability in certain neuromuscular diseases (e.g. myasthenia gravis) that are characterized by an ocular presentation (Porter et al, 1996).

1.2.3 Development of the human NMJ

Development and maintenance of the vertebrate NMJ is well documented, through the study of multiple animal models (Sanes and Lichtman, 1999; 2001). In comparison, there are relatively few studies of human NMJ development (almost certainly due to the ethical difficulties associated with human embryonic/fetal work), although ontogenesis in utero is better established than the details of subsequent maturation through childhood to adulthood.

The basic structure of a recognizable NMJ (nerve terminal, motor endplate, Schwann cell; approximately 20μm diameter) is present at 9 weeks (Fidzianska, 1980; *quadriceps femoris*). Prior to this, AChRs have a diffuse distribution throughout the myotube or primitive muscle fibre (Hesselmans et al, 1993; thigh). The important landmarks of the pre- and post-synaptic changes then occur on slightly different timelines.

In terms of the post-synaptic region, endplate length gradually decreases until 16 weeks and remains static (at 10μm) during synapse elimination (Hesselmans et al, 1993), although the junctional folds themselves undergo continuous modification (increasing in number and length) from 10 weeks to 20 weeks (Fidzianska, 1980). Fetal AChRs (gamma type) have been replaced by adult AChRs (epsilon type) by 30 weeks (Hesselmans et al, 1993). Endplate length gradually increases again from 40 weeks (birth) to 1 year, plateauing thereafter at approximately 20 to 25μm diameter (Hesselmans et al, 1993; *intercostals*).

With regard to the pre-synaptic changes, multiple terminal axons (covered by a single Schwann cell) overlie the endplate at 9 weeks (Fidzianska, 1980). The change from poly-innervation to mono-innervation (synapse elimination) then occurs from 16 weeks to 25 weeks (Hesselmans et al, 1993). Regression of polyneuronal innervation has also been studied in the human *psoas* muscle (Gramsbergen et al, 1997); poly-innervation (1-5 axons per NMJ) was present until 25 weeks, with mono-innervation predominating from 3 months after birth. Nerve terminal complexity (and motor endplate size) increased from birth to a year and a half, at which point NMJs were described as comparable to those of young adults (2 controls aged 29 and 44 years).

During childhood and adolescence however, there is a marked gap in the understanding of the human NMJ. For example, changes equivalent to the 'plaque to pretzel' maturation of mouse NMJs over 2 postnatal weeks (Marques et al, 2000) have not been documented. Again, this lack of knowledge is almost certainly a consequence of the difficulties associated with obtaining paediatric tissue samples.

1.2.4 Aging of the human NMJ

Age related remodeling of the NMJ (e.g. denervation, fragmentation, etc.) is typical in rodents (Valdez et al, 2010; Willadt et al, 2016). In contrast, the effects of aging on the human NMJ are limited to a small number of studies, with very conflicted findings.

Oda (1984) studied NMJs on *intercostal* muscles from middle to old age (in individuals of ages: 32, 33, 47, 54, 57, 60, 66, 72, 76 years). Both pre- and post-synaptic variables increased in a linear manner with age: nerve terminal branching (with a decrease in T1 endings* from 95 to 50%), endplate length (from 40 to 80μm) and endplate fragmentation (with a greater

number of small clusters with age; from 3 or 4 in younger cases to 6 or 7 in older cases). [*Tuffery classification, 1971]

Wokke et al (1990) also studied NMJs on *intercostal* muscles (including ultrastructure) in a wider age range (children: 4, 4½, 8 years; young adults: 24, 27, 31; old adults: 46, 54, 58, 62; aged adults: 71, 73, 75, 77). No changes were found in nerve terminal branching (2-6 branches per NMJ) or endplate length (static at 20-25μm) with age, whilst endplate fragmentation was not assessed. Ultrastructure was measured semi-quantitatively (regularity of nerve terminals, branching and degeneration of junctional folds) with the post-synaptic region (mainly) becoming more complex with age. The greater post-synaptic area in adults compared with children was also demonstrated by Arizono et al (1984).

Gambino et al (1990) studied NMJs on the *posterior cricoarytenoid* muscle of the larynx (in very young: 4 days, 3 months, 1 year; middle aged: 20, 22, 28, 55, 57; and old individuals: 64, 70, 73, 80, 95). Both pre- and post-synaptic variables (number of branches, length of endplate) increased from youth to middle age, but remained stable from middle to old age.

Périé et al (1999) also studied development and aging of NMJs in laryngeal muscles, but with particular regard to their unusual multi-innervation (see Section 1.2.2.2). The fetal/infant pattern (at 31 weeks, birth and 7 months) was compared to the adult pattern (at 41 and 54 years). In adult muscles, innervation was exclusively mono-neuronal (with either single or multiple endplates per fibre); at 7 months of age, both mono- and poly-neuronal innervation was found (and both in both cases, with single or multiple endplates) (Figure 1.1). Multi-innervation (multiple endplates) was ≈ 25% at 7 months, and decreased with age; conversely, the size of each endplate and the degree of its fragmentation increased with age.

1.2.5 The human NMJ in health

To date (and 25 years after its first publication) the primary reference work on the human NMJ in health remains the seminal paper by Slater et al from 1992; the methods, results and conclusions of this study are therefore discussed in some detail below. The morphology of the 'normal' human NMJ has been described (albeit intermittently) both prior to this work and in the intervening years (see other sections) but usually as the control for another research question or pathology, rather than the main focus of an independent study.

Slater et al (1992) described the structure and function of human NMJs in *vastus lateralis*, obtained at motor point biopsy, in 9 individuals (22-44 years). The patients were in 2 groups: one with muscle pain of unknown origin, the other with primary myopathic conditions. Nerve conduction was normal in all patients excluding primary neurogenic disturbances. A variety of techniques were utilized, including both light and electron microscopy, and various electrophysiological approaches. The structural studies (1-4) included assessment of: 1) muscle fibres, 2) intramuscular nerves, 3) subneural apparatus and 4) ultrastructure. In total, approximately 200-300 NMJs were quantified.

Muscle fibre diameters averaged 50-60μm, with fibre type proportions of 40% (type 1, slow twitch) and 60% (type 2, fast twitch). Intramuscular nerves displayed a predominantly T1 innervation pattern (Tuffery, 1971) with 5-10% sprouts, 15% collaterals (Barker and Ip, 1966) and a functional terminal innervation ratio (FTIR) of ≈ 1.10 (Coërs and Woolf, 1959; FTIR is defined later, see Section 4.4.1.4). These innervation data are in keeping with previous results reported by Coërs and Woolf (1959) and Engel (1986) for other human muscles (*deltoid, biceps, brachioradialis, flexor carpi radialis, vastus medialis* and *tibialis anterior*).

The 'subneural apparatus' (motor endplate) on light microscopy was small and fragmented (average length ≈ 40μm, average area ≈ 200μm^2, approximately 5-6 fragments per endplate), with the AChE distribution extending slightly beyond the footprint of the AChR clusters. Endplate area was found to correlate positively with fibre diameter, in keeping with similar results in other species (mouse, Harris and Ribchester, 1979; frog, Kuno et al, 1971).

Ultrastructure was defined in relation to 18 pre- and post-synaptic variables on transverse sections (based on the method described by Engel and Santa, 1971). Of particular note, the derived variable 'occupancy' as described here and applied to human NMJs (≈ 40% in *VL*), has been the source of much contention and confusion in the intervening years, leading to the spurious notion of 'partial occupancy' of human NMJs (discussed in detail in Section 4.4.1.3; see also Figure 4.4).

From a functional point of view, the extensive junctional folding of the motor endplate was presumed to explain the 'safety factor' for neurotransmission at the human NMJ (Slater, 2003), with a post-synaptic to pre-synaptic membrane area ratio of ≈ 20 to 1 (absolute =

1616μm^2 : 79μm^2), since the nerve terminals were otherwise small, with low quantal content. This observation was contrasted with the essentially pre-synaptic mechanism of safety factor homeostasis in species with larger nerve terminals and higher quantal content, such as the frog, with a post-synaptic to pre-synaptic area ratio of only 2.5 to 1 (= 3000μm^2 : 1200μm^2) (Torri-Tarelli et al, 1990; frog *cutaneous pectoris* muscle).

1.2.6 The human NMJ in disease

Although the NMJ is a pathological target in several neuromuscular disorders (either as the primary focus or a secondary consequence), the morphological changes at the NMJ have been largely determined from animal models of disease, with pathological effects at the human NMJ being described relatively intermittently.

1.2.6.1 Myasthenia gravis (MG)

Myasthenia gravis is an autoimmune disease characterized by a reduction in the number of AChRs at the NMJ, which presents clinically as weakness and fatigue of specific muscles (Vincent, 2002).

Morphologically, a spectrum of changes are seen at the NMJ both pre- and post-synaptically, ranging from mild to severe. The key structural abnormality is the loss of post-junctional folding, with distortion of the primary and secondary synaptic clefts (Engel and Santa, 1971; Albuquerque et al, 1976; *intercostal* muscles in both studies). These post-synaptic changes are coupled with a reduction in the size of nerve terminals (and the number of synaptic vesicles) and eventual denervation. The observation of leucocytic cells within the synaptic clefts reflects the autoimmune pathogenesis of the condition (Albuquerque et al, 1976).

1.2.6.2 Lambert-Eaton myasthenic syndrome (LEMS)

The Lambert-Eaton myasthenic syndrome (LEMS) is an autoimmune disease characterized by a reduction in the release of acetylcholine at the NMJ, which presents clinically as muscle weakness (Titulaer et al, 2011).

The ultrastructural abnormality at the NMJ is confined to the post-synaptic membrane, although the findings themselves differ between studies. Initial descriptions of characteristic hypertrophy of the junctional folds (Engel and Santa, 1971; *intercostals*) are in complete

contrast to later reports of a decrease in the length of the post-synaptic membrane, due to atrophy of the junctional folds (Tsujihata et al, 1987, *biceps brachii*; Hesselmans et al, 1992, *intercostals*). The dimensions of the nerve terminal are not changed, and no significant differences are observed at light microscopy (Hesselmans et al, 1992). At the molecular level however, changes are described in the pre-synaptic 'active zones' (see Chapter 5), with a decrease in both size and density in LEMS (Fukunaga et al, 1982; Engel et al, 1987).

1.2.6.3 Congenital myasthenic syndromes (CMS)

The congenital myasthenic syndromes (CMS) are a diverse group of genetic disorders that present in a similar manner to myasthenia gravis and the Lambert-Eaton myasthenic syndrome, but in contrast, have a non-immune aetiology (Engel et al, 2015).

The morphological changes in congenital myasthenia are equally heterogeneous, and vary considerably between individual patients. In cases where the structural abnormalities are confined to the motor endplate, post-synaptic changes range from elongation of the endplate (Vincent et al, 1981; *intercostals*) to almost total loss of secondary synaptic clefts (Smit et al, 1984; *soleus*). Where loss of nerve terminals has also been reported, atrophic junctional folds with unusual 'labyrinthine membranous networks' have been described (Engel et al, 1977; *intercostals*, *extensor digitorum*).

1.2.6.4 Motor neuron disease (ALS and SMA)

Amyotrophic lateral sclerosis (ALS) is an adult-onset condition characterized by progressive degeneration of motor neurons (Rowland and Shneider, 2001). Spinal muscular atrophy (SMA) is an inherited paediatric disorder caused by loss or mutation of the *survival motor neuron 1* (*SMN1*) gene, leading to reduced levels of SMN protein and motor neuron dysfunction (Burghes and Beattie, 2009). Both diseases lead to premature death, usually from respiratory failure. As noted earlier, an increasing body of evidence implicates the NMJ in the early pathogenesis of both conditions (Murray et al, 2010).

In ALS, earlier studies of fine structure report a variety of morphological abnormalities at the NMJ. In keeping with the dying-back mechanism of distal axonopathy (Maselli et al, 1993), denuded post-synpatic regions are a feature of NMJs on electron microscopic analysis, although the junctional folds in the denuded regions are usually well preserved (Tsujihata et

al, 1984; *biceps brachii*). Similar preservation of the secondary synaptic clefts has been described in the NMJs of laryngeal muscles in ALS (Yoshihara et al, 1998), along with an increase in the size of some endplates. Endplate elongation and segmentation (fragmentation) has also been reported on light microscopic analysis of NMJs in both ALS and more benign forms of MND (Bjornskov et al, 1975; *intercostals*).

A more recent study investigating the role of muscle histone deacetylase 4 upregulation in ALS demonstrated clear evidence of NMJ denervation on confocal microscopy (Bruneteau et al, 2013; *deltoid* and *anconeus*). The same study demonstrated (pathological) fragmentation and reinnervation of ALS endplates; in light of the present findings however, these NMJs appear no different to many of the healthy human NMJs described later (Chapter 4), lying well within the accepted range of normal variation.

In SMA, both pre- and post-synaptic defects have been described on confocal microscopy. These defects include neurofilament accumulation and poor nerve terminal arborization (Kariya et al, 2008; infant of 6 months, *diaphragm*) and smaller, non-perforated endplates (Harding et al, 2015; child of 10 years, *diaphragm*) compared to age-matched controls. As noted earlier, the development and maturation of the normal human NMJ is only poorly understood (Sections 1.2.3 and 1.2.4), so these findings represent early insights rather than definitive observations.

1.2.6.5 Duchenne muscular dystrophy (DMD)

Duchenne muscular dystrophy is a genetic disease caused by mutations in the *dystrophin* gene (Blake et al, 2002); *dystrophin* protein is essential for muscle integrity, and its absence leads to muscle weakness and eventual respiratory failure (Nowak and Davies, 2004). Historically, the origin of the pathology (neurogenic vs myogenic) remained obscure for many years, with the abnormalities noted on electron microscopy shedding no real light on the underlying cause.

At the NMJ, the characteristic ultrastructural finding is focal atrophy of the postsynaptic folds, without degeneration of the nerve terminals (Jerusalem et al, 1974; *peroneus brevis*). In addition, there is separation of the nerve terminal from the motor endplate, but in contrast to denervating conditions (e.g. peripheral neuropathy, ALS, SMA, peroneal muscular atrophy*)

there is no evidence of dissection of the terminal from the endplate by invading Schwann cells (Harriman, 1976; mainly *vastus medialis*). [*Charcot–Marie–Tooth disease.]

1.2.6.6 Miscellaneous conditions

NMJs have been studied in cases of muscle paralysis caused by infective agents. In patients with chronic botulism (caused by *Clostridium botulinum*), NMJs are characterized by pre-synaptic changes (similar to those of motor neurone disease; Section 1.2.6.4), including shrunken nerve terminals and denuded motor endplates (Tsujihata et al, 1987; *biceps brachii*). In the post-polio syndrome (PPS; the sequela to the condition caused by the poliovirus), abnormalities of the NMJ are common (fragmentation and dispersion of the endplate) but not invariable (with frequently normal ultrastructure), and are not considered pathognomonic of the syndrome (Maselli et al, 1995; *anconeus* and *peroneus brevis*).

Finally, motor point biopsy of patients with hemiplegia (Chokroverty et al, 1976; *vastus medialis* and *peroneus brevis*) has demonstrated NMJs with very complex appearances, including endplates with ring-like, chain-like and plexiform morphologies, although again, these appearances are not necessarily pathological (as will be discussed in reference to the current work; Chapters 4 and 5).

1.3 Aims of project

The primary aim of the project was to provide the first comprehensive description of the cellular and molecular architecture of the human neuromuscular junction.

On review of the existing literature, the absence of similar previous studies almost certainly relates to the technical difficulties associated with obtaining healthy human tissue of sufficient quality and quantity to perform large-scale data analysis. Thus, one of the major technical hurdles to overcome was establishing the necessary methods and protocols to achieve robust and reliable sampling of human NMJs.

Furthermore, since there is no accepted standard for NMJ analysis at present, it was also necessary to develop and validate a robust system for quantifying NMJ morphology before proceeding to the human work. This exercise facilitated a comparative study of natural

variation in mouse NMJs, using a number of advanced statistical approaches for large-scale data analysis that were subsequently applied to the human study.

Having established these methodological approaches, it was then possible to address the primary research hypotheses, and attempt to establish:

1. The degree to which human NMJ morphology differs from that of other mammalian species, such as rodents.

2. Whether or not the human NMJ undergoes synaptic destabilization with age, typical of other mammals such as rodents.

3. To what extent the molecular organization of the human NMJ is adapted in parallel with any cellular differences, in relation to active zone architecture and proteomic composition.

Chapter 2

NMJ-morph

2.1 Chapter summary

This chapter discusses the development and validation of a new approach to morphometric analysis of the neuromuscular junction – 'NMJ-morph'. Existing morphometric techniques are critically reviewed and expanded upon to develop standardized image acquisition and thresholding approaches, using a subset of muscles from the mouse study (Chapter 3). To validate the approach, 2 independent investigators used NMJ-morph to analyze a series of 600 NMJs, and the effects of sample size and inter-user variability were assessed.

2.2 Introduction

Historically, the earliest approaches to visualizing the NMJ used gold and silver techniques to demonstrate 'en grappe' (grape-like) and 'en plaque' (plate-like) nerve terminals in various vertebrate species (Tschiriew, 1879 and Kühne, 1887; respectively). With the advent of cholinesterase staining (Koelle and Friedenwald, 1949) both the pre- and post-synaptic components of the NMJ could be visualized. Subsequent studies of muscle innervation in various mammalian species utilized these combined techniques (Coërs and Woolf, 1959; Figure 1.2) and a wide variety of qualitative methods have since been used to categorize nerve terminals (e.g. Tuffery, 1971) and motor endplates (e.g. Harris and Ribchester, 1979).

With the advent of immunohistochemistry, confocal microscopy and modern computer software, the possibilities for quantitative approaches to morphometric analysis have increased exponentially. To date however, no general consensus or accepted standard exists, preventing the easy comparison of data from different research groups, and complicating future studies of NMJ morphology.

To address this problem, existing approaches to NMJ morphometry were used as the starting point for developing a comprehensive and fully validated software-based approach to NMJ analysis, with the aim of providing a standard methodology for future work. This methodology ('NMJ-morph') was then utilized throughout the project.

2.3 Methods

A subset of muscles forming part of a wider morphological study of mouse NMJs (Chapter 3) was first used to develop and validate a robust ImageJ-based methodology for quantifying NMJs (NMJ-morph). The following sections describe the image acquisition and analysis protocol; muscle dissection and NMJ immunohistochemistry is described along with the experimental design of the mouse study in Chapter 3.

In this initial series of experiments, 600 NMJs from the *1st deep lumbrical* muscle of the pelvic limb (hindlimb) were imaged and analyzed. Data was pooled from the right/left muscle pairs of 6 mice (3 male, 3 female); 50 NMJs were imaged in each muscle.

2.3.1 Image acquisition

Images were acquired on a Zeiss LSM 710 confocal microscope. The aim with each image was to capture a single en face NMJ and a short length of its terminal axon in the centre of the field of view. This determined the basic settings of x63 magnification and x1.5–2.0 optical zoom. Standard 8 bit pixel images provided an adequate range for capturing the variation in labeling intensity, with the power/gain/offset adjusted accordingly for each NMJ to utilize the full 8 bit range, with minimal over- and under-saturation.

Given the anticipated volume of imaging (a total of 8385 NMJs for the entire project), it was important to establish an appropriate work rate from the outset. A single NMJ was imaged using different combinations of frame size and z stack interval to determine the best compromise between image quality and acquisition rate (Figure 2.1).

Frame sizes of 128x128 and 256x256 were unsatisfactory, with images appearing too 'pixelated'. Conversely, there were no major differences in image quality at frame sizes of 512x512 and 1024x1024. These latter frame sizes were then compared using different z stack intervals. With a frame of 1024x1024 pixels and an optimal z stack interval (sub-micron, approximately 30 slices), images took around 5 minutes to acquire. With a 512x512 frame and 1μm interval (approximately 10 slices), images took only a minute or so to acquire, with no significant difference in the quality of the maximum intensity projections; these settings were utilized for all subsequent imaging.

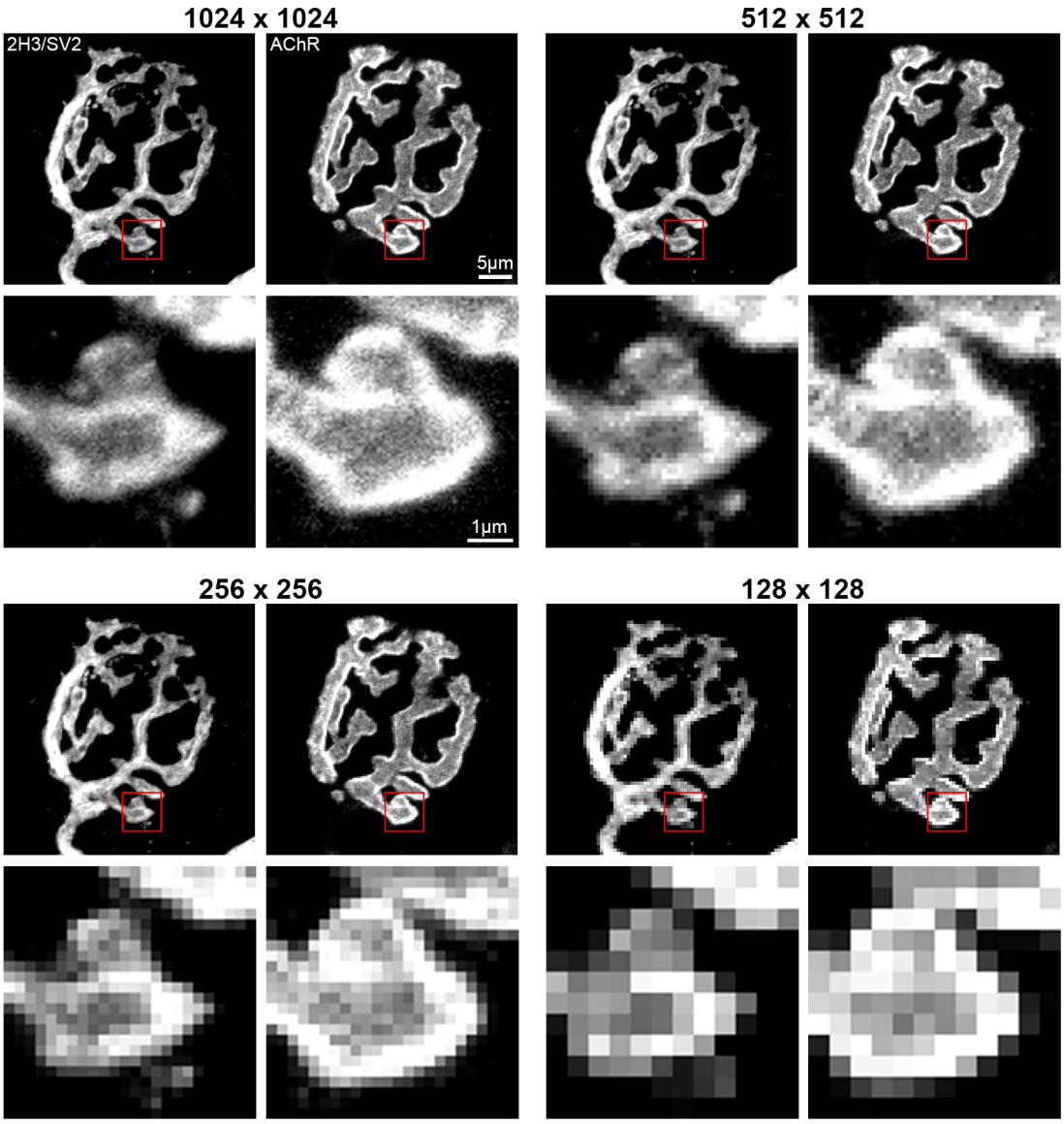

Figure 2.1 | Image acquisition
The same NMJ has been imaged at 4 different frame sizes: 1024x1024, 512x512, 256x256 and 128x128 pixels. The boxed area in red (highlighting a single nerve terminal bouton and accompanying AChRs) has been enlarged to emphasize the difference in image quality between varying frame sizes. Frame sizes of 256x256 and 128x128 are too pixelated. The 1024x1024 image was captured with an optimal z stack interval (sub-micron, ≈ 30 slices) in over 5 minutes. The 512x512 image was captured with a 1µm interval (≈ 10 slices) in only 1 minute. The latter combination of frame size and z stack interval (512x512 pixels and 1µm interval) provided the best compromise between image quality and acquisition time. Scale bars = 5µm and 1µm. *Note:* In this and other figures, the abbreviation '2H3/SV2' is used to inicate the labeling of pre-synaptic neurofilament and synaptic vesicle proteins, with reference to the specific epitopes of these proteins that the antibodies are raised against.

2.3.2 Image selection

Figure 2.2a illustrates two examples of completely en face NMJs, ideal for quantification. An adequate length of terminal axon is captured, and the overall image intensity is well balanced, with a minimal degree of over- and under-saturation. These examples were the 'gold standard' for image analysis. For NMJs captured at varying degrees of obliquity to the image plane (often only apparent on the maximum intensity projection, Figure 2.2b), images were only selected for quantification if the oblique portion represented < 10% of the total endplate area. Borderline NMJs were only included (if required) to achieve an adequate sample size (see Section 2.4.1.2). Grossly oblique and side-on NMJs were rejected. Based on these selection criteria, 6340 NMJs were selected for analysis from a total image bank of 8385 NMJs (a yield of ≈ 75%).

2.3.3 Image thresholding

Following image selection, the maximum intensity projections were converted to a binary format for analysis using ImageJ. To set the threshold of the binary image, two copies of the maximum intensity projection were opened simultaneously in ImageJ; the first was used as a reference, while selecting the threshold for the second.

Accurate thresholding of images was of paramount importance to the subsequent analysis, and a systematic approach to thresholding was adopted (Figure 2.3). The various automatic thresholding algorithms in Image J (17 in total) were trialed in the initial series of 600 NMJs. The *'Huang'* threshold (Huang and Wang, 1995) provided the most accurate binary representation of the NMJ in the majority of images (79%); the *'Yen'* (Yen et al, 1995) threshold was more suitable in a small minority of images (3%). In the remaining images (18%), none of the automatic methods were appropriate, and the threshold was adjusted manually.

Thresholded images were cleaned of extraneous background noise using the 'despeckle' and 'paintbrush' functions in ImageJ. These 'cleaned' NMJ images were then quantified using NMJ-morph.

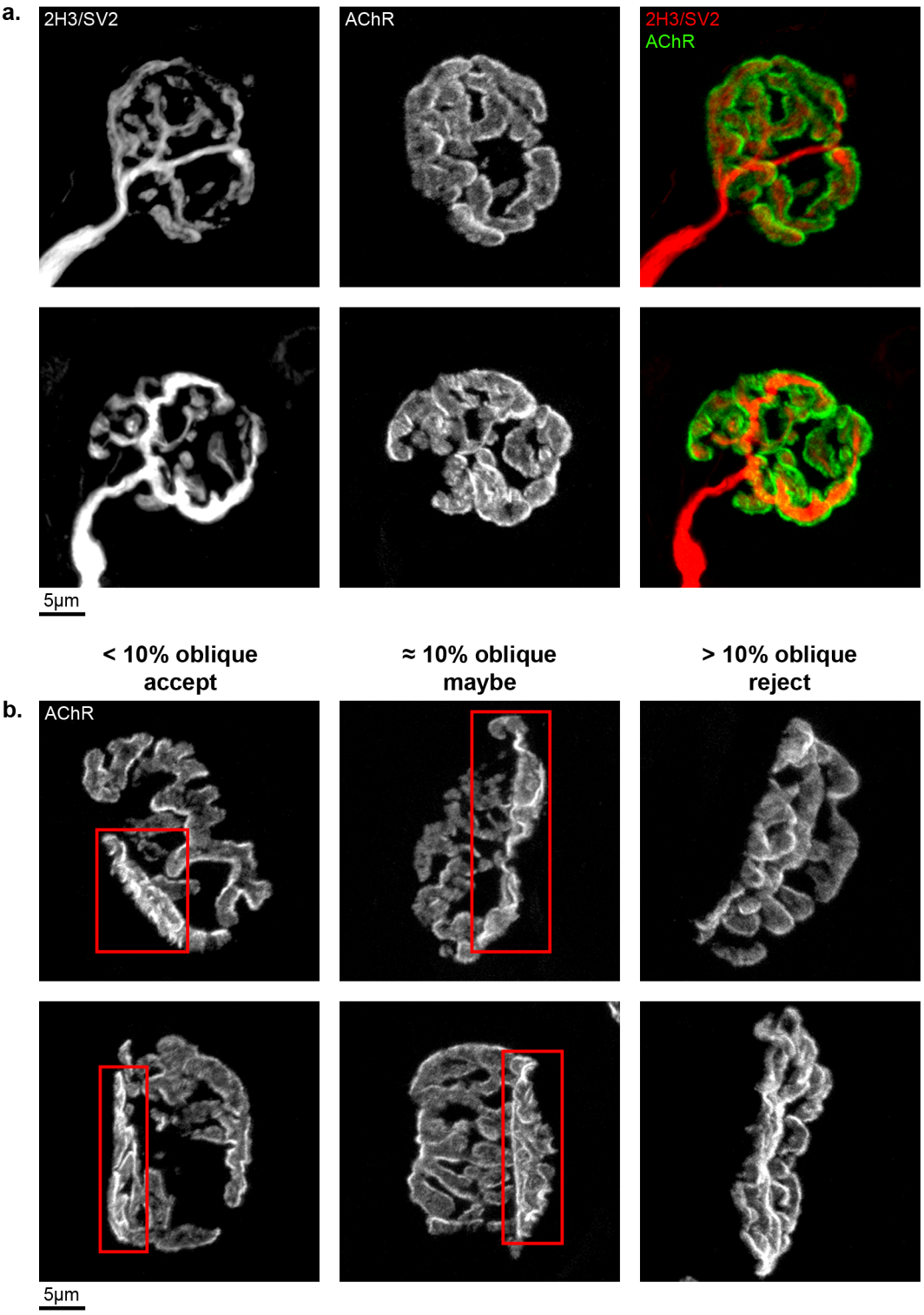

Figure 2.2 | Image selection
Criteria for robust image selection. **a.** Examples of 'en face' NMJs. All parts of the endplate are facing the image plane; these images are the 'gold standard' for quantification.
b. Example NMJs captured at varying degrees of obliquity to the image plane. NMJs with an oblique portion representing <10% of the total endplate area (on inspection) were included in the analysis (left); side-on NMJs (and those clearly >10% oblique) were rejected (right). Borderline NMJs (middle) were only included (on occasion) to achieve an adequate sample size of 40 NMJs per muscle, required for accurate reporting of mean values (see Figure 2.7). Scale bar = 5µm.

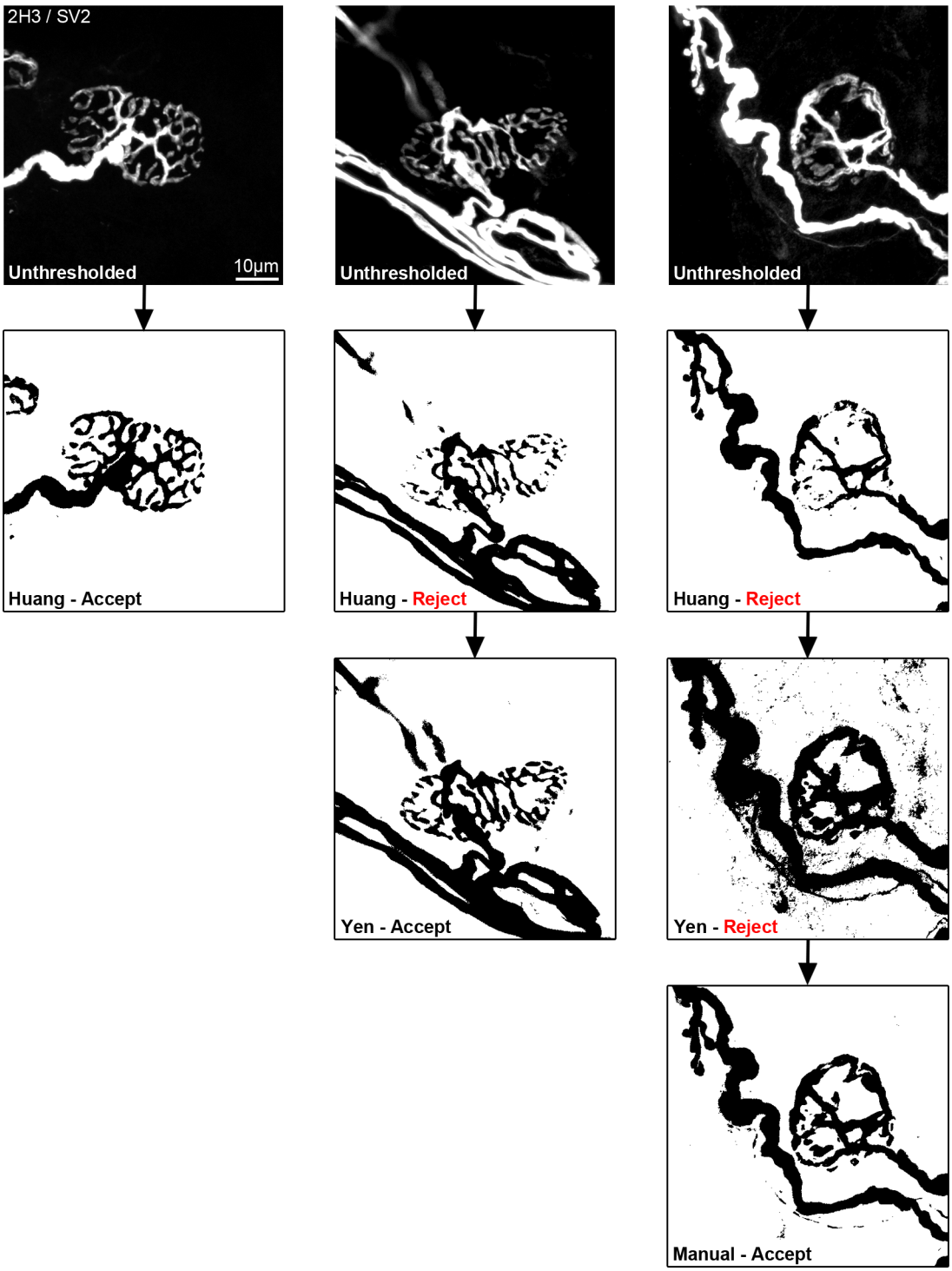

Figure 2.3 | Image thresholding
Accurate thresholding of images was of paramount importance for subsequent image quantification. A systematic approach to thresholding is demonstrated. For the majority of images (79%) the Huang method provided the most accurate thresholding (left panels). A small minority of images (3%) were better represented with the Yen method (middle panels), whilst the remaining images (18%) required manual thresholding (right panels).
Scale bar = 10µm.

2.3.4 NMJ-morph

The complete developed workflow, NMJ-morph (Jones et al, 2016), is illustrated in Figure 2.4. In total, 21 individual morphological variables were defined, including 18 direct measurements of pre- and post-synaptic structure, along with 3 associated nerve and muscle variables. The pre- and post-synaptic measurements were grouped into 11 'core' and 7 'derived' variables. A complete list of variables can be found in Tables 3.1 and 4.2.

2.3.4.1 Pre- and post-synaptic variables

Basic dimensions, such as the area, perimeter and diameter of pre- and post-synaptic structures, were measured using standard ImageJ functions, and comprised the majority of the 'core variables' (Figure 2.4 and Tables 3.1, 3.2, 4.2, 4.3). Step-by-step details of the individual measurements are described in Appendix 1 (NMJ-morph User Guide).

Measurement of nerve terminal branching was more involved. Previous studies have often used complex terminology to define branches – proximal and distal segments (Tomas et al, 1990), orders of branching (Prakash et al, 1996) – all of which are impractical for large volume data acquisition. To simplify measurement and avoid ambiguity in defining branches, the 'skeletonize' function was used to generate a one-pixel-thick 'skeleton' of the nerve terminals. Terminal branches (Hopkins et al, 1985) and branch points were then easily defined. The counting procedure was automated using an ImageJ plugin – BinaryConnectivity (Landini, 2008). BinaryConnectivity has been used in a similar manner to describe motor endplate branching (Pratt et al, 2013, 2015), but this is the first time it has been applied to nerve terminal branching (Figure 2.5).

The individual branch measurements were combined into a single index termed 'complexity'. Previous methods for generating a single descriptive pre-synaptic index have ranged from relatively straightforward (e.g. length of branches × number of branch points/ 100; Tomas et al, 1990) to more complex (e.g. average distance between points of origin of secondary branches on primary branch; Prakash et al, 1996). The following derivation was used, with a logarithmic scale to provide a more convenient numerical value:

$$Complexity = Log_{10}(No.\ Terminal\ Branches \times No.\ Branch\ Points \times Total\ Length\ of\ Branches)$$

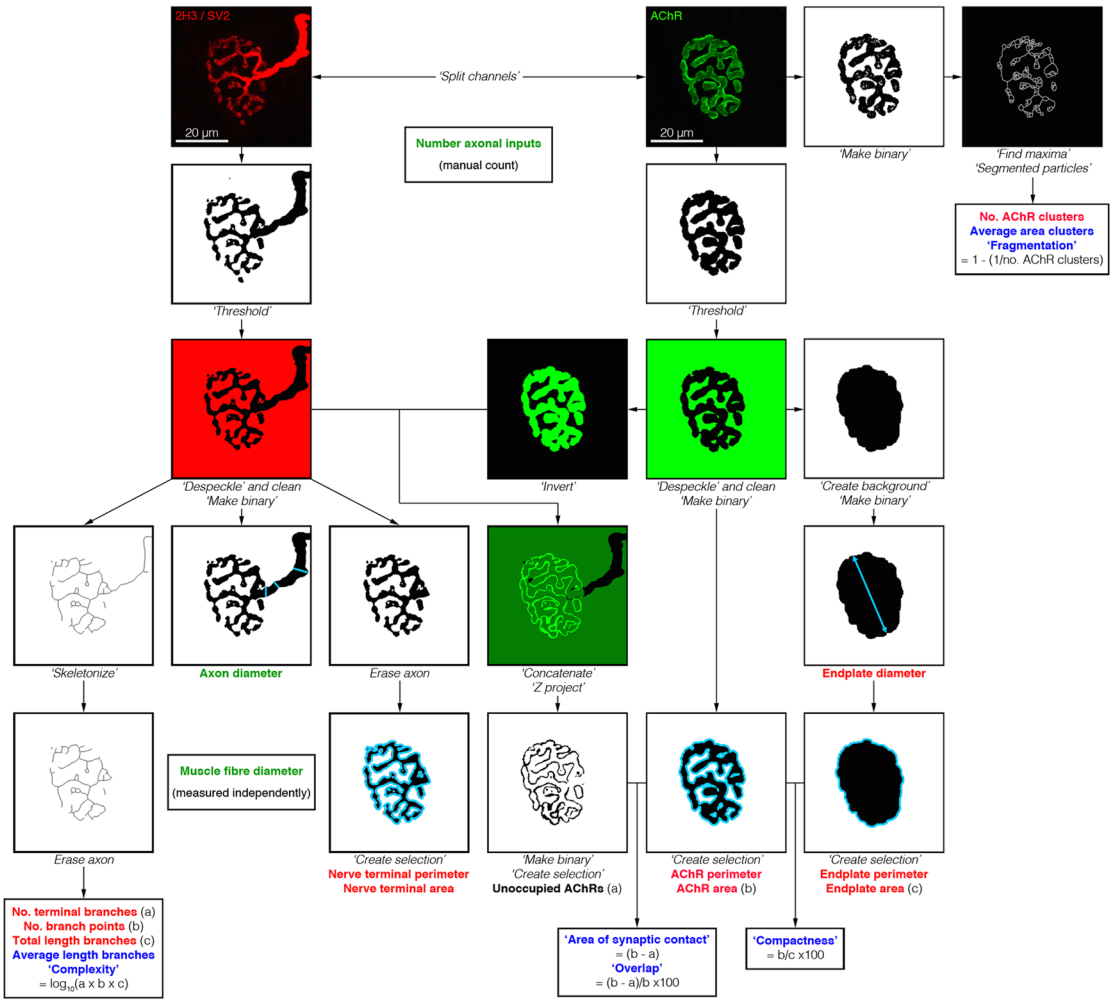

Figure 2.4 | NMJ-morph
Flowchart of image analysis using 'NMJ-morph'. For each NMJ, 21 individual morphological variables were quantified: the 11 'core variables' are shown in red typeface, the 7 'derived variables' in blue and the 3 'associated nerve & muscle variables' in green. Specific operations within NMJ-morph are shown in italics. Scale bar = 20µm.

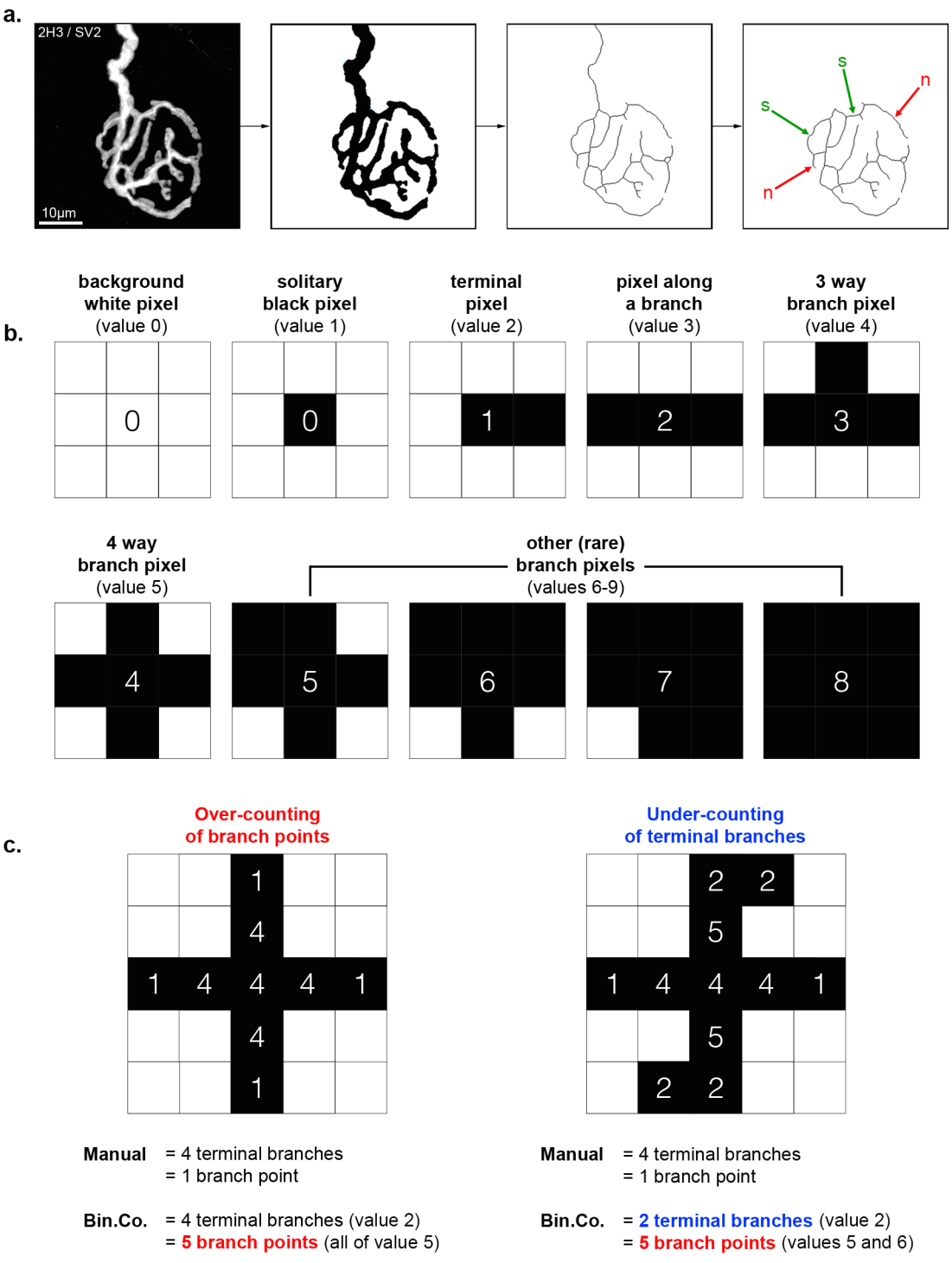

Figure 2.5 | Binary connectivity analyses
Branch analysis of NMJs was performed using the BinaryConnectivity plugin. **a.** Binary images were first 'skeletonized' to produce a one-pixel-wide 'skeleton'. Terminal branches (n) and intermediate segments (s) are labelled. **b.** BinaryConnectivity calculates the total number of different pixel types ('values' 0-9) in the binary image; the 10 types of pixel ('values' 0-9) are shown in the centres of the 3x3 grids. The number in the centre pixel refers to the number of neighbouring black pixels. The number of terminal branches (n) in the skeleton is given by the total of the value 2 pixels. The number of branch points is given by the sum of the value 4 and 5 pixels, to which a correction factor was applied to compensate for the 'over-counting' and 'under-counting' of pixels, as shown in **c.**

As before, basic endplate dimensions were measured using standard ImageJ functions. Counting the number of discrete AChR clusters that comprised the endplate was more problematic. Although previous studies report simple manual counts (Kong and Anderson, 1999), this was difficult in practice, particularly when the edges of AChR clusters were ill defined or lying in close proximity. This difficulty was circumnavigated by using the 'segmented particles' function to resolve the endplate into discrete clusters that could be easily counted (Figure 2.6). This function is a type of 'watershed segmentation for grayscale images that provides a means of automatically separating particles that touch' (Ferreira and Rasband, 2012).

The number of AChR clusters was then used to derive a 'fragmentation' index, whereby endplates comprised of a single cluster were designated a numerical value of zero (0), and highly fragmented endplates tended towards a numerical value of one (1):

$$Fragmentation = 1 - (1 / Number\ of\ AChR\ Clusters)$$

The area of the AChR clusters was also expressed in relation to the area of the endplate (or 'footprint') and defined as the 'compactness' of the endplate:

$$Compactness = (AChR\ Area / Endplate\ Area) \times 100$$

This same derivation has been used in previous studies and termed 'dispersion' (Pratt et al , 2013; Deschenes et al, 2013), although 'compactness' seems a more appropriate descriptor for the number of clusters in a given area. Furthermore, it helps to draw a clearer distinction between this characteristic and the 'fragmentation' of the endplate.

Two further variables were defined, providing information about pre- and post-synaptic 'coupling' of the NMJ. Although the nerve terminal and AChR area provide important structural information, the exact 'area of synaptic contact' between the two is more important from a functional point of view, and was calculated as follows (after a similar method by Prakash et al, 1996):

$$Area\ of\ Synaptic\ Contact = Total\ Area\ of\ AChRs - Unoccupied\ Area\ of\ AChRs$$

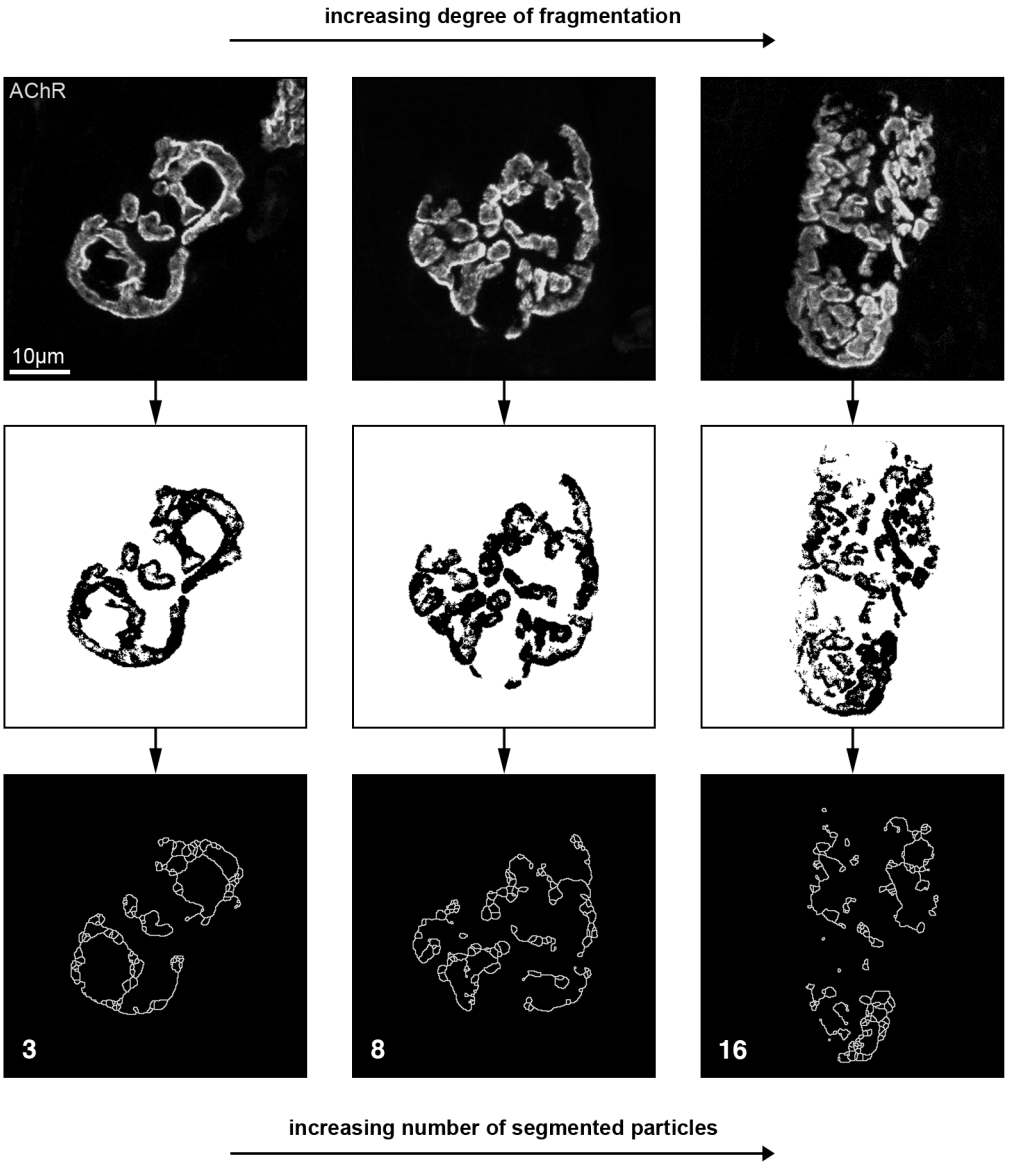

Figure 2.6 | Segmented particles analyses
The segmented particles function provided a reproducible means of counting the number of AChR clusters per endplate. The example endplates have been arranged in order of increasing fragmentation (from left to right) based on visual assessment (top panels). The original images have been converted to binary versions (middle panels) and the segmented particles function has then been applied (bottom panels). The number of discrete 'segmented particles' (individual clusters) in each image (3, 8 and 16 respectively) reflects the increasing degree of endplate fragmentation in this series. Scale bar = 10µm.

The area of synaptic contact (or occupied area of AChRs) was finally expressed in relation to the total area of AChRs, to determine the 'overlap' of the pre- and post-synaptic structures:

$$Overlap = Area\ of\ Synaptic\ Contact / Total\ Area\ AChRs \times 100$$

Since 'overlap' describes the degree to which the nerve terminals overlap the AChR clusters, it provides an exact measure of the 'occupancy' of AChRs. The term occupancy is typically used in relation to pathology, where partially occupied and vacant AChRs/endplates are a key hallmark of dying back pathology (e.g. ALS and SMA) and Wallerian degeneration (Murray et al, 2010). Previous studies have tended to rely on semi-quantitative measures of occupancy, assigning NMJs on inspection to various categories, ranging from vacant to partially or fully occupied (Parson et al, 2004). Thus, the present derived variable 'overlap' offers a means of calculating an exact 'percentage occupancy by area'.

2.3.4.2 Associated nerve and muscle variables

These included the number of axonal inputs to the NMJ (to indicate mono- or poly-innervation), and measurement of motor axon and muscle fibre diameter. The axonal variables were assessed on the confocal images. Measurements of muscle fibre diameter were performed on separate images: after confocal imaging, slide preparations were re-imaged at x20 magnification using an Olympus IX71 light microscope fitted with a Hamamatsu C4742-95 camera. Images were captured with Openlab Improvision software and measurement of muscle fibre diameter was performed manually in ImageJ.

2.3.5 Validation of NMJ-morph

To determine the accuracy and reproducibility of data obtained using NMJ-morph, a second investigator performed an independent analysis of the same series of 600 NMJs, on a separate workstation. Correlation analyses were performed to determine the degree of inter-user variability, and the effect of sample size on the estimation of mean values was investigated.

2.4 Results and Discussion

The biological significance of NMJ morphology in the *1st deep lumbrical* muscle is discussed as part of the wider mouse study (Chapter 3). The focus in the following sections is on the validation of NMJ-morph. The datasets obtained by the two investigators were compared using GraphPad Prism software. Spreadsheets were manually checked for data input errors prior to analysis.

2.4.1 Validation of NMJ-morph

Results are summarized in Figure 2.7 and the remainder of the analysis is collected together in Appendix 2.

2.4.1.1 Inter-user variability

An inconsistent approach to thresholding can lead to significant problems with image analysis. It was therefore important, from the outset, to address the potential impact of user-dependent thresholding decisions on the data generated using NMJ-morph. In the present series of 600 NMJs, investigator 1 selected the *Huang* threshold for 83% of the images (14% manual, 3% *Yen*), whilst investigator 2 selected *Huang* for 74% of the images (22% manual, 4% *Yen*). Overall, the two investigators selected the same threshold (either *Huang, Yen* or manual) for 77% of the images, suggesting a generally consistent approach to thresholding.

The results for each NMJ variable were then correlated between the 2 investigators (Figure 2.7, Appendix 2). Despite the user-dependent variations in thresholding and the manual measurement of some variables (e.g. axon diameter), concordance between the two investigators was strong for all NMJ variables. Correlation coefficients (r) ranged from 0.844 (axon diameter) to 0.999 (4 variables: endplate area, endplate perimeter, number AChR cluesters, fragmentation), with $p < 0.0001$ for all variables. The pre-synaptic variables displayed a greater range in correlation coefficients (0.844 to 0.983) compared to the post-synaptic variables (0.990 to 0.999), reflecting the manual aspects of some parts of the pre-synaptic analysis.

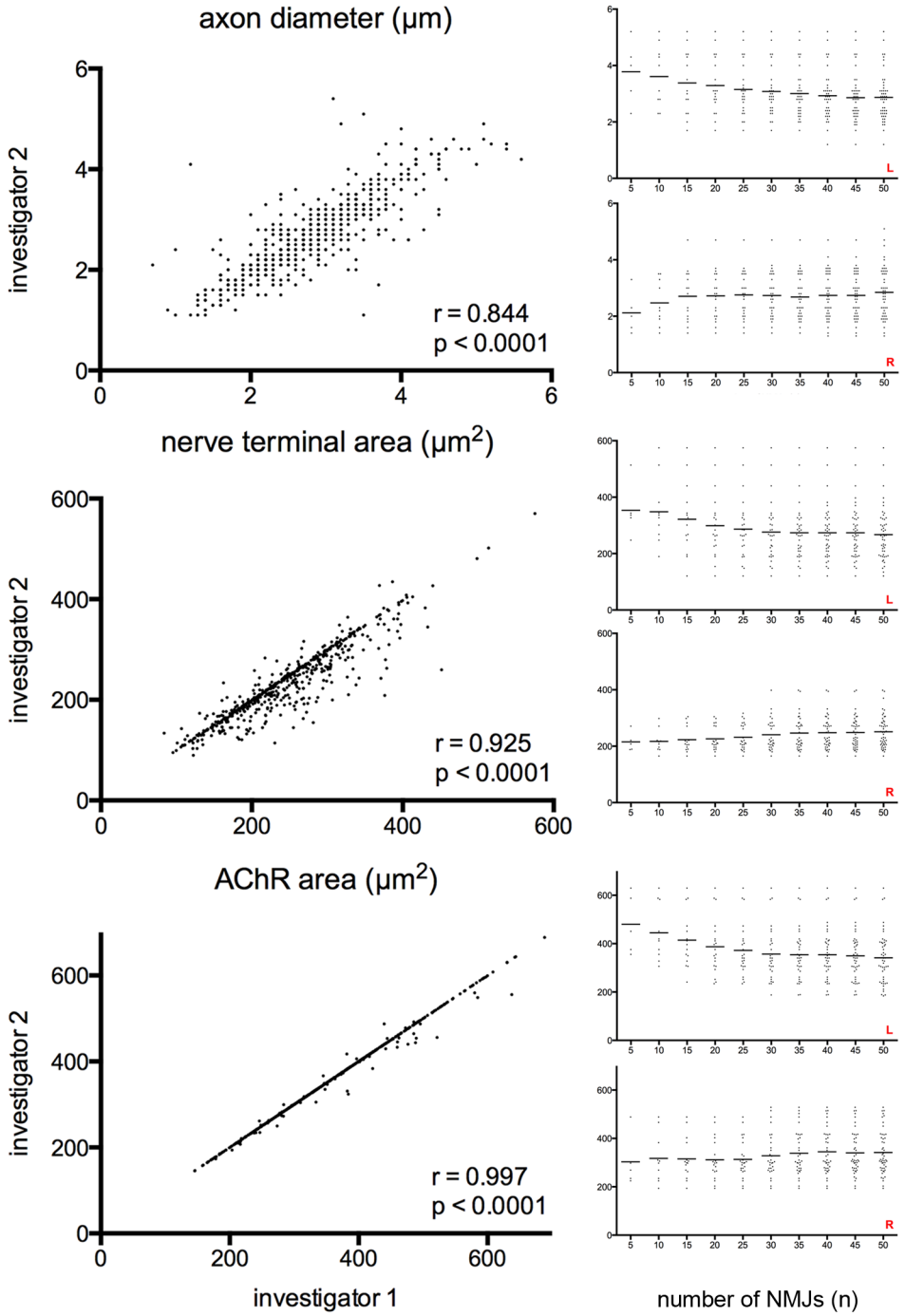

Figure 2.7 | Validation of NMJ-morph
Two independent investigators used NMJ-morph to analyze a series of 600 NMJs. The effect of inter-user variability (left panels) and sample size (right panels) was assessed. Strong concordance between investigators was demonstrated for all measured variables. The example scatterplots (left) demonstrate the range in correlation coefficients, from lowest (axon diameter) to highest (AChR area). For all variables, inter-observer correlation was high ($r \geq 0.844$) and statistically significant ($p < 0.0001$). Pearson correlation. Sample size was also crucial for accurate reporting of mean values (right). Each plot is constructed from a single sample of 50 NMJs (from an individual muscle, left or right). Increasing the number of NMJs resulted in a gradual plateauing of the mean; on the basis of these data, a sample of 40 NMJs per muscle was used to calculate mean values. See Appendix 2 for other variables.

The strength and significance of these correlation analyses were critical to the success of NMJ-morph as a robust and reliable platform for morphometric data acquisition. Only after this rigorous validation process was NMJ-morph used for the other parts of the project.

2.4.1.2 Effect of sample size

The initial series of NMJs was also used to assess the effect of sample size on the accuracy of reported mean values. For each of the variables in Figure 2.7, the NMJ sample from a left/right pair of lumbricals is shown, demonstrating the effect on the mean of gradually increasing the sample size in increments of 5 NMJs. As expected, a gradual plateauing of the mean occurred with increasing sample size (in some instances by a non-monotonic convergence towards a consistent mean, as seen in the lowermost graph). Based on these observations, sample sizes of 40 NMJs per muscle were used to report mean values throughout the remainder of the study (Chapters 3 and 4).

2.4.2 Sexual dimorphism

The dataset for this test series comprised 600 NMJs pooled from 3 male and 3 female mice, 2 muscles per mouse (right/left pair), 50 NMJs per muscle. The mean weights for the mice were: male, 33.0g (individual weights: 32.7g, 32.8g, 33.5g) and female, 25.3g (24.5g, 24.9g, 26.5g). There were no significant differences in NMJ morphology when comparing male and female mice, nor was there any correlation between NMJ morphology and body weight. Due to the lack of sexual dimorphism, the remainder of the mouse study (Chapter 3) was therefore focused on a single sex (arbitrarily females), to reduce the (nevertheless significant) volume of data processing. The effects of animal weight and muscle fibre diameter are further explored in the mouse study (Chapter 3).

2.4.3 Caveats and limitations of NMJ-morph

In recommending NMJ-morph for general use beyond the present study (e.g. by other laboratories), there are several caveats (and potential limitations) that must be taken into account by future users, in order to obtain the very best results that this approach can offer.

Firstly, to ensure the highest degree of correlation/reproducibility between datasets, any images that cannot be accurately rendered using the *'Huang'* threshold (accurate in ≈ 80% of images; Section 2.3.3) are best discarded from the analysis at the outset. For users more

familiar with NMJ-morph, the yield of the dataset can of course be increased with the inclusion of manual or *'Yen'* thresholding, since the small user-dependent differences (in experienced hands) have no significant effect on data reproducibility (Section 2.4.1.1).

Secondly, in situations where the signal-to-noise ratio of the images is lower than in the present study, it is inevitable that more images will require manual thresholding, resulting in greater variability between investigators. Such situations may occur in pathology, during development, or with simultaneous study of NMJ structure and function, where intense labelling may not be consistent with normal function. More challenging analyses such as these highlight the importance of thresholding one copy of an image with reference to the original, to ensure that the binary reproduction is an accurate version of the original image.

The third point to highlight concerns the *absolute* accuracy of the measurements obtained. Thresholded, binary images are a pre-requisite for most of the automated functions within ImageJ, and NMJ-morph is both quick and reliable if the workflow is applied systematically. If *absolute* accuracy of individual measurements is a priority, however, the analysis of raw, unthresholded images is likely to prove superior, where subtly different judgements can be made for individual NMJs (e.g. precise boundaries of AChR clusters). Inevitably, this approach is more time consuming, but may be the preferred option in certain settings.

Finally, if confocal microscopy is not available (or not possible, e.g. simultaneous recording of structure/function in the same NMJ), a similar standardized approach using wide field fluorescence microscopy can be utilized in conjunction with NMJ-morph analysis (data not shown), but confocal z-stack projections are recommended for optimal results.

Chapter 3

Natural variation of the mouse NMJ

3.1 Chapter summary

This chapter considers various factors influencing the natural morphological variation of mouse NMJs. NMJ-morph was used to quantify NMJ morphology in 9 anatomically distinct muscles from a single litter of wild type mice. A number of advanced statistical approaches were then used to assess the degree of NMJ variation both within and between individual muscles and animals, and investigate the influence of the pre- and post-synaptic cells (motor axon and muscle fibre). These results were used to guide the design and interpretation of the subsequent human NMJ study (Chapter 4).

3.2 Introduction

Despite the commonplace use of mouse models of neuromuscular disease (Burgess et al, 2016), surprisingly little has been documented on the normal morphology and natural variation of the mouse NMJ (and even less in the way of comparative anatomy; Section 1.2.1), although the consequences of natural selection on genetic variation in the mouse have been studied (Guénet and Bonhomme, 2003; Reuveni et al, 2010).

Certain key muscles are routinely used in studies of NMJ structure, function and pathology, including: *levator auris longus* (Angaut-Petit et al, 1987; Eržen et al, 2000; Murray et al, 2010) and the other cranial muscles: *abductor auris longus, auricularis dorsalis** and *interscutularis* (Murray et al, 2010), the *lumbrical* muscles (Clark et al, 1987; Sleigh et al, 2014), *triangularis sterni* (McArdle et al, 1981), *diaphragm* (Wu and Mei, 2013) and *transversus abdominis* (Murray et al, 2014). All of the aforementioned muscles have the advantage of being small and/or thin enough for whole-mount preparation, which has in addition facilitated the description of individual muscle 'connectomes' (e.g. *interscutularis*, Lu et al, 2009; *4th deep lumbrical* muscle, Hirst and Ribchester, 2013). Despite these applications, there remains a lack of basic knowledge concerning the normal/comparative morphology of the NMJs in these muscles. [*The synonym *auricularis 'superior'* is often encountered in the literature. In quadrupeds however, 'dorsal' is a more suitable term when referencing the anatomical position.]

One of the key aims of this chapter therefore was to gather basic data about the normal morphology and natural variation of the mouse NMJ, in addition to developing the statistical approaches that could be applied to the human NMJ study.

3.3 Methods

A single litter of adult CD1 mice (6 male, 6 female) was selected for study, at approximately 6-8 weeks of age. During the initial development of NMJ-morph (Chapter 2), no significant differences in NMJ-morphology were found when comparing male and female mice, and the study therefore focused on a single sex (arbitrarily females). All mouse experiments were covered by the appropriate project (PPL) and personal (PIL) licenses granted by the UK Home Office.

3.3.1 Muscle selection

Nine distinct muscles were selected from three anatomical regions. The muscles chosen were: *interscutularis*, *levator auris longus – rostral* and *levator auris longus – caudal* from the cranial region, *triceps brachii* and the *2nd* and *4th lumbrical* muscles from the thoracic limb (forelimb), and *quadriceps femoris* and the *1st* and *4th lumbrical* muscles from the pelvic limb (hindlimb). The initial plan was to include the *1st* and *4th lumbrical* muscles from both limbs, but it was not possible to reliably harvest the *1st lumbrical* muscle from the pelvic limb due to its small size and variable morphology.

In selecting the muscles for study, a broad range of criteria were taken into consideration, to anticipate possible differences in NMJ morphology on a purely regional basis. These criteria included representation of all body regions, proximal and distal positions within the limbs, functional homology of muscle groups, differing nerve supply, etc. All muscle selected are in routine experimental use (Murray et al, 2010; Sleigh et al, 2014).

In the present study, the 2 parts of *levator auris longus* (*rostral* and *caudal* bands) were treated as separate muscles, despite the shared nerve supply (facial nerve), based on the differential vulnerability that is known to exist in SMA (Murray et al, 2010). In contrast, *triceps* and *quadriceps* were treated as single discrete muscles (with a single nerve supplying all individual parts; radial and femoral nerves, respectively), as were the individual *lumbrical*

muscles selected (each with a different nerve supply, including contributions from the median and ulnar nerves, the medial and lateral plantar nerves, and the sural nerve).

3.3.2 Muscle dissection and NMJ immunohistochemistry

Mice were sacrificed by overdose of inhaled isoflurane, weighed and the selected muscles dissected out from both sides within 30 minutes post-mortem. Muscles were fixed in 4% paraformaldehyde (PFA) for 30 minutes then washed in 1x phosphate buffered saline (1xPBS). All residual connective tissue was then removed. Muscles suitable for whole-mount (*cranial* and *lumbrical* muscles) where immediately prepared according the immunohistochemistry protocol below. The larger muscles that required sectioning (*triceps, quadriceps*) were first cryoprotected by immersion in 30% sucrose overnight. After rinsing in 1xPBS, 100μm sections were cut on a Thermo Scientific Microm HM 450/KS 34 freezing microtome.

Neuromuscular junctions (NMJs) were then labeled using a modified laboratory protocol for visualizing pre-synaptic 2H3/SV2 proteins (medium weight neurofilament/synaptic vesicle protein) and post-synaptic AChRs (Parson et al, 2004; Murray et al, 2010; Sleigh et al, 2014; Wishart et al, 2014). Muscles were placed in the following sequence of solutions (made up in 1xPBS unless otherwise specified): α-bungarotoxin (αBTX) for 30 minutes; 4% Triton X for 1½ hours; a blocking solution of 2% Triton X and 4% bovine serum albumin (BSA) for 30 minutes; the primary antibodies (made up in block) for 3 days at 4°C; 4 washes of 20 minutes with 1xPBS; additional blocking with 4% BSA for 30 minutes; the secondary antibodies (made up in 1xPBS) for 2½ hours; 4 washes of 20 minutes with 1xPBS. Muscles were mounted in Mowiol on glass slides, and stored at -20°C prior to imaging.

Antibodies

Primary: 1:50 mouse anti-2H3 IgG and 1:50 mouse anti-SV2 IgG (DSHB).
Secondary: 1:100 Cy3 AffiniPure donkey anti-mouse IgG (Jackson ImmunoResearch).
BTX: 1:500 FITC α-bungarotoxin (Biotium).

3.3.3 Confocal imaging and NMJ-morph analysis

Images of en face NMJs were captured with a Zeiss LSM 710 confocal microscope in a standardized manner (described in Chapter 2), with sequential image acquisition to

minimize bleed through (red channel – 543nm excitation, 565-615nm collection; green channel – 488nm excitation, 500-550nm collection). In total, 3090 NMJs were imaged, of which 2160 NMJs were selected for final analysis. Image analysis was performed using NMJ-morph as outlined in Chapter 2.

3.3.4 Measurement of muscle fibre diameter

After confocal imaging, slides were re-imaged at x20 magnification using an Olympus IX71 microscope and Hamamatsu C4742-95 camera. Images of the teased/sectioned muscles were captured with Openlab Improvision software and measurement of fibre diameter was performed manually in ImageJ. Individual muscle fibres were measured perpendicular to their long axis at 3 separate points, and an average taken. An equivalent number of muscle fibres to NMJs were measured (2160 muscle fibres in total).

3.4 Results and Discussion

In total, 2160 NMJs were analyzed from 9 distinct muscles (54 individual specimens). A number of statistical techniques were applied to the baseline data to determine the relative importance of different factors influencing the natural variation of NMJs.

3.4.1 Morphological heterogeneity of mouse NMJs

Initial qualitative comparisons of NMJs from the nine different muscles revealed a striking degree of heterogeneity in overall morphology (Figure 3.1). NMJs displayed marked differences in size, shape and complexity of both pre- and post-synaptic components. The extent of the natural variation in NMJ morphology was explored both within and between individual muscles.

3.4.1.1 Intra-muscle variability

Coefficients of variation calculated in collaboration with Martin W Simmen (Centre for Integrative Physiology, University of Edinburgh) using SPSS software.

Figure 3.2 demonstrates the degree of variability within a single stand-alone muscle. In this example, NMJs from one of the six *triceps brachii* specimens are illustrated. Endplates have been arranged in size order, and demonstrate a 3.4x fold difference in AChR area between

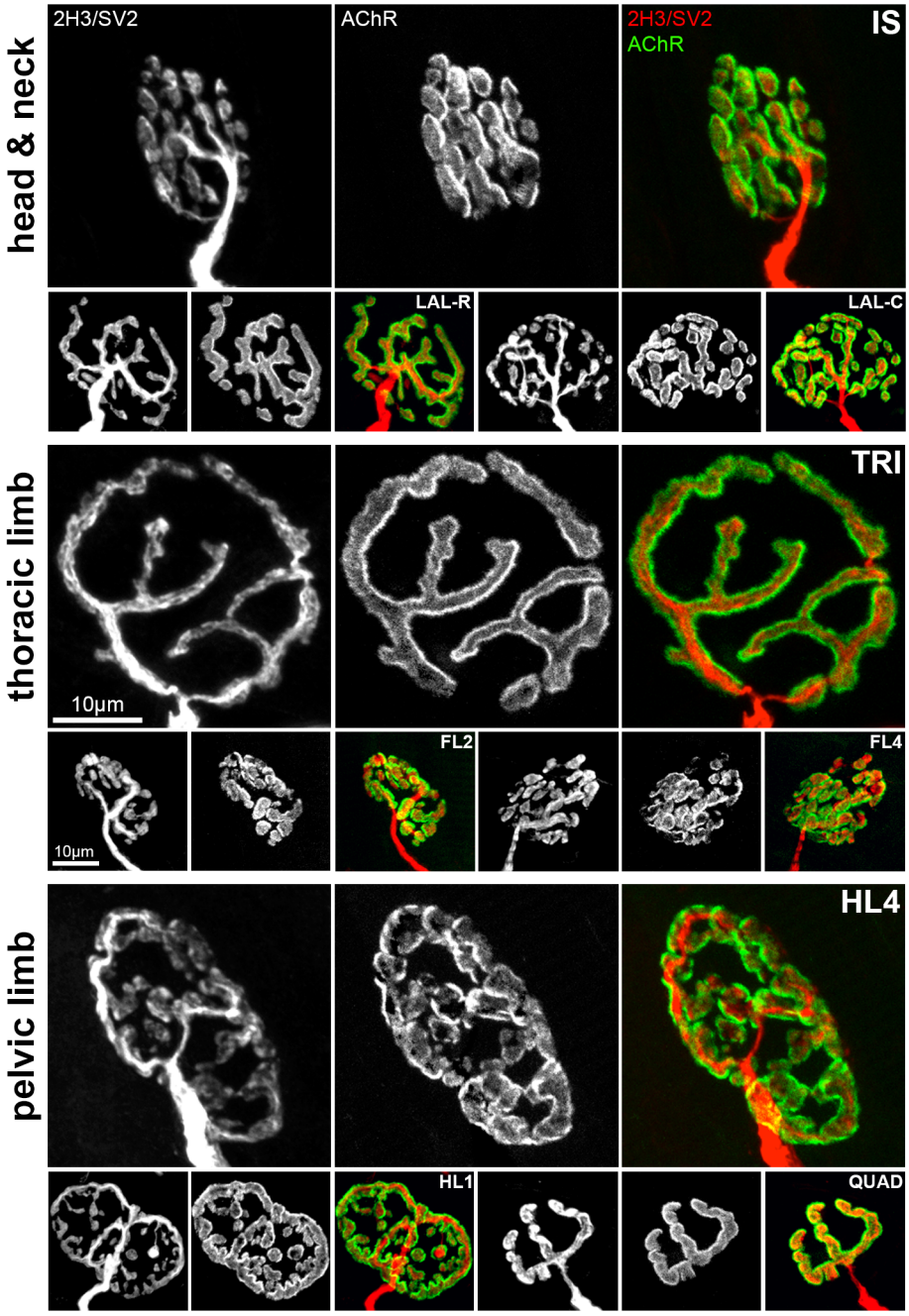

Figure 3.1 | Morphological heterogeneity of mouse NMJs
Example NMJs from 9 distinct muscles across 3 anatomical regions: head & neck, thoracic limb (or forelimb) and pelvic limb (or hindlimb). The NMJs display marked differences in size, shape and overall morphology, with no obvious relationship to body region or muscle fibre type. Abbreviations: interscutularis, IS; levator auris longus – rostral and caudal bands, LAL-R and LAL-C; triceps brachii, TRI; forelimb lumbricals 2 and 4, FL2 and FL4; quadriceps femoris, QUAD; hindlimb lumbricals 1 and 4, HL1 and HL4. Scale bar = 10µm.

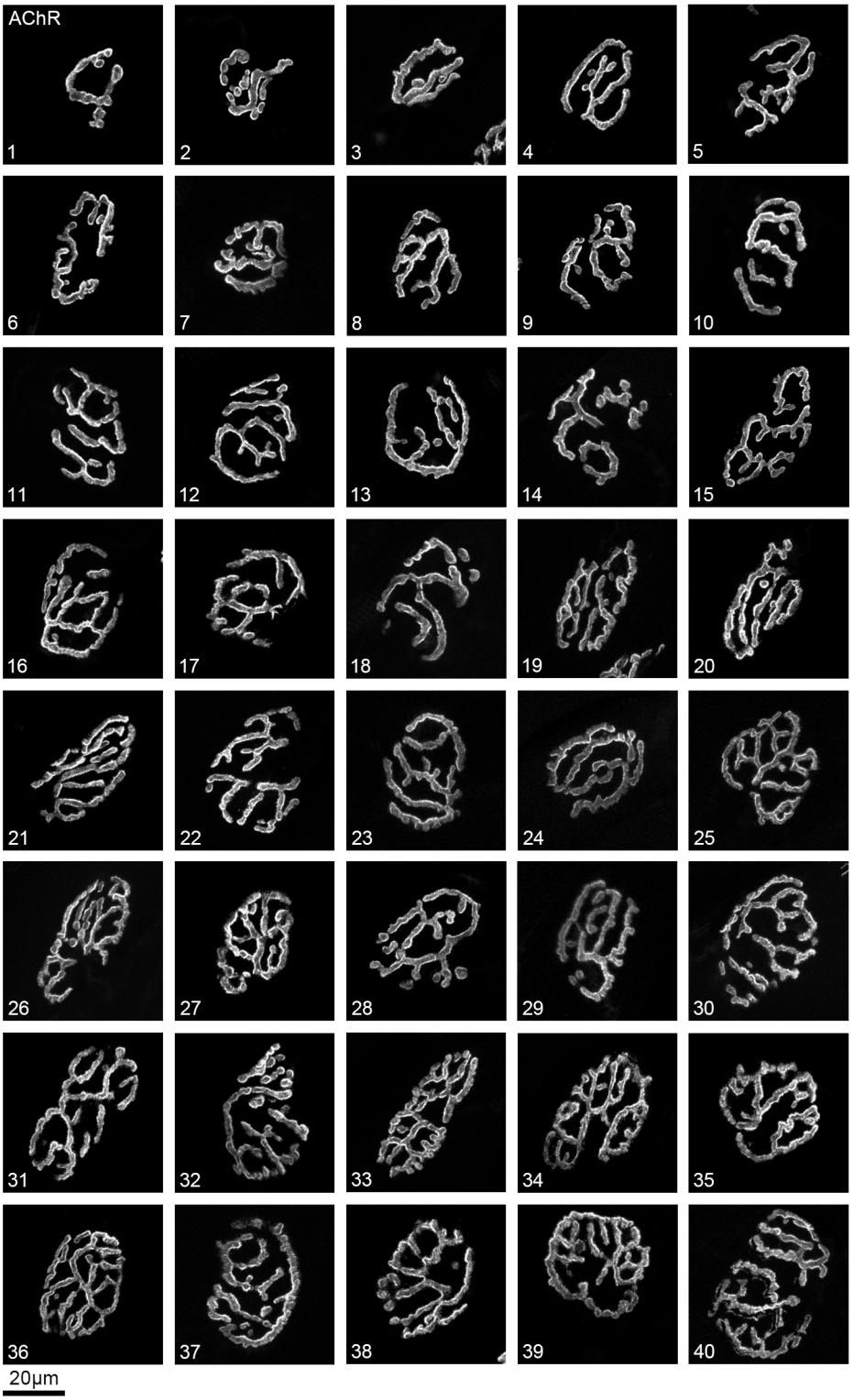

Figure 3.2 | Intra-muscle variation of mouse NMJs
A single sample of 40 NMJs from an individual muscle (triceps), arranged in size order (based on AChR area) from smallest to largest (images 1 to 40). There is a marked degree of natural variation in both the size and shape of individual NMJs within a single muscle, with a 3.4 fold difference in AChR area between the largest and smallest NMJs in this particular series (the sample mean falls between images 19 and 20). Scale bar = 20µm.

the smallest and largest NMJ. Each endplate also has a unique morphology with respect to the shape and arrangement of the AChR clusters. Qualitatively, a similar degree of variation was noted within the 54 individual specimens from the 9 different muscles.

To quantify this intra-muscle variability, the coefficient of variation (CV = standard deviation/mean) was calculated for each of the 11 core morphological variables in the 54 individual muscle specimens. The median CV was 0.30, with the central 90% of CVs ranging between 0.16 and 0.67. These results are in keeping with the observed variation in Figure 3.2 and reflect a substantial degree of intra-muscle variability. These results will be revisited in the context of human NMJ variability (Chapter 4).

3.4.1.2 Inter-muscle variability

NMJ morphology was then compared between the 9 different muscles from the 3 anatomical regions (Figure 3.3, Table 3.1, Appendix 3). In keeping with the qualitative observations (Figure 3.1), quantitative analyses confirmed significant inter-muscle variability in NMJ morphology between the 9 different muscles.

Average NMJ morphology in each of the 9 muscles was calculated for the 21 individual synaptic variables. For each variable, muscles were ranked in size order (Figure 3.3, Appendix 3) and the maximum/minimum values and fold-change differences between the top-ranked and bottom-ranked muscles were calculated (Table 3.1).

The associated nerve and muscle variables were at the extremes of these analyses. Muscle fibre diameter showed the single greatest fold difference (x3.21) between the top and bottom-ranked muscles (*quadriceps* and *2nd forelimb lumbrical*, respectively). Conversely, all NMJs examined were mono-innervated, entirely in keeping with the expected pattern in adult NMJs. With regard to the pre- and post-synaptic variables, average area of AChR clusters showed the greatest fold difference (x3.17) and complexity the smallest (x1.17).

'Overlap' showed the next smallest fold difference between the top and bottom-ranked muscles (x1.23), implying that the physical congruence between the pre- and post-synaptic components is highly conserved in all NMJs. Given this 'size matching' across the synapse, there was a striking *lack* of consistency in the muscle rankings for individual variables

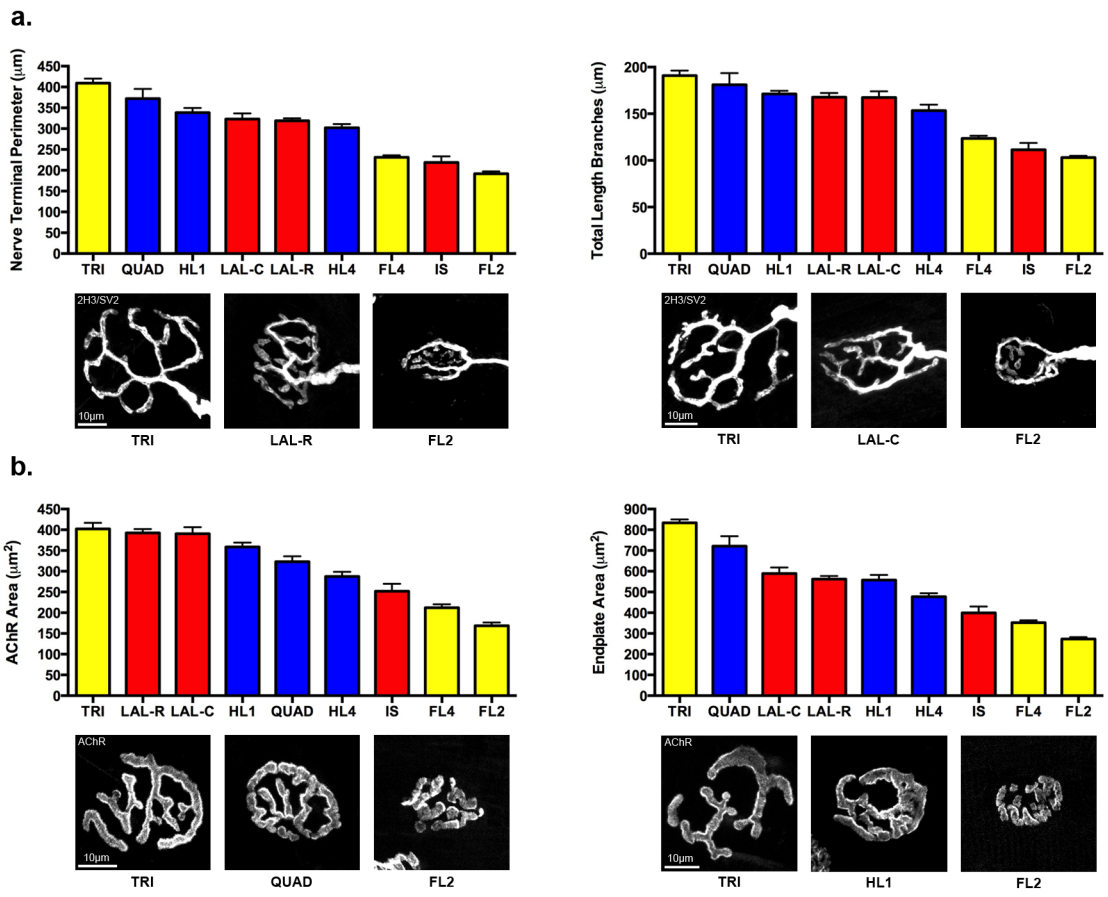

Figure 3.3 | Inter-muscle variation of mouse NMJs
Bar charts demonstrating the natural variation in NMJ morphology of 9 distinct muscles; 2 pre-synaptic and 2 post-synaptic variables are shown (**a.** and **b.** respectively). Muscles are ranked in size order and colour-coded to body region (head & neck, red; forelimb, yellow; hindlimb, blue). Each column depicts the mean (± SEM) of 240 NMJs (pooled from 3 left/right muscle pairs from 3 mice). The example images are an accurate representation of the mean values depicted on the bar charts (to within ± 5%), and correspond to the maximum, median and minimum values. There is no discernable relationship between NMJ morphology, muscle type or anatomical region. Scale bar = 10µm. See Figure 3.1 for abbreviations and Appendix 3 for other variables.

Baseline morphological data for mouse NMJ					
	maximum	mimimum	fold difference	correlation with axon diameter	correlation with muscle fibre diameter
core varaibles					
pre-synaptic					
1) nerve terminal area (μm^2)	287.1	159.0	1.81 ****	0.576 **	0.221 **
2) nerve terminal perimeter (μm)	409.2	192.0	2.13 ****	0.433 **	0.387 **
3) number of terminal branches	47	22	2.14 **	0.198 **	0.293 **
4) number of branch points	32	19	1.68 **	0.303 **	0.066 **
5) total length of branches (μm)	191.0	103.1	1.85 ****	0.471 **	0.311 **
post-synaptic					
6) AChR area (μm^2)	402.3	168.4	2.39 ****	0.528 **	0.235 **
7) AChR perimeter (μm)	400.4	199.1	2.01 ****	0.376 **	0.420 **
8) endplate area (μm^2)	834.0	273.6	3.05 ****	0.467 **	0.457 **
9) endplate perimeter (μm)	134.2	71.2	1.88 ****	0.429 **	0.474 **
10) endplate diameter (μm)	43.0	24.6	1.75 ****	0.449 **	0.429 **
11) number of AChR clusters	7.3	3.4	2.15 **	0.057 **	0.017
derived variables					
pre-synaptic					
12) average length of branches (μm)	6.1	4.5	1.35 **	0.110 **	-0.051 *
13) complexity	5.28	4.52	1.17 **	0.349 **	0.205 **
post-synaptic					
14) average area of AChR clusters (μm^2)	185.0	58.3	3.17 ***	0.185 **	0.029
15) fragmentation	0.78	0.53	1.47 **	-0.070 **	-0.046 *
16) compactness (%)	70.3	46.4	1.52 **	-0.010	-0.460 **
17) overlap (%)	71.4	57.9	1.23 *	0.065 **	-0.220 **
18) area of synaptic contact (μm^2)	266.0	115.2	2.31 ****	0.585 **	0.140 **
associated nerve & muscle variables					
19) axon diameter (μm)	3.3	2.3	1.43 ***		
20) muscle fibre diameter (μm)	57.1	17.8	3.21 ****		
21) number of axonal inputs	1	1	1.00		

Table 3.1 | Baseline morphological data for mouse NMJ
Maximum and minimum values for each variable correspond to the 'average' NMJ (mean of 240 NMJs) in the top and bottom ranked muscles (in Figure 3.3 and Appendix 3). Fold difference is between maximum and minimum values. Correlation coefficients (r) obtained from principal components analysis (PCA) of complete dataset (2160 NMJs). ****p<0.0001, ***p<0.001, **p<0.01, *p<0.05.

(compare the order of the muscles for each of the pre- and post-synaptic variables in Figure 3.3 and Appendix 3). Likewise, there was no logical grouping of NMJ variables by muscle type or anatomical region (e.g. NMJs in the forelimb muscles were found at each end of the spectrum; compare *triceps* and *2nd forelimb lumbrical* in Figure 3.3).

3.4.2 Principal components analysis

Principal components analysis performed in collaboration with Martin W Simmen (Centre for Integrative Physiology, University of Edinburgh) using SPSS software.

Given the absence of clear predictors of NMJ morphology based on muscle type or anatomical region, a more advanced statistical approach was employed in an attempt to determine underlying principles that could explain the observed heterogeneity.

A principal components analysis (PCA) was performed on the complete multivariate dataset in relation to the 11 'core' morphological variables at each of the 2160 individual NMJs (Figure 3.4 and Appendices 4 and 5). By systematically assessing the correlations between the variables, PCA identifies the 'principal components' that account for the majority of the variability within the dataset. In high-dimensional datasets (11 variables in the current analysis), PCA allows the data to be visualized in a much smaller number of dimensions or 'principal components' (typically just two or three) (Krzanowski, 1988).

PCA demonstrated that the majority of the variance within the dataset (81%) could be captured in a 2-dimensional plot (Figure 3.4), with the 1st principal component (PC1) accounting for ≈72% of the variance, and the 2nd principal component (PC2) accounting for a further ≈9%. In structural terms, the principal components PC1 and PC2 are best understood with reference to the PCA loading plot (Appendix 4), which shows the relative positions of the 11 'core' morphological variables.

On the PCA loading plot, the majority of 'size-related' variables (area, perimeter, diameter, length, etc) are found to cluster high up on the x-axis (PC1). Similarly, these 'size-related' variables show markedly positive correlations on the PCA matrix (Appendix 5). Thus, PC1 can be regarded as a measure of the 'overall size' of the NMJ.

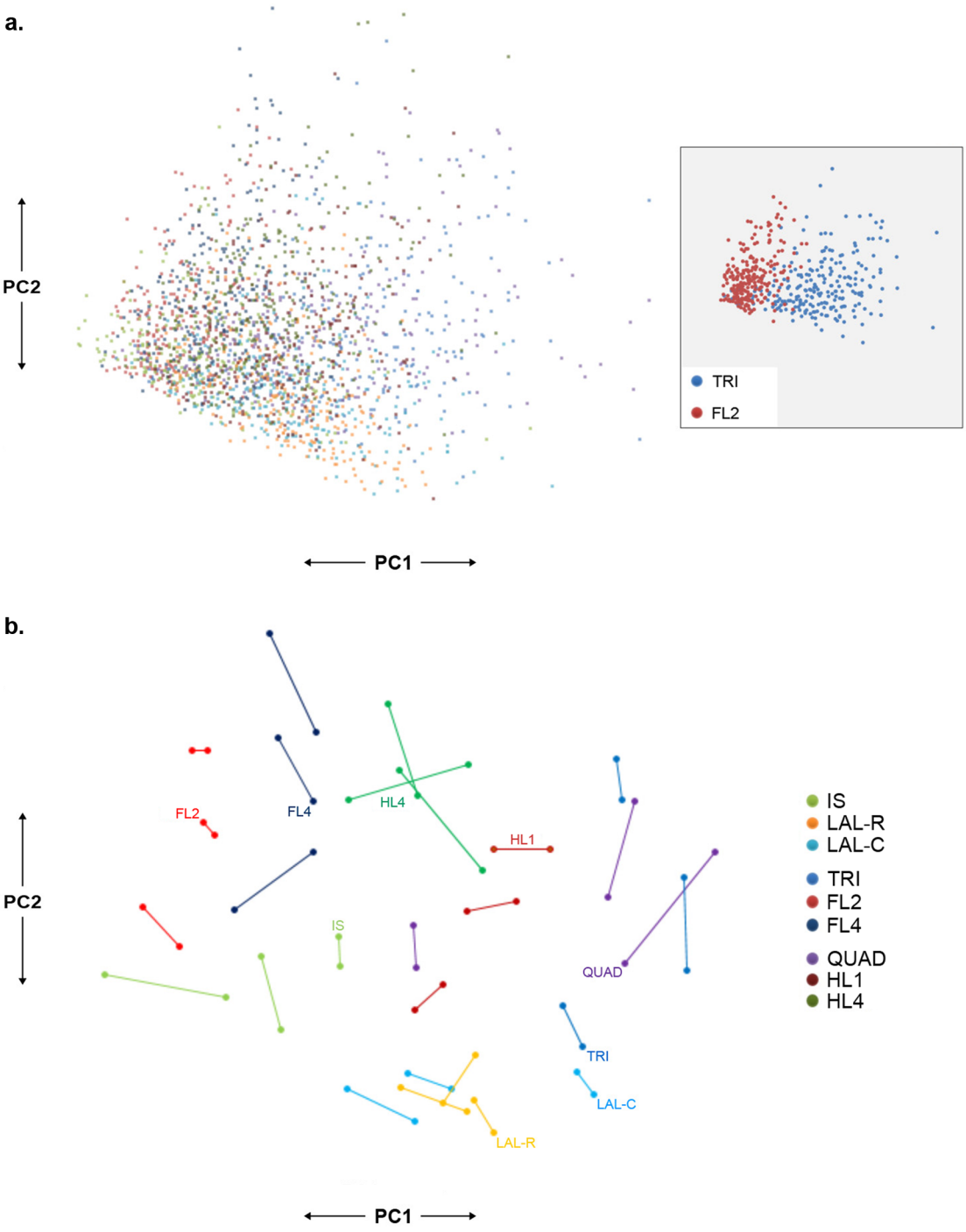

Figure 3.4 | Principal components analysis of mouse NMJs
2-dimensional principal components analysis (PCA) of mouse NMJs, based on the 11 'core' morphological variables. **a.** PCA map of the complete set of 2160 individual NMJs, colour-coded according to muscle type (as for panel **b.**). The x-axis displays the first principal component (PC1, co-ordinates from -3 to +5), the y-axis the second (PC2, -5 to +5). The boxed panel (inset) represents the same data, but is restricted to NMJs from triceps (TRI) and forelimb lumbrical 2 (FL2) only, illustrating the ability of PCA to separate morphologically distinct NMJs. **b.** PCA map derived from panel **a.** but aggregated over individual muscles (n = 9 left/right pairs per mouse) and animals (n = 3 mice). Each data-point represents a single muscle (left or right) from an individual animal, and is the centroid of the map positions for the 40 NMJs sampled. Left/right muscle pairs are connected by a line; one line has been labeled for each distinct muscle type. For both PC1 and PC2, co-ordinates run from -1.5 to +1.5.

In contrast, PC2 reflects a quite different physical characteristic of the NMJ. The number of AChR clusters isolate high up on the y-axis (PC2) of the PCA loading plot, separate from the 'size-related' variables. Along with the weaker correlation between the number of AChR clusters and the 'size-related' variables in the PCA matrix, PC2 can be regarded as a measure of NMJ 'fragmentation'.

Thus, the 2 principal components can be thought of as a 'distillation' of the 11 core variables into the essential physical characteristics that define the NMJ and its natural variation. A simple analogy is to consider natural variation in skull anatomy – a large number of individual variables can be measured (e.g. height, breadth, circumference, etc), but the overall variability may be dependent on a much smaller number of principal components (e.g. 'size of skull', 'shape of skull', etc) (Krzanowski, 1988).

In summary therefore, the PCA demonstrates that the observed variation in NMJ morphology is principally explained by differences in the 'overall size' of the NMJ, with 'fragmentation' making a small but significant contribution. It is equally true that the morphology of individual NMJs is not predicted (per se) by any single variable. Having determined and defined the principal components in this manner, a retrospective evaluation of the NMJs in Figure 3.1 clearly demonstrates that the physical characteristics of 'overall size' and 'fragmentation' do indeed account for the observed variation.

A similar standardized approach to NMJ morphometrics using principal components analysis and a Fiji-based algorithm (analogous to NMJ-morph) has also been used recently to provide insights into *Drosophila* NMJ morphology (Nijhof et al, 2016), although the approach utilized here was limited to 9 synaptic parameters. Interestingly however, PCA also identified NMJ size (≈38% of variance) and geometry (≈22% variance) as the principal components accounting for the majority of variation in *Drosophila* NMJs, suggesting that these 2 features of NMJ morphology may have differential molecular regulation.

3.4.3 Influence of pre- and post-synaptic cells

Having considered the pre- and post-synaptic variables in relation to morphological heterogeneity of the NMJ, the associated nerve and muscle variables were now considered (i.e. the pre- and post-synaptic cells themselves). The aim was to explore the tacit

assumption that the size of an NMJ is determined (simply and solely) by the size of the muscle fibre it innervates. Earlier studies have demonstrated correlations between neurotransmitter release and the size of both the nerve terminal (in the frog; Kuno et al, 1971) and the motor endplate (mouse; Harris and Ribchester, 1979). In addition, the relationship between endplate size and fibre diameter has been studied directly in 3 muscle groups of the rat (*levator palbebrae superioris*, *LPS*; *extensor digitorum longus*, *EDL* and *sternomastoid*; Oda, 1985). Here, linear correlations between endplate size and fibre diameter were demonstrated, with each muscle group having a characteristic ratio of endplate size to fibre diameter (much higher in *LPS* cf. *EDL*).

Furthermore, it is known that NMJs shrink and expand as muscle fibres atrophy and hypertrophy (Balice-Gordon et al, 1990; mouse, *bulbocavernosus* muscle) without loss or addition of junctional folds (simply changes to their spacing; rather like the pattern on a balloon as it is inflated). However, the factors that determine the ratio of endplate size to fibre diameter (Oda, 1985) remain unknown; hence, the primary question of what determines NMJ size remains unanswered.

To explore these relationships, the individual pre- and post-synaptic variables were correlated with the diameter/calibre of both axon and muscle fibre, independently, for the 'average' NMJ in each muscle (Figure 3.5 and Appendix 6). The associated correlation coefficients (r) and significance levels (p) were obtained for each pairing (Table 3.1).

For the majority of NMJ variables (13 out of 18), correlation coefficients were greater in relation to axon diameter (Table 3.1). In contrast, only 3 'core' variables correlated more strongly with muscle fibre diameter. These results suggest that the morphology of the NMJ is more closely linked with the physical characteristics of the pre-synaptic cell as represented by the motor axon.

The nature of these relationships also differed (Figure 3.5). For the majority of NMJ variables, the relationship with axon diameter was linear for all diameters of axon; the relationship with muscle fibre diameter was more complicated. Here, the initially strong linear relationship for the smaller caliber fibres (of *interscutularis*, *levator auris longus* and the

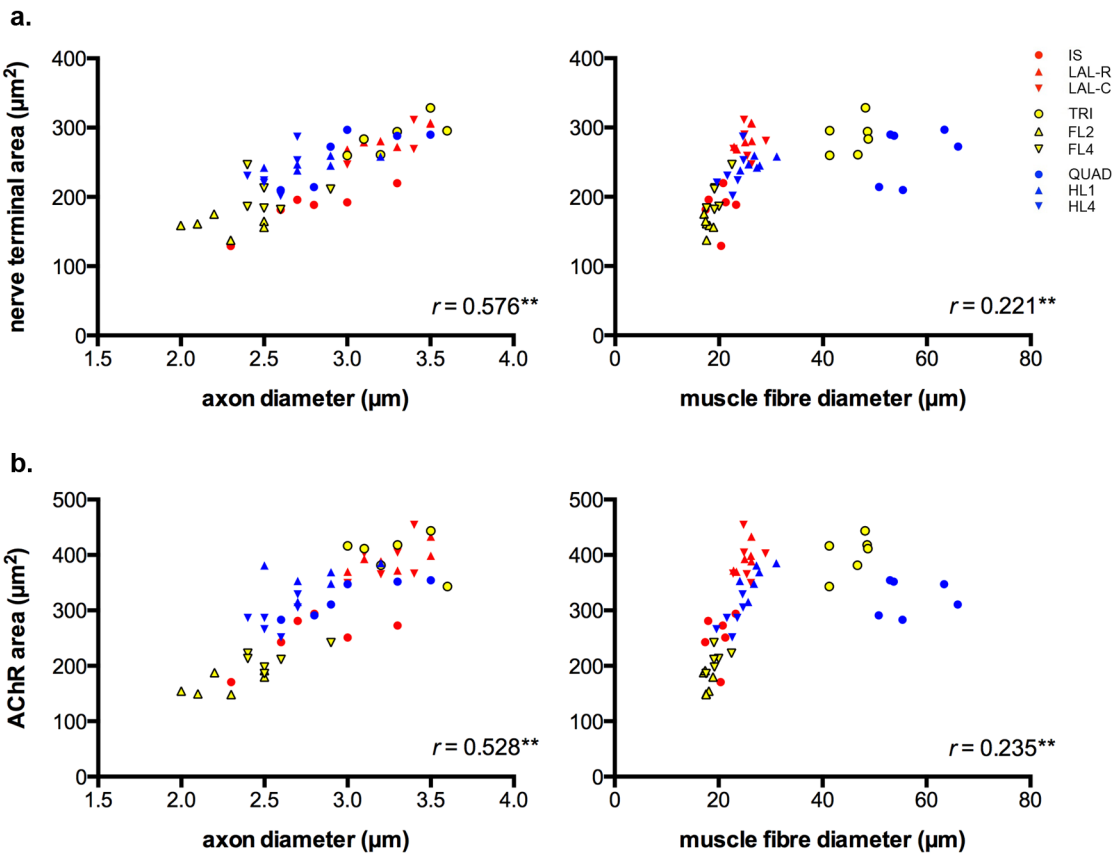

Figure 3.5 | Influence of pre- and post-synaptic cells on mouse NMJ morphology
Scatterplots of individual NMJ variables correlated with both axon and muscle fibre diameter; pre- and post-synaptic examples are shown (**a.** and **b.** respectively). Each data point represents the average NMJ for an individual muscle (the mean of 40 NMJs); 54 muscles are plotted in total (3 right/left pairs for each of the 9 distinct muscles). The majority of NMJ variables correlated more strongly with axon diameter. The relationship between NMJ morphology and muscle fibre diameter was non-linear, with muscles grouped in two subsets (cranials/lumbricals and triceps/quadriceps). Pearson correlation. **p< 0.01. See Figure 3.1 for abbreviations and Appendix 6 for other variables.

lumbrical muscles) was not continued for the larger caliber fibres (of the *triceps* and *quadriceps*). In the latter group, the observed NMJs were smaller (relative to fibre diameter) than the initial linear relationship would have predicted.

These observations suggest that the 'size' of an NMJ is not a simple function of the 'size' of the muscle fibres it innervates. However, it remains to be determined whether or not the stronger correlations with axon diameter imply a greater influence of the pre-synaptic cell. For example, retrograde signaling from the muscle fibre is thought to underpin intrinsic differences in the assembly and maintenance of NMJs in different muscles (Pun et al, 2002), but these observations are not synonymous with size correlation.

The discrepancy between the predicted and observed sizes of NMJs on the larger calibre muscle fibres (*triceps* and *quadriceps*), leading to an apparent 'plateauing' of NMJ size with increasing fibre calibre, has not been demonstrated in previous studies of endplate size and fibre diameter relationships (Oda, 1985). Here, distinct muscle groups (not including *triceps* and *quadriceps*) were noted to have a characteristic ratio of endplate size to fibre diameter (potentially reflecting the innervation of specific muscles by specific motor neuron pools; Buller et al, 1960; Guth, 1968) although the underlying factors that determine this correlation remain unknown. It is possible that the observed 'plateauing' of NMJ size with increasing fibre calibre could be explained by a 'volume limitation' of the pre-synaptic neuronal cytoplasm, i.e. that the total volume of a motor neuron is limited by what the metabolism of the cell can support, though this concept/hypothesis would need further exploration in future studies.

It is also of note that the relationship between NMJ morphology and muscle fibre diameter was independent of the 'size' of individual animals (by weight). No correlation was found between size of animal and size of NMJ, or between size of animal and size of muscle fibre (data not illustrated). The correlation between size of animal and size of NMJ is further explored in the human work (Chapter 4, Section 4.4.6).

3.4.4 Global factors influencing NMJ morphology

3-way ANOVA performed in collaboration with Martin W Simmen (Centre for Integrative Physiology, University of Edinburgh) using SPSS software.

Having explored the variability of NMJs within and between muscles (Section 3.4.1) and the influence of pre- and post-synaptic cells (Section 3.4.3) a number of 'global' factors were then investigated. By considering NMJs in a collective manner in relation to different 'defined' populations (i.e. a single muscle, a single side of the body, a single individual), additional statistical techniques were used to investigate the relative influence of each of these factors (muscle, side, individual) on NMJ morphology.

The graphs in Figure 3.6a and Appendix 7 illustrate the 'average' NMJ on each side of the body for 9 different muscles in 6 littermate mice (and for each NMJ variable individually). Given the degree of variability inherent in the dataset, the relative effect of each factor (side, muscle, individual) is not immediately apparent. Figure 3.6b illustrates a subset of the data, restricted to 2 muscles in 2 littermate mice, where the relative influence of each factor becomes clearer on pairwise comparison of side, muscle and mouse (qualitatively, the major differences are observed in the muscle comparisons).

To quantify the significance and hierarchy of these factors across the whole litter, a three-way analysis of variance (3-way ANOVA) was performed on the complete dataset of 2160 NMJs (Table 3.2). This confirmed that muscle identity exerts the greatest influence on NMJ morphology (highly significant in all 20 variables), with side having no effect. Individual identity exerts a modest influence on NMJ morphology (in 7 of 20 variables).

Intuitively, the absence of left/right differences is not surprising. Nevertheless, it was conceivable that the use of pooled data in the 3-way ANOVA masked genuine left/right differences in NMJ morphology (when comparing different muscles/individuals). To address this possibility, a series of t-tests were performed, comparing the mean values for a single NMJ variable (AChR area) in each of the left/right muscle pairs (27 pairs in total) (Appendix 8). In this series of comparisons, only one showed a statistically significant ($p < 0.05$) difference (after Bonferroni correction). An equivalent series of left/right comparisons for a different variable (fragmentation) also failed to demonstrate any statistically significant differences. Thus, NMJ morphology was consistently replicated across left/right pairs of each muscle in every animal.

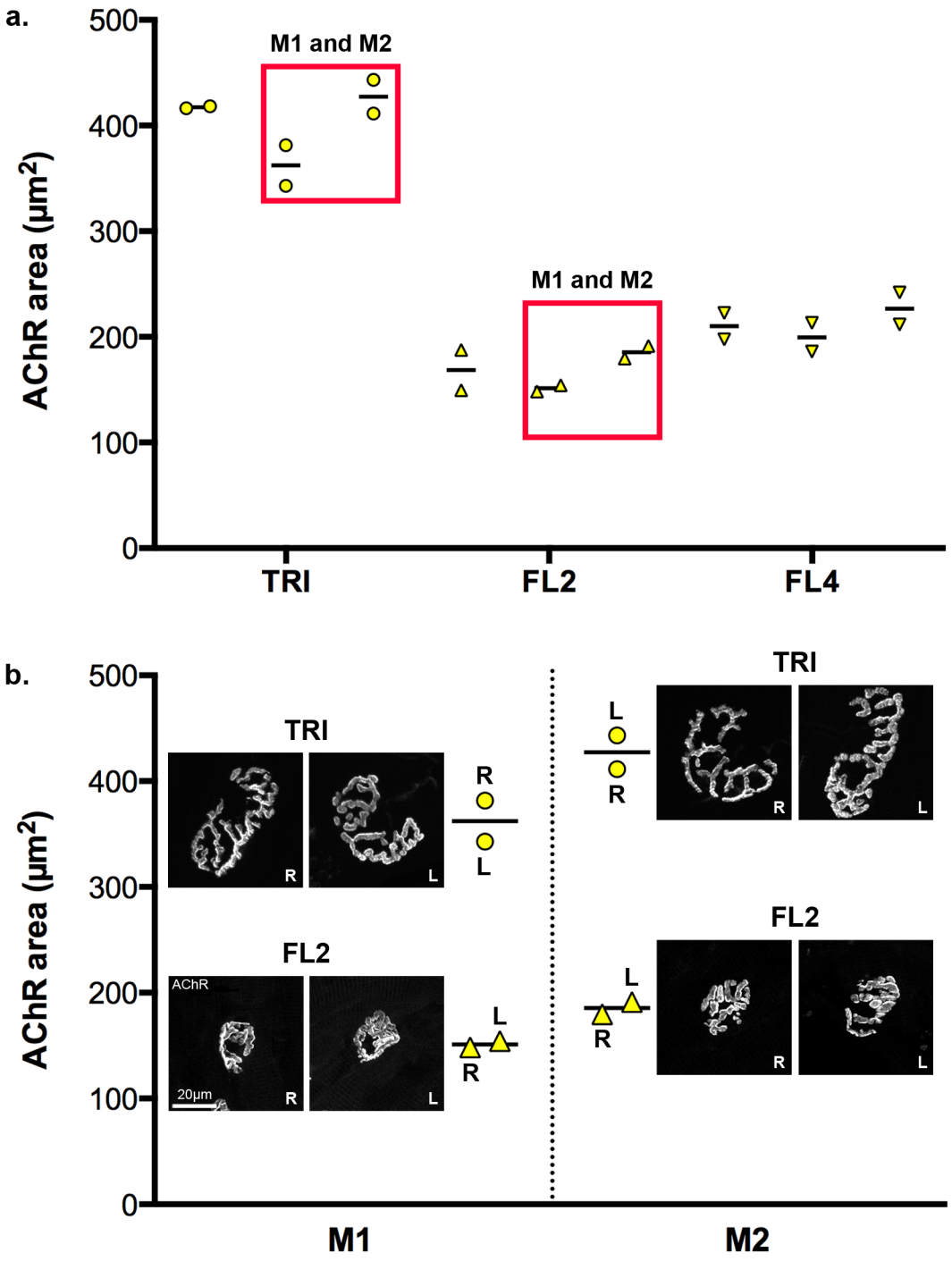

Figure 3.6 | Influence of side, muscle and individual on mouse NMJ morphology
The influence of side, muscle and individual on synaptic variability was explored. **a.** Comparison of NMJ morphology (based on AChR area) in left/right muscle pairs of 3 forelimb muscles (triceps, TRI and lumbricals 2 and 4, FL2 and FL4) in 3 littermate mice. Data points are grouped in pairs on the graph; each point represents the average NMJ for an individual muscle (mean of 40 NMJs) from the right or left side of the body; the intervening line is the average of the 2 sides. The highlighted muscle pairs (red boxes), enlarged in **b.** compare the average NMJs in left/right pairs of 2 muscles (TRI and FL2) from 2 mice (M1 and M2). Representative pairs of NMJs are shown alongside. Factors influencing synaptic variability are hierarchical: muscle identity (TRI cf. FL2) accounts for more variation in NMJ form than animal identity (M1 cf. M2), with side having no effect. Scale bar = 20µm. See Appendix 7 for other variables.

Influence of side, muscle and individual (mouse NMJ)			
	muscle	individual	side
core varaibles			
pre-synaptic			
1) nerve terminal area (µm^2)	***		
2) nerve terminal perimeter (µm)	***		
3) number of terminal branches	***	**	
4) number of branch points	**		
5) total length of branches (µm)	***		
post-synaptic			
6) AChR area (µm^2)	***		
7) AChR perimeter (µm)	***	*	
8) endplate area (µm^2)	***		
9) endplate perimeter (µm)	***	*	
10) endplate diameter (µm)	***	*	
11) number of AChR clusters	***		*
derived variables			
pre-synaptic			
12) average length of branches (µm)	*	**	
13) complexity	***		
post-synaptic			
14) average area of AChR clusters (µm^2)	***		
15) fragmentation	**		
16) compactness (%)	***	*	
17) overlap (%)	**	*	
18) area of synaptic contact (µm^2)	***		
associated nerve & muscle variables			
19) axon diameter (µm)	***		
20) muscle fibre diameter (µm)	***		

Table 3.2 | Influence of side, muscle and individual (mouse NMJ)
Significance levels obtained from 3-way analysis of variance (ANOVA). Influencing factors are hierarchical: muscle identity has the greatest influence; side has no effect. ***p<0.001, **p<0.01, *p<0.05.

3.4.5 Other aspects of natural variation

The present study has focused on the natural variation of NMJ morphology in a single litter of CD1 mice. Given the (perhaps) unexpected degree of NMJ variability between different muscles and individual animals, it remains to be seen whether such variation also extends to 'between-litter' and 'between-strain' comparisons, and such analyses certainly warrant further exploration. For these reasons, the values reported here for individual NMJ variables in specific muscles should not be regarded as 'typical' for all mice of every strain.

If a high degree of NMJ heterogeneity is demonstrated universally across different strains of mice, this will represent an additional factor that needs to be taken into careful consideration when undertaking future translational research using mouse models of NMJ disease.

Chapter 4

Cellular architecture of the human NMJ

4.1 Chapter summary

This chapter provides a detailed description of the cellular architecture of the human NMJ. A robust and reliable method for harvesting human NMJs from non-pathological regions of surgical discard material suitable for high-resolution cellular and molecular analyses was first developed. Human NMJs from 4 lower limb muscles were then analyzed using the same morphological and statistical approaches developed in Chapters 2 and 3, and compared with the same muscles obtained from wild type mice. The unique morphology of the human NMJ, the influence of the pre- and post-synaptic cells, and the effects of aging and pathology are described.

4.2 Introduction

Our current understanding of the human NMJ, discussed in detail in Chapter 1, highlights the relative paucity of morphological studies in humans compared with other species. In addition to the important ethical considerations, the technical obstacles posed by changes in clinical diagnostics, with a gradual shift away from invasive procedures (such as motor point biopsy) make it difficult to obtain healthy human tissue of sufficient quality and quantity to perform large-scale, high-resolution, cellular and molecular studies. In contrast to post-mortem sampling that has been employed very successfully in other settings (e.g. studies of human brain synapses; Kay et al, 2013), equivalent sampling of human NMJs is not suitable for high-resolution and proteomic work, due to the rapid rate of tissue degradation that occurs within minutes post-mortem (Jones and Gillingwater; unpublished findings).

Historically, previous studies of human NMJs have typically relied on motor point biopsy (Coërs and Woolf, 1959; Slater et al, 1992), a once commonly indicated diagnostic procedure that is now seldom performed in modern clinical practice (largely replaced by non-invasive electromyographic and serological methods). Motor point biopsy has been used to sample various muscles of the upper and lower limbs (see Table 1.1) and although generally well

tolerated, is subject to the same potential complications associated with any invasive procedure (e.g. bleeding, infection, damage to surrounding structures).

The other main source of human tissue in previous studies has been intercostal muscle obtained at thoracotomy for other indications (e.g. cardiothoracic surgery; Wokke et al, 1990). This has the advantage of sampling 'normal' muscle that is not typically subject to atrophy or sarcopenia (due to continuous respiratory activity), nor many of the other pathologies affecting the limb musculature. Conversely, this approach yields only a limited group of muscles for study, all with a very similar structure and fibre type composition.

Given the limitations and caveats associated with these previous sampling techniques, a different approach was therefore required to undertake a comprehensive cellular and molecular characterization of the healthy human NMJ in several muscles across the lifespan.

4.3 Methods

A robust method for sampling human NMJs in surgical patients was first established, with equivalent NMJs harvested from wild type mice. Comparative morphometric analysis of human and mouse NMJs was then performed using NMJ-morph. Other analyses were performed to address the effects of aging and pathology on human NMJs.

4.3.1 Ethics

The use of human tissue samples was approved by the NHS Lothian Ethics Committee (Reference Numbers: REC 2002/1/22 and 2002/R/OST/02) and NRS BioResource (Reference Numbers: SR719, 15/ES/0094 and SR589, 15/SS/0182).

4.3.2 Case series

Human muscle samples were obtained from patients during lower limb amputation surgery, primarily for the complications of peripheral vascular disease (PVD), typically either critical ischaemia in a non-salvageable limb, or failure of previous vascular reconstruction. One of the key advantages afforded by this source of tissue is the frequency with which lower limb amputation is performed (over 4,000 per year in England from 2003-2009; Ahmad et al,

2014). In addition, from a practical point of view, the use of 'surgical discard' material is more amenable to non-clinicians than 'formal' biopsies, which require specific training. In total, twenty-one sets of muscle samples were obtained from twenty patients (15 male, 5 female) – one patient required a bilateral procedure. The clinical details for each patient are summarized in Table 4.1. The majority of patients (16 out of 20) underwent amputation for the complications of peripheral vascular disease (PVD), typically either critical ischaemia in a non-salvageable limb, or failure of previous vascular reconstruction. Most of these cases (12 out of 16) were below knee amputations (BKA); only four patients required above knee amputation (AKA). Of the four non-PVD-related cases, BKA was performed in two patients for chronic pain following previous orthopaedic surgery (49 year old female, 50 year old male), in one patient for chronic osteomyelitis refractory to antibiotic treatment (female, 42 years) and in a final patient (male, 34 years) who required bilateral amputation for acute ischaemia (secondary to thromboembolism from infective endocarditis). Mean age at surgery was 67 years (range 34-92 years).

4.3.3 Tissue harvesting

Four distinct muscles were selected for analysis: *extensor digitorum longus* (*EDL*), *soleus* (*S*), *peroneus longus* (*PL*) and *peroneus brevis* (*PB*). The choice of muscles was primarily dictated by the logistics and reproducibility of sampling, given the variation in level and quantity of discard material for each amputation, but with a view to including a range of muscle fibre types (fast, slow, mixed). The original technique of motor point biopsy (for the peroneal muscles) as described by Coërs and Woolf (1959) was used as a guide (Figure 4.1). In the majority of cases, a complete set of samples were obtained; in some instances, muscles were lost and/or damaged during surgery, or were not sampled due to tissue necrosis (Table 4.1). In total, 72 individual muscles were sampled (*EDL*=19, *S*=18, *PB*=18, *PL*=17).

Tissue was harvested from the amputation specimen in the operating theatre immediately after disconnection of the limb. Muscle samples were obtained from the proximal end of the specimen, close to the line of incision, in areas demonstrating good back bleeding and muscle fasciculation, and away from areas of necrosis and infection. Any muscle that appeared obviously devitalized on gross inspection was not sampled.

Patient case series											
case ref	age	sex	side	procedure	indication	DM	function	EDL	PB	PL	S
1R	34	m	R	BKA	non PVD	non DM	mobile	MEPs	MEPs		MEPs
1L	34	m	L	BKA	non PVD	non DM	mobile	MEPs	MEPs		MEPs
2	42	f	L	BKA	non PVD	non DM	mobile				
3	49	f	R	BKA	non PVD	non DM	mobile				
4	49	m	R	BKA	PVD	DM	mobile	MEPs			MEPs
5	50	m	R	BKA	non PVD	non DM	n/a	MEPs			MEPs
6	52	f	L	BKA	PVD	DM	n/a				
7	56	f	L	BKA	PVD	DM	n/a	MEPs	MEPs	MEPs	MEPs
8	58	m	L	AKA	PVD	DM	mobile		MEPs		
9	64	m	R	BKA	PVD	DM	n/a				
10	66	m	R	BKA	PVD	DM	mobile		30 NMJs	30 NMJs	
11	68	m	R	BKA	PVD	DM	mobile				
12	77	m	L	BKA	PVD	DM	n/a				
13	79	m	R	BKA	PVD	DM	mobile				
14	80	m	R	BKA	PVD	non DM	n/a				
15	80	m	R	BKA	PVD	DM	mobile				
16	84	m	L	AKA	PVD	DM	mobile	MEPs		MEPs	
17	85	m	R	AKA	PVD	DM	n/a				
18	89	m	L	AKA	PVD	non DM	n/a				
19	92	f	L	BKA	PVD	non DM	mobile	MEPs			
20	92	m	L	BKA	PVD	non DM	n/a				

	age	sex	side	procedure	indication	DM	function	EDL	PB	PL	S
summary	mean: 67.3	15 m	11 R	17 BKA	16 PVD	12 DM	11 mobile	19 samples	18 samples	17 samples	18 samples
	range: 34 - 92	5 f	10 L	4 AKA	4 ºPVD	8 ºDM	9 n/a				

decade	30s	40s	50s	60s	70s	80s	90s	12 muscles	n/a	18 muscles	40 MEPs
no. cases	1	3	4	3	2	5	2	52 muscles	40 NMJs	2 muscles	30 NMJs

Table 4.1 | Patient case series
Summary of clinical details and sample data. Age is in years. In total, 2860 NMJs from 72 muscles were analysed. **Colour coding:** *light pink* = complete sample of 40 NMJs with pre- and post-synaptic labelling; *mid & dark pink* = incomplete sample – endplate data only (MEPs) or smaller sample size (30 NMJs); *grey* = not sampled. **Abbreviations:** m, male; f, female; R, right limb; L, left limb; BKA, below knee amputation; AKA, above knee amputation; PVD, peripheral vascular disease; DM, diabetes mellitus; n/a, data not available; EDL, extensor digitorum longus; PB, peroneus brevis; PL; peroneus longus; soleus, S; MEPs, motor endplates; NMJ, neuromuscular junction.

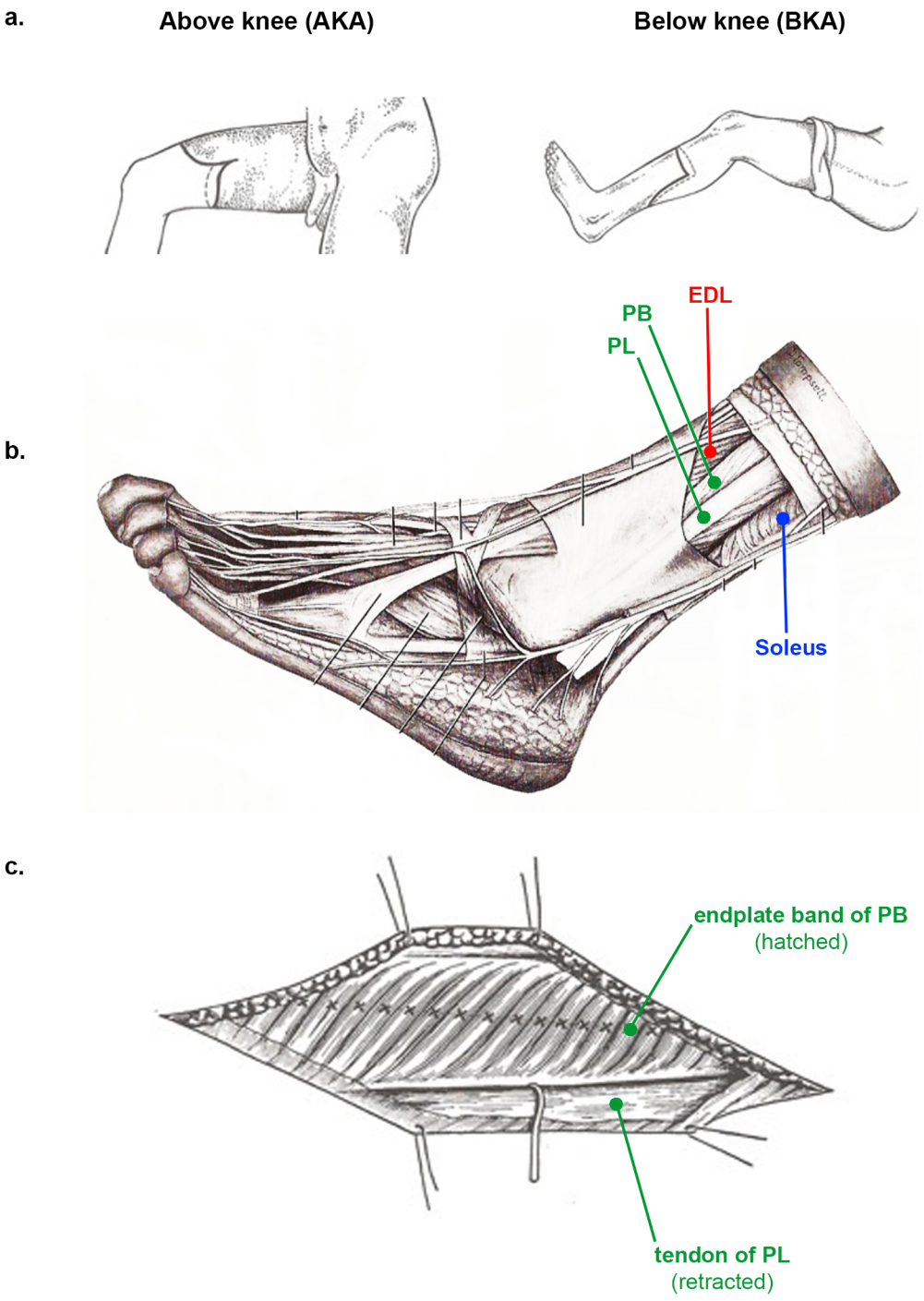

Figure 4.1 | Method of human tissue harvesting
Muscle samples were harvested from lower limb amputation specimens. **a.** The skin incisions are shown for above knee (AKA) and below knee (BKA) amputations. Muscle samples were obtained from the discard tissue near to the incision lines, distant from pathological tissue (from Farquharson and Moran, 2005). **b.** Four muscles were sampled: *extensor digitorum longus* (EDL, in red; a fast twitch muscle), *soleus* (in blue; a slow twitch muscle), *peroneus longus* and *peroneus brevis* (PL and PB, in green) (from McMinn, 1994). **c.** Small blocks of tissue containing full-length muscle fibres from origin to insertion were removed and placed immediately in fix or on ice. NMJs are located at the midpoint of muscle fibres; the endplate band in *peroneus brevis* (PB) is shown hatched (from Coërs and Woolf, 1959).

Small blocks of tissue, containing full-length muscle fibres from origin to insertion (approx. 2cm in length) were removed from each of the muscles selected and either immediately fixed in 4% paraformaldehyde for 1 hour or placed on wet ice (depending on the subsequent analyses; see below and Chapter 5). All specimens were then transferred from theatre to laboratory for immediate processing.

The major concern relating to the use of tissue harvested from amputation specimens is the potential effect of chronic tissue ischaemia and diabetes mellitus (DM). Although twelve of the twenty patients had one or other form of diabetes, the functional status of all patients (where documented) was commensurate with standing and some degree of walking prior to surgery (with one 92-year-old female able to walk half a mile; Table 4.1).

At surgery, the level of amputation is principally determined by the likelihood of wound healing; a more distal amputation is the preferred option from a functional point of view, but not at the expense of healing. For the amputation stump to heal fully the local blood supply must be adequate; thus, tissue sampled close to the line of incision (level of amputation) should also be of adequate health. The final decision on the level of amputation is determined during the procedure itself, by assessing the degree of back bleeding from the stump after disconnection of the limb. If the tissues are clearly devitalized, the amputation is immediately revised to a level at which these conditions are satisfied. In addition to these basic principles, all samples were harvested from muscle that demonstrated visible contraction during dissection.

4.3.4 Muscle dissection and NMJ immunohistochemistry

Following muscle harvest, small bundles of 25-30 muscle fibres were teased out from the larger blocks, and of a size suitable for whole-mount preparation. NMJs were then labeled for presynaptic 2H3/SV2 and postsynaptic AChRs as before (see Chapter 3), but with omission of the additional blocking stage, and overnight incubation in secondary antibodies.

Antibodies

Primary: 1:50 mouse anti-2H3 IgG and 1:50 mouse anti-SV2 IgG (DSHB).
Secondary: 1:50 Alexa Fluor 488 donkey anti-mouse IgG (Thermo Fisher Scientific).
BTX: 1:500 TRITC α-bungarotoxin (Biotium).

4.3.5 Confocal imaging and NMJ-morph analysis

Images were acquired and analyzed using NMJ-morph as described previously (see Chapters 2 and 3). In some instances, where the pre-synaptic labeling was unsatisfactory, only motor endplates were imaged (see Table 4.1). In total, 4,007 human NMJs were imaged, from which 2,860 NMJs were selected for analysis (≈ 70% yield). Measurement of muscle fibre diameter was also performed as before (Chapters 2 and 3).

4.3.6 Comparative mouse study

To allow direct comparison with human NMJs, the equivalent muscles were dissected from both sides of three CD1 littermates (adult females, approximately 12 weeks old). Mice were prepared as described in Chapter 3, with muscle dissection and the remainder of the analysis as for the human samples. In total, 960 NMJs were analyzed from 24 individual muscles.

The gross architecture of the equivalent muscles is somewhat different in the mouse (Greene, 1963) and care was required during dissection. Comparatively, *soleus* is a much smaller muscle in the mouse (with a unipennate structure), whilst *plantaris* is much larger (both being sources of confusion). *Soleus* was positively identified by tracing its insertion into the side of the tendo calcaneus. In addition, the peroneal compartment of the mouse contains 2 other muscles, *peroneus digiti quarti* and *quinti*; again, care was taken to remove only *peroneus longus* and *brevis*. *Extensor digitorum longus* is similar in both species.

4.4 Results and Discussion

Baseline data was obtained for 2,860 human NMJs from 72 individual specimens of 4 different muscles, in 20 patients aged from 34 to 92 years, and with a range of clinical presentations. Comparative morphometric analysis was performed, using the equivalent mouse NMJs as a reference, to describe human NMJ morphology, variability and the influence of the pre- and post-synaptic cells. Further analyses were undertaken to determine the effects of age and pathology, and assess other factors including laterality and sexual dimorphism.

4.4.1 Morphology of human NMJs

Initial qualitative observations revealed striking morphological differences between human and mouse NMJs in all muscles examined (*EDL, PB, PL, soleus*; Figure 4.2a). Human NMJs were universally smaller than mouse NMJs, with much thinner pre-terminal axons, rudimentary nerve terminals and distinctive 'nummular' endplates (nummular – resembling a series of coins). These observations were confirmed quantitatively by comparing the 'average' NMJ in each species (by pooling the data from the four muscle; Figure 4.2b, Appendix 9 and Table 4.2; differences between individual muscles are considered in Section 4.4.1.2). Axon diameter and average area of AChR clusters showed the greatest fold differences between species (3.69 fold**** and 3.33 fold**** respectively; higher in mice), with over half of the morphological variables studied (12 of 21) showing a fold difference of at least 150% between humans and mice. In comparison, endplate diameter and compactness showed the smallest significant fold differences (1.17*** and 1.05** respectively).

Overall, the quantitative analyses confirmed the initial observations: human NMJs are smaller, less complex and more fragmented (pre- and post-synaptically), with much thinner axons than their mouse counterparts. These differences were observed across all 4 muscles, albeit with small variations between individual muscles. Importantly, given the source of tissue from surgical discard material, no significant morphological differences at the human NMJ could be attributed to patient co-morbidities (see below).

4.4.1.1 Heterogeneity of human NMJs

Coefficients of variation and principal components analysis performed in collaboration with Martin W Simmen (Centre for Integrative Physiology, University of Edinburgh) using SPSS software.

In addition to the clear differences in 'average' NMJ morphology *between* humans and mice, the degree of morphological heterogeneity *within* individual muscles also differed markedly between the species. Figure 4.3 compares the variability in NMJ morphology for a single example (one specimen) of *extensor digitorum longus* in each species. The human NMJs demonstrate a greater range of sizes (with a 4.2x fold difference between the top and bottom ranked) than the mouse NMJs (3.2x fold difference). In addition, the 2 samples can be clearly differentiated on inspection, based upon the unique morphological traits described above, with the human endplates in this example demonstrating the characteristic

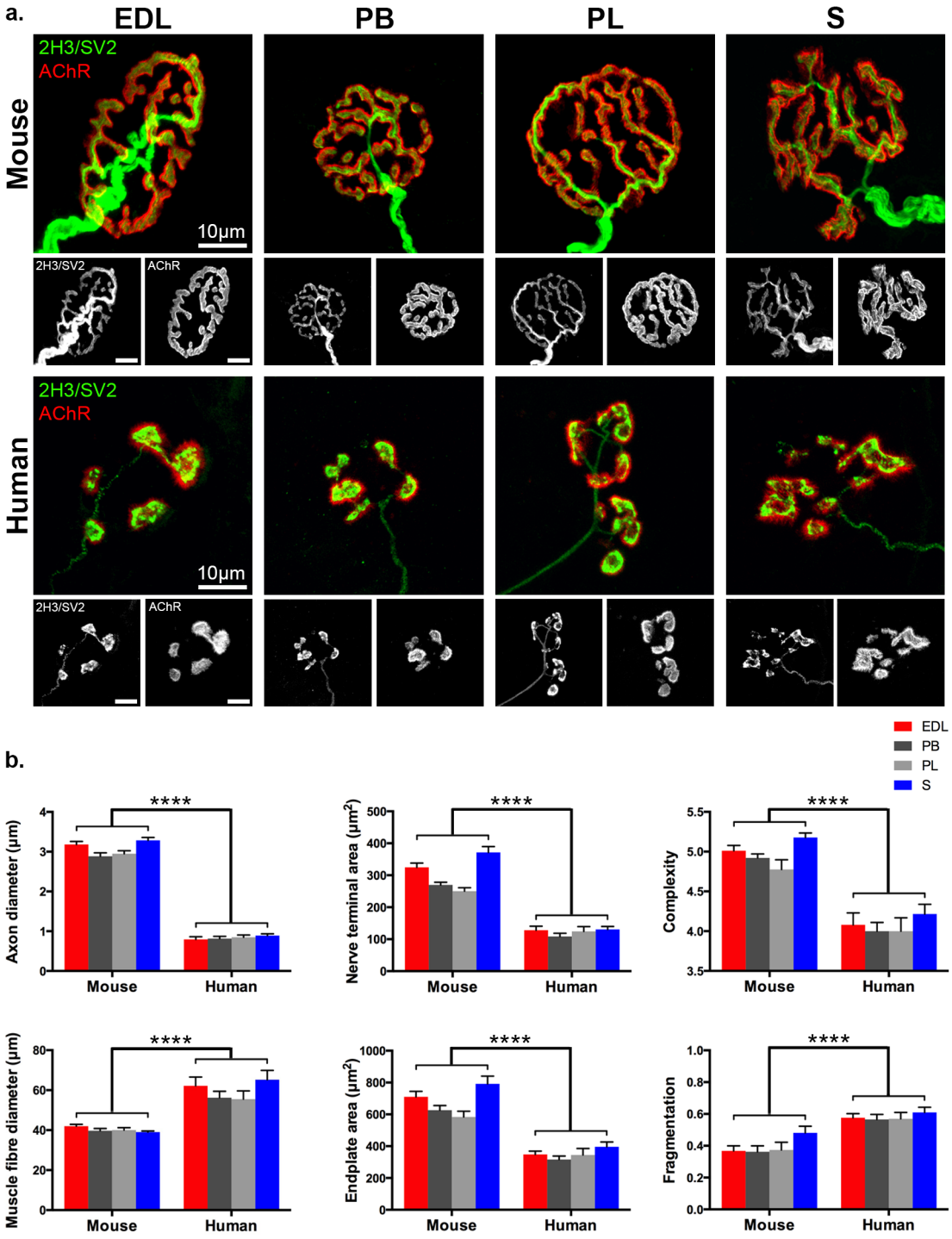

Figure 4.2 | Morphology of human NMJs
Comparison of human and mouse NMJs in 4 lower limb muscles: *extensor digitorum longus* (EDL*), peroneus brevis* (PB), *peroneus longus* (PL) and *soleus* (S). **a.** Human NMJs display unique morphological characteristics, including small size, thin axons, rudimentary nerve terminals and distinctive 'nummular' endplates, all of which distinguish them from equivalent mouse NMJs. Scale bar = 10µm. **b.** Bar charts demonstrating significant differences in 6 morphological variables, including both pre- and post-synaptic cells/NMJ variables. Each bar represents the mean (± SEM) of > 600 human NMJs and 240 mouse NMJs. Mann-Whitney and unpaired t-tests performed on the mean value for each variable pooled across the 4 muscle groups. ****p< 0.0001. See Appendix 9 for other variables.

Baseline morphological data for human NMJ							
				human NMJ		mouse NMJ	
	average human NMJ	average mouse NMJ	fold difference	correlation with axon diameter	correlation with muscle fibre diameter	correlation with axon diameter	correlation with muscle fibre diameter
core varaibles							
pre-synaptic							
1) nerve terminal area (μm²)	122.7	304.0	2.48 ****	0.548 ****	0.358 **	0.694 ***	0.099
2) nerve terminal perimeter (μm)	151.1	327.4	2.17 ****	0.435 **	0.408 **	0.429 *	0.273
3) number of terminal branches	28	30	1.07	0.248	0.355 **	0.370	0.016
4) number of branch points	14	26	1.86 ****	0.553 ****	0.250	0.609 **	-0.025
5) total length of branches (μm)	69.3	166.7	2.41 ****	0.533 ****	0.320 *	0.577 **	0.193
post-synaptic							
6) AChR area (μm²)	206.7	424.2	2.05 ****	0.329 *	0.385 ***	0.572 **	0.076
7) AChR perimeter (μm)	152.2	275.8	1.81 ****	0.179	0.297 *	0.279	0.378
8) endplate area (μm²)	351.5	678.2	1.93 ****	0.302 *	0.373 **	0.510 *	0.158
9) endplate perimeter (μm)	98.7	118.8	1.20 ****	0.363 **	0.373 **	0.521 **	0.060
10) endplate diameter (μm)	36.0	42.2	1.17 ***	0.350 *	0.344 **	0.421 *	0.069
11) number of AChR clusters	3.9	2.6	1.50 ****	0.225	0.151	0.306	0.181
derived variables							
pre-synaptic							
12) average length of branches (μm)	3.0	6.7	2.23 ****	0.522 ****	-0.146	-0.397	0.114
13) complexity	4.07	4.97	1.22 ****	0.424 **	0.275 *	0.582 **	0.064
post-synaptic							
14) average area of AChR clusters (μm²)	71.7	238.5	3.33 ****	0.202	0.305 **	0.117	-0.085
15) fragmentation	0.58	0.40	1.45 ****	0.304 *	0.089	0.353	0.175
16) compactness (%)	61.6	64.4	1.05 **	0.000	-0.025	0.097	-0.357
17) overlap (%)	49.6	64.2	1.29 ****	0.382 **	-0.129	0.359	0.454 *
18) area of synaptic contact (μm²)	105.2	267.9	2.55 ****	0.461 ***	0.370 **	0.660 ***	0.147
associated nerve & muscle variables							
19) axon diameter (μm)	0.84	3.10	3.69 ****				
20) muscle fibre diameter (μm)	59.9	40.2	1.49 ****				
21) number of axonal inputs	1	1	1.00				

Table 4.2 | Baseline morphological data for human NMJ
The 'averages' listed (average human NMJ, average mouse NMJ) for each variable represent the mean for the complete dataset pooled across all muscles (*extensor digitorum longus, soleus, peroneus longus, peroneus brevis*; 2860 human NMJs; 960 mouse NMJs). Fold difference (between human and mouse) is the ratio of the larger value to the smaller value; most variables were larger in mice. Correlation data listed as coefficient (r, numerical) and significance level (p, asterisk). ****p< 0.0001, ***p< 0.001, **p< 0.01, *p< 0.05.

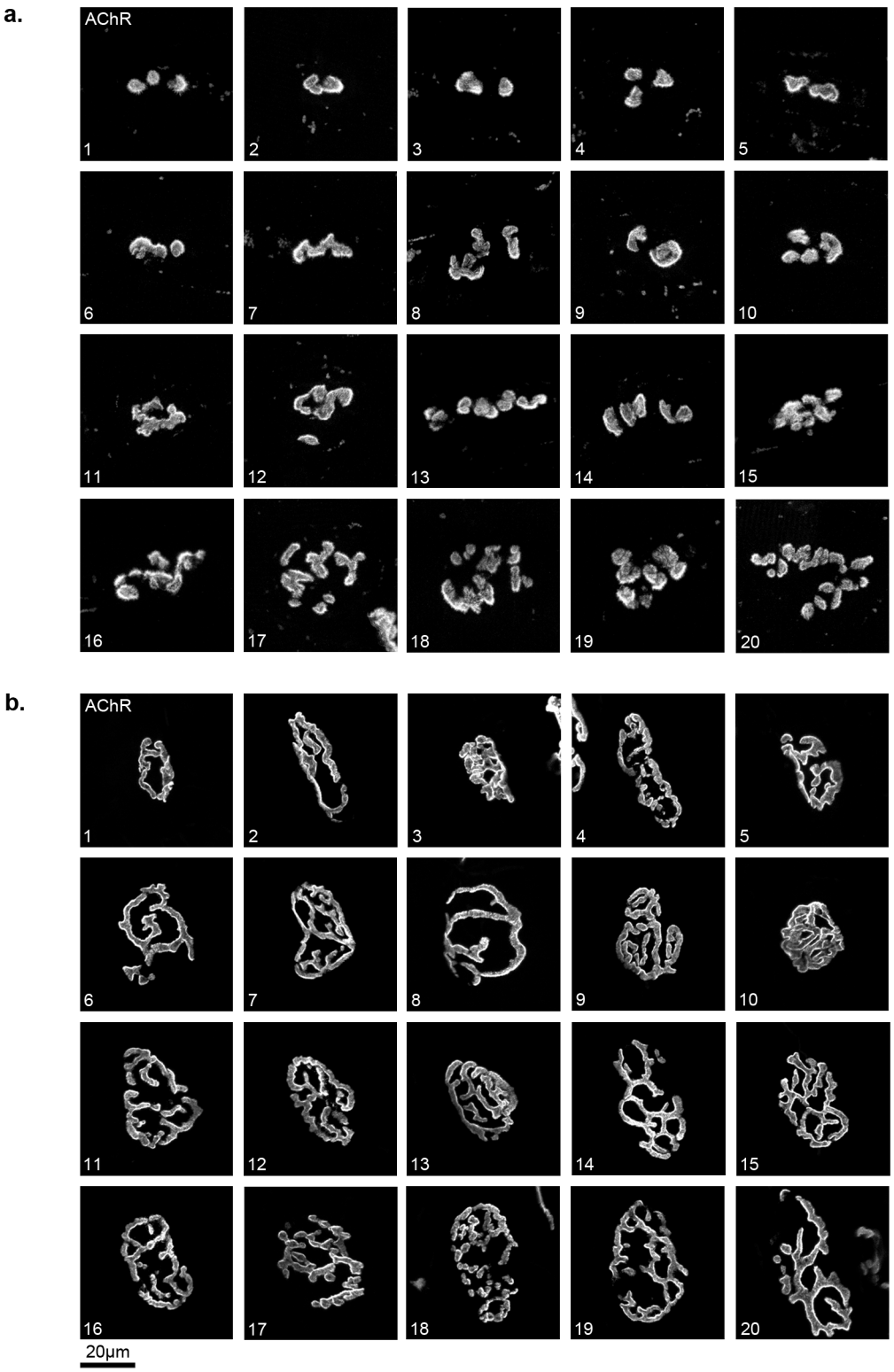

Figure 4.3 | Heterogeneity of human NMJs
Comparison of intra-muscular variability in human and mouse NMJs (**a.** and **b.** respectively). Each panel shows a series of 20 endplates from an individual muscle (*extensor digitorum longus*) arranged in ascending order of size (based on AChR area). There is marked variation in NMJ morphology within an individual muscle, but distinct and recognizable differences in overall morphology exist between the species. Intra-muscular variability is greater in human NMJs. Size differences are 4.2 fold across the human endplates, 3.2 fold across the mouse endplates. Scale bar = 20µm.

'nummular' appearance, in contrast to the typical 'pretzel' appearance of the mouse endplates.

Qualitatively, a similar degree of variation was noted within the 72 individual human specimens across the 4 different muscles. As in the mouse study (Chapter 3), this intra-muscle variability was quantified by calculating the coefficients of variation (CV = standard deviation/mean) for each of the 11 core morphological variables in both species (72 human specimens, 24 mouse specimens).

In humans, the mean coefficients of variation ranged from 0.35 to 0.77 (median = 0.48); in mice, the range was 0.20 to 0.71 (median = 0.30), with 10 out of the 11 coefficients being higher in human NMJs for the equivalent morphological variables (Appendix 10). Quantitatively therefore, there was a greater degree of intra-muscle variability in human NMJs, in keeping with the naked eye observations. [In mice, the mean coefficients of variation for the present muscles (*EDL, PB, PL, S*) were very similar to those of the initial series (*triceps*, *quadriceps*, *cranial* and *lumbrical* muscles) with both groups having a median CV = 0.30]

A principal components analysis (PCA) was also performed on both human and mouse datasets (as described in Chapter 3) in an attempt to assess the relative contribution of different physical characteristics to the natural variation inherent in the NMJs. For both datasets, the majority of the variance (81-83%) could be captured in a 2-dimensional plot (Appendix 10), with the individual principal components (PC1 and PC2) contributing ≈73% and ≈10% (human) and ≈72% and ≈9% (mouse) of the natural variation, respectively.

These results are very similar to those of the original mouse series (PC1 ≈72% PC2 ≈9%; see Chapter 3). Once again, in both human and mouse datasets, PC1 reflects the 'overall size' of the NMJ (based on the clustering of the majority of 'size-related' variables high up on the x-axis of the loading plots; Appendix 10). In contrast to the earlier PCA, attributing a physical characteristic to PC2 was less clear-cut, with none of the core variables in either series (human or mouse) loading quite as separately on the y-axis as did the number of AChR clusters in the original series (where PC2 could be regarded as a measure of 'fragmentation'; compare the loading plots in Appendix 4 and Appendix 10).

The difficulty of ascribing a physical characteristic to the individual principal components is one of the esoteric aspects of PCA (Krzanowski, 1988), but this should not detract from the value and importance of the results; that the majority of natural variation in human NMJs (as in mice) is principally explained by differences in the overall size of the synapse.

With respect to future research, the value of this observation lies in the knowledge that *any* single size-related variable provides a robust measure of NMJ morphology (and variation). For example, if a study were designed to compare human and other mammalian NMJs, the measurement of a single variable (e.g. endplate area) would be sufficient to determine whether or not any marked species differences exist. A full morphological analysis may only then be needed to address additional questions (e.g. differences in shape, etc.).

4.4.1.2 Fibre type differences

Comparison of NMJ morphology in the separate muscles (*EDL, PB, PL, soleus*) revealed similar trends in both humans and mice. Individual NMJ variables tended to be greater in *EDL* and *soleus* than in the peroneal muscles, with those of *soleus* being generally higher than those of *EDL* (Figure 4.2; Appendix 9).

Although formal fibre typing was not undertaken, *soleus* and *EDL* are often cited as paradigm examples of 'slow' and 'fast' muscles (type I and II, respectively) based on their fibre type preponderance (Schiaffino and Reggiani, 2011), with the peroneal muscles having a mixed pattern. In mice, typical percentages of slow twitch fibres are: *soleus* 58%, *peroneus longus* and *brevis* 0-6% and *extensor digitorum longus* 0% (Burkholder et al, 1994; based on classification by Peter et al, 1972). In humans, equivalent values are: *soleus* 88%, *peroneus longus* 63% and *extensor digitorum* 47% (Johnson et al, 1973; based on classification by Brooke and Kaiser, 1970).

Morphological differences in the NMJs of fast (*EDL*) and slow (*soleus*) twitch fibres have been reported previously in the mouse (see example NMJs in Figure 1.2d; Fahim et al, 1984); the present findings support these descriptions, with the nerve terminals of *EDL* appearing thinner (and with more numerous diverticula) than those of *soleus*, resulting in a 'coarser' overall appearance of NMJs in *soleus* (compare Figures 1.2d and 4.2).

However, whereas Fahim et al (1984) reported larger NMJs in *EDL* (mean endplate lengths: *EDL* ≈ 63μm; *soleus* ≈ 44μm), the mouse NMJs of the present study were larger in *soleus* (*EDL* ≈ 42μm; *soleus* ≈ 48μm); values for muscle fibre diameter were in broad agreement (Fahim et al, 1984: *EDL* ≈ 35μm, *soleus* ≈ 30μm; present study: *EDL* ≈ 42μm, *soleus* ≈ 39μm).

In humans, there was no clear morphological distinction between the NMJs of *soleus* and *EDL* at the level of light microscopy, perhaps a result of the universally simpler nerve terminals and endplate fragmentation compared to mice (Fahim et al, 1984). In some instances, there was the faint suggestion of a subtle difference between the NMJs of *soleus* and *EDL* (e.g. the sample images in Figure 4.2) that might warrant further study with a higher-resolution technique (e.g. transmission electron microscopy).

4.4.1.3 Occupancy of human NMJs

One of the key morphological findings was the degree of overlap between the pre- and post-synaptic components of the human NMJ (Figure 4.4). This observation helped to clarify the longstanding (but spurious) notion of 'partial occupancy' in human NMJs (Slater et al, 1992), which has largely arisen from inconsistencies of nomenclature. A significant difference was found in the degree of *overlap* between the pre- and post-synaptic structures in the two species (49.6% in humans, 64.2% in mice, x1.29**** fold difference). In contrast, there was no difference in the degree of *occupancy* of the NMJs; in both species, nerve terminals were found to *occupy* all of the AChR clusters of the endplate (Figure 4.4a), with the differences in *overlap* reflecting the degree to which the AChRs extended beyond the limits of the nerve terminals. None of the human (or mouse) NMJs analyzed were *partially occupied* in the accepted pathological sense of the term (Murray et al, 2010).

The descriptions of 'partial occupancy' by Slater et al (1992) in relation to human NMJs of *vastus lateralis* (part of the *quadriceps femoris* muscle of the thigh) were based on electron micrographs of transverse sections of NMJs. Here, *occupancy* was defined as the ratio of the 'pre-synaptic length' (of the nerve terminals) to the 'surface length' (of the motor endplate, measured along the tops of the junctional folds), similar to the present definition of *overlap*, but quite different from the pathological use of the term (Murray et al, 2010). Based on this definition, average *occupancy* in NMJs of *vastus lateralis* was ≈ 40%, similar to the average *overlap* in the present leg muscles (≈ 50%). The percentage discrepancy is probably a

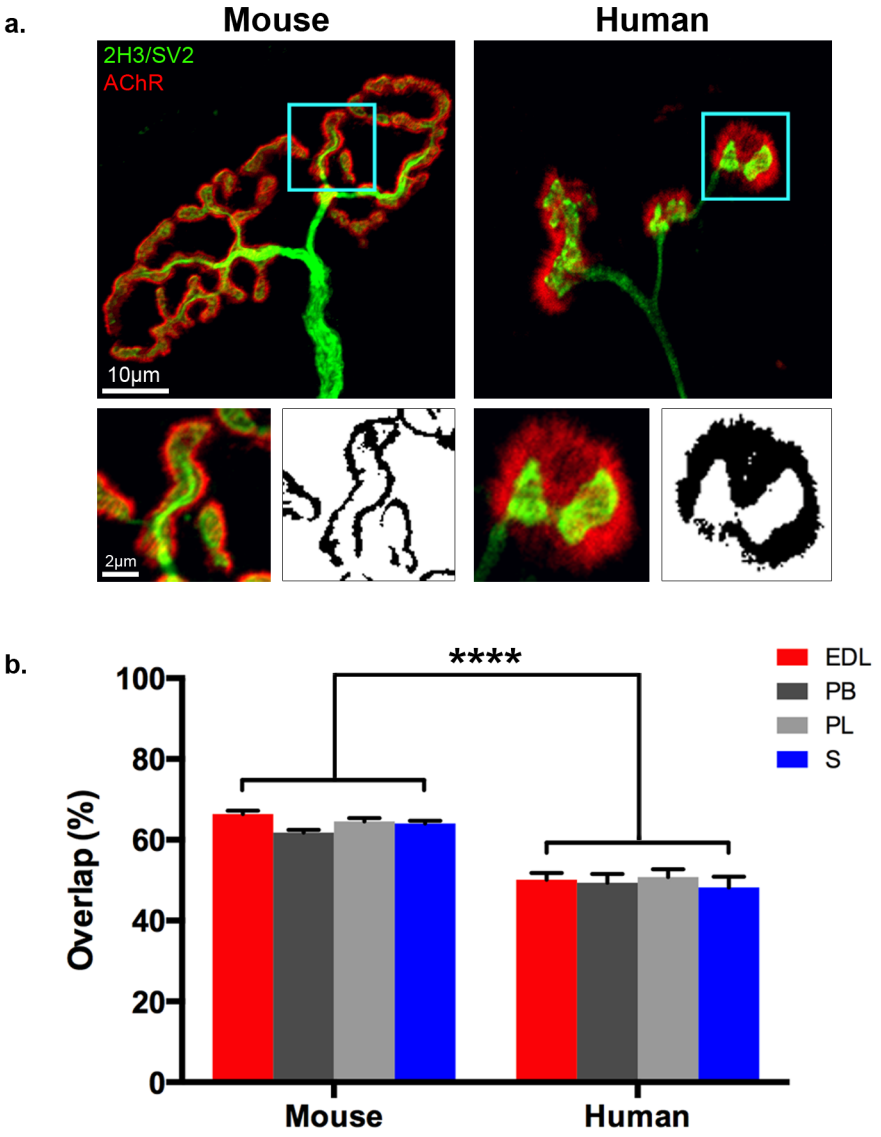

Figure 4.4 | Occupancy and overlap of human NMJs
Comparison of the percentage overlap (by area) of the pre- and post-synaptic components in human and mouse NMJs. **a.** The nerve terminal boutons outlined in the blue boxes have been enlarged (below main images) to highlight the differing degrees of overlap in each species. In both human and mouse NMJs, nerve terminals occupy all parts of the endplate. In human NMJs however, the AChRs of the endplate project beyond the nerve terminals to a greater degree, and hence the percentage overlap between the pre- and post-synaptic components is lower, **b.** (Bar chart as per Figure 4.2). This observation disproves the previous notion of 'partial occupancy' of human NMJs (Slater et al, 1992). ****p< 0.0001. Scale bars = 10µm and 2µm.

consequence of the linear/planar measurements used for the pre- to post-synaptic ratios (*lengths* on transverse section, Slater et al, compared with *areas* en face, present study).

Thus, in health, the endplates of both species can be described as *fully occupied* but *partially overlapped* by nerve terminals (and to differing degrees: ≈ 50% in humans, ≈ 65% in mice).

4.4.1.4 Unusual features of human NMJs

In addition to the unique morphological characteristics of the human NMJ already noted, several other unusual features were encountered. The major finding was the presence of nerve terminal 'hot spots' – discrete areas of intense fluorescence – noted almost universally in human NMJs, but almost entirely absent from comparable mouse NMJs (Figures 4.2 and 5.1). These were subsequently found to relate to differences in the distribution of active zone proteins at the human NMJ, and are described in detail in Chapter 5.

'En passant' NMJs were noted in ≈ 10% of the human NMJs analyzed (Figure 4.5), but were entirely absent from the equivalent mouse muscles. The morphology of these en passant NMJs was highly variable, with nerve terminals typically arising as either 'swellings' along the main axonal trunk, or via a small side branch of varying length. Less frequently, a single afferent/efferent loop was replaced by an atypical series of multiple loops suggesting an unusual 'network-like' distribution of nerve terminals. The overall morphology of the intra-muscular nerve branching was not possible to determine on preparations of teased muscle fibres, and the gross architecture and distribution of these en passant NMJs remains to be determined.

The presence of these en passant NMJs influences the so called 'terminal innervation ratios' of the muscle (Coërs and Woolf, 1959). Two innervation ratios are defined: the *absolute* terminal innervation ratio (ATIR = number NMJs/number terminal axons) and the *functional* terminal innervation ratio (FTIR = number muscle fibres/number terminal axons). Terminal axons giving rise to more than one NMJ through bifurcation or in passing (en passant) mean that both ratios are usually greater than one (> 1); the functional ratio is typically lower than the absolute ratio however, as 2 NMJs are occasionally present on 1 muscle fibre. These ratios can change in relation to nerve and muscle degeneration, and have been calculated for several human muscles (*deltoid, biceps, brachioradialis, flexor carpi radialis, tibilais anterior,*

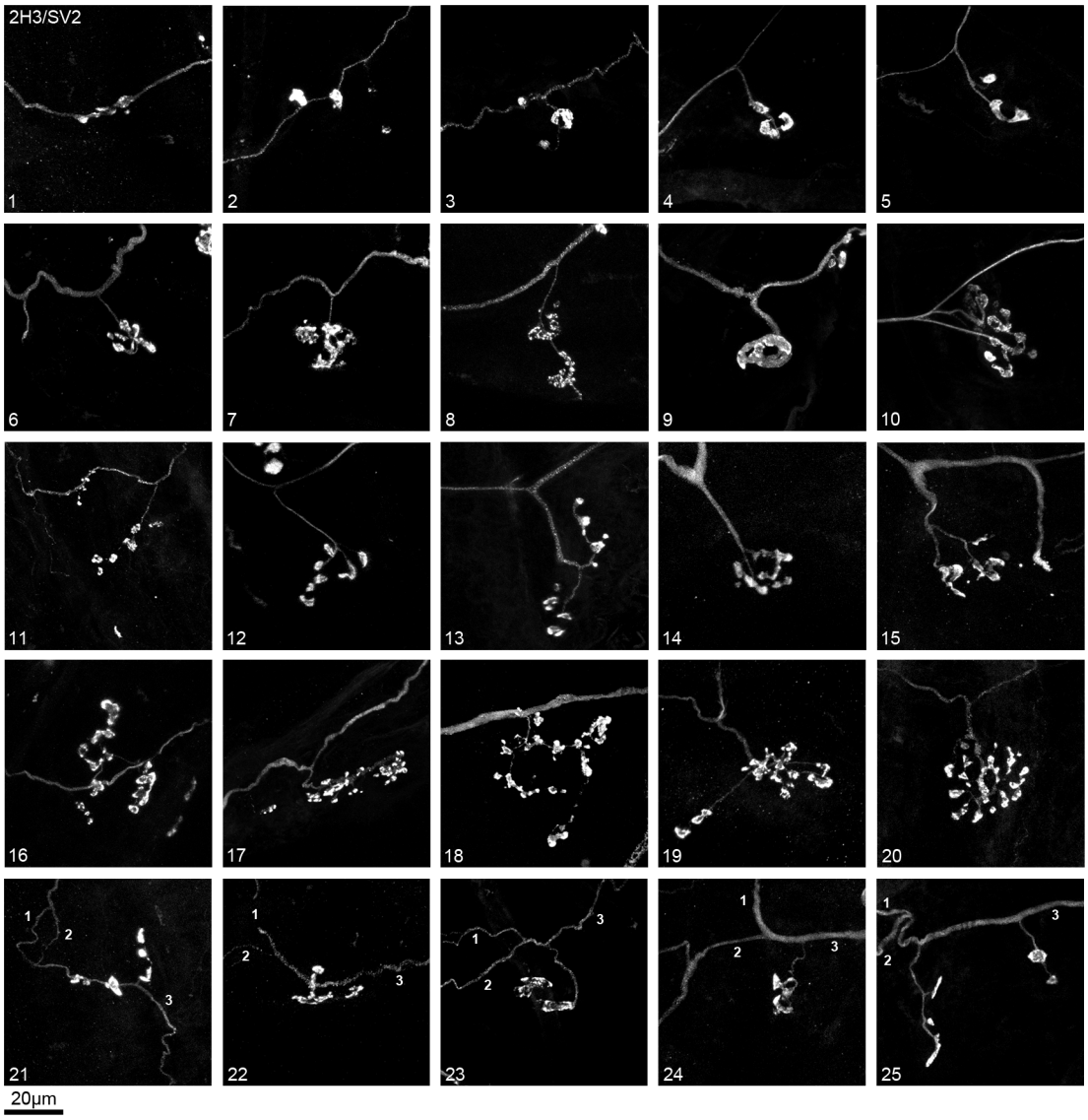

Figure 4.5 | 'En passant' nerve terminals (human NMJ)
'En passant' NMJs were noted in ≈10% of the human NMJs analyzed. The example NMJs are arranged in approximate groups according to the length of the side branch from the main axonal trunk and the size of the nerve terminals. Images 1 to 20 show examples of typical en passant NMJs possessing a single afferent and efferent axonal loop. The nerve terminals are seen to arise as either 'swellings' along the axonal trunk itself (images 1, 2, 16, 21, 22), or via a small side branch of varying length. Images 21 to 25 show examples of less typical en passant NMJs that appear to arise in close relation to three separate afferent/efferent axonal loops (numbered 1-3), suggesting a network-like distribution. Scale bar = 20µm.

vastus medialis, average ATIR = 1.13, average FTIR = 1.09, Coërs and Woolf, 1959; *vastus lateralis*, average FTIR = 1.10, Slater et al, 1992). Given the variable axonal labeling in these teased fibre preparations, it was not possible to calculate the innervation ratios, but the percentage of en passant NMJs encountered (≈ 10%) would suggest a general consensus with these previous studies.

Finally, a very small number of human endplates demonstrated an unusual 'spiculated' appearance (Figure 4.6). Spiculated endplates were noted in all muscles across the lifespan, and their frequency did not appear to correlate with age or gender; neither were they associated with any obvious changes in the overlying nerve terminals (Figure 4.6), arguing against a degenerative cause. The appearance may be in keeping with an exaggeration of the post-synaptic junctional folds, but the explanation for this finding and its significance remains unclear.

4.4.2 Influence of pre- and post-synaptic cells

Generally, although human NMJs were only half the size of mouse NMJs, with axons only a third of the calibre, they were found to innervate muscle fibres of up to twice the diameter (Figure 4.7). The relationship between NMJ morphology and the pre- and post-synaptic cells was therefore assessed, by correlating each morphological variable with motor axon and muscle fibre diameter, independently, as in the earlier mouse work (Chapter 3). In both species, axon diameter correlated more strongly with overall NMJ morphology (Figure 4.7, Appendix 11, Table 4.2). Correlation coefficients (r) were higher in relation to axon diameter for the majority of NMJ variables in both species (10 of the 18), with only a minority (6 in humans, 1 in mice) being more closely correlated with muscle fibre diameter (Table 4.2).

Again, as in the earlier mouse work (Chapter 3), these results suggest that the morphology of the human NMJ is more closely linked with the physical properties of the pre-synaptic cell as represented by the motor axon. As before however, this does not necessarily imply a stronger influence of the pre-synaptic cell in determining NMJ morphology.

Figure 4.7 also presents the results of the earlier mouse work alongside the current mouse correlations. Interestingly, the results of the later mouse series (*EDL, PB, PL, soleus*) fall approximately in the middle (based on size criteria) of the original series of muscles,

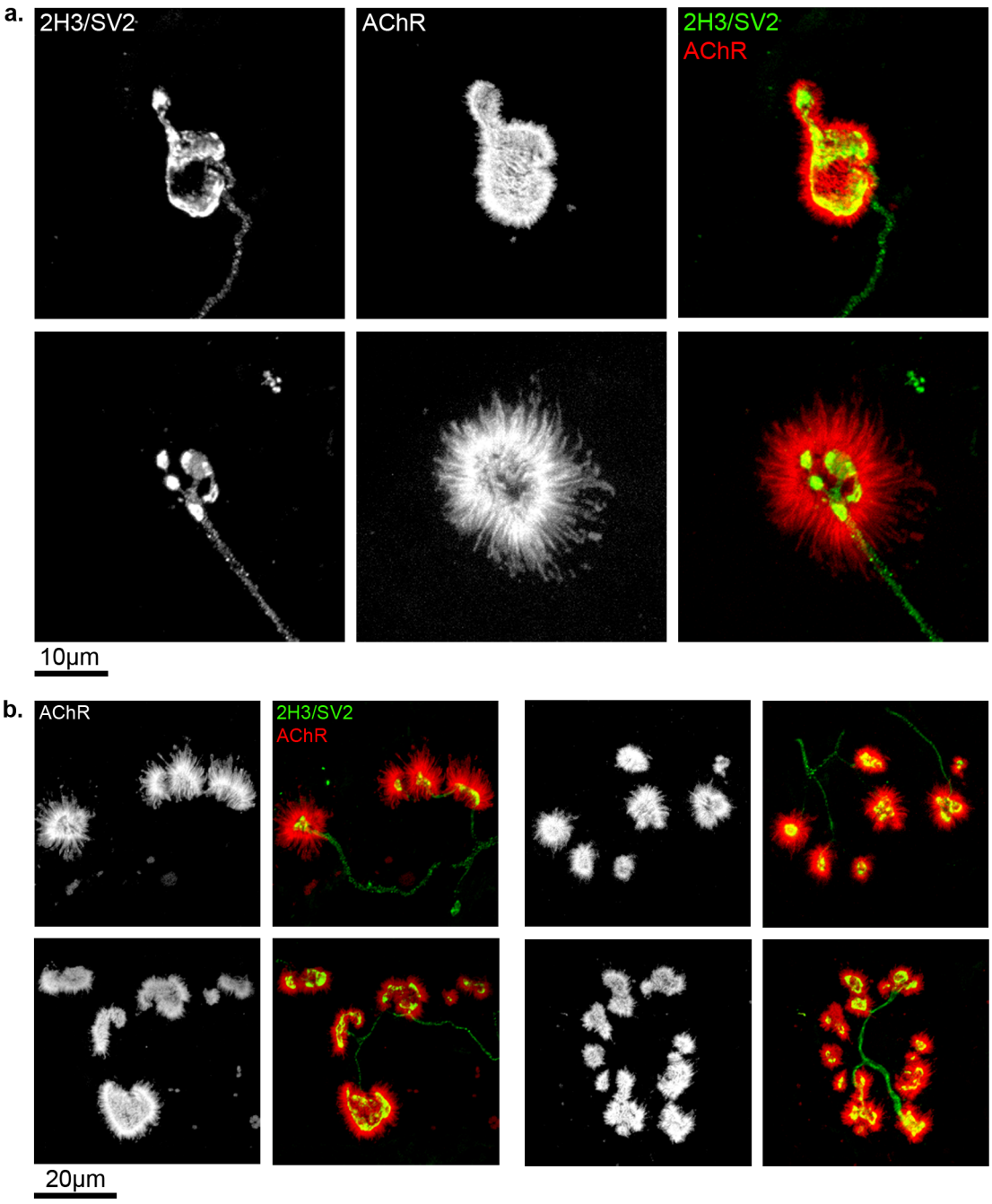

Figure 4.6 | 'Spiculated' endplates (human NMJ)
A small percentage of human endplates demonstrated an unusual 'spiculated' appearance. **a.** Examples of single NMJs with normal (top panel) and spiculated (bottom panel) endplates on neighbouring fibres in the same individual muscle (soleus, 92 year old male). Spiculated endplates were noted in NMJs from all muscles across the lifespan, and do not appear to correlate with age; the explanation for the appearance and its significance is unclear. Spiculation was not noted in equivalent mouse NMJs. Scale bar = 10µm. **b.** Other example NMJs with differing degrees of endplate spiculation (all from *soleus*). Scale bar = 20µm.

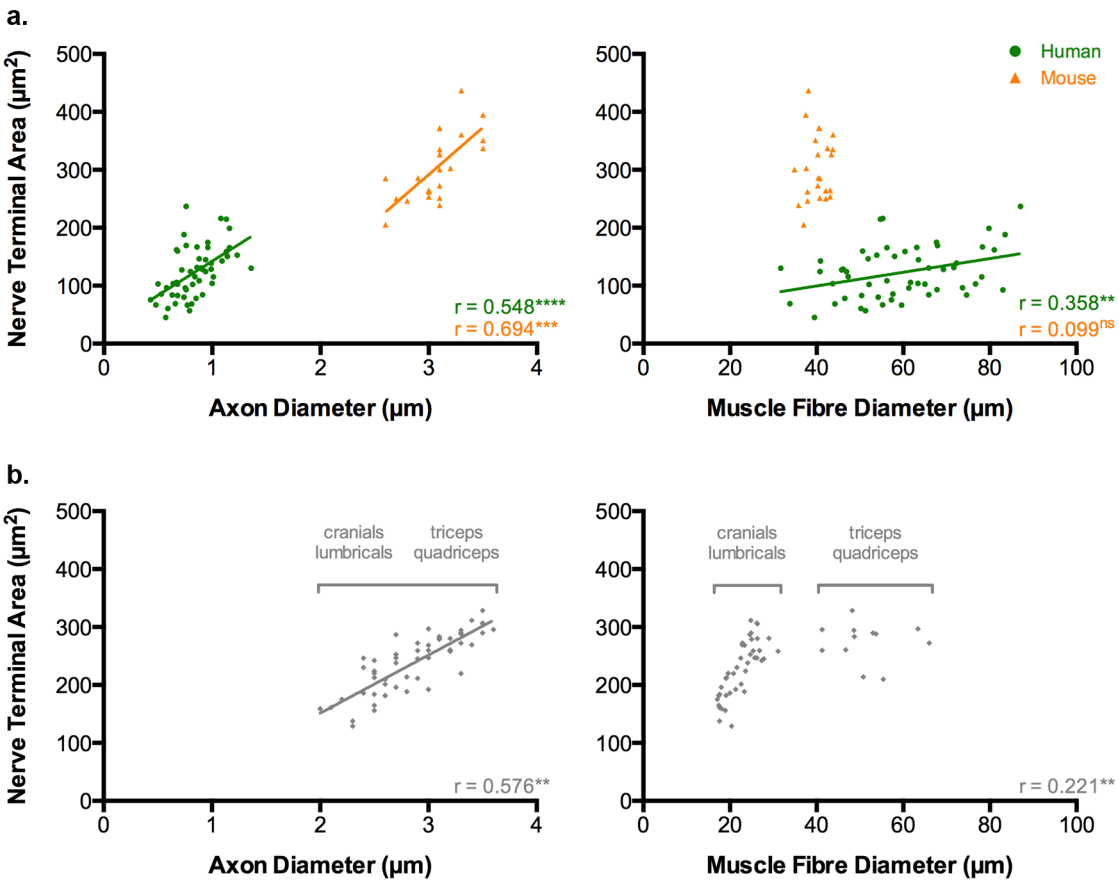

Figure 4.7 | Influence of pre- and post-synaptic cells on human NMJ morphology
NMJ variables were correlated with axon/muscle fibre diameter for human and mouse NMJs. **a.** Scatter plots for nerve terminal area correlation data. Each data point represents the average NMJ for an individual muscle (the mean of 40 NMJs); 72 human muscles (green) and 24 mouse muscles (orange) are included (pooled from the 4 lower limb muscles: EDL, S, PL, PB). NMJ morphology is more closely correlated with the pre-synaptic cell (axon diameter) in both species. **b.** Re-plot of correlation data from original mouse series (see Figure 3.5) comprising different muscles (cranials, lumbricals, triceps and quadriceps). Comparison of scatterplots **a.** and **b.** reveals that the correlation data from the 4 lower limb muscles concurs with the findings of the original series. Pearson correlation. ****p< 0.0001, ***p< 0.001, **p< 0.01. See Appendix 11 for other variables.

comprising the *cranial* and *lumbrical* muscles (smaller) and the *triceps* and *quadriceps* (larger). The correlations with axonal diameter for the NMJs of the leg muscles follow the earlier linear relationship, but the correlations with myofibre diameter fall at the transition point between the liner and non-linear parts of the relationship in the original series (see also Figures 3.5 and Appendix 6). Thus, the weaker relationships with muscle fibre diameter in the present series may be partially explained if the pre-synaptic cells are close to reaching the potential 'cytoplasmic volume limit' that was hypothesized earlier (Chapter 3).

4.4.3 Effects of pathology

The major concerns relating to the use of surgical discard tissue from amputation specimens are the potential effects of chronic tissue ischaemia due to peripheral vascular disease (PVD) and the neuropathic sequelae of diabetes mellitus. However, no significant differences were noted in the majority of 'core' morphological variables, when comparing NMJs in patients with or without either PVD (n.s. for 8 of 11 variables) or diabetes (n.s. for 10 of 11) (Table 4.3). Nor were any significant differences found in mean muscle fibre diameter (Table 4.3), excluding any significant sarcopenia and/or disuse atrophy in the present case series. In addition, the gross appearance of NMJs in patients with pathological changes (PVD, DM) was no different to NMJs from the healthy controls (see later Figure 4.9). These findings support the use of the tissue harvesting method described, and it seems reasonable therefore to regard the human NMJs presented in this series as reflecting 'normal' morphology.

As an additional preliminary comparison, tissue was also harvested from the *rectus abdominis* muscle of a 71-year-old male undergoing total gastrectomy for stomach cancer (Figure 4.8). Muscle samples were processed as described earlier (Sections 4.3.4 and 4.3.5) and assessed qualitatively. NMJs displayed a range of morphologies (including en passant), but the overall size and appearances were very similar to the NMJs already quantified in the lower limb muscles. Although these qualitative observations only represent a single case in one other muscle, the similarity of the NMJs from anatomically distinct regions and in patients with different underlying pathological processes (control, atherosclerosis, neoplasia) suggests a common general morphology of human NMJs (at least in the trunk and limbs), and argues against any major effects on the NMJs of the underlying conditions (PVD, cancer), adding further support to the use of surgical discard material for study of human NMJs in future work.

Effects of aging, pathology and sex (human NMJ)				
	correlation with age	DM	PVD	M/F
core varaibles				
pre-synaptic				
1) nerve terminal area	0.454 ***		*	**
2) nerve terminal perimeter	0.313 *			*
3) number of terminal branches	0.234			*
4) number of branch points	0.582 ****		**	*
5) total length of branches	0.460 ***		*	*
post-synaptic				
6) AChR area	0.315 **			****
7) AChR perimeter	0.000			***
8) endplate area	0.187			****
9) endplate perimeter	0.286 *			****
10) endplate diameter	0.295 *			***
11) number of AChR clusters	-0.156	*		***
derived variables				
pre-synaptic				
12) average length of branches	0.259			
13) complexity	0.409 **			**
post-synaptic				
14) average area of AChR clusters	0.605 ****		**	
15) fragmentation	-0.145	*	*	**
16) compactness	0.370 **		*	
17) overlap	0.154			
18) area of synaptic contact	0.423 **		*	**
associated nerve & muscle variables				
19) axon diameter	0.529 ****		*	*
20) muscle fibre diameter	0.059			*

Table 4.3 | Effects of aging, pathology and sex (human NMJ)
Correlation data for effect of age listed as coefficient (r, numerical) and significance level (p, asterisk). Significance levels for effects of diabetes mellitus (DM vs. non-DM), peripheral vascular disease (PVD vs. non-PVD) and sex (male vs. female) obtained from unpaired t-tests/Mann-Whitney tests. ****p< 0.0001, ***p< 0.001, **p< 0.01, *p< 0.05.

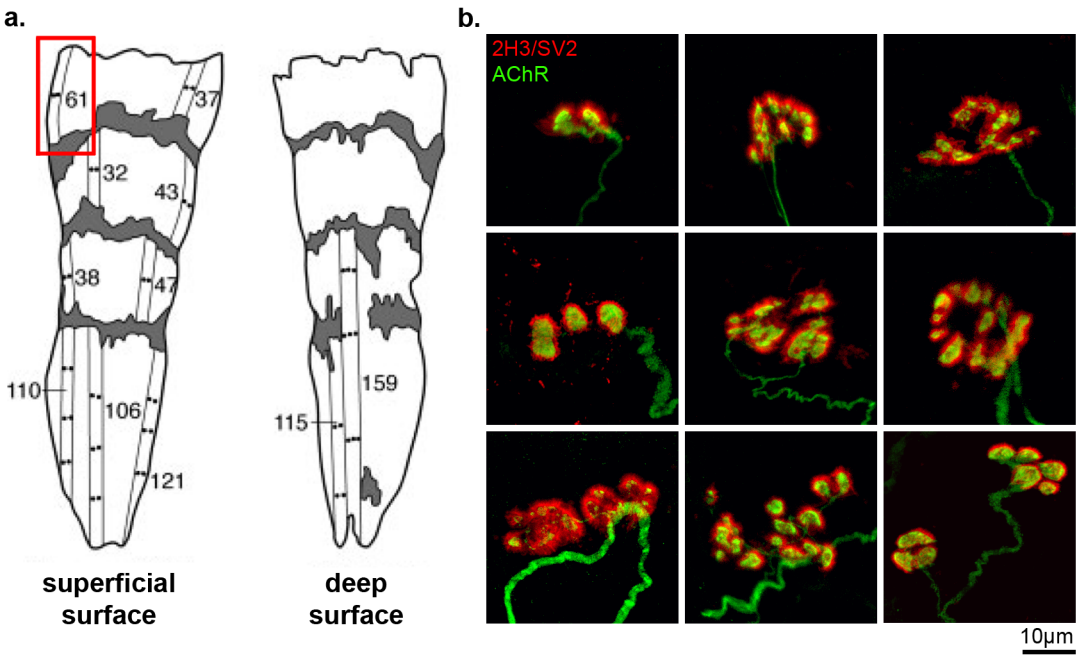

Figure 4.8 | Human NMJs in rectus abdominis
NMJs from *rectus abdominis* in a 71 year old male undergoing total gastrectomy for stomach cancer. **a.** *Rectus abdominis* has an 'in-series' muscle fibre architecture, lacking discrete endplate bands. The first tendinous intersection on the superficial surface (red box) was used as a guide for muscle harvest (from Woodley et al, 2007; numbers indicate muscle fibre lengths in mm). **b.** Example NMJs from *rectus abdominis* showing a range of morphologies, including 'en passant' NMJs (bottom row). Their overall appearance is very similar to NMJs from the lower limb muscles (*extensor digitorum longus, soleus, peroneus longus et brevis*) in patients with and without vascular disease. Scale bar = 10µm.

4.4.4 Effects of age

The present series included patients from the fourth to the tenth decades of life, with an approximately even distribution of patients across the age range, including 3 or more individuals from most decades (Table 4.1). Given the general assumption that the NMJ is inherently unstable with age (based largely on animal studies; discussed below), initial observations revealed a surprising conservation of NMJ morphology across the lifespan (Figure 4.9).

Correlations with age were then assessed quantitatively for each NMJ variable in turn for the complete human NMJ series (Table 4.3, Appendix 12). Whilst some morphological variables (12 of 20) did show a statistically significant correlation with age, albeit to varying degrees, the overall magnitude of change over the entire lifespan was minimal. Axon diameter ($r = 0.529^{****}$) and the core pre-synaptic variables (with r values ranging from 0.313^{*} to 0.582^{****}) were more strongly correlated with age than the core post-synaptic variables (with r values from 0.295^{*} to 0.315^{**}) (Table 4.3). Thus, the modest degree of synaptic remodeling observed with age was predominantly on the pre-synaptic side of the NMJ, and was not indicative of any degenerative-type changes. Notably, there was no significant change in the degree of overlap between the pre- and post-synaptic components of the NMJ, and this robust 'coupling' across the synapse was maintained throughout life.

Interestingly, there was no evidence of age-associated fragmentation of the endplate that has been reported previously in human intercostal muscle (Oda, 1984). Nor was there any significant decrease in muscle fibre diameter with age, excluding any marked degree of sarcopenia or atrophy from other causes (disuse, disease) in the present series. Thus, the modest degree of pre-synaptic remodeling that occurred with age was 'de-coupled' from equivalent changes in the muscle fibre itself, further supporting the earlier observation that NMJ morphology is more closely correlated with the pre-synaptic cell (Section 4.4.2).

As noted earlier (Section 1.2.4), the existing literature in relation to age related changes at the human NMJ is both limited and often conflicting (Oda, 1984; Wokke et al, 1990). These earlier studies were much smaller in scale, and used lower resolution techniques than those available today, which may in part explain the disparate findings reported.

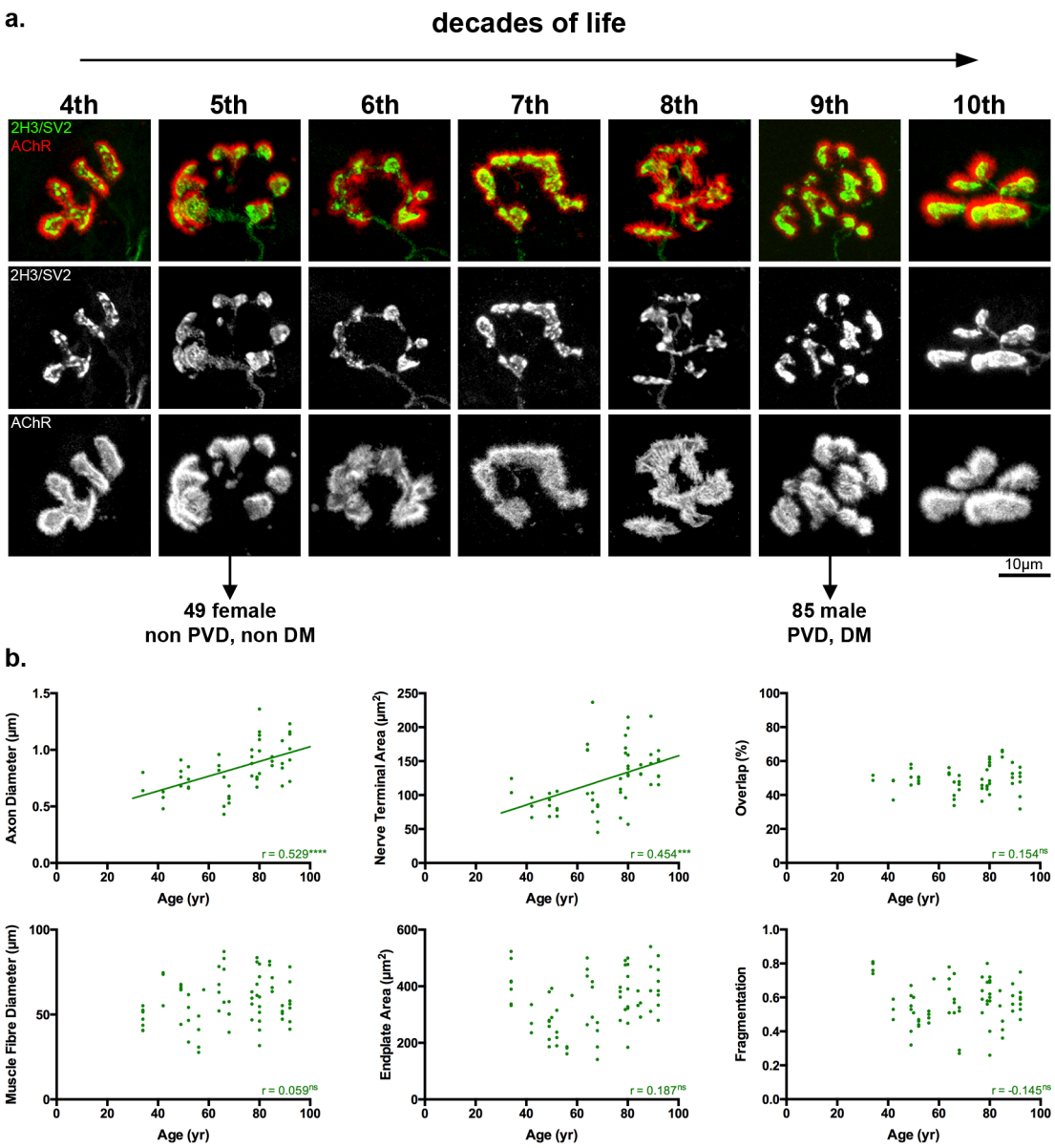

Figure 4.9 | Effect of age on human NMJs
The effect of age on NMJ morphology was assessed in patients aged from 34 to 92 years. **a.** Representative NMJs from *peroneus longus* from the 4th to the 10th decades of life. Despite the heterogeneity of individual NMJs, overall morphology appears to be relatively conserved across the 70-year age range. In addition, there is no visible difference in the appearance of the example NMJs from the 5th and 9th decades, which are from patients of different sex and co-morbid status. Scale bar = 10µm. **b.** Scatterplots demonstrating age correlations for 6 morphological variables, including both pre- and post-synaptic cells/NMJ variables. Each data point represents the average NMJ for an individual muscle (the mean of 40 NMJs); 72 human muscles are included (pooled across the 4 lower limb muscles: EDL, S, PL, PB). Although axon diameter and nerve terminal area showed a modest correlation with age, the overall synaptic morphology remained remarkably stable, with no evidence of sarcopenia in the present series. Pearson and Spearman correlation. ****p < 0.0001, ***p < 0.001. See Appendix 12 for other variables.

Both Oda (1984) and Wokke et al (1990) studied *intercostal* muscle only (cf. *EDL, PB, PL, soleus* in the present study), the cases were fewer in number and more limited in age range (12 adults, 32-76 years; Oda, 1984 cf. 20 adults, 34-92 years; present study) and the NMJ analyses were also based on smaller sample sizes and less detailed morphometry (<500 NMJs, 3 variables per NMJ; Wokke et al, 1990 cf. > 2,000 NMJs, 18 variables per NMJ; present study). In addition, lower resolution staining techniques were used in the earlier studies (e.g. silver-cholinesterase). The conclusions of the studies by Oda (1984) and Wokke et al (1990) are contradictory; our findings of relative stability of the NMJ with age are in closer agreement with those of Wokke et al (1990), as opposed to the increasing complexity of the NMJ (both pre- and post-synaptic) reported by Oda (1984).

The finding of relative stability with age of human NMJs is in contrast to the extensive remodeling that occurs in other species (typically mice) over a much shorter lifespan. In mice, structural and functional changes occur both pre- and post-synaptically with age (Gonzalez-Freire et al., 2014), including fragmentation of the endplate during early development, continued growth (Balice-Gordon & Lichtman, 1990; 1993; respectively) and advancing age (Valdez et al, 2010; Willadt et al, 2016). On the background of these general age changes however, diverse strain-specific age changes are known to exist (Anis and Robbins, 1987; CB57 and BALB/C mice). Recent evidence points to loss of skeletal muscle as the driver of these age changes at the NMJ (Liu et al., 2017).

The differences in aging at the human NMJ (present study) compared to the mouse NMJ (previous studies cited) might in part be explained by the recent observation of conserved and species-specific molecular changes in aging skeletal muscle of different mammalian species (mouse, rat, monkey, human; Mercken et al., 2017).

In summary, the present findings reveal the human NMJ to be remarkably stable across a 70+ year lifespan, lacking much of the age-related remodeling that has been reported in other species (including mice) over a much shorter lifespan. Concurrent age-related changes in the functional capacity of the human NMJ with age remain to be determined.

4.4.5 Other factors influencing NMJ morphology

In the present case series, tissue samples were obtained from one or other side of the body in different individuals. However, a single case of bilateral amputation provided a rare opportunity to compare NMJ morphology on the left and right sides of the body in the same individual (Figure 4.10, Appendix 13). Furthermore, the procedure was performed in an otherwise healthy young male (34 years, for acute ischaemia secondary to thromboembolism from infective endocarditis). Data was compared with a similar series of left/right NMJs in the 3 littermate mice. Although the observations could not be confirmed statistically in a single human case, there were no overt left/right differences in the NMJ variables analyzed, in keeping with the observation of consistent replication of NMJ morphology across left/right muscle pairs in the previous mouse work (Chapter 3).

Sexual dimorphism was also assessed in the human series (Table 4.3). Sex differences were found to be statistically significant for the majority of NMJ variables (16 out of 20) including all of the core variables and muscle fibre diameter. All variables were greater in males than females. This is in stark contrast to the lack of any significant sexual dimorphism in mice (Chapter 2), but is perhaps not surprising given the heterogeneous nature of the patient case series compared with the homogeneous genetic background of mice from a single litter.

4.4.6 Comparative anatomy of mouse, rat and human NMJs

As noted in the General Introduction (Section 1.2.1; Comparative anatomy of the NMJ), there appears to be a general trend toward smaller NMJs in larger animals (Figure 1.2). To explore the possibility of a simple inverse relationship with body size, the human and mouse data was compared with rat NMJs from the equivalent muscles (*EDL*, *PB*, *PL*, *soleus*).

Sprague Dawley rats were used for the comparisons, with a mean weight of > 200g (cf. ≈ 25g for *CD1* mice; ≈ 10-fold weight difference). Muscle dissection, NMJ immunohistochemistry and confocal imaging were performed as described previously (Section 3.3). As an initial look-see experiment, rat NMJs were not formally quantified with NMJ-morph, but a sample of 40 NMJs per muscle were inspected alongside the equivalent human and mouse NMJs.

As anticipated, rat NMJs were much larger than the equivalent human NMJs (Figure 4.11). Side-to-side comparison of rat and mouse NMJs was less clear-cut however. Although there

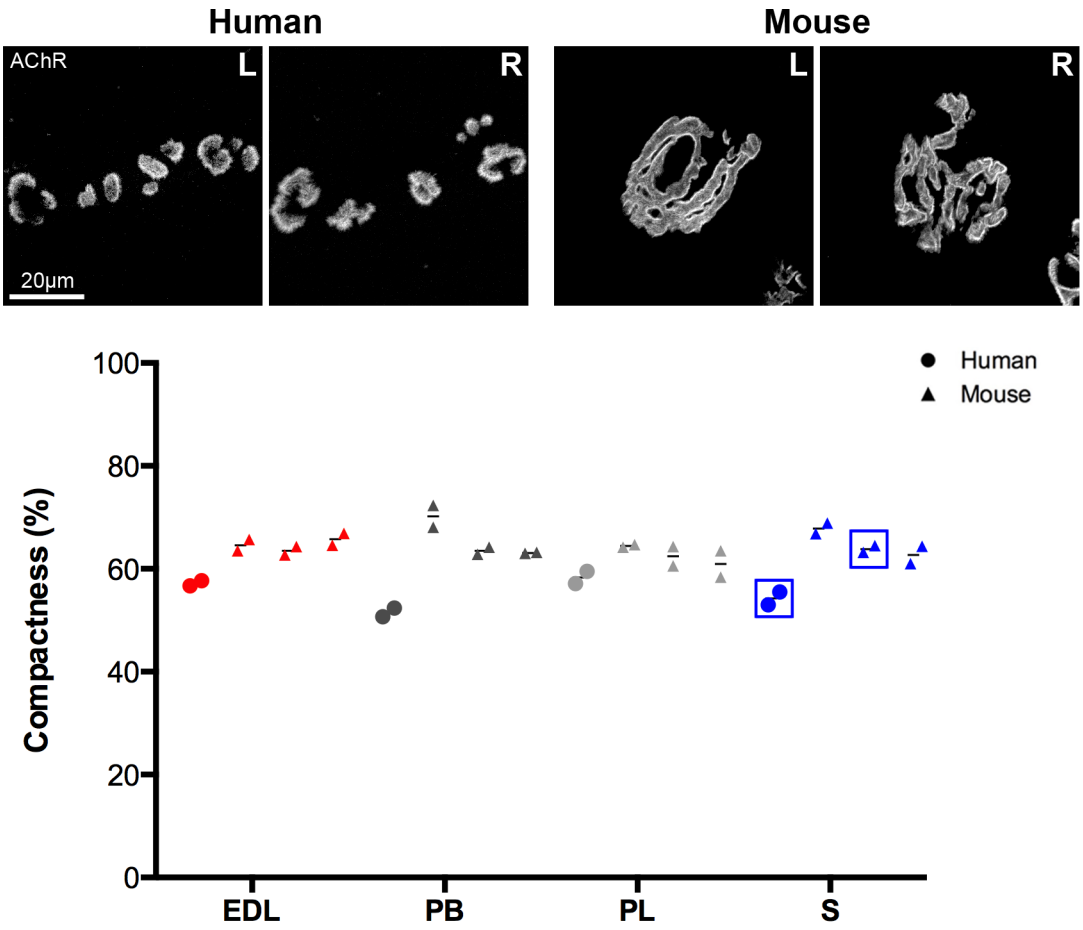

Figure 4.10 | Influence of side on human NMJ morphology
One patient in the case series underwent bilateral lower limb amputation, providing a rare opportunity to compare NMJ morphology on the right and left sides of the body in a single individual. Data points are grouped in pairs on the graph; each point represents the average NMJ for an individual muscle (mean of 40 NMJs) from the right or left side of the body; the intervening line is the average of the 2 sides. Data from the single patient in question (circles) is presented alongside equivalent data from 3 individual mice (triangles) for the morphological variable 'compactness'. Example NMJs from soleus are shown for the 2 data-sets highlighted (blue boxes). In both species, average NMJs were similar on the right and left sides of the body. Scale bar = 20µm. See Appendix 13 for other variables.

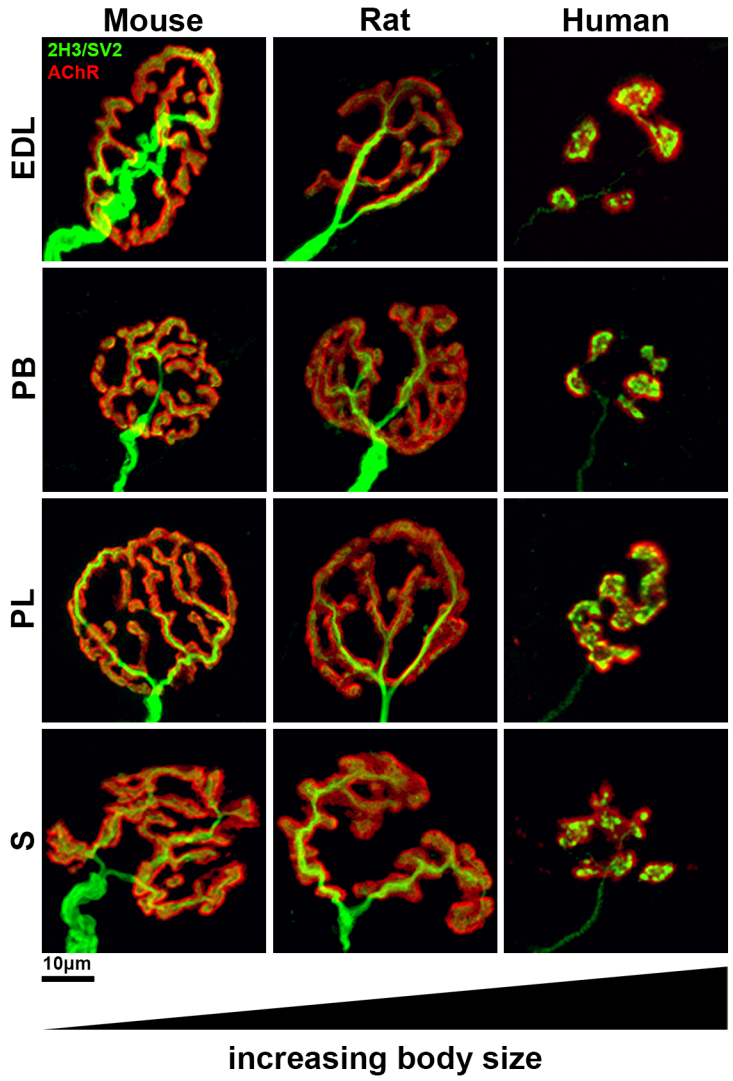

Figure 4.11 | Comparative anatomy of mouse, rat and human NMJs
Example NMJs from equivalent muscles in the 3 species, arranged according to body size. Although human NMJs are smaller, on average, than mouse NMJs, the varying sizes of rat NMJs do not support a simple inverse relationship between NMJ size and body size. Scale bar = 10µm.

were subtle (but definite) morphological differences in the shape of NMJs in rats and mice (e.g. wider and coarser AChR clusters of rat endplates), there were *no* clear differences in the overall size of NMJs (Figure 4.11), despite a 10-fold weight difference between the animals, i.e. the rat NMJs did *not* occupy an intermediate position between mouse and human NMJs.

Although this is a crude comparison, given the non-uniform weight intervals between the species (≈ 10-fold, mouse to rat; ≈ 350 fold rat to human*), these findings would suggest that the smaller NMJs in humans are not simply a consequence of increased body size/mass. It is possible that the weights of mice and rats in this example are too similar to one another (and too different to humans) to appreciate any genuine inverse relationship (whether linear or otherwise). It would therefore be telling to include other large animals in this comparison (e.g. sheep ≈ 50-150kg, horse > 350kg, cattle > 700kg) before making any definite conclusions about the relationship between NMJ size and body mass. [*for an average 70kg human]

Chapter 5

Molecular architecture of the human NMJ

5.1 Chapter summary

In the preceding chapter, the cellular architecture of the human NMJ was described. This final chapter will focus on 'sub-cellular' features, both in terms of structure (revealed by super-resolution imaging of the nerve terminal 'active zones') and function (via comparative proteomic profiling of the NMJ and its muscle fibre). These early insights into the molecular architecture of the human NMJ provide a foundation for future research into human NMJ biology and translational studies of neurodegenerative disease.

5.2 Introduction

The 'active zone' refers to the region of the pre-synaptic nerve terminal that houses the molecular machinery responsible for neurotransmitter release (Zhai and Bellen, 2004; Ackermann et al, 2015), and comprises all of the various structural and functional proteins contributing to the synaptic vesicle cycle. The cycle itself has a number of recognized stages (capture, docking, priming, anchoring and fusion; Ackermann et al, 2015) whilst vesicle recycling occurs by several different mechanisms ['kiss-and-run' (Zhang et al, 2007), clathrin-mediated endocytosis (Ackermann et al, 2015), bulk endocytosis (Wu et al, 2014) and ultrafast endocytosis (Watanabe et al, 2013)]. In this synaptic vesicle cycle, individual proteins can be grouped according to their general function(s) e.g. scaffolding, vesicle priming, vesicle adhesion, calcium channel localization, endocytosis (Ackermann et al, 2015).

5.2.1 Morphology of active zones

In reviewing active zone structure in different synapses (e.g. CNS, NMJ) and different species (i.e. invertebrate, vertebrate), a recurring theme is the preservation of structure through evolution (Zhai and Bellen, 2004; Ackermann et al, 2015). This becomes apparent when comparing the key structural features that have been elucidated in various species (*Caenorhabditis elegans*, *Drosophila melanogaster*, frog, mouse) through a variety of techniques (typically electron microscopy and tomography), though the individual proteins responsible for these appearances remain obscure in many instances.

5.2.1.1 Invertebrate active zones

In invertebrates, the active zones of the NMJ have been studied in some detail in both *Caenorhabditis elegans* and *Drosophila melanogaster*. In *C. elegans*, the key structural feature of the active zone is the so-called 'dense projection' (Watanabe et al, 2013) composed of the scaffolding protein *SYD-2*. Synaptic vesicles are seen anchored to these dense projections by a number of filaments (of unknown protein composition), with the overall arrangement bearing a similar appearance to CNS synapses in vertebrates (see below). *Drosophila* has a more complex 'T-bar' structure (Fouquet et al, 2009) composed of the scaffolding protein *Bruchpilot*, with calcium channels found clustered near the base of the T-bar.

5.2.1.2 Vertebrate active zones

In comparison, the major difference seen in vertebrate active zones is the degree of protein diversity (Wilhelm et al, 2014). This diversity is reflected in the (generally) more complex nature of their active zones, which may facilitate the corresponding functional diversity.

CNS synapses (e.g. rat hippocampus) display a 'simple filamentous' structure (Siksou et al, 2007) similar to the NMJ active zones of *C. elegans*, but lacking the discrete dense projection to which the vesicles and filaments are tethered. Several of the proteins identified at these active zones are homologues of those found in invertebrates (e.g. the vertebrate protein *liprin-α* is equivalent to the invertebrate protein *SYD-2*; Ackermann et al, 2015).

The so-called 'ribbon synapses' of photoreceptor cells (e.g. rat retina) are more complex, with the active zones comprising a central 'ribbon' organelle (not dissimilar to the 'T-bar' of *Drosophila*) attached to an 'archiform' density of the cell membrane (Schmitz, 2014). The multi-domain proteins *Piccolo* and *Bassoon* are thought to play pivotal roles in ribbon shape and ribbon attachment, respectively, and are the first active zone proteins (to date) that have been studied using super-resolution microscopy (Nishimune et al, 2016; see below).

The highest resolution work on vertebrate active zones has focused on the frog NMJ (Szule et al, 2012; Harlow et al, 2013). Whereas the active zones of CNS synapses have a 'simple filamentous' structure, those of the frog NMJ have a distinctly 'complex filamentous' architecture, similar again to the 'T-bar' of *Drosophila*. Using electron tomography and three-dimensional computer reconstruction, a complex arrangement of filaments has now been

described (including vertically disposed *'beams'*, *'steps'* and *'masts'* and horizontally disposed *'ribs'*, *'spars'* and *'booms'*). These individual units polymerize in a relatively simple fashion, resulting in a linear array of active zones, similar to those of *C. elegans*. Similar structural components (*beams, ribs,* etc), albeit in a different arrangement, have also been demonstrated in the mouse NMJ (Nagwaney et al, 2009). The nature of the individual proteins comprising each of these named structures remains undetermined however.

5.2.2 Distribution of active zones and human NMJs

In addition to contributing some of the earliest information on active zone distribution, freeze-fracture electron microscopic studies provide the only description of human active zones to date.

Studies in patients with Lambert-Eaton myasthenic syndrome (LEMS) describe active zones composed of intra-membrane particles arranged in parallel double rows (like two railroads side-by-side) and clusters (Fukunaga et al, 1982). Individual active zones varied in size (number of particles per row/cluster) and orientation (relative to the long axis of the nerve terminal) in control patients, whilst both the size and density of active zones were reduced in LEMS patients. These studies were limited to the biceps brachii and intercostal muscles. A similar distribution of active zone particles (and effect of LEMS) is seen in mice (Fukunaga et al, 1983), although here, the rows of particles are generally more perpendicular to the long axis of the nerve terminals (than the more varied orientation in humans).

The particles revealed by these freeze-fracture studies are thought to be calcium channels, but this has not been confirmed in humans. Similarly, data relating to the spacing and density of active zones is typically quoted in relation to other species, with approximate values for active zone spacing and density of 0.5μm and 2.5/μm^2 respectively (the former in *Drosophila* and *Sarcophaga*, Meinertzhagen, et al 1998; the latter in mice, Fukuoka et al, 1987).

5.2.3 Super-resolution imaging of active zones

As discussed above, active zone ultrastructure has been largely elucidated by means of electron microscopy. In attempting to determine the identity of the individual proteins contributing to many of the gross morphological features already noted, super-resolution fluorescence microscopy now offers a significant step forward.

Super-resolution microscopy circumvents the diffraction-imposed resolution limit of conventional light microscopy, allowing high resolution imaging in the 'mesoscale' range of 10 to 100 nanometers (Maglione and Sigrist, 2013). Various super-resolution approaches exist, e.g. STORM (**st**ochastic **o**ptical **r**econstruction **m**icroscopy) and STED (**st**imulated **e**mission **d**epletion) microscopy, all based on similar underlying principles (Huang et al, 2010).

STED microscopy has now been used for the first time to study the active zone proteins *Piccolo* and *Bassoon* in mouse NMJs, revealing a 'sandwich' structure of these proteins in a 2:1 ratio, respectively (Nishimune et al, 2016). The present work includes the first ever use of super-resolution imaging to study human active zone architecture.

In summary then, although a large body of work now exists in relation to the active zone architecture of various species/synapses, very little is known about the active zones of human synapses, or their comparative proteomic make-up in relation to other animals. This chapter aims to provide some of the first insights into the molecular organization of the human NMJ, including its active zone architecture and general proteomic composition.

5.3 Methods

The molecular architecture of the human NMJ was investigated using two approaches: super-resolution imaging and proteomic profiling.

5.3.1 Super-resolution imaging

The finding of intense 'hot spots' of SV2 labeling in human NMJs during the initial confocal experiments (that were not present at the mouse NMJ; Figure 5.1), together with the known species differences in active zone structure, provided a clear rationale for re-examining the fine structure of the nerve terminal with super-resolution imaging techniques.

Antibodies against several active zone proteins were trialed (including SNAP25, Bassoon and Piccolo), but anti-SNAP25 (Alomone Labs) was found to produce the most consistent labeling of both human and mouse NMJs, and could be reproducibly imaged using both

confocal and super-resolution microscopy (Figure 5.1, Appendix 14). A single muscle was selected (arbitrarily) for study – *peroneus longus*.

5.3.1.1 Tissue preparation

For optimal results, tissue was obtained prospectively from three successive human cases (aged 66, 68 and 79 years; case references 10, 11 and 13 in Table 4.1). For comparison, an equivalent set of *peroneus longus* muscle fibres was obtained from three adult CD1 mice. Muscle dissection was performed in a similar manner to that described previously (see Section 4.3.4) to obtain teased preparations of single-fibre thickness suitable for super-resolution imaging. NMJ immunohistochemistry was also performed as before, but with a number of modifications to label NMJs for pre-synaptic SNAP25. After incubation in the primary and secondary antibodies (listed below), tissue samples were washed and mounted in dSTORM mounting medium (90% glycerol, 1xPBS, 100mM MEA) (Hou et al, 2015). The human samples then underwent an additional 70-minute treatment with 1mM CuSO4 in 50mM ammonium acetate buffer, pH5 to remove lipofuscin-like autofluorescence following immunolabeling (Schnell et al, 1999).

Antibodies

Primary: 1:100 rabbit anti-SNAP25 IgG (Alomone).

Secondary: 1:100 Alexa Fluor 647 goat anti-rabbit IgG (Thermo Fisher Scientific).

BTX: 1:500 TRITC α-bungarotoxin (Biotium).

5.3.1.2 dSTORM super-resolution imaging

dSTORM imaging performed and validated in collaboration with Carl Harrison and Christian Soeller, Physics and Astronomy, University of Exeter.

Following tissue preparation, super-resolution dSTORM imaging was performed on a customized Nikon Ti Eclipse inverted fluorescence TIRF microscope (as above). Given the restricted frame size and depth of field possible with super-resolution imaging, only single NMJs (on occasion) or parts thereof (in most instances) were imaged (Figures 5.1 and 5.2). In either case, only the in-focus boutons were selected for later analysis.

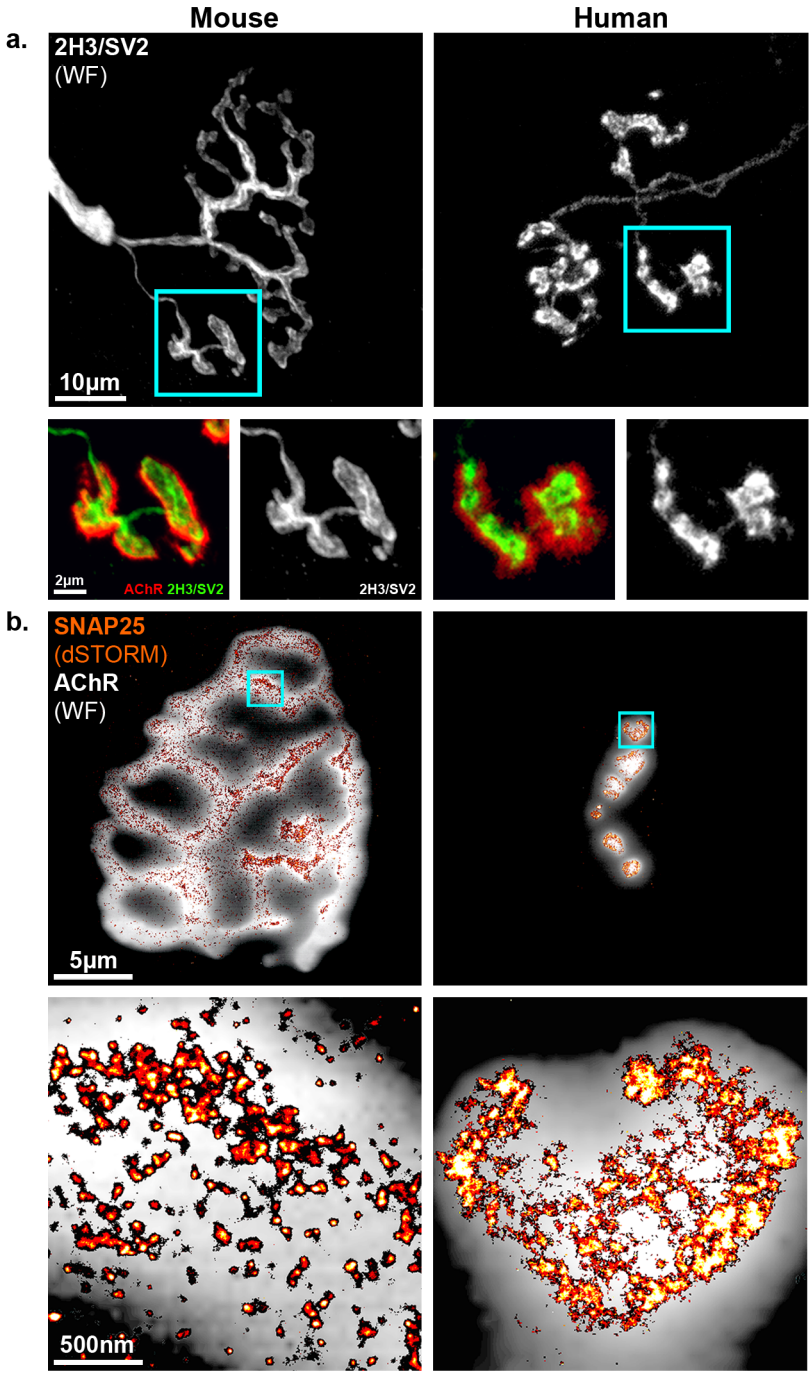

Figure 5.1 | Nerve terminal 'hot spots' and relation to active zones in human NMJs
Differential labeling of SV2 protein in human NMJs corresponded with active zone distribution revealed by super-resolution imaging of SNAP25 protein. **a.** Standard confocal images (wide-field) of human and mouse NMJs, with nerve terminals labeled for SV2 protein. The boutons highlighted in blue have been enlarged (below main images) to reveal distinct 'hot spots' of labeling in the human NMJ, compared with the homogeneous labeling in the mouse NMJ. **b.** Super-resolution dSTORM images of human and mouse NMJs, labeled for the active zone protein SNAP25, overlaid on the corresponding wide-field images of α-bungarotoxin-labeled AChRs. The boutons highlighted in blue have been enlarged (below main images) to highlight the clear differences in SNAP25 labeling between human and mouse; the SNAP25 puncta in human NMJs are much brighter and more densely packed, giving rise to 'mega-islands' of SNAP25 that closely resemble the 'hot spots' of SV2 in the confocal images.

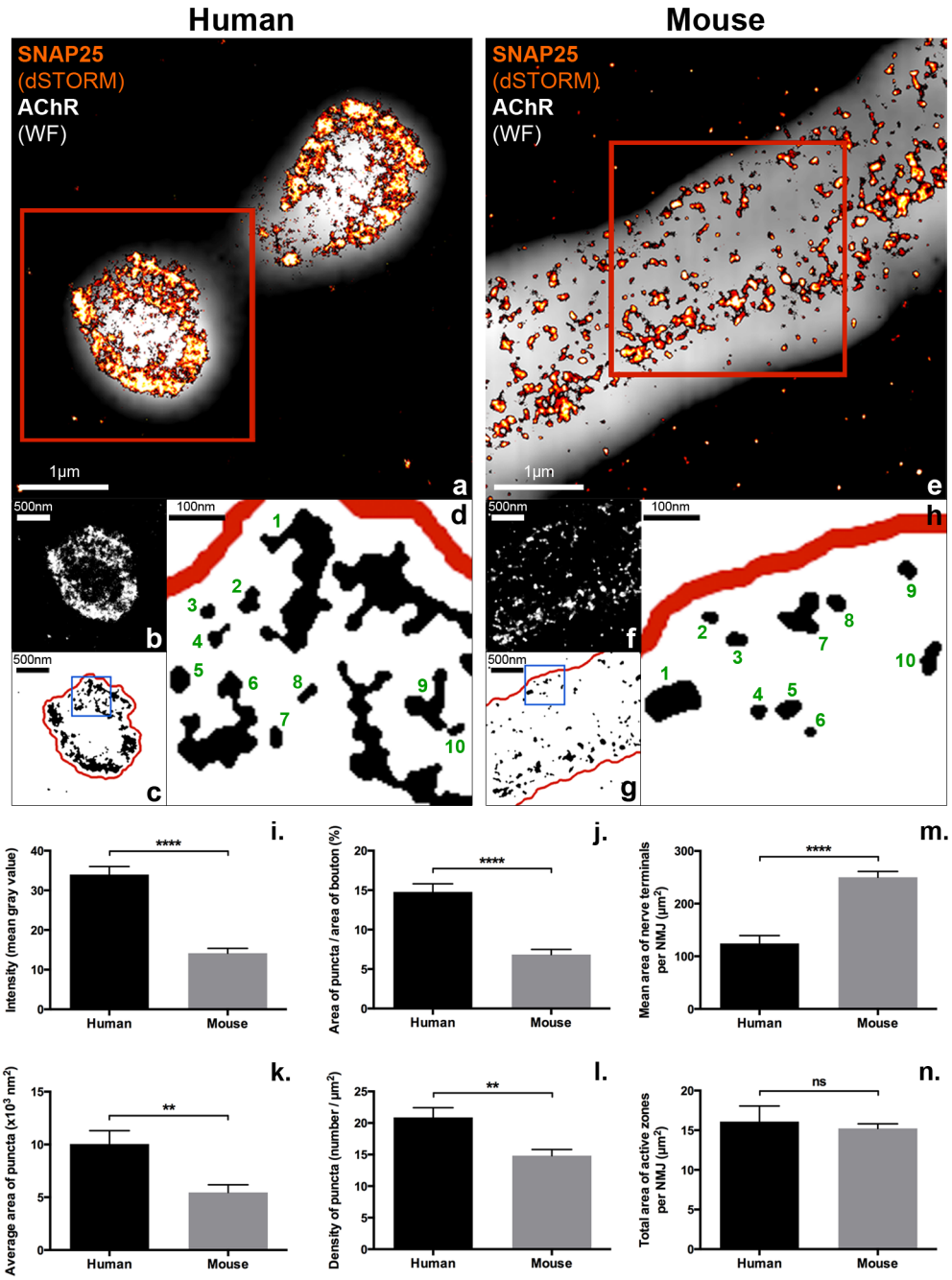

Figure 5.2 | Super-resolution imaging of the human NMJ
Side-to-side comparison of human and mouse dSTORM image analysis. **a./e.** Composite images of SNAP25 (dSTORM) and AChRs (wide-field) as in Figure 5.1b. Boxed areas in red correspond to **b./f.** Scale bar = 1µm. **b./f.** Greyscale images of single boutons (or parts thereof) used to quantify intensity of labelling (**i.**). Scale bar = 500nm. **c./g.** Despeckled, binary versions of images **b./f.** used to quantify other variables (**j./l.**). The boxed areas in blue have been enlarged (**d./h.**) to depict individual SNAP25 puncta that could be counted easily; 10 discrete puncta have been labelled. Scale bar = 100nm. **i./l.** Results of dSTORM image quantification. The 4 variables measured were significantly greater in human NMJs. In both datasets, n=50 boutons (from 3 patients/mice); bar charts depict mean (± SEM). **m./n.** Bar charts comparing the 'average size' of NMJs (nerve terminal area, **m.**) with the 'total size' of their active zones (SNAP25 area per NMJ, **n.**). Although the human NMJ is significantly smaller (**m.**), the total 'quantity' of active zone machinery is the same in both species (**n.**). Mann-Whitney test and unpaired t-test. ****p< 0.0001, **p< 0.01.

As with the standard confocal imaging (see earlier Chapters), dSTORM images of SNAP25-labeled nerve terminals were captured as a series of z-stacks, with an interval of 200nm. Z-stack limits were set manually, slightly above and below the plane of interface between nerve terminal and motor endplate. Corresponding wide-field images of α-bungarotoxin-labeled AChRs were captured using the same settings, to act as a 'mask' for the subsequent image analysis.

5.3.1.3 SNAP25 quantification and active zone analysis

Quantification of SNAP25 distribution was performed using standard ImageJ functions, in an identical manner for all images. The 'masked' images (SNAP25/AChR overlays) were used as a reference to determine the boundaries of individual boutons and SNAP25 puncta, and exclude background noise.

dSTORM images (SNAP25 only) were then cropped to focus on individual boutons (human) or parts thereof (mouse) and converted into 8 bit grayscale images, from which fluorescence 'intensity' measurements (mean gray value) could be taken (Figures 5.2b and 5.2f). These grayscale images were then converted into binary counterparts, 'despeckled' to reduce background noise and sharpen individual puncta, and used to quantify the remaining variables: the average area of individual puncta and their density within each bouton, and the total area of all puncta relative to the area of each bouton (Figures 5.2c and 5.2g).

The derived variable 'total area of active zones per NMJ' (Figures 5.2n) was calculated by multiplying the 'area of puncta : area of bouton' (human: 14.8%, mouse: 6.8%; Figure 5.2j) by the 'mean area of synaptic contact'* for NMJs in *peroneus longus* (human: 108.9μm^2, mouse: 222.3μm^2). *The 'mean area of synaptic contact' is marginally smaller than the 'mean area of nerve terminals' shown in Figure 5.2m (human: 124.4μm^2, mouse: 250.0μm^2; Figure 5.2m), and only includes the region of the nerve terminal in direct contact with the underlying AChRs (see Section 2.3.4.1).

Overall, SNAP25 distribution was quantified in 50 boutons (n) from 10 NMJs in three individuals (N) – a total of 2,945 (human) and 10,666 (mouse) individual SNAP25 puncta.

5.3.2 Proteomic profiling

As with the super-resolution work, proteomic profiling was performed in *peroneus longus* muscle samples.

5.3.2.1 Tissue preparation

For optimal results, tissue was obtained prospectively from four successive human cases (aged 56, 80, 80 and 92 years; case references 7, 14, 15 and 20 in Table 4.1). For comparison, an equivalent set of *peroneus longus* muscle fibres were obtained from four adult CD1 mice. After tissue harvest, muscle dissection was performed on *unfixed* tissue, in a manner otherwise similar to that described previously, to obtain small bundles of 25-30 muscle fibres. The endplate bands of the teased fibres were then labeled with α-bungarotoxin for 5 minutes, and the NMJ-enriched portions of the muscle fibres were micro-dissected out under a Nikon Eclipse 50i fluorescence microscope (Figure 5.3). The NMJ-enriched samples along with NMJ-devoid muscle 'ends' were then frozen and stored at -80°C prior to protein extraction and mass spectrometry. All muscle dissection and endplate labeling was performed within 30 minutes of tissue harvest to limit the degree of protein degradation.

5.3.2.2 Protein extraction and mass spectrometry

Protein extraction and validation of synaptic enrichment performed in collaboration with Samantha L Eaton, Maica Llavero Hurtado and Laura C Graham, Roslin Institute, University of Edinburgh. Mass spectrometry performed by Douglas J Lamont, Fingerprints Proteomics, University of Dundee.

The 4 sets of pooled tissue samples (human and mouse, NMJ-enriched and NMJ-devoid) were then processed as above. Validation of synaptic enrichment (NMJ samples cf. muscle samples) was confirmed by western blot prior to mass spectrometry, demonstrating that the technique of NMJ sampling was sound (Figure 5.3; but see also Section 5.4.2). Tandem mass tagging and mass spectrometry was performed according to a standardized protocol (Hughes et al, 2014).

5.3.2.3 Bioinformatics analysis and proteome quantification

Bioinformatics analysis and proteome quantification performed in collaboration with Thomas M Wishart, Roslin Institute, University of Edinburgh.

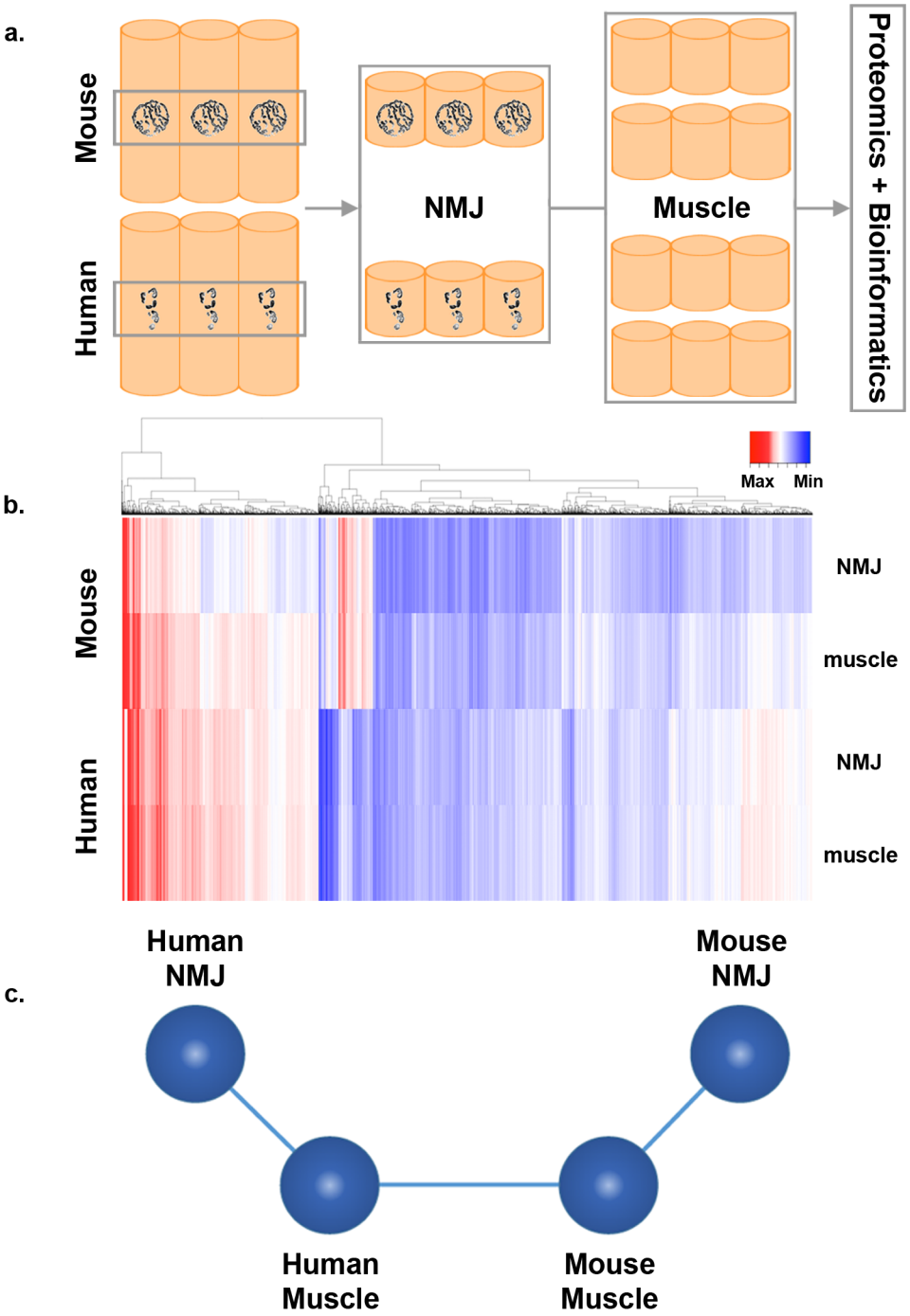

Figure 5.3 | Proteomic profiling of the human NMJ
Proteomic profiling and bioinformatics analysis revealed the unique molecular profile of the human NMJ. **a.** Muscle fibres were micro-dissected under a fluorescence microscope to obtain NMJ-rich and NMJ-devoid samples (using AChR α-bungarotoxin labeling as a guide). **b.** Heat map of proteomic data. Relative abundance is indicated by colour intensity, from high (red) to low (blue). Clear differences can be seen when comparing the 4 samples, especially between the NMJ bands in human and mouse. **c.** Schematic representation of proteomic data (from Biolayout). Each disc represents the expression data for an individual sample; the spatial arrangement indicates their relative similarity or otherwise. Thus, muscle samples (human cf. mouse) are more similar than NMJ samples (human cf. mouse).

The raw mass spectrometry data obtained for each of the 4 experiments (human and mouse, NMJ-enriched and NMJ-devoid) was collated into a single dataset using *MaxQuant* (Cox and Mann, 2008) and *Andromeda* search engine software (Cox et al, 2011).

An explorative approach to data analysis was adopted using *Ingenuity Pathway Analysis* (*IPA*) software to filter and quantify the data. This software generates 'protein interaction networks' based on a dynamic 'expert-curated' database (assembled from full-text articles of peer-reviewed journals) and calculates how relevant specific networks are based on the raw input data (Wishart et al, 2007). Given the potential pitfalls of such large-scale data analysis, the overall approach was to determine, in as simple a way as possible, the broad similarities and differences in protein composition between the human and mouse NMJ.

By concentrating on breadth rather than depth, the intention was to guide the more detailed future analysis of specific proteins and pathways identified in the dataset. With this goal in mind, stringent inclusion/exclusion criteria were applied. The complete dataset was filtered to include only candidate proteins identified by >1 peptide and demonstrating a >20% change between species. The resulting database was then searched manually for pathways relevant to the neuromuscular system, e.g. 'skeletal and muscular development/function and diseases/disorders' and 'neurotransmitter and nervous system signalling'. Filtered data was utilised for all statistical analyses and bioinformatics presentations (maps, schematics) in *Ingenuity Pathway Analysis* (*IPA*) and *Biolayout Express 3D* software (Table 5.1, Figure 5.3, 5.4).

5.4 Results and Discussion

The comparative molecular architecture of human and mouse NMJs is discussed in relation to SNAP25 distribution within the active zone, and in terms of the broader similarities and differences between the respective NMJ and muscle proteomes. All analysis was performed on NMJs obtained from *peroneus longus* muscle.

5.4.1 Super-resolution imaging

In the earlier confocal experiments, the nerve terminals of human NMJs were clearly distinguished from mouse NMJs by characteristic 'hot spots' of intense SV2 labeling (Chapter 4 and Figure 5.1). Since the functional architecture of active zones varies

considerably between species (Slater, 2015), the differential SV2 labeling observed with confocal microscopy invited detailed re-evaluation with the greater resolving power of dSTORM imaging, to ascertain potential differences in active zone architecture.

5.4.1.1 Human active zone architecture revealed by SNAP25 distribution

Active zone architecture was assessed by comparative super-resolution imaging of SNAP25 protein at human and mouse NMJs. SNAP25 is a component of the SNARE complex, a series of structural active zone proteins responsible for the fusion of synaptic vesicles with the plasma membrane during exocytosis (Han et al, 2017).

In the initial mouse experiments, the distribution of SNAP25 revealed by dSTORM imaging appeared remarkably similar to that of the active zone proteins Bassoon and Piccolo as demonstrated by previous STED microscopy (Nishimune et al, 2016; Appendix 15). In the latter study, the density of Bassoon/Piccolo was around 5-10 puncta per μm^2, with individual puncta having diameters of 100-125 nm. In the present study, the density of SNAP25 was around 15 puncta per μm^2, with individual puncta having areas of 5 $x10^3$ nm^2 (with comparatively smaller linear dimensions; Figure 5.2).

These results are in keeping with the known differences in size and distribution of the individual proteins. Bassoon and Piccolo are the largest of the pre-synaptic active zone proteins, with molecular weights of 420 kDa and 530 kDa, respectively (Garner et al, 2000). In comparison, SNAP25 is a much smaller protein (only 25 kDa; Antonucci et al, 2016) but is more abundant at the active zone, with an approximate copy ratio of 5 to 1 (5 copies of SNAP25 to 1 copy of Bassoon/Piccolo; Ackermann et al, 2015; Wilhelm et al, 2014).

Having established the distribution of SNAP25 in mouse NMJs, parallel dSTORM imaging of human NMJs revealed clear differences in the functional architecture of human active zones (Figure 5.2). Overall, a total of 2,945 (human) and 10,666 (mouse) individual SNAP25 puncta were quantified, pooled from 50 boutons (10 NMJs) of 3 individuals (patients/mice). All of the measured variables were found to be significantly greater in human NMJs: intensity of SNAP25 labeling (****$p<0.0001$), average area of individual SNAP25 puncta and their density within each bouton (both **$p<0.01$) and the total area of all puncta relative to the area of each bouton (****$p<0.0001$) (Figure 5.2).

The greater density of SNAP25 in human NMJs contrasted with the significantly smaller area of synaptic contact available for neurotransmission (consequent on both the smaller bouton size and the smaller pre/post-synaptic overlap; Figure 4.2 and Appendix 9). To assess the combined effect of these molecular and cellular differences (SNAP25 density cf. bouton size) the 'total area of active zone material per NMJ' was calculated (Figure 5.2j x Figure 5.2m; but see Methods, Section 5.3.1.3). In both species, this figure was identical – 15μm^2 of SNAP25 per NMJ (Figure 5.2). Therefore, although the human NMJ is significantly smaller than the mouse NMJ, the total quantity of active zone material remains the same, albeit packaged into smaller boutons in the human NMJ. This observation suggests the presence of a homeostatic mechanism to preserve the functional architecture of the pre-synaptic active zones in the face of significant morphological heterogeneity of the nerve terminals. In conjunction with the extensive post-synaptic junctional folding of the motor endplate demonstrated previously (Slater et al, 1992), this pre-synaptic adaptation could play a role in the maintenance of effective neurotransmission at the human NMJ.

5.4.2 Proteomic profiling

Having noted species differences in the distribution of SNAP25, the proteomic profiling techniques aimed to establish broader conclusions about the differential proteomic make-up of human and mouse NMJs.

In total, for the combined human and mouse datasets, *Ingenuity Pathway Analysis* confirmed the identification of peptides associated with 6,737 proteins. Application of stringent filtering parameters (protein identification by >1 peptide, fold changes of >20% between species) yielded a final total of 5,026 proteins for bioinformatics analyses. This represents a high yield from a single proteomic analysis, comparing favorably with a recent database of human proteins identified by mass spectrometry that listed 5,431 individual proteins across 38 peer-reviewed publications (Gonzalez-Freire et al, 2017).

Initial inspection of the proteomic data 'heat map' showed clear differences when comparing the relative abundance of proteins in the 4 samples – human NMJ, human muscle, mouse NMJ, mouse muscle (Figure 5.3). The differences that were apparent when comparing relative protein abundance in the NMJ and muscle samples (in the same species) provided clear proof of principle that synaptic enrichment could be adequately achieved in a relatively

simple manner (i.e. manual dissection; see Section 5.3.2.1) in the absence of more sophisticated techniques such as laser capture microdissection (Espina et al, 2006). From a biological standpoint however, the major insights were revealed by the between species comparison of the muscle samples (human cf. mouse) and the NMJ samples (human cf. mouse) as discussed below.

5.4.2.1 Conservation of the muscle proteome (human cf. mouse)

Comparative analysis of the proteomic profiles of the muscle samples (human cf. mouse) revealed clear similarities (Figure 5.3, Table 5.1). In silico analysis of these NMJ-devoid samples identified a total of 200 metabolic pathways common to both species, with the majority of the cascades (66%) showing no significant species differences.

Conversely, only 68 individual pathways (34%) showed a significant differential proteomic expression between the species (i.e. pathways with a $-\log_{10}(\text{p value}) \geq 1.3$). These findings support a conclusion of broad conservation of the muscle proteomes of the two species.

5.4.2.2 Divergence of the NMJ proteome (human cf. mouse)

In contrast, comparative analysis of the proteomic profiles of the NMJ samples (human cf. mouse) revealed clear differences (Figure 5.3, Table 5.1). In silico analysis of these NMJ-enriched samples identified a total of 36 nervous system related pathways common to both species, with the majority of the cascades (97%) showing statistically significant species differences. Many of these cascades are known to impact on NMJ form and function, including core synaptic pathways such as 'agrin interactions at the NMJ' (Table 5.1, Figure 5.4).

Within each of the identified pathways, individual proteins varied in their comparative abundance: some were more abundant in humans (cf. mice), some were more abundant in mice (cf. humans), whilst others were of similar abundance in both species (differing by < 20%) (Figure 5.4). For example, major differences in relative abundance were observed in 24 individual proteins contributing to agrin interactions at the NMJ (Figure 5.4). Since each pathway contained examples of proteins that were more abundant in one or other species, it can be concluded that present observations are not an artefact of relative enrichment during tissue processing (and therefore support the technical aspects of the proteomic techniques).

NMJ proteome (H vs M) Neurotransmitter and nervous system signaling					
Ingenuity canonical pathways	-$\log_{10}$(*p* value)	Upregulated (H vs M)		Downregulated (H vs M)	
agrin interactions at NMJ	13.30	13%	9/70	46%	32/70
NGF signaling	8.93	2%	2/123	40%	49/123
axonal guidance signaling	8.73	3%	14/456	29%	133/456
ephrin receptor signaling	8.61	3%	6/177	37%	65/177
regulation of actin-based motility by rho	8.43	5%	5/93	45%	42/93
CREB signaling in neurons	7.92	4%	7/192	32%	62/192
reelin signaling in neurons	4.94	7%	6/92	32%	29/92
GDNF family ligand-receptor interactions	4.57	3%	2/79	35%	28/79
neurotrophin/TRK signaling	3.09	1%	1/81	33%	27/81
amyotrophic lateral sclerosis signaling	2.59	2%	2/120	30%	36/120

Muscle proteome (H vs M) Metabolic pathways					
Ingenuity canonical pathways	-$\log_{10}$(*p* value)	Upregulated (H vs M)		Downregulated (H vs M)	
sulfite oxidation IV	0.24	0%	0/4	25%	1/4
trehalose degradation II	0.22	0%	0/10	30%	3/10
β-alanine degradation I	0.22	0%	0/10	20%	2/10
adenine and adenosine salvage VI	0.18	0%	0/5	20%	1/5
anandamide degradation	0.18	0%	0/5	20%	1/5
asparagine degradation I	0.18	0%	0/5	20%	1/5
glutamine degradation I	0.18	0%	0/5	20%	1/5
melatonin degradation III	0.18	0%	0/5	20%	1/5
methylthiopropionate biosynthesis	0.18	0%	0/5	20%	1/5
sorbitol degradation I	0.18	0%	0/5	20%	1/5

Table 5.1 | Proteomic profiling of the human NMJ
In silico analysis of the NMJ samples (top) and muscle samples (bottom) identified canonical cascades common to both species. Ten example pathways are listed for each. Values are the percentage (and number) of proteins in each cascade that are upregulated (red) or downregulated (blue) in human compared with mouse. Significance levels are listed as $-\log_{10}$(p value), i.e. $-\log_{10}(p<0.05) \approx 1.3$, $-\log_{10}(p<0.0001) = 4$, etc. The proteomic profiles of the NMJ samples (human cf. mouse) revealed clear differences: of the 36 nervous system pathways identified, 97% showed significant species differences (all but one pathway). Conversely, the proteomic profiles of the muscle samples (human cf. mouse) revealed clear similarites: of the 200 metabolic pathways identified, only 34% showed significant species differences, whilst the majority of cascades (66%) were similarly regulated.

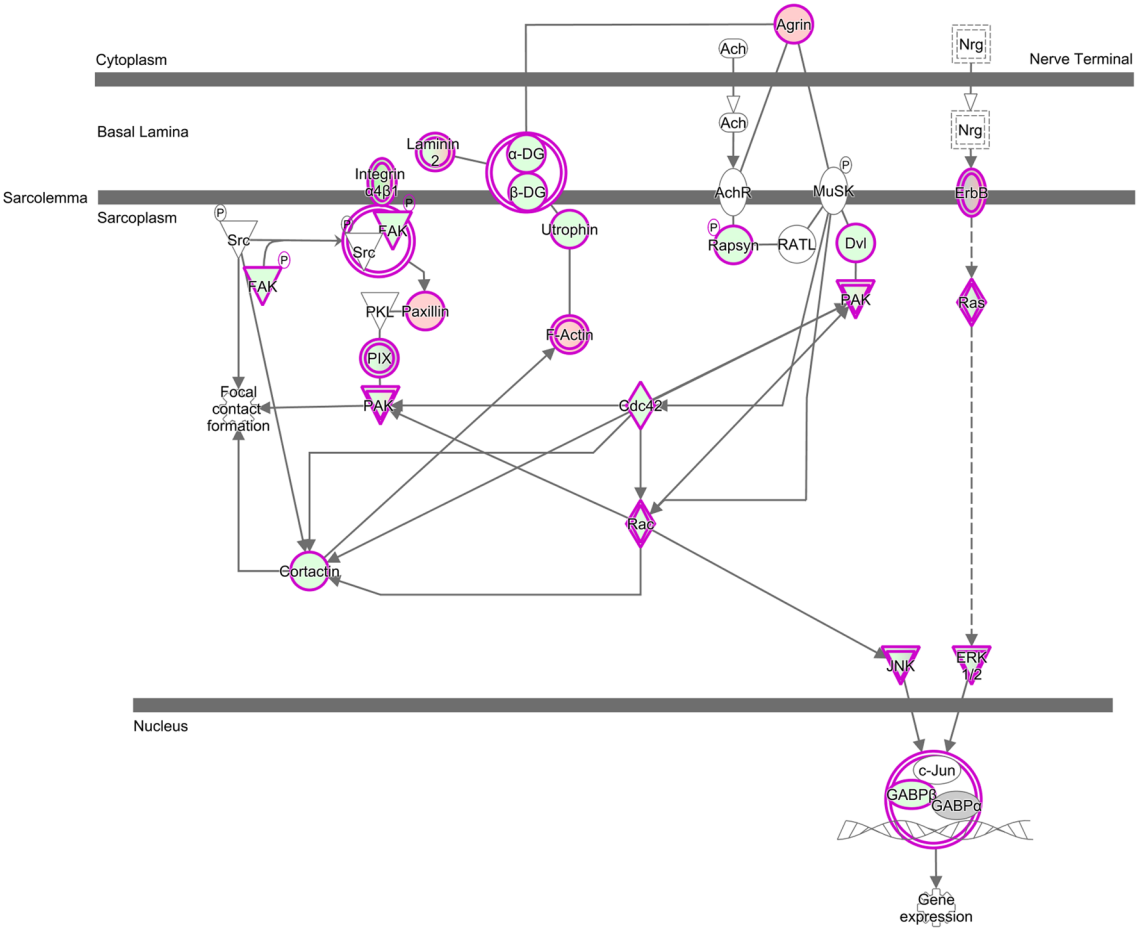

Figure 5.4 | Agrin interactions at the NMJ
IPA canonical pathway analysis of the NMJ samples (human cf. mouse) identified significant changes in a number of core synaptic pathways, e.g. agrin interactions at the NMJ (as shown). Nodes in red represent proteins more abundant in humans (by >20% cf. mice); nodes in green represent proteins more abundant in mice (by >20% cf. humans); the darker the colour of the node, the greater the difference in protein expression. Grey nodes represent proteins that differ by <20% in humans cf. mice. In this example of agrin interactions at the NMJ, major differences in relative abundance were observed for 24 individual proteins. Note: each pathway contains proteins that are more abundant in one or other species; the observed changes are not therefore an artefact of relative enrichment during tissue processing.

Conversely, only 1 pathway in the NMJ-enriched samples ('GABA receptor signaling') showed no significant differential proteomic expression between the species. Together, these data suggest that the human NMJ has a distinct molecular composition to the mouse NMJ. This finding is consistent with the recent observation of species-specific gene expression in developing neurons of humans and mice (Qiu et al, 2016).

The large differences between the NMJ proteomes of the two species but close similarity of their muscle proteomes are summarized visually in the *Biolayout* schematic (Figure 5.3).

Chapter 6

General Discussion

6.1 Chapter summary

This final chapter will review the major findings of the project and discuss the implications for translational studies of neurodegenerative disease and future research directions.

6.2 Major findings

Despite the clinical importance of the NMJ in the context of human disease, there have been few dedicated studies of human NMJ structure and function to date. The primary aim of this project therefore was to provide the first comprehensive description of the cellular and molecular architecture of the human NMJ. To this end, the current study has generated four major research findings:

1. Human NMJs have unique morphological characteristics, including small size, thin axons, rudimentary nerve terminals and distinctive 'nummular' endplates, all of which distinguish them from comparable synapses in other experimental animal models such as mice.

2. Human NMJs are remarkably stable across the entire lifespan, in contrast to the synaptic destabilization that is typical of more short-lived mammals such as rodents.

3. Human active zones have a unique functional architecture; this pre-synaptic specialization may contribute to the safety factor of neurotransmission at the smaller human NMJ.

4. Human NMJs demonstrate proteome-wide differences in molecular composition (cf. mice) whilst the metabolic pathways of the muscle fibre are relatively conserved.

In addition to these major research findings, significant progress has also been made in the methodological approaches required to undertake detailed comparative studies of NMJ form and function, which should facilitate future research collaborations in this field:

1) A comprehensive and fully validated approach to morphometric analysis has been developed (NMJ-morph), with the aim of providing a standard framework for reporting NMJ morphology. NMJ-morph has been made freely available in the public domain to facilitate the comparison of NMJ data from different research laboratories in the future.

2) A number of advanced statistical approaches including principal components analysis, have been utilized to reveal underlying principles accounting for natural variation in NMJ morphology, that are otherwise difficult to appreciate with simpler statistical techniques. These approaches are particularly suited to the large scale data analyses presented here.

3) A robust and reliable method of sampling human NMJs from disease-free regions of surgical discard material in patients undergoing lower limb amputation was developed. This approach represents a unique and valuable resource, with significant advantages compared with previous techniques such as motor point biopsy.

4) Novel approaches to facilitate super-resolution imaging of active zone architecture and comparative proteomic profiling of the human and mouse NMJ were developed.

6.3 Future research

Now that both a standardized analysis platform (NMJ-morph) and a robust method for sampling human NMJs has been developed, various lines of enquiry can now be followed, investigating both specifics of human NMJ structure, function and pathology, and broader aspects of comparative anatomy and neurobiological research.

6.3.1 Human NMJ research

Possible directions for future research include additional studies of basic human NMJ structure and function, especially in the years from birth to adulthood where present knowledge is particularly lacking, and the crucial clinical aspects of NMJ pathology.

6.3.1.1 Structural studies

To conclude the basic structural survey of the human NMJ described in the present work, the other cellular components of the NMJ now require definitive investigation in humans,

specifically, the number and arrangement of terminal Schwann cell(s) and the presence or absence of NMJ-capping cells (kranocytes). These analyses could be extended to include neighboring cell types such as fibroblasts, macrophages, satellite cells, etc. Further light microscopic work may also be warranted to address a number of specific questions in relation to the gross innervation of human muscle and NMJ pathology (discussed below).

Given the markedly different active zones in human and mouse NMJs revealed by super-resolution imaging, the fine details of human active zone ultrastructure now need to be elucidated with electron microscopy. Building on the present SNAP25 data, further super-resolution imaging is also required to determine the spatial arrangement of other active zone proteins; in this regard, good candidates would include bassoon and piccolo, as comparative STED data already exists for these proteins at the mouse NMJ (Nishimune et al, 2016).

In terms of the gross innervation of human muscle, the observation of 'en passant' nerve terminals in ≈ 10% of human NMJs also requires further study. One of the limitations of teased fibre preparations (used in the present work) is the inevitable distortion of normal muscle fibre architecture, and unavoidable sampling of only parts of a whole muscle. Thus, earlier studies of terminal motor innervation typically utilized fetal muscles (Christensen, 1959), although endplate distribution has been studied in whole adult muscles using specialized equipment (e.g. heavy cryostat microtome; Aquilonius et al, 1982; 1984). However, the availability of new approaches to immunolabeling of large tissue samples for volume imaging such as iDISCO (**i**mmunolabeling-enabled three-**d**imensional **i**maging of **s**olvent-**c**leared **o**rgans; Renier et al, 2014) could potentially facilitate the topographic study of terminal innervation in whole adult muscles. Since this technique has already been successfully utilized in whole-mount immunolabeling of 14-week fetuses (with a crown-rump length of > 5 cm; Belle et al, 2017), it could in theory be used to study the connectome of an individual small human muscle, and further delineate the pattern of 'en passant' innervation. Suitable muscles would include lower limb *lumbrical* muscles harvested at orthopaedic amputation, where the foot itself is free of disease (e.g. cases 1-3 & 5, Table 4.1); in addition, the equivalent connectome of the *4th deep lumbrical* muscle of the mouse has already been described, providing a useful comparison (Hirst and Ribchester, 2013). All of the above studies could be performed on tissue obtained using the present sampling

technique (lower limb amputation), but other sources of tissue would be required to address certain specific questions.

The presence of multiple NMJs per muscle fibre in various muscle groups of the head and neck (e.g. laryngeal, facial and ocular muscles; Figure 1.1) also warrants re-evaluation in light of the present techniques (immunolabeling, confocal microscopy, NMJ-morph). Potential sources of tissue include discard specimens obtained at laryngectomy and eye enucleation, and surgery for cleft lip and palate or other plastic procedures (facial muscles).

Formal fibre typing of human muscle was not undertaken in the present work, but could easily be included in many of the above studies, as new methods of fibre typing based on slow and fast isoforms of myosin (Behan et al, 2002) offer several advantages over the standard ATPase method, including application to fixed tissue (and archival material).

6.3.1.2 Functional studies

The proteomic profiling of the human NMJ undertaken in the present study represents the very the tip of the iceberg in terms of the molecular characterization of human NMJ form and function, and the current database provides a valuable resource for future data mining and bioinformatics. In depth analysis of individual proteins and pathways in the existing database will aid in the design and interpretation of future studies of human proteomics. An appropriate starting point would be a focused analysis of the neurotransmitter and nervous system signaling cascades that demonstrated significantly different regulation at the human and mouse NMJs, e.g. agrin interactions at the NMJ (Figure 5.4); other potential pathways of interest are listed in Table 5.1.

The present muscle harvesting techniques could also be modified (relatively easily) to obtain en-bloc nerve-muscle preparations for electrophysiological and/or other structure-function studies, e.g. full-length intact muscle fibres of *peroneus longus* or *brevis* (≈ 2 cm) with the corresponding intramuscular branches of the superficial peroneal nerve. These nerve-muscle preparations could be used to further investigate the safety factor at the human NMJ (Slater et al, 1992) in light of the present findings of pre-synaptic active zone specialization.

Fibre-optic confocal microendoscopy (CME) is an emerging technique that allows real time visualization of NMJs in situ (Brown et al, 2014). To date, the technique has been used to successfully image mouse NMJs in vivo, and has potential diagnostic applications in the clinical management of human neuromuscular diseases. The nerve-muscle preparations discussed above would provide an ideal model for preliminary tests of CME in humans.

6.3.1.3 The human NMJ from birth to adulthood

Although the current study provides significant insights into the relative stability of the human NMJ with age (Section 4.4.4), the case series does not include any individuals from the first three decades of life, though the absence of data from this age group is problematic in many areas of human research. The small number of studies into aging of the human NMJ (see Section 1.2.4) has included a limited amount of data from children and young adults, but not adolescents (Wokke et al, 1990; Gambino et al, 1990).

Paediatric amputations (both upper and lower limb) are indicated in certain circumstances, with the majority being due to trauma (Khan et al, 2016); malignant tumours are the most common non-traumatic indication, with a peak incidence of 12 to 21 years (Tooms, 2002). In the present study, human NMJs have been obtained successfully from *rectus abdominis* at laparotomy (Section 4.4.3), therefore paediatric abdominal surgery may provide a better (and more frequent) opportunity to source tissue in this age range (0 to 30 years). Based on animal studies of the NMJ demonstrating typical 'plaque to pretzel' development (Marques et al, 2000), the human NMJ may be predicted to undergo analogous 'plaque to nummular' development from *in utero* through to full maturation.

6.3.1.4 The human NMJ in disease

Now that a large reference database of normal human NMJ variables has been established, informative comparisons can be made with NMJ samples obtained from patients with neurodegenerative conditions such as motor neuron disease (e.g. ALS and SMA). Although patients with such disorders who also require lower limb amputation are likely to be rare*, NMJ samples obtained for research purposes from elsewhere in the body (e.g. other limb and trunk muscles) now have a more robust control in the present database of lower limb muscles (*EDL, PB, PL, soleus*) than has been available previously. For example, a recent study investigating the role of muscle histone deacetylase 4 upregulation in ALS reported

(pathological) fragmentation and reinnervation of ALS endplates in samples obtained from *deltoid* and *anconeus* (Bruneteau et al, 2013). Based on the natural variation that is now known to exist at the human NMJ, these 'pathological' examples are likely, in retrospect, to be 'normal' human NMJs, having similar appearance to many of the healthy human NMJs described in the present study (Chapter 4).

[*Amputation of both the upper and lower limbs is occasionally indicated for patients with neurological disease or the complications thereof, e.g. paralysis and deformity (Farquharson and Moran, 2005). Indeed, two of the patients in the present series required below knee amputation for such complications: case 2, for chronic osteomyelitis secondary to cauda equina syndrome; and case 5, for chronic pain secondary to spinal surgery with foot drop.]

Other diseases that are not currently known to involve NMJ dysfunction may also merit investigation, facilitated by the technological developments reported in the current study. For example, although one of the clinical manifestations of cancer cachexia is skeletal muscle wasting (Fearon et al, 2011; Skipworth et al, 2006; 2007), the only known link between cancer and the NMJ to date (excluding the Lambert-Eaton myasthenic syndrome presenting as a paraneoplastic manifestation of small-cell lung cancer; Antoine and Camdessanché, 2007) is the contribution of agrin to the molecular pathways implicated in hepatocellular carcinoma (liver cancer; Xiong and Mei, 2017). Although preliminary data from a single patient with stomach cancer (Figure 4.8) does not appear to demonstrate any gross evidence of NMJ dysmorphia compared to healthy NMJs in the lower limb muscles (*EDL, PL, PB, soleus*), this data represents the first of its kind in cancer cachexia, and certainly merits a full morphological study.

Finally, although care was taken to control for the effects of diabetes mellitus (DM) and peripheral vascular disease (PVD) in the present work (by harvesting tissue close to the level of amputation; see Section 4.3.3), the potential effects of these conditions on the NMJ could now be studied directly. By sampling tissue from more distally in the limb, where the effects of pathology are more overt (i.e. microvascular disease in DM, LoGerfo and Coffman, 1984 and vascular calcification in PVD, Demer and Tintut, 2008), a direct comparison could be made with NMJs obtained from more proximal (healthy) tissue.

6.3.2 Animal research and comparative anatomy

In terms of the present mouse study (Chapter 3), one of the key findings to warrant further investigation is the significant level of natural variation observed in mouse NMJs across different muscles and animals within the same litter. Given the reliance on animal models of neurodegenerative disease, such levels of natural variation must now be taken into account in future studies, if potential NMJ pathology is to be accurately interpreted and translated. Equivalent studies are now required to fully investigate NMJ variation across different litters and strains, and provide accurate reference data on normal NMJ morphology.

A further unexpected finding to emerge from the mouse study was the peculiar non-linear relationship between NMJ size and muscle fibre diameter on the larger calibre fibres of *triceps* and *quadriceps*, raising the possibility of a cytoplasmic volume limit at the NMJ (or perhaps more accurately, the motor neurone as a whole; Section 3.4.3).

In the present study, the measurements of NMJ size and muscle fibre diameter were performed *independently* of one another (i.e. the 2 sets of measurements were performed on different fibres at different times, albeit in the same muscle samples); it is conceivable therefore that the correlation observed in *triceps*/*quadriceps* is not truly accurate. Although this possibility is unlikely, given that the linear correlation observed in the smaller diameter *cranial* and *lumbrical* muscles was obtained using the same methods (and supports previous observations in other muscles; Oda, 1985), repeating this part of the study using single fibre preparations (which facilitates dual measurement of NMJ size and fibre diameter), would conclusively demonstrate whether this non-linear relationship is truly accurate.

If the present result stands, it would be interesting to study the same correlations in other muscles with large calibre fibres (e.g. the *gluteal* muscles). In addition, the volume limit hypothesis could be further explored by studying the effect of exercise-induced hypertrophy on the relationship between NMJ and fibre diameter in small and large calibre muscle fibres.

In terms of comparative anatomy, the general trend toward smaller NMJs in larger animals warrants further investigation. The preliminary work on the comparative anatomy of mouse, rat and human NMJs (Section 4.4.6) suggests that a simple inverse relationship between NMJ size and body mass does not exist, but this would need to be confirmed with

studies of other large mammals such as sheep, pigs, horses and cattle. In addition, although the evolution of bipedalism has been the focus of comparative research at a gross anatomical level (Crompton and Günther, 2004), equivalent evolutionary traits at the NMJ have not been formally studied.

Finally, current research into neurodegenerative diseases (such as ALS and SMA) relies heavily on small animal models of disease (typically rodents, including mice and rats). In comparison, although large animal models of disease are in less frequent use, they provide a far more appropriate model of the human condition from an evolutionary standpoint. Comparative work on large animals would therefore help to establish a reference database of normal synaptic morphology for use in models of human disorders such as Batten disease, where large animal models already exist, e.g. sheep (Amorim et al, 2015).

6.4 Concluding remarks

Despite the clinical importance of the NMJ in the context of human disease, the present study represents, to date, the first comprehensive work on the comparative anatomy of the human neuromuscular junction. The cellular and molecular architecture of the human NMJ is now known to be fundamentally different to that of other mammalian species. These differences must be taken into consideration when translating animal models of disease to the human condition.

Appendices

Appendix 1

NMJ-morph User Guide

User guide reproduced from Edinburgh DataShare, http://dx.doi.org/10.7488/ds/1490 (Jones and Gillingwater, 2016). For use in conjunction with the Open Biology article, doi: 10.1098/rsob.160240 (Jones et al, 2016).

This user guide comprises a workflow that has been designed for use in conjunction with Figure 2 (and Supplementary Figures 2 and 3) of the manuscript and the downloadable spreadsheets and image bank. The following descriptions guide the user through the stages of analysis for each NMJ using ImageJ (or Fiji), and correspond in order to the workflow depicted in Figure 2 of the manuscript. Instructions in italics refer to the selectable functions in the ImageJ menus. Variables listed in red typeface are defined as 'core variables', those in blue as 'derived variables' and those in green as 'associated nerve and muscle variables'. See manuscript for further explanation and definition of individual terms.

Basic Image Details

Before entering numerical values into the spreadsheet for any of the NMJ variables, the basic properties of the image must be noted first. This is the frame size of the image, which must be recorded as both length in pixels and length in metric units. For the sample NMJs provided in the image bank, the frame size is 512×512 pixels and 67.48×67.48 μm (entered into the relevant cells as '512' and '67.48').

Initial Image Processing

ImageJ Operations → Open maximum intensity projection in ImageJ → *Image* → *Colour* → *Split channels*. Then, for each channel separately → *Image* → *Adjust* → *Threshold* (select *'Huang'*, *'Yen'*, or adjust threshold manually with top slider. To allow accurate threshold selection, a second maximum intensity projection should be opened for comparison. Once the threshold has been selected, close the window at the top left – don't select '*Apply*') → *Process* → *Noise* → *Despeckle* → Select background colour using colour picker tool, then manually erase extraneous background detail with paintbrush tool (to isolate the relevant NMJ on a white background) → *Process* → *Binary* → *Make binary* (Keep all options selected – the resulting binary image will have either a red or green background. Selecting *Make binary* for a second time at this stage creates a white background; the coloured backgrounds are required however for 'overlap' to be calculated – see later) → *Save* the 'cleaned' pre- and post-synaptic images separately (as tiff files). All subsequent analysis is performed on these images (with the exception of the 'segmented particles' function – see number of AChR clusters, average area of AChR clusters, 'fragmentation').

Presynaptic Measurements

Number of Axonal Inputs

ImageJ Operations → The original maximum intensity projection should be inspected for any evidence of polyneuronal innervation and the number of individual axonal inputs per NMJ noted in the spreadsheet.

Axon Diameter

ImageJ Operations → Open saved 'clean' image → *Measure* axon diameter with line tool at points of maximum and minimum diameter, and at edge of endplate (this latter measurement should be either the point at which the axon crosses the edge of the endplate, or the point at which the axon ramifies, if this lies outside the area of the endplate) → *Results* → *Summarize* → Record mean diameter in spreadsheet.

Nerve Terminal Perimeter
Nerve Terminal Area

ImageJ Operations → Open saved 'clean' image → Select background colour with colour picker tool, then manually erase axon with paintbrush tool → *Edit* → *Selection* → *Create selection* (this will automatically outline the remaining nerve terminals) → *Analyze* → *Measure* → Record area & perimeter in spreadsheet.

Number of Terminal Branches (n)
Number of Branch Points
Total Length of Branches (l)
Average Length of Branches (l/n)
'Complexity'

ImageJ Operations → Open saved 'clean' image → *Process* → *Binary* → *Make binary* (background becomes white) → *Process* → *Binary* → *Skeletonize* → Select background colour with colour picker tool, then manually erase axon with paintbrush tool → *Plugins* → *BinaryConnectivity* (keep *'white particles on black background'* selected – the binary image then 'disappears' – this is correct) → *Analyze* → *Histogram* → *List* → Enter the count for values 0, 2, 4 & 5 into the spreadsheet → Branch analysis will be performed automatically for the above 5 variables.

Postsynaptic Measurements

AChR Perimeter
AChR Area

ImageJ Operations → Open saved 'clean' image → *Edit* → *Selection* → *Create selection* (this will automatically outline the AChR clusters) → *Analyze* → *Measure* → Record area & perimeter in spreadsheet → Continue analysis below.

Endplate Diameter

ImageJ Operations → (Continued from above) → *Process* → *Subtract background* → Select '*Create background'* (keep '*rolling ball radius'* at 50.0 pixels)→ *Process* → *Binary* → *Make binary* (background becomes white and edge of endplate becomes sharper) → *Measure* maximum endplate diameter with line tool → Record maximum diameter in spreadsheet → Continue analysis below.

Endplate Perimeter
Endplate Area

ImageJ Operations → (Continued from above) → *Edit* → *Selection* → *Create selection* (this will automatically outline the endplate) → *Analyze* → *Measure* → Record area & perimeter in spreadsheet.

'Compactness'

ImageJ Operations → 'Compactness' is calculated automatically once the values for AChR cluster area and endplate area have been entered into the spreadsheet.

'Area of Synaptic Contact'
'Overlap'

ImageJ Operations → Open saved 'clean' images of both nerve terminals and endplate. For endplate → *Edit* → *Invert*. With both images now open → *Image* → *Stacks* → *Tools* → *Concatenate* (select *'OK'* – images will be merged into one stack) → *Image* → *Stacks* → *Z project* (keep *'average intensity'* selected – a 3 colour image will be produced in black and 2 tones of either red or green, as in Figure 2) → *Process* → *Binary* → *Make binary* (this will leave just the unoccupied AChRs) → *Edit* → *Selection* → *Create selection* (this will automatically outline the area of unoccupied AChRs) → *Analyze* → *Measure* → Enter this value into the spreadsheet and the 'area of synaptic contact' and 'overlap' and will be calculated automatically.

Number of AChR Clusters

Average Area of AChR Clusters

'Fragmentation'

ImageJ Operations → Open original maximum intensity projection (*not* the 'clean' image) → *Image* → *Colour* → *Split channels* and select endplate channel → *Process* → *Binary* → *Make binary* → *Process* → *Find maxima* → Select *'Segmented particles'* (keep '*noise tolerance'* at 10) → Manually count the number of clusters of segmented particles – this is recorded in the spreadsheet as the 'number of AChR clusters'; 'average area of AChR clusters' and 'fragmentation' will be calculated automatically.

Muscle Fibre Diameter

Measured independently. See manuscript for methods.

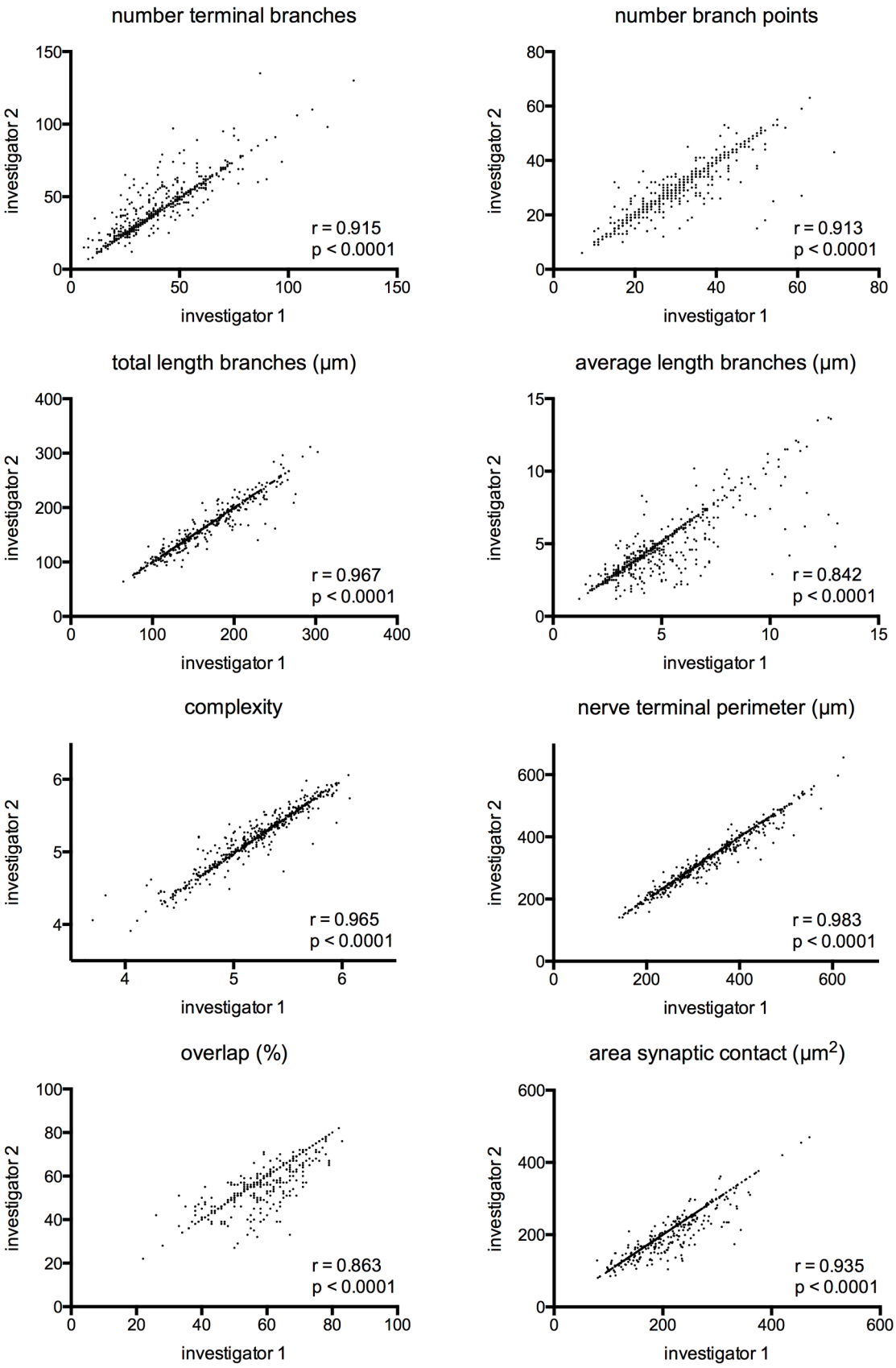

Appendix 2.1 | Validation of NMJ-morph (See Fig. 2.7 for details)

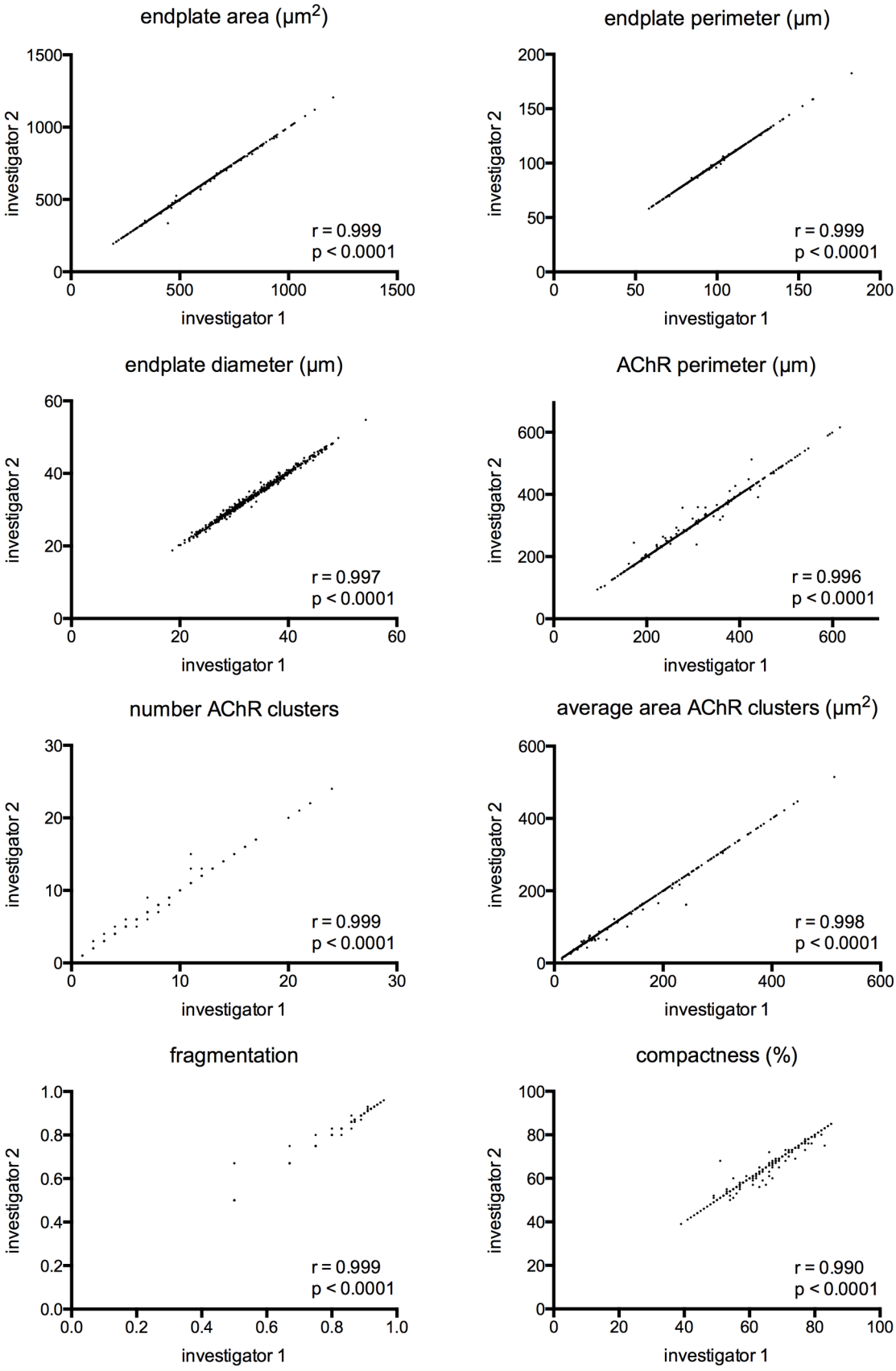

Appendix 2.2 | Validation of NMJ-morph (See Fig. 2.7 for details)

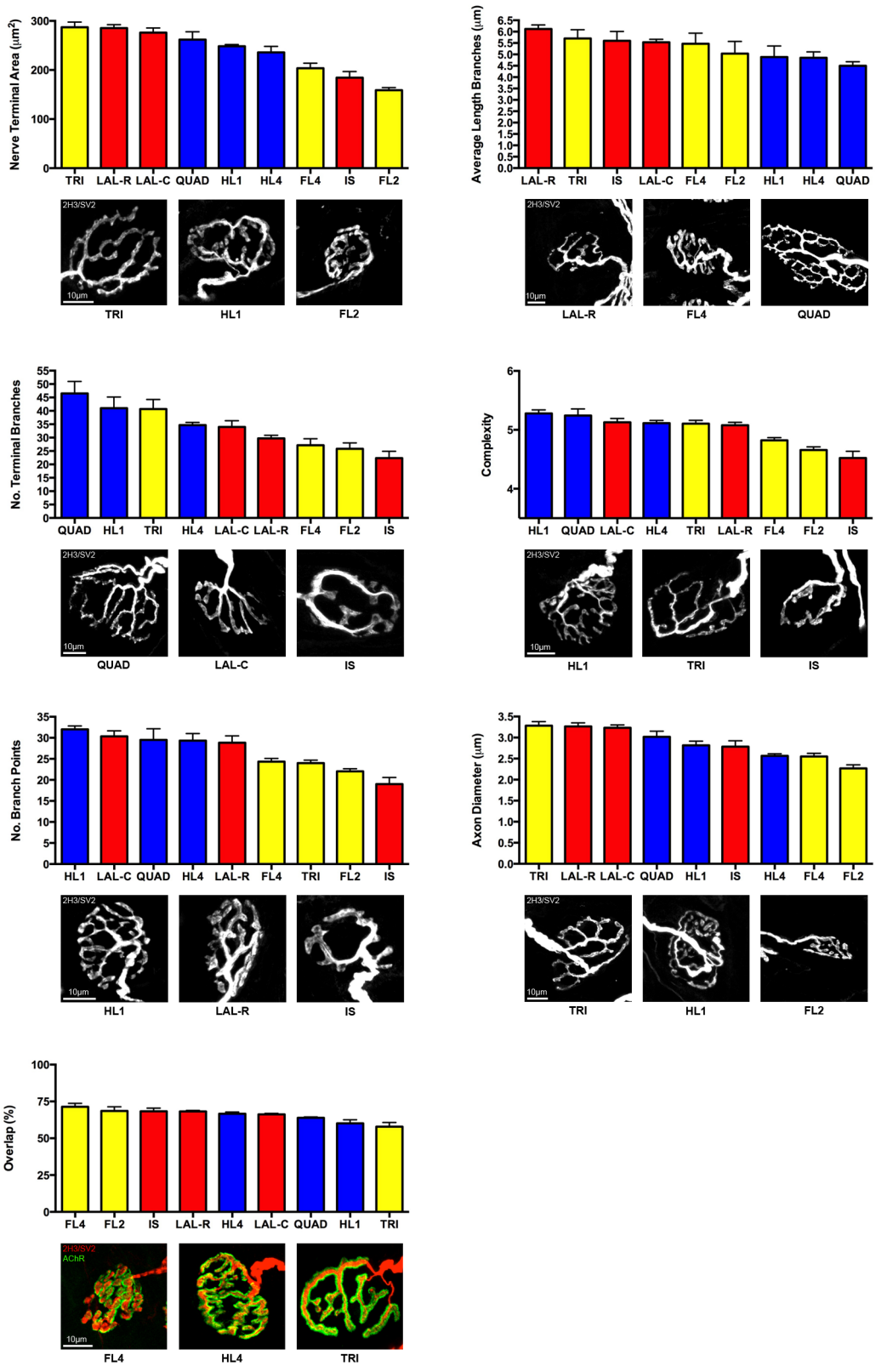

Appendix 3.1 | Morphology of mouse NMJs (See Fig. 3.3 for details)

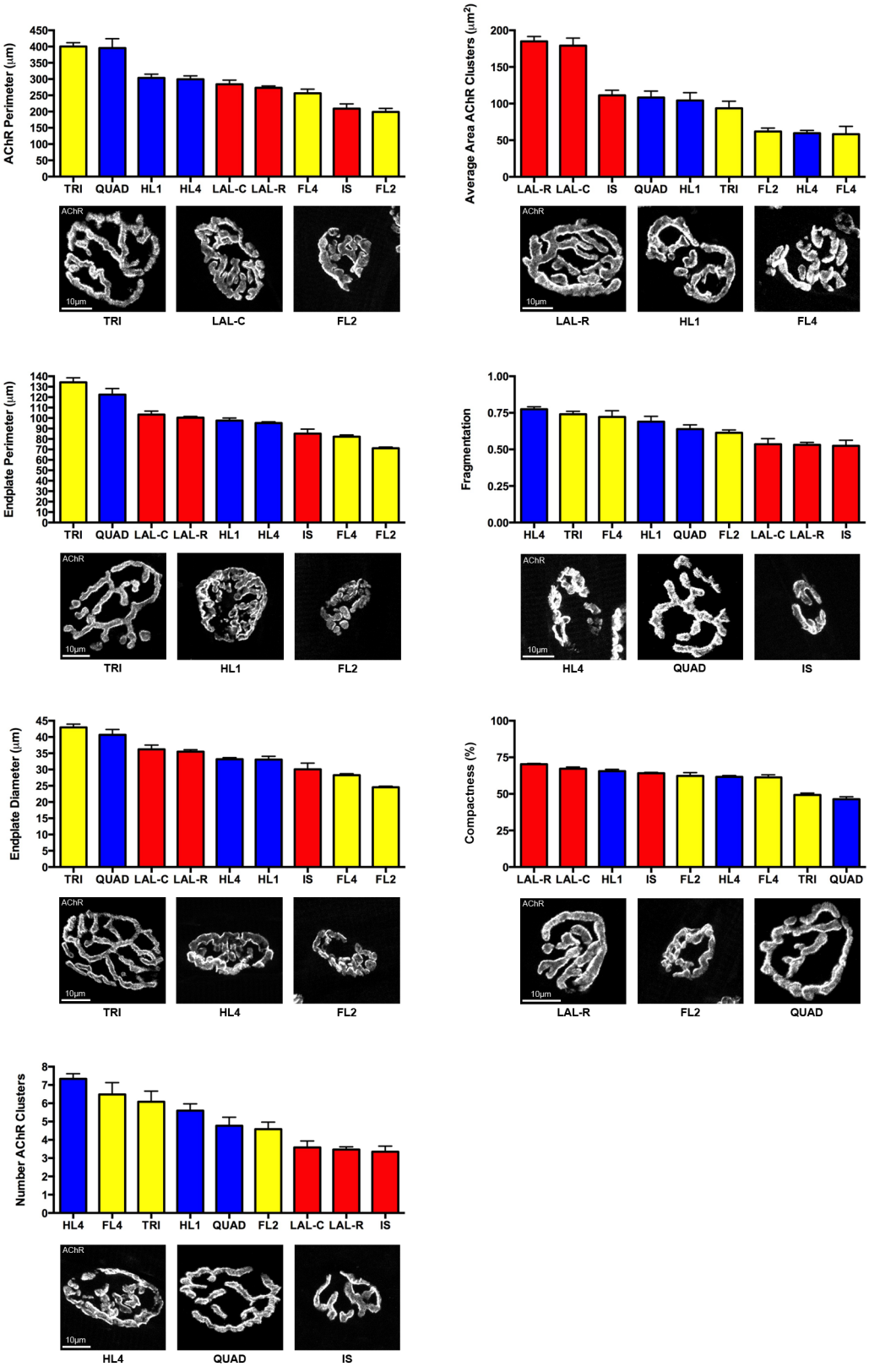

Appendix 3.2 | Morphology of mouse NMJs (See Fig. 3.3 for details)

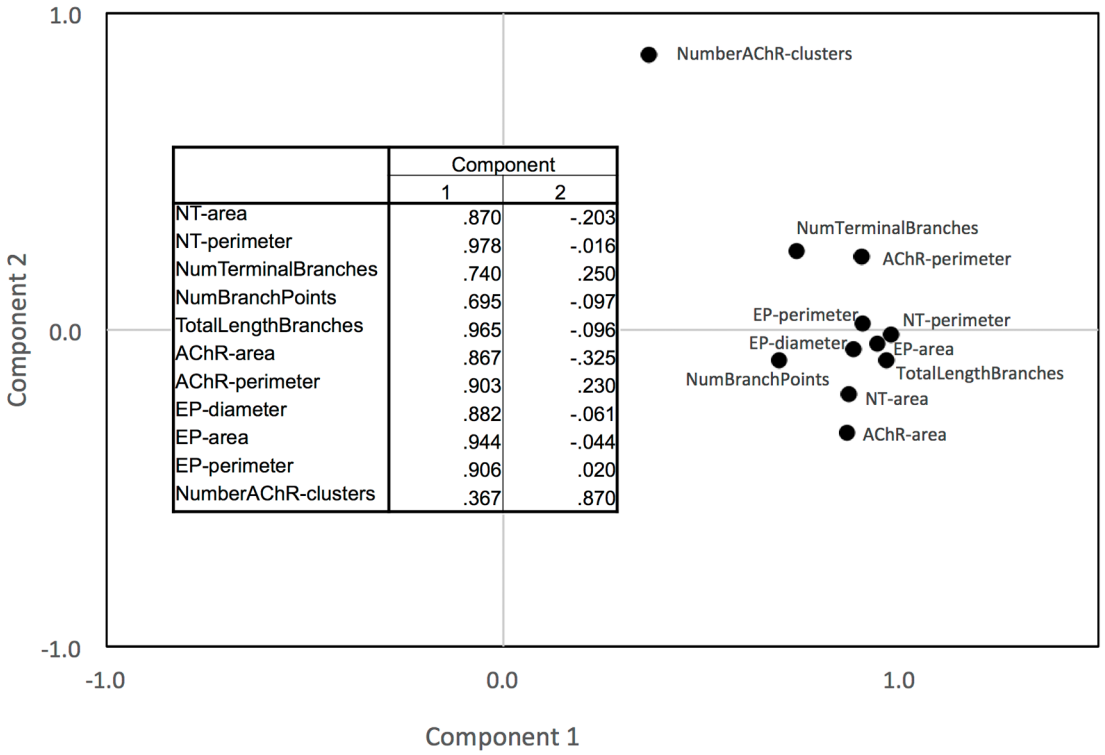

	Component	
	1	2
NT-area	.870	-.203
NT-perimeter	.978	-.016
NumTerminalBranches	.740	.250
NumBranchPoints	.695	-.097
TotalLengthBranches	.965	-.096
AChR-area	.867	-.325
AChR-perimeter	.903	.230
EP-diameter	.882	-.061
EP-area	.944	-.044
EP-perimeter	.906	.020
NumberAChR-clusters	.367	.870

Appendix 4 | PCA loading plot
Relationship between the 11 core morphological varaibles and the principal components determined by 2-dimensional principal components analysis (2D PCA). The unrotated PCA loading plot is shown. Analysis performed using SPSS software.

	Nerve terminal area	Nerve terminal perimeter	Number terminal branches	Number branch points	Total length of branches	AChR area	AChR perimeter	Endplate area	Endplate perimeter	Endplate diameter	Number AChR clusters	Average length of branches	Complexity	Average area AChR clusters	Fragmentation	Compactness	Overlap	Area synaptic contact	Axon diameter	Fibre diameter
Nerve terminal area	1	0.836	0.423	0.649	0.897	0.827	0.713	0.794	0.742	0.742	0.25	0.154	0.695	0.175	-0.228	-0.13	0.087	0.905	0.576	0.221
Nerve terminal perimeter	0.836	1	0.739	0.666	0.966	0.848	0.883	0.923	0.872	0.833	0.332	-0.164	0.842	0.107	-0.296	-0.327	-0.345	0.73	0.433	0.387
Number terminal branches	0.423	0.739	1	0.63	0.684	0.536	0.701	0.645	0.617	0.569	0.344	-0.621	0.824	-0.016	-0.282	-0.311	-0.565	0.311	0.198	0.293
Number branch points	0.649	0.666	0.63	1	0.794	0.576	0.526	0.496	0.446	0.461	0.189	-0.162	0.862	0.164	-0.144	0.035	-0.064	0.587	0.303	0.066
Total length of branches	0.897	0.966	0.684	0.794	1	0.847	0.83	0.869	0.812	0.792	0.293	-0.068	0.876	0.155	-0.255	-0.22	-0.2	0.796	0.471	0.311
AChR area	0.827	0.848	0.536	0.576	0.847	1	0.672	0.856	0.747	0.756	0.098	-0.029	0.711	0.342	-0.124	0.039	-0.305	0.905	0.528	0.235
AChR perimeter	0.713	0.883	0.701	0.526	0.83	0.672	1	0.88	0.833	0.784	0.475	-0.192	0.728	-0.081	-0.406	-0.551	-0.292	0.566	0.376	0.42
Endplate area	0.794	0.923	0.645	0.496	0.869	0.856	0.88	1	0.909	0.86	0.292	-0.101	0.699	0.111	-0.272	-0.431	-0.337	0.731	0.467	0.457
Endplate perimeter	0.742	0.872	0.617	0.446	0.812	0.747	0.833	0.909	1	0.91	0.321	-0.103	0.66	0.051	-0.293	-0.457	-0.319	0.632	0.429	0.474
Endplate diameter	0.742	0.833	0.569	0.461	0.792	0.756	0.784	0.86	0.91	1	0.259	-0.073	0.651	0.098	-0.258	-0.376	-0.264	0.671	0.449	0.429
Number AChR clusters	0.25	0.332	0.344	0.189	0.293	0.098	0.475	0.292	0.321	0.259	1	-0.184	0.315	-0.601	-0.715	-0.427	-0.098	0.055	0.057	0.017
Average length of branches	0.154	-0.164	-0.621	-0.162	-0.068	-0.029	-0.192	-0.101	-0.103	-0.073	-0.184	1	-0.398	0.114	0.156	0.174	0.559	0.186	0.11	-0.051
Complexity	0.695	0.842	0.824	0.862	0.876	0.711	0.728	0.699	0.66	0.651	0.315	-0.398	1	0.113	-0.278	-0.153	-0.342	0.611	0.349	0.205
Average area AChR clusters	0.175	0.107	-0.016	0.164	0.155	0.342	-0.081	0.111	0.051	0.098	-0.601	0.114	0.113	1	0.816	0.376	-0.032	0.357	0.185	0.029
Fragmentation	-0.228	-0.296	-0.282	-0.144	-0.255	-0.124	-0.406	-0.272	-0.293	-0.258	-0.715	0.156	-0.278	0.816	1	0.383	0.101	-0.081	-0.07	-0.046
Compactness	-0.13	-0.327	-0.311	0.035	-0.22	0.039	-0.551	-0.431	-0.457	-0.376	-0.427	0.174	-0.153	0.376	0.383	1	0.14	0.11	-0.01	-0.46
Overlap	0.087	-0.345	-0.565	-0.064	-0.2	-0.305	-0.292	-0.337	-0.319	-0.264	-0.098	0.559	-0.342	-0.032	0.101	0.14	1	0.088	0.065	-0.22
Area synaptic contact	0.905	0.73	0.311	0.587	0.796	0.905	0.566	0.731	0.632	0.671	0.055	0.186	0.611	0.357	-0.081	0.11	0.088	1	0.585	0.14
Axon diameter	0.576	0.433	0.198	0.303	0.471	0.528	0.376	0.467	0.429	0.449	0.057	0.11	0.349	0.185	-0.07	-0.01	0.065	0.585	1	0.161
Fibre diameter	0.221	0.387	0.293	0.066	0.311	0.235	0.42	0.457	0.474	0.429	0.017	-0.051	0.205	0.029	-0.046	-0.46	-0.22	0.14	0.161	1

Heat map of r values: 1.000 .500 .000 -.500 -1.000

Appendix 5 | PCA correlation matrix

Correlation matrix obtained from the 2-dimensional principal components analysis (2D PCA), showing Pearson correlation (r) values assessed over the complete dataset of 2160 NMJs examined. ‘Heat map’ of r values is shown below the correlation matrix.

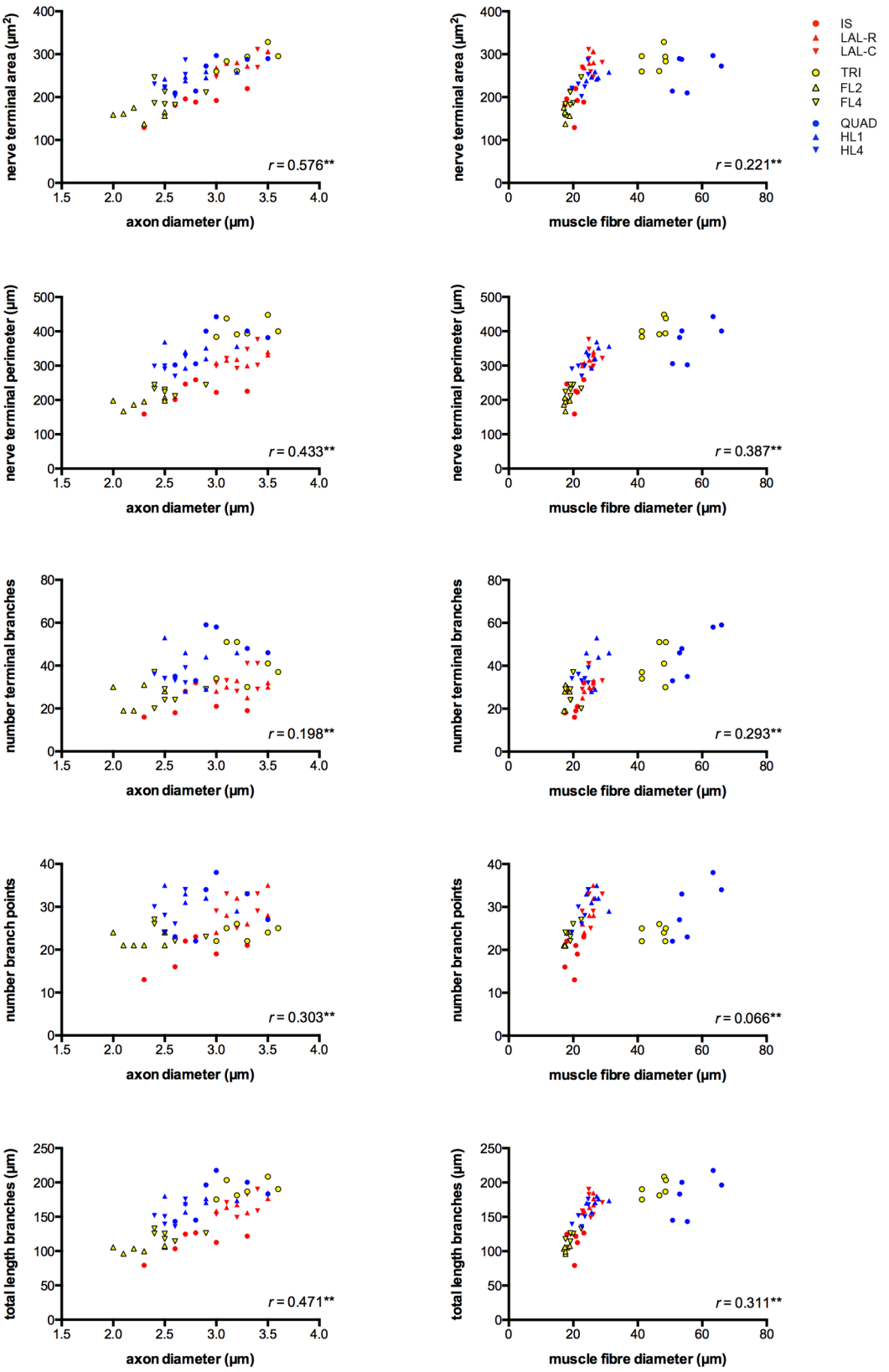

Appendix 6.1 | Influence of pre- and post-synaptic cells, mouse (See Fig. 3.5 for details)

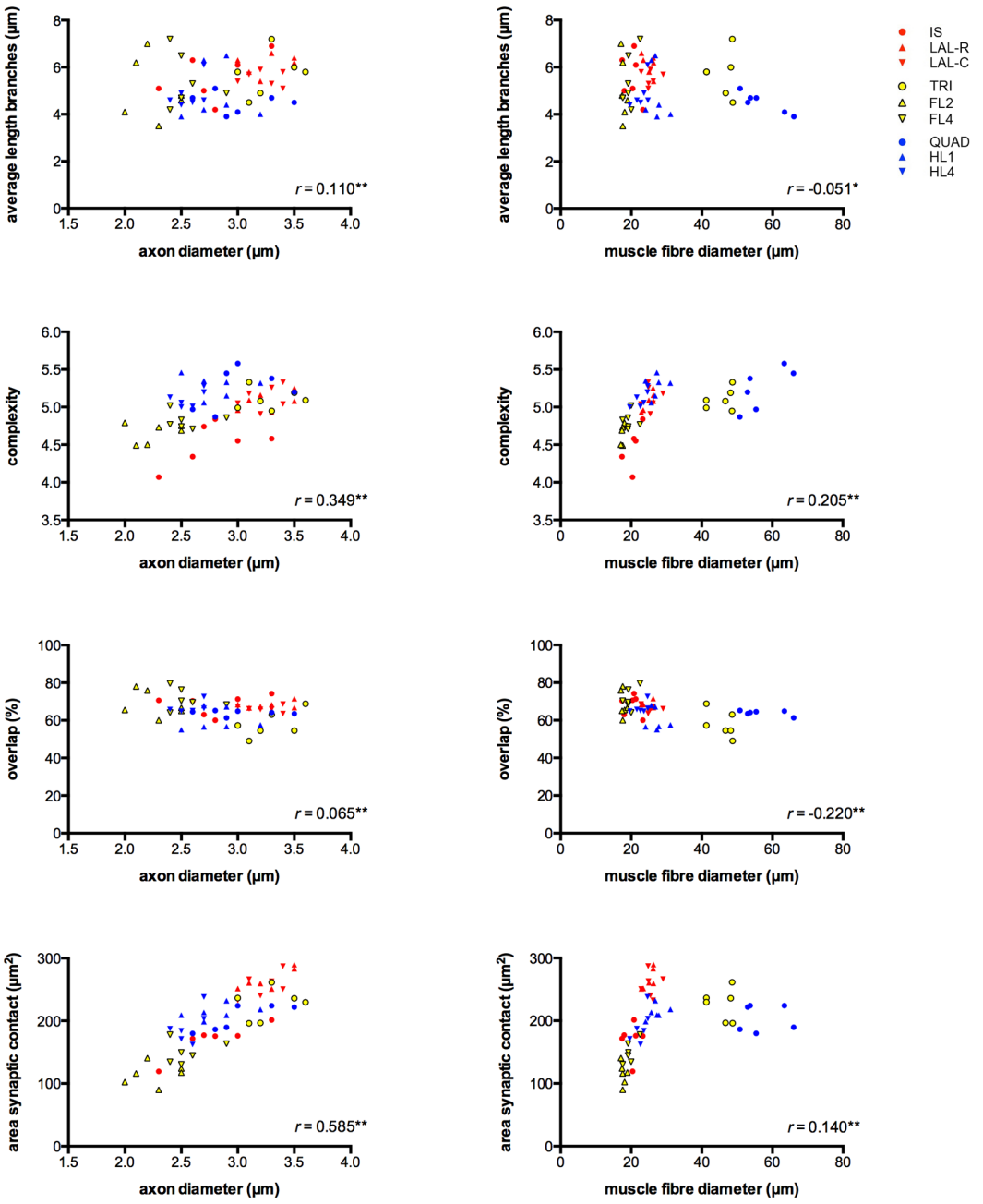

Appendix 6.2 | Influence of pre- and post-synaptic cells, mouse (See Fig. 3.5 for details)

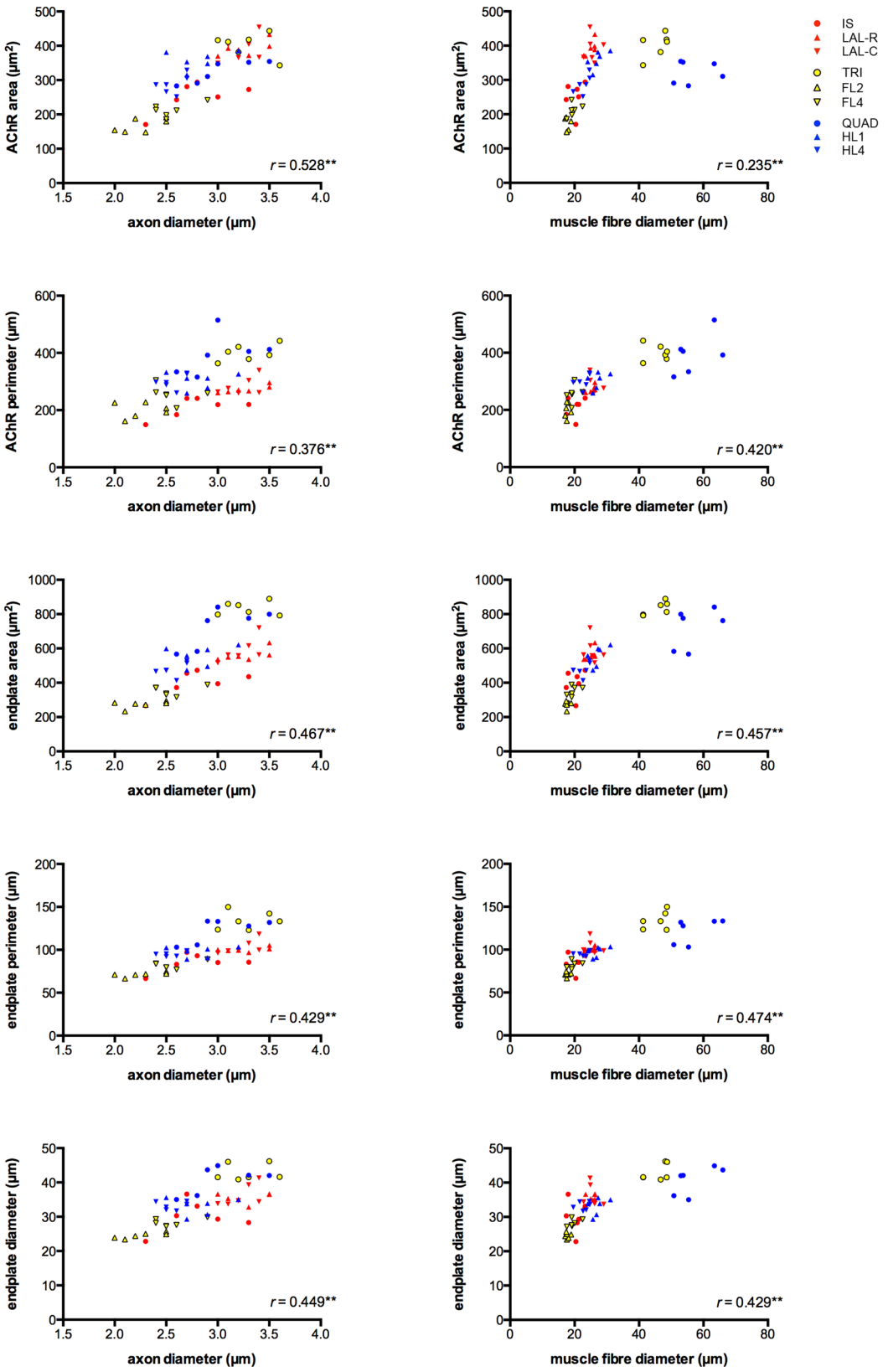

Appendix 6.3 | Influence of pre- and post-synaptic cells, mouse (See Fig. 3.5 for details)

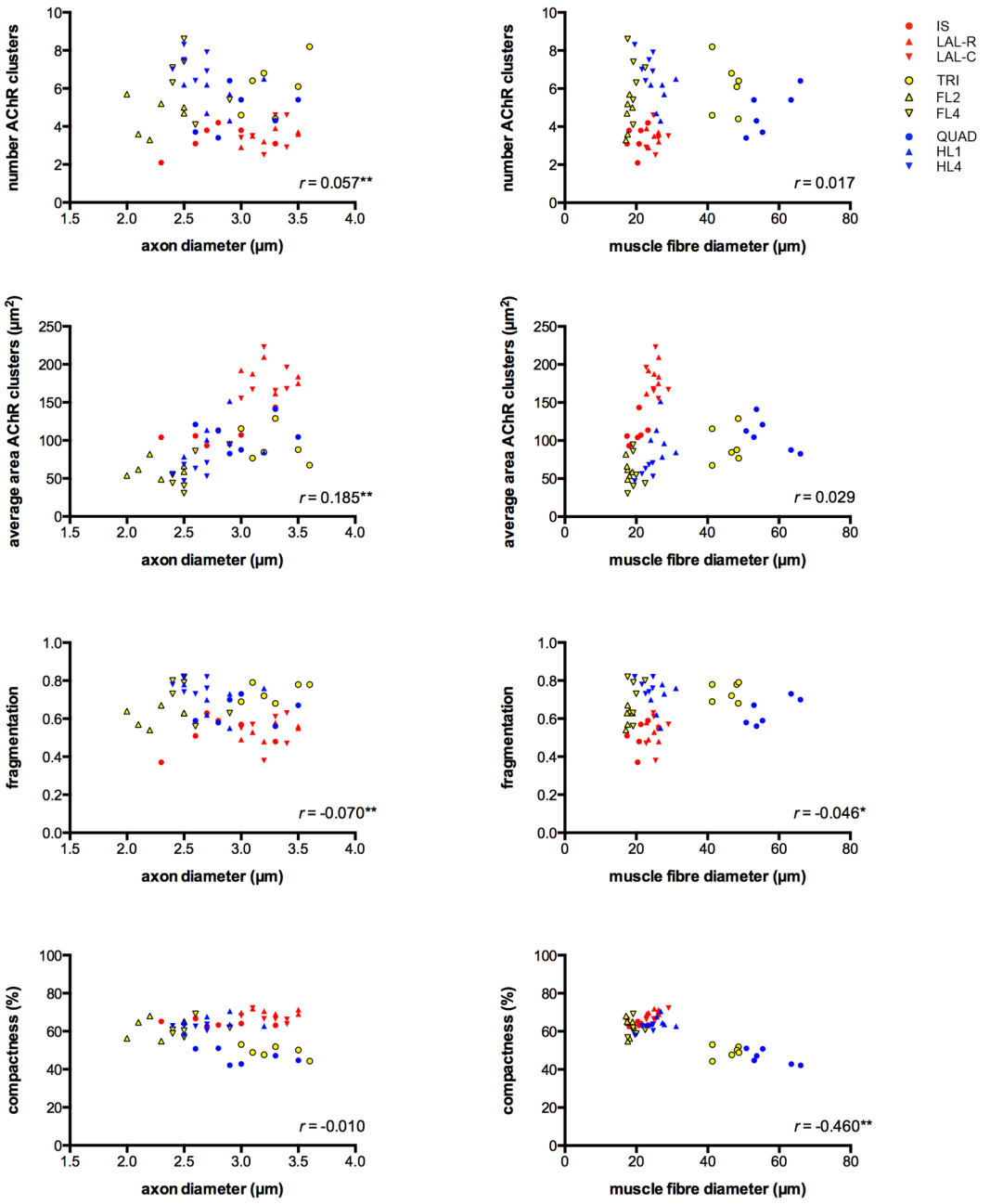

Appendix 6.4 | Influence of pre- and post-synaptic cells, mouse (See Fig. 3.5 for details)

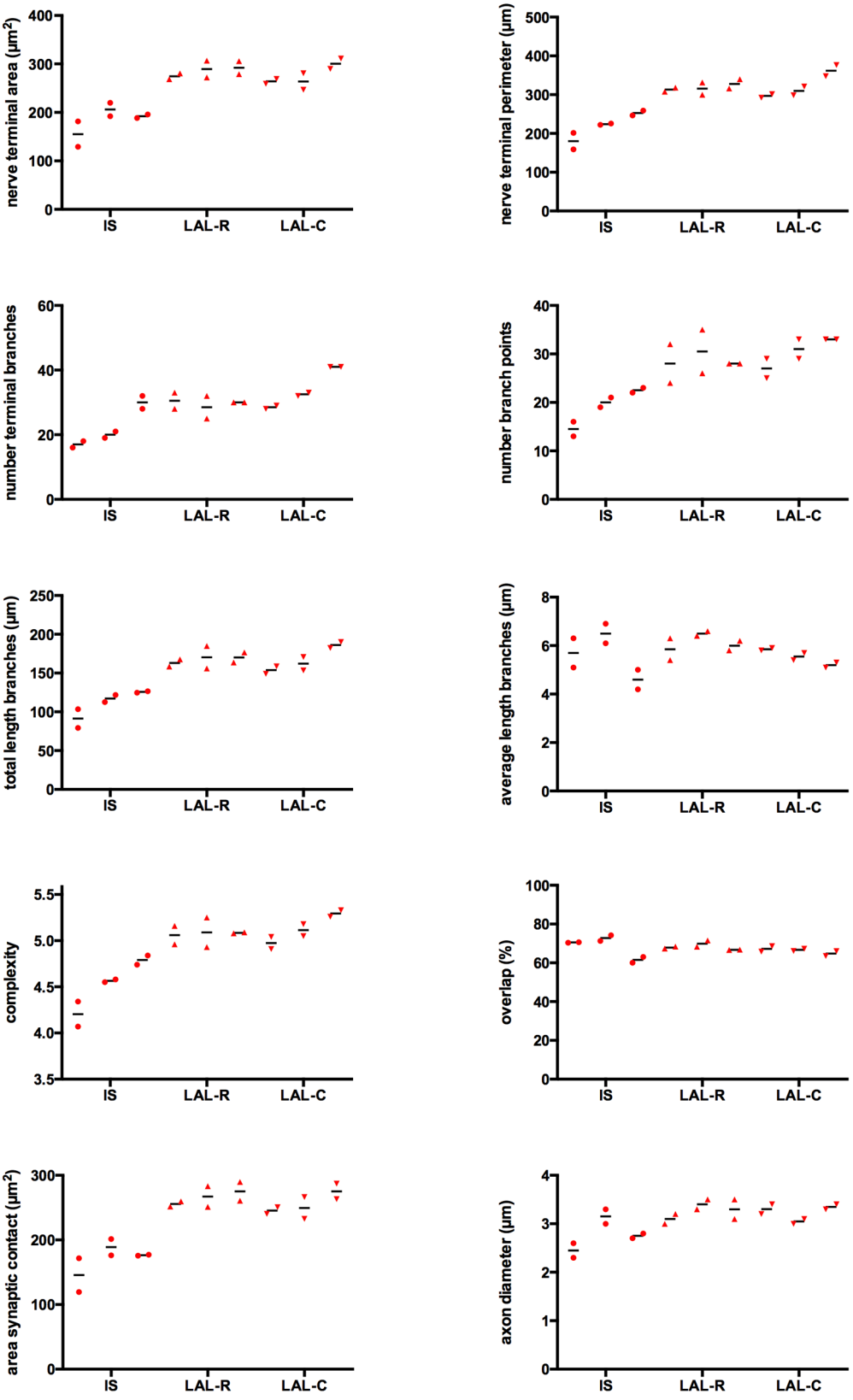

Appendix 7.1 | Influence of side on NMJs, mouse (See Fig. 3.6 for details)

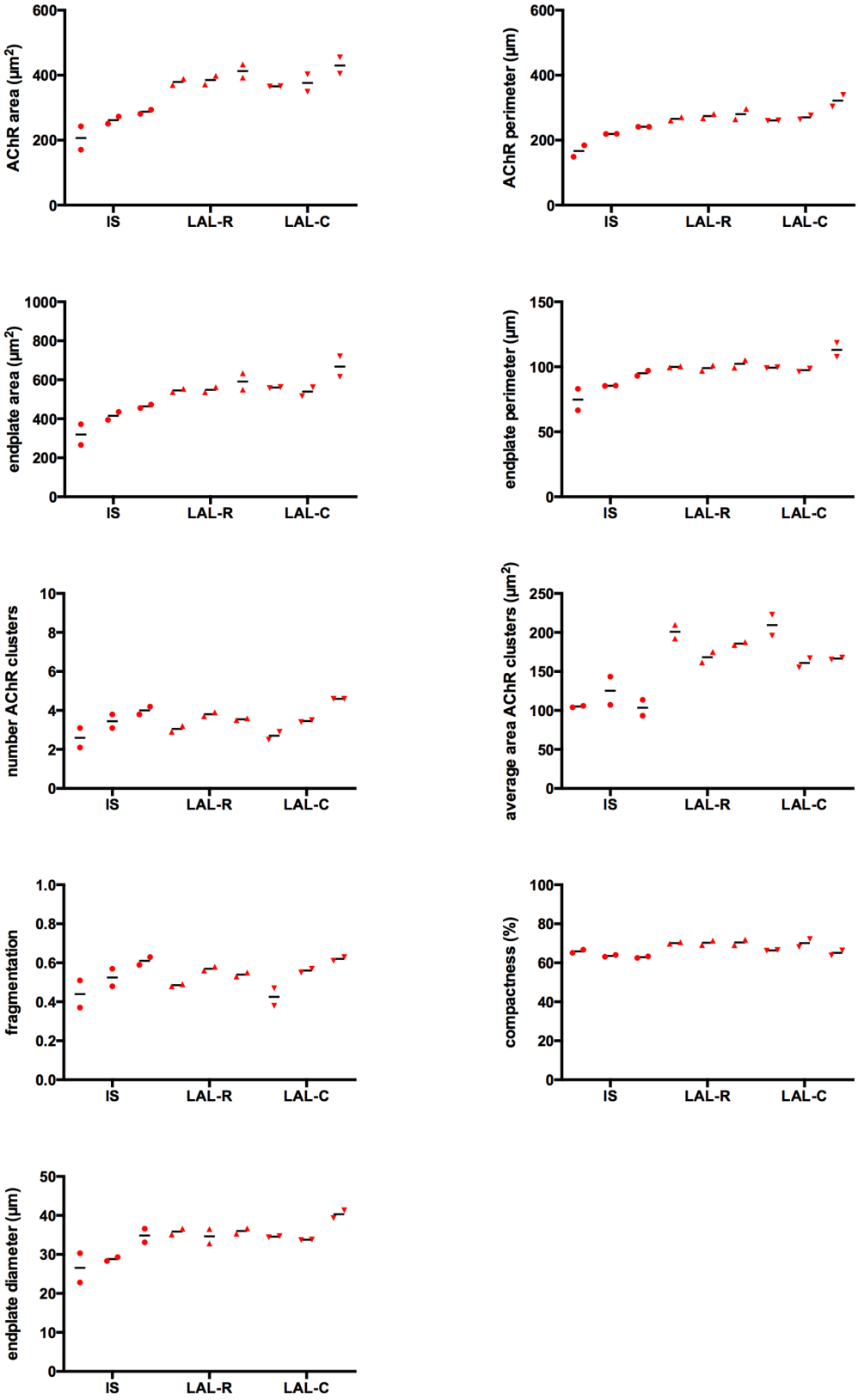

Appendix 7.2 | Influence of side on NMJs, mouse (See Fig. 3.6 for details)

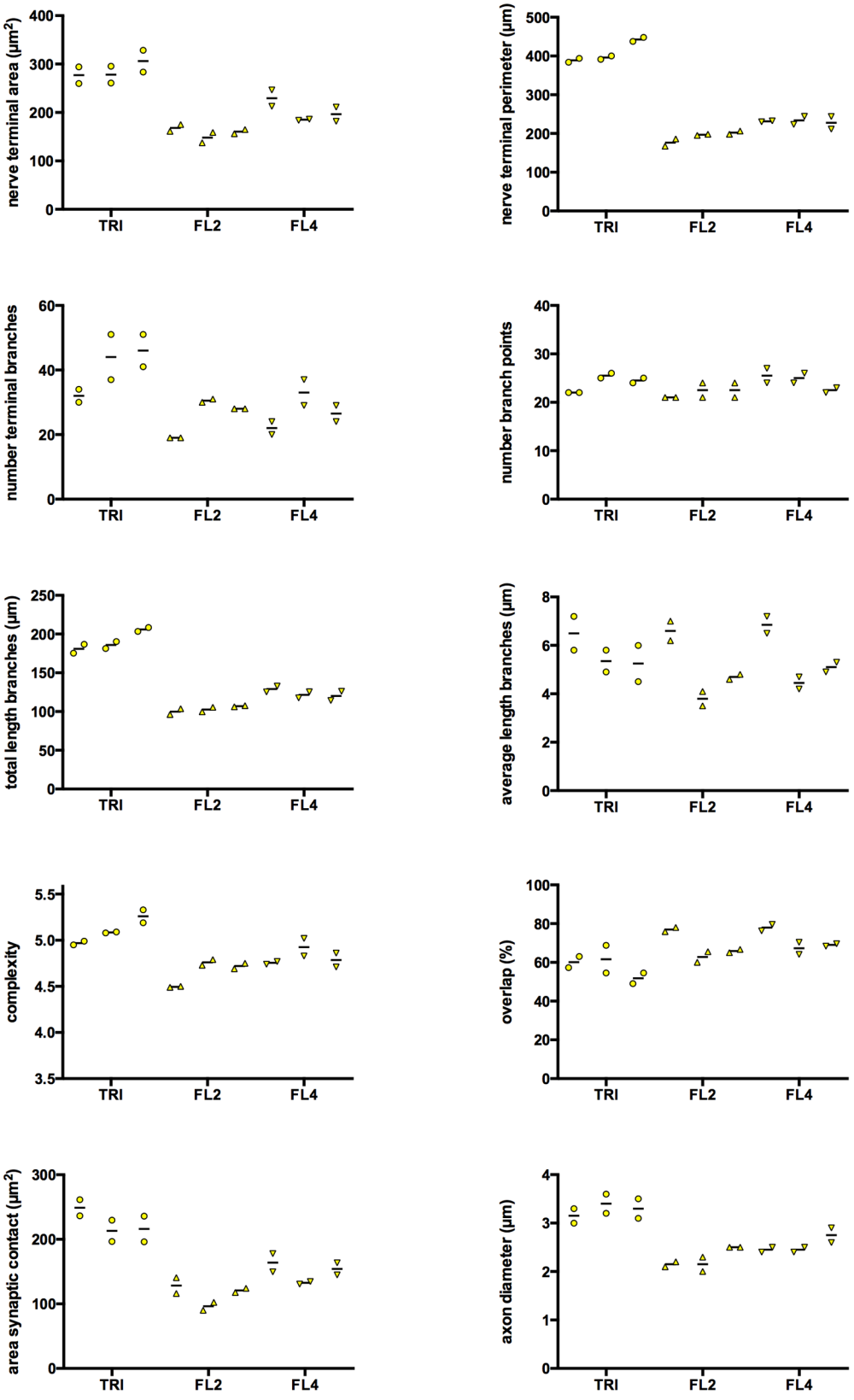

Appendix 7.3 | Influence of side on NMJs, mouse (See Fig. 3.6 for details)

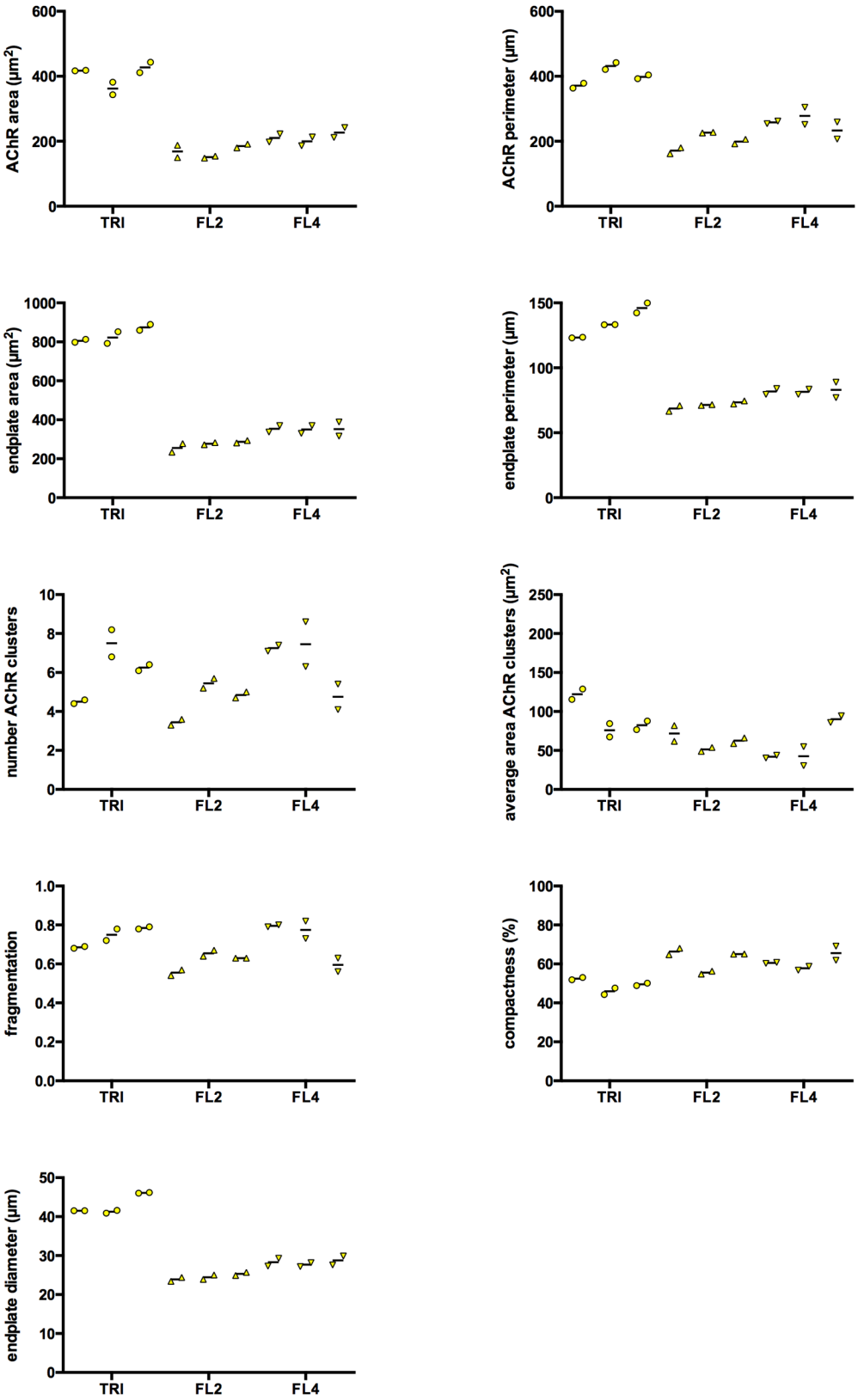

Appendix 7.4 | Influence of side on NMJs, mouse (See Fig. 3.6 for details)

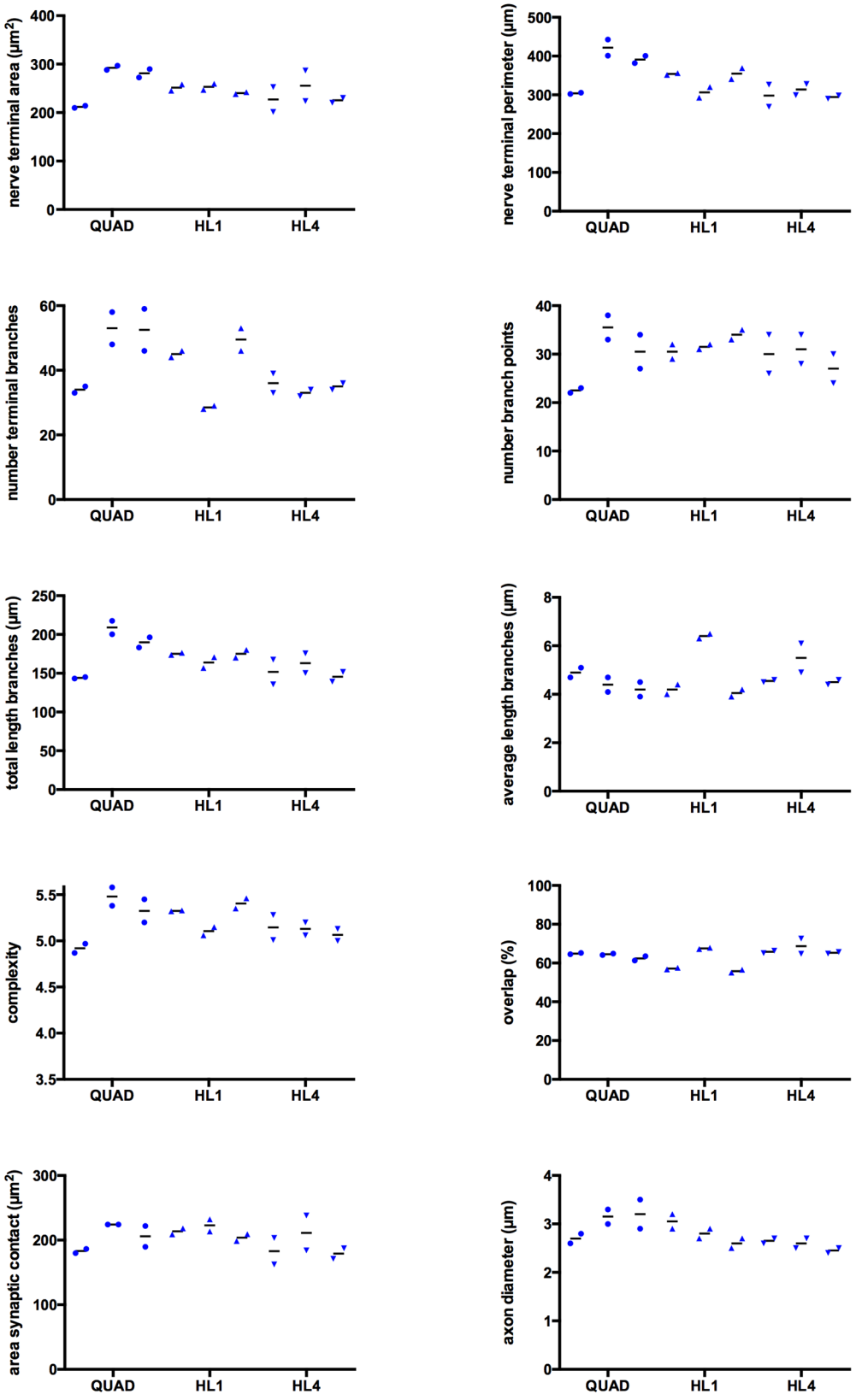

Appendix 7.5 | Influence of side on NMJs, mouse (See Fig. 3.6 for details)

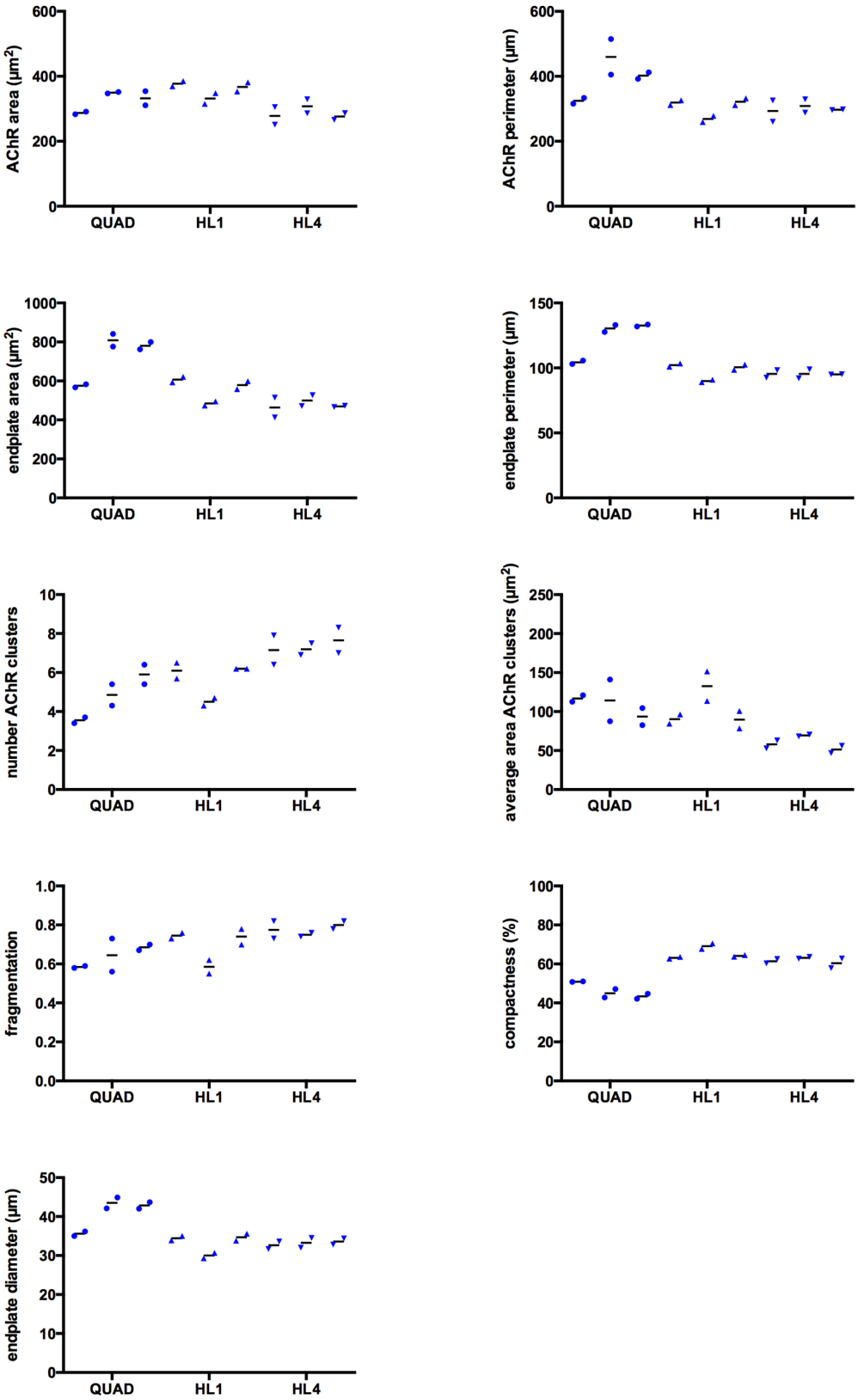

Appendix 7.6 | Influence of side on NMJs, mouse (See Fig. 3.6 for details)

		AChR area: L vs R		Fragmentation: L vs R	
Muscle	Animal	raw *p*	Significance after Bonferroni correction	raw *p*	Significance after Bonferroni correction
IS	1	0.003	n.s	0.011	n.s
IS	2	0.220	n.s	0.168	n.s
IS	3	0.601	n.s	0.902	n.s
LAL-R	1	0.059	n.s	0.316	n.s
LAL-R	2	0.446	n.s	0.215	n.s
LAL-R	3	0.411	n.s	0.736	n.s
LAL-C	1	0.157	n.s	0.745	n.s
LAL-C	2	0.126	n.s	0.409	n.s
LAL-C	3	0.461	n.s	0.815	n.s
TRI	4	0.944	n.s	0.619	n.s
TRI	5	0.176	n.s	0.127	n.s
TRI	6	0.222	n.s	0.884	n.s
FL2	4	0.001	sig.diff	0.664	n.s
FL2	5	0.549	n.s	0.798	n.s
FL2	6	0.429	n.s	0.973	n.s
FL4	4	0.077	n.s	0.977	n.s
FL4	5	0.026	n.s	0.015	n.s
FL4	6	0.079	n.s	0.165	n.s
QUAD	4	0.690	n.s	0.799	n.s
QUAD	5	0.846	n.s	0.047	n.s
QUAD	6	0.140	n.s	0.510	n.s
HL1	1	0.062	n.s	0.526	n.s
HL1	2	0.666	n.s	0.406	n.s
HL1	3	0.023	n.s	0.934	n.s
HL4	1	0.003	n.s	0.137	n.s
HL4	2	0.033	n.s	0.689	n.s
HL4	3	0.250	n.s	0.202	n.s

Appendix 8 | Left/right comarisons, mouse

Results of statistical tests comparing the mean values for AChR area and fragmentation in each left / right muscle pair (27 pairs in total) of 9 different muscles in 6 littermate mice (numbered 1-6). For AChR area, an unpaired t-test was used. For fragmentation, the Mann Whitney test was used (as values are restricted from 0 to 1). Individual comaprisons were regarded as statistically significant using a Bonferroni corrected α value = 0.05 / 27.

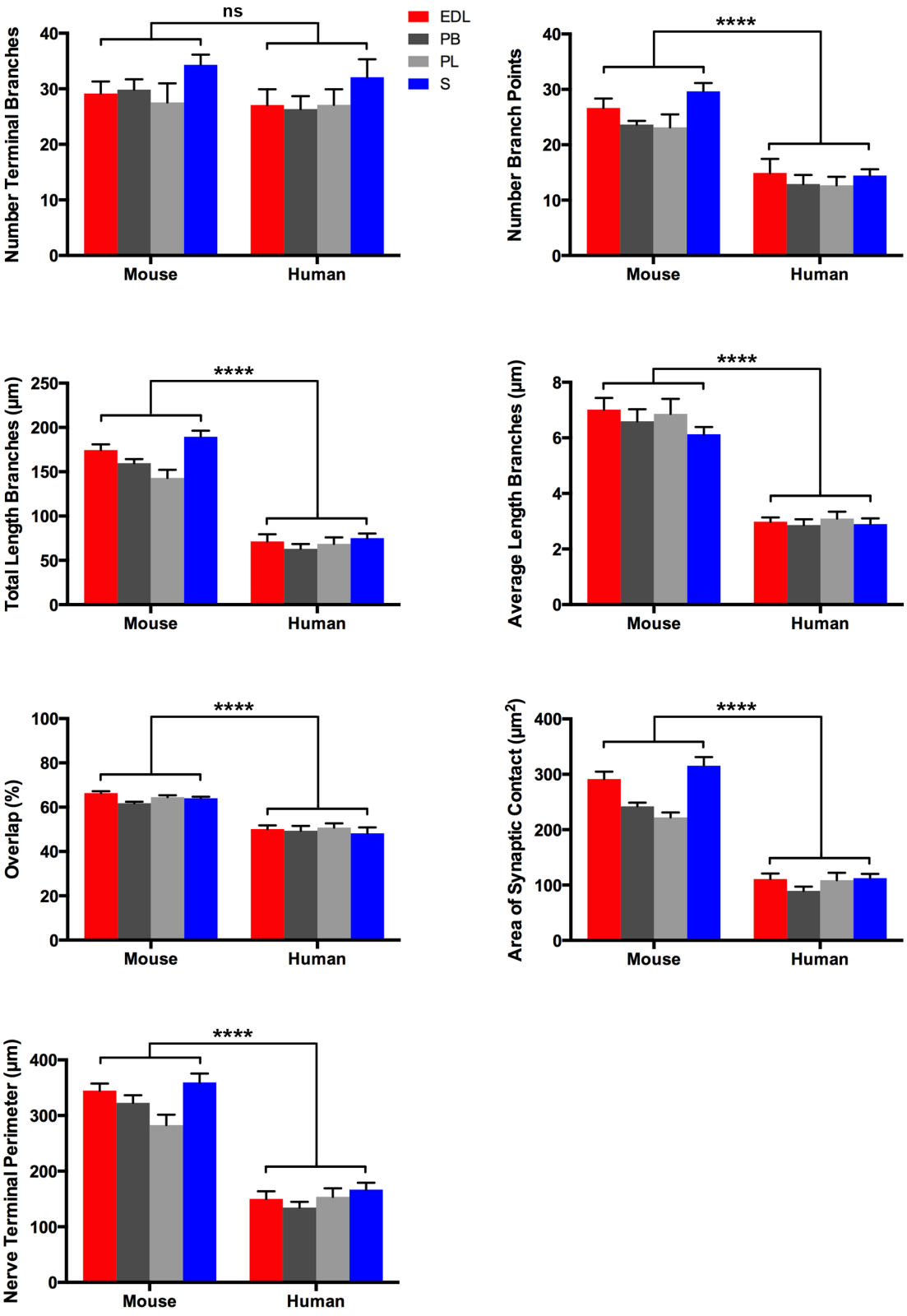

Appendix 9.1 | Morphology of human NMJs (See Fig. 4.2 for details)

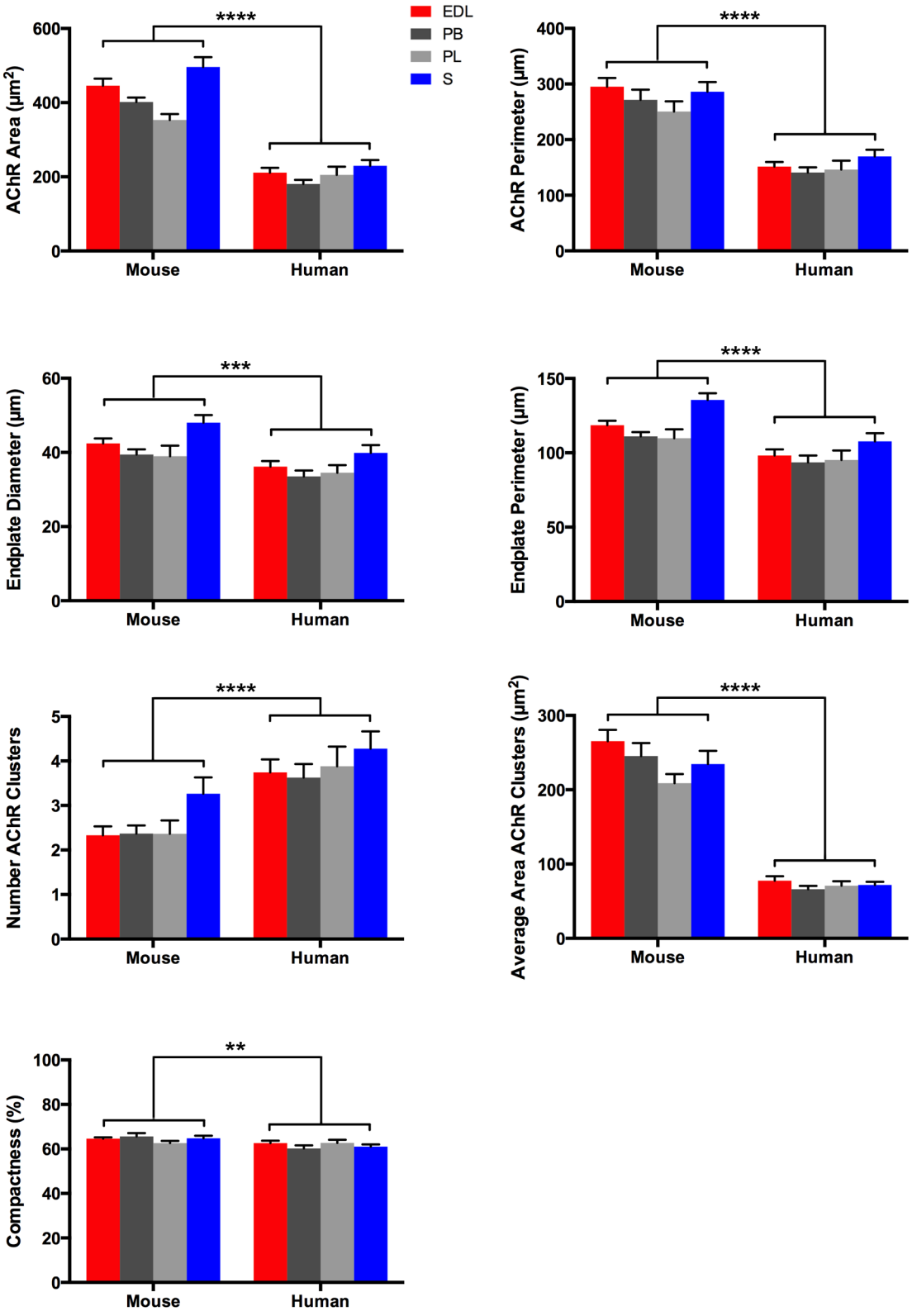

Appendix 9.2 | Morphology of human NMJs (See Fig. 4.2 for details)

a.

	Coefficient of Variation	
	Human	Mouse
NerveTerminalArea	0.48	0.30
NerveTerminalPerimeter	0.48	0.30
NumberTerminalBranches	0.62	0.50
NumberBranchPoints	0.77	0.46
TotalLengthofBranches	0.53	0.30
AChRArea	0.44	0.30
AChRPerimeter	0.45	0.33
EndplateArea	0.49	0.35
EndplatePerimeter	0.35	0.20
EndplateDiameter	0.37	0.23
NumberAChRClusters	0.59	0.71

b.

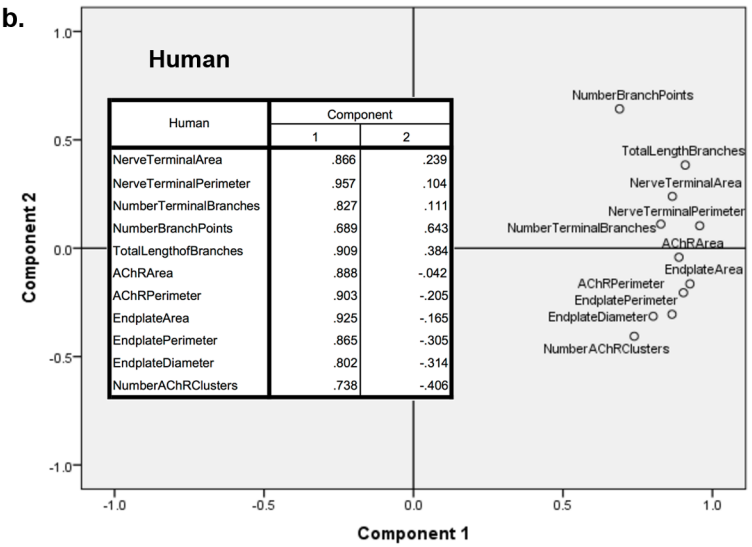

Human	Component	
	1	2
NerveTerminalArea	.866	.239
NerveTerminalPerimeter	.957	.104
NumberTerminalBranches	.827	.111
NumberBranchPoints	.689	.643
TotalLengthofBranches	.909	.384
AChRArea	.888	-.042
AChRPerimeter	.903	-.205
EndplateArea	.925	-.165
EndplatePerimeter	.865	-.305
EndplateDiameter	.802	-.314
NumberAChRClusters	.738	-.406

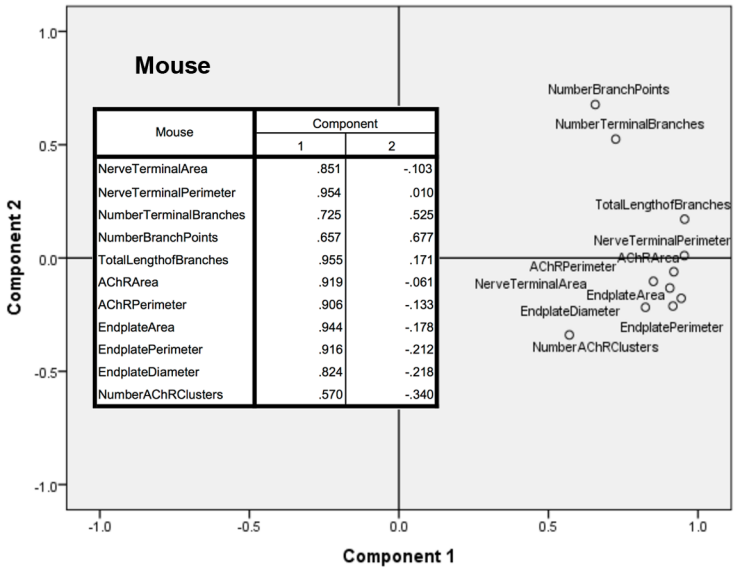

Mouse	Component	
	1	2
NerveTerminalArea	.851	-.103
NerveTerminalPerimeter	.954	.010
NumberTerminalBranches	.725	.525
NumberBranchPoints	.657	.677
TotalLengthofBranches	.955	.171
AChRArea	.919	-.061
AChRPerimeter	.906	-.133
EndplateArea	.944	-.178
EndplatePerimeter	.916	-.212
EndplateDiameter	.824	-.218
NumberAChRClusters	.570	-.340

Appendix 10 | Coefficients of variation and PCA loading plots (human cf. mouse) Human cf. mouse (muscles: EDL, PB, PL, S). **a.** Mean coefficients of variation were higher for human NMJs in 10 of the 11 core variables. **b.** PCA loading plots. For both human and mouse NMJs, component 1 reflects overall size of NMJ; component 2 is more difficult to define physically, as none of the individual variables isolate on the y-axis separate to the main cluster (cf. 'number AChR clusters' in Appendix 4). Analysis performed using SPSS.

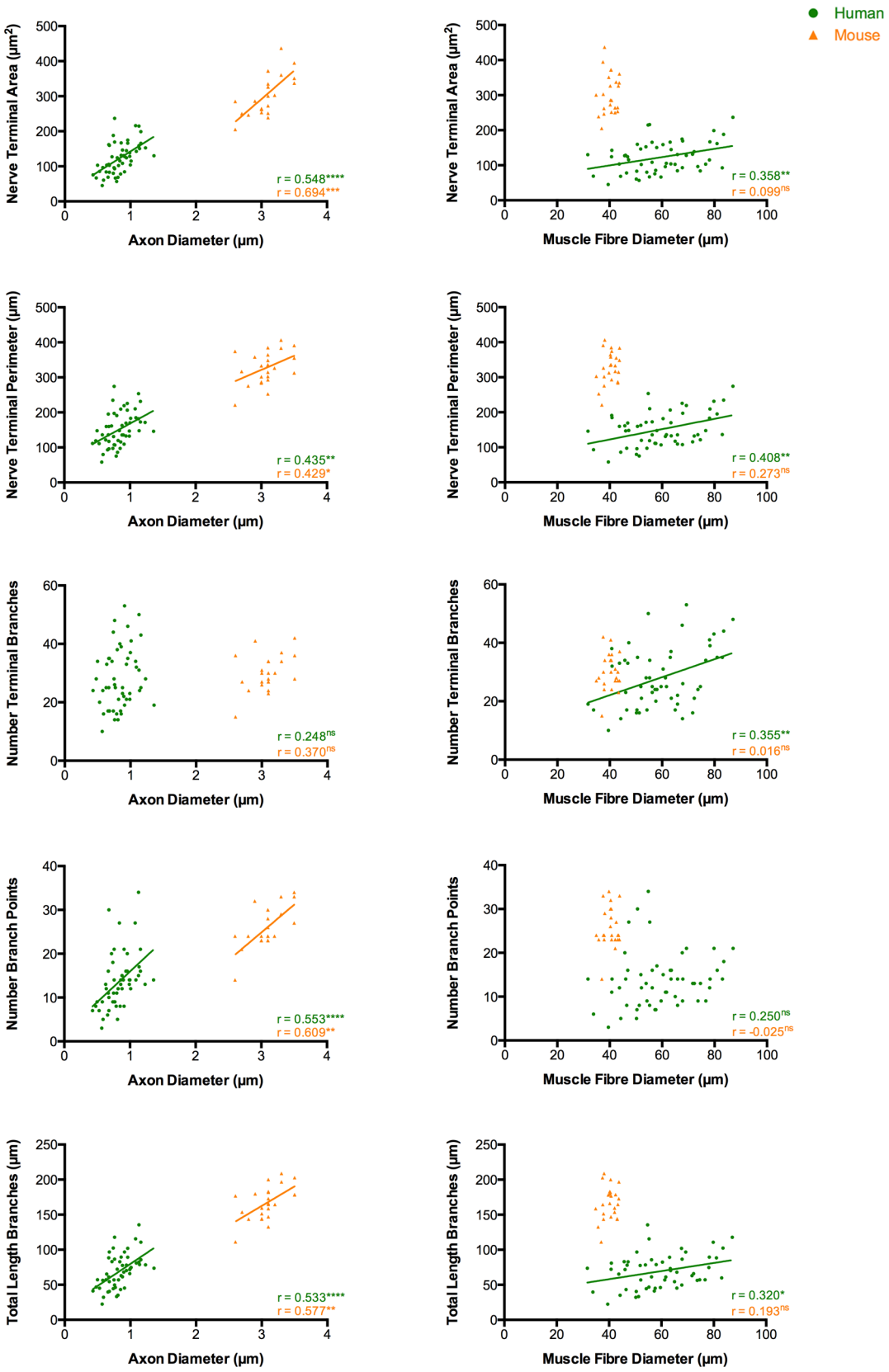

Appendix 11.1 | Influence of pre- and post-synaptic cells, human (See Fig. 4.7 for details)

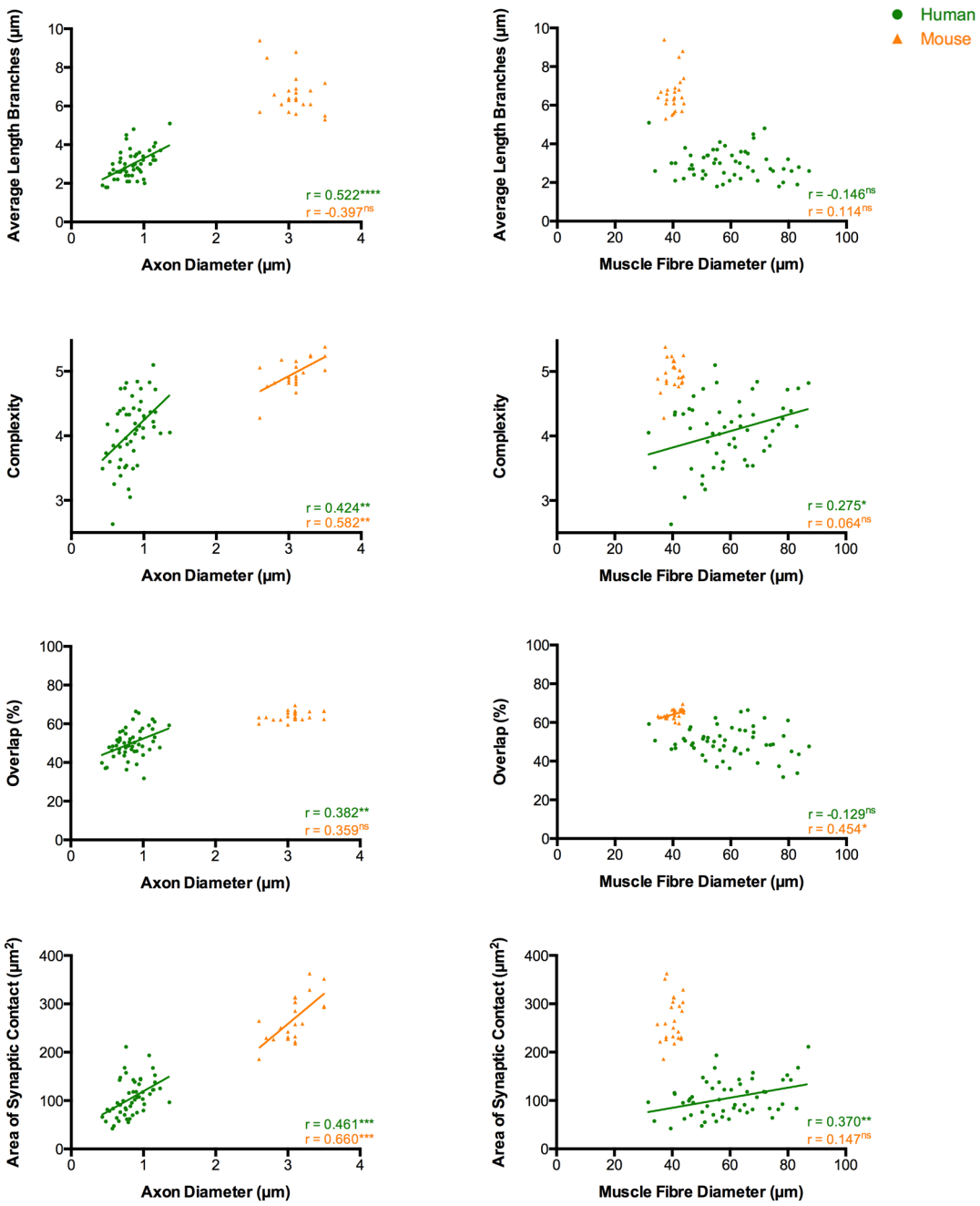

Appendix 11.2 | Influence of pre- and post-synaptic cells, human (See Fig. 4.7 for details)

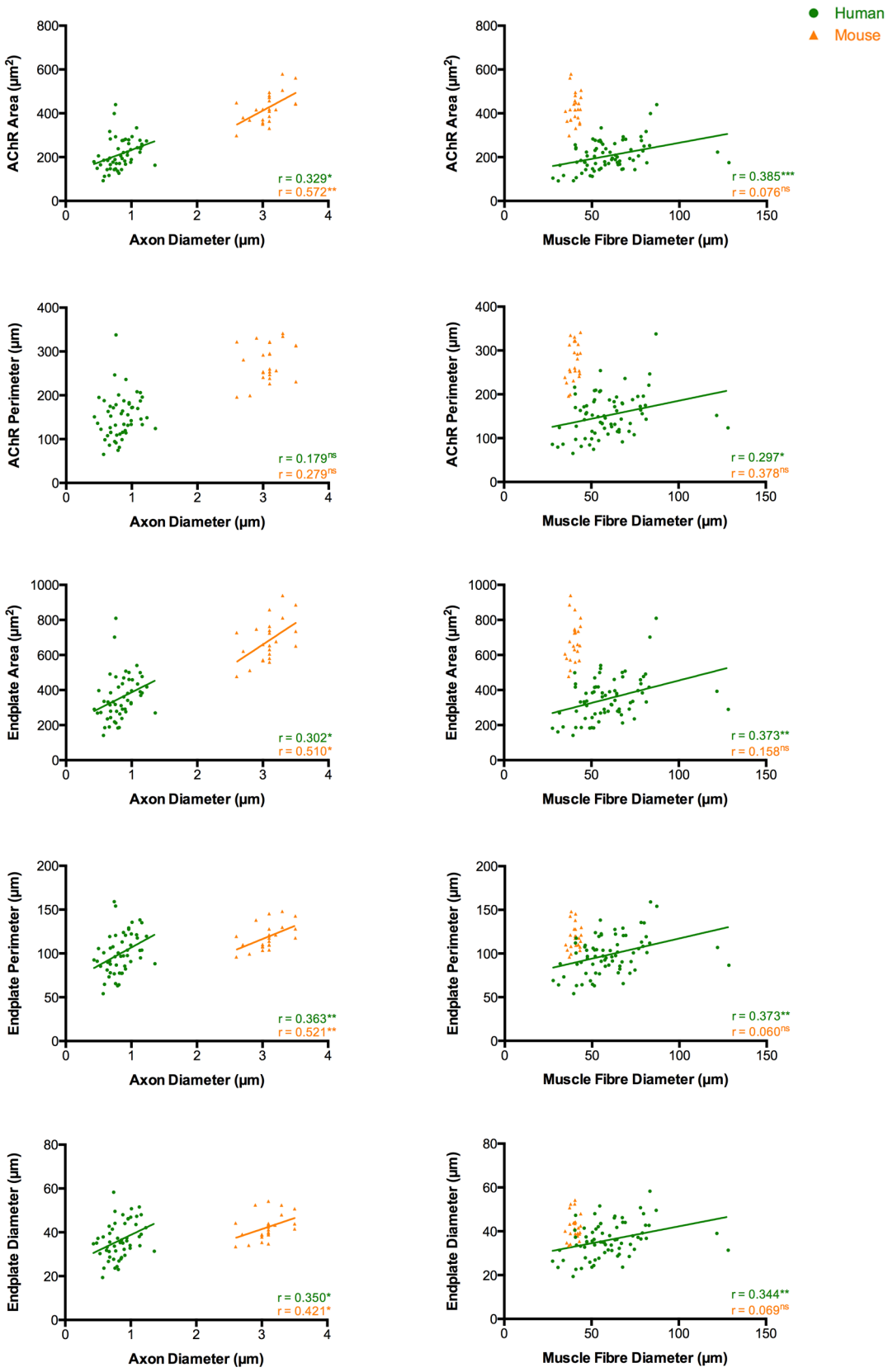

Appendix 11.3 | Influence of pre- and post-synaptic cells, human (See Fig. 4.7 for details)

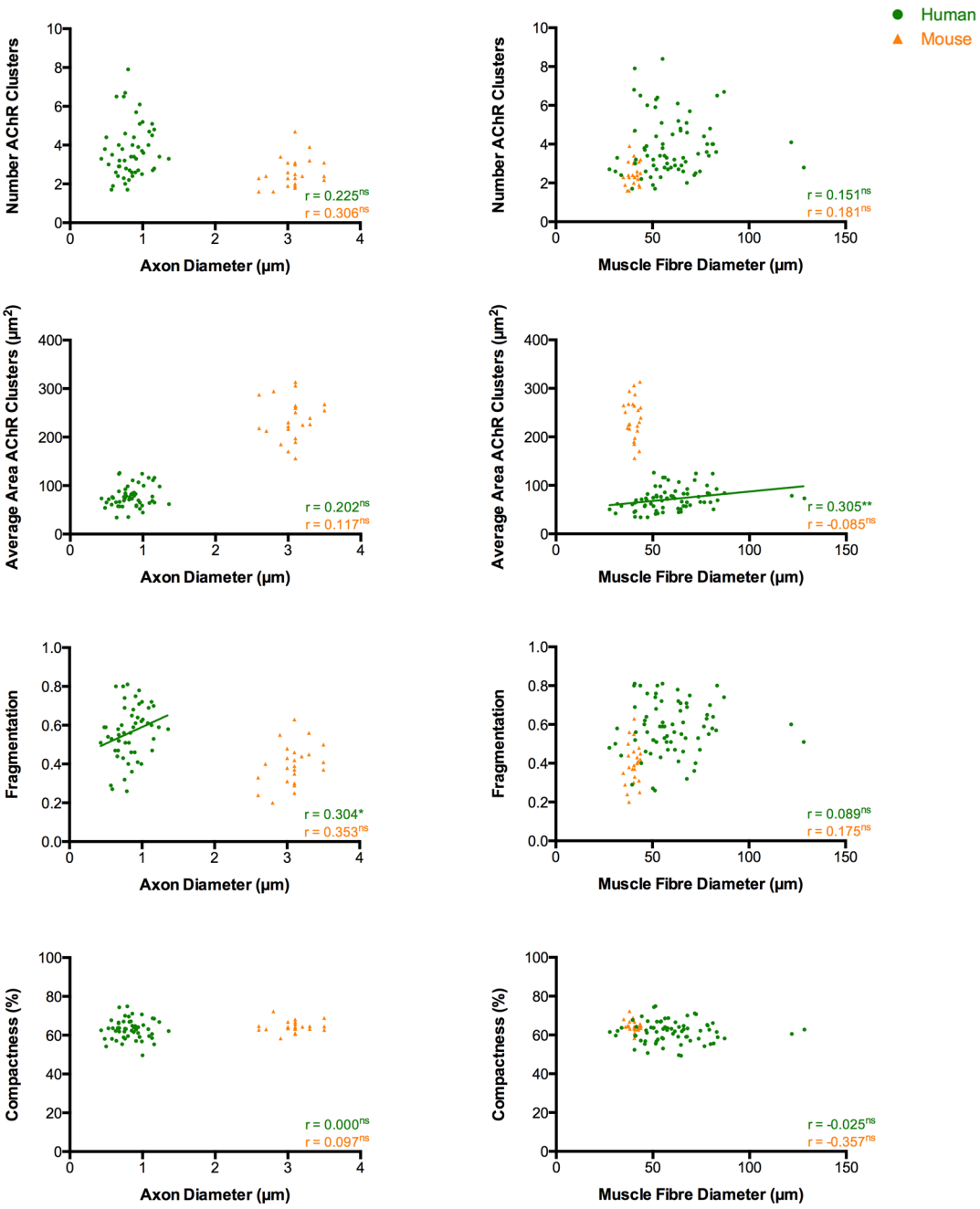

Appendix 11.4 | Influence of pre- and post-synaptic cells, human (See Fig. 4.7 for details)

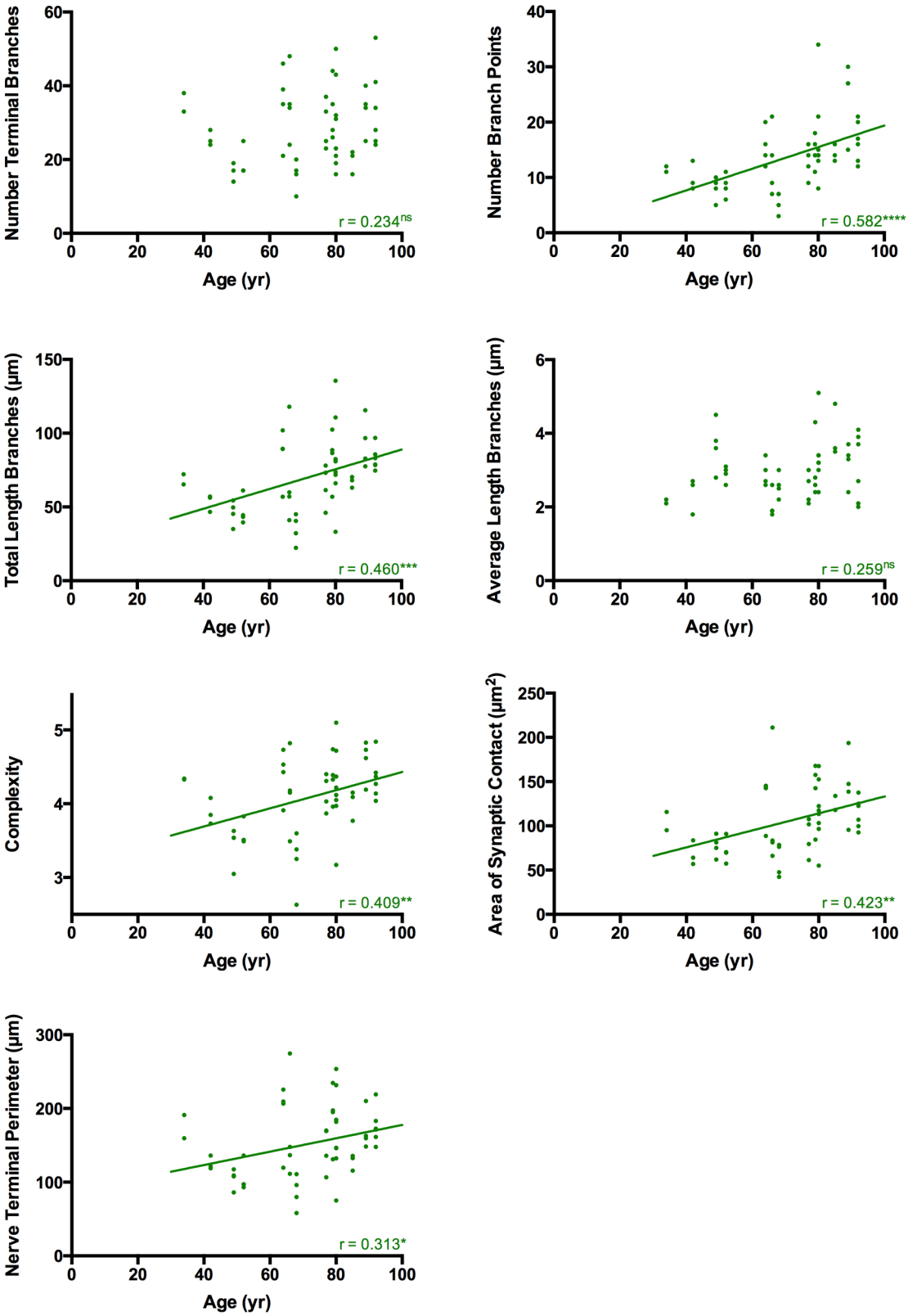

Appendix 12.1 | Effect of age on NMJs, human (See Fig. 4.9 for details)

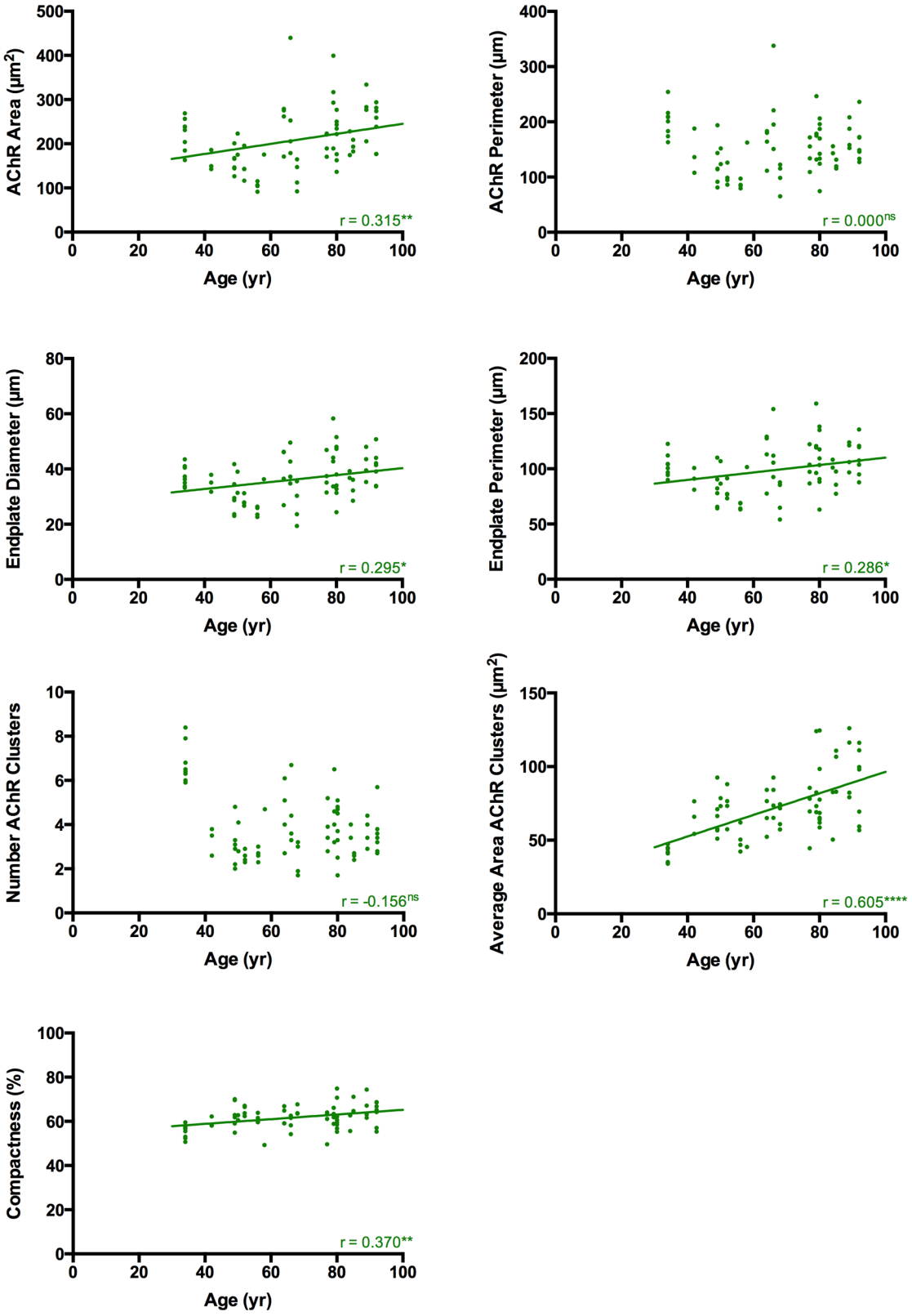

Appendix 12.2 | Effect of age on NMJs, human (See Fig. 4.9 for details)

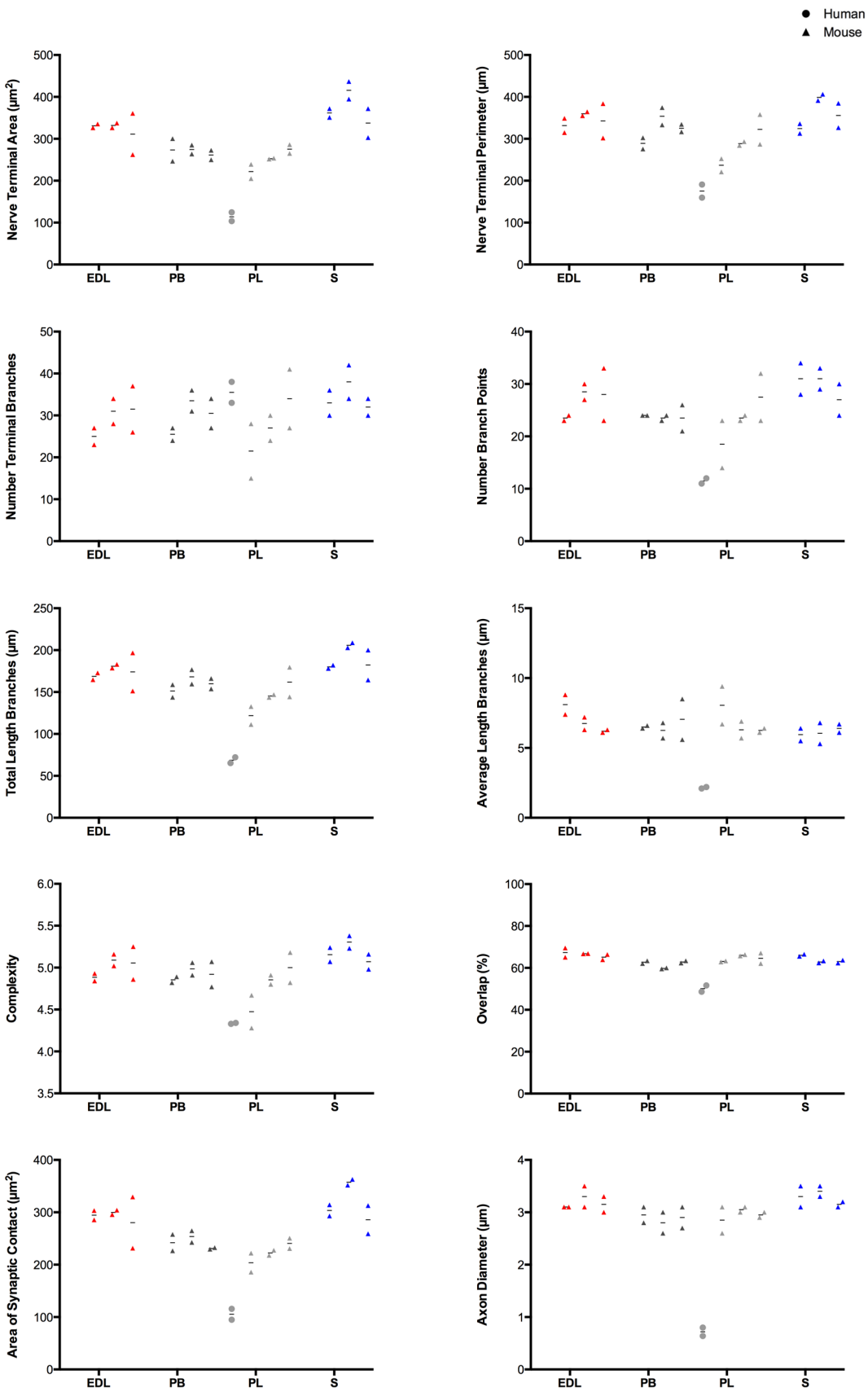

Appendix 13.1 | Influence of side on NMJs, human (See Fig. 4.10 for details)

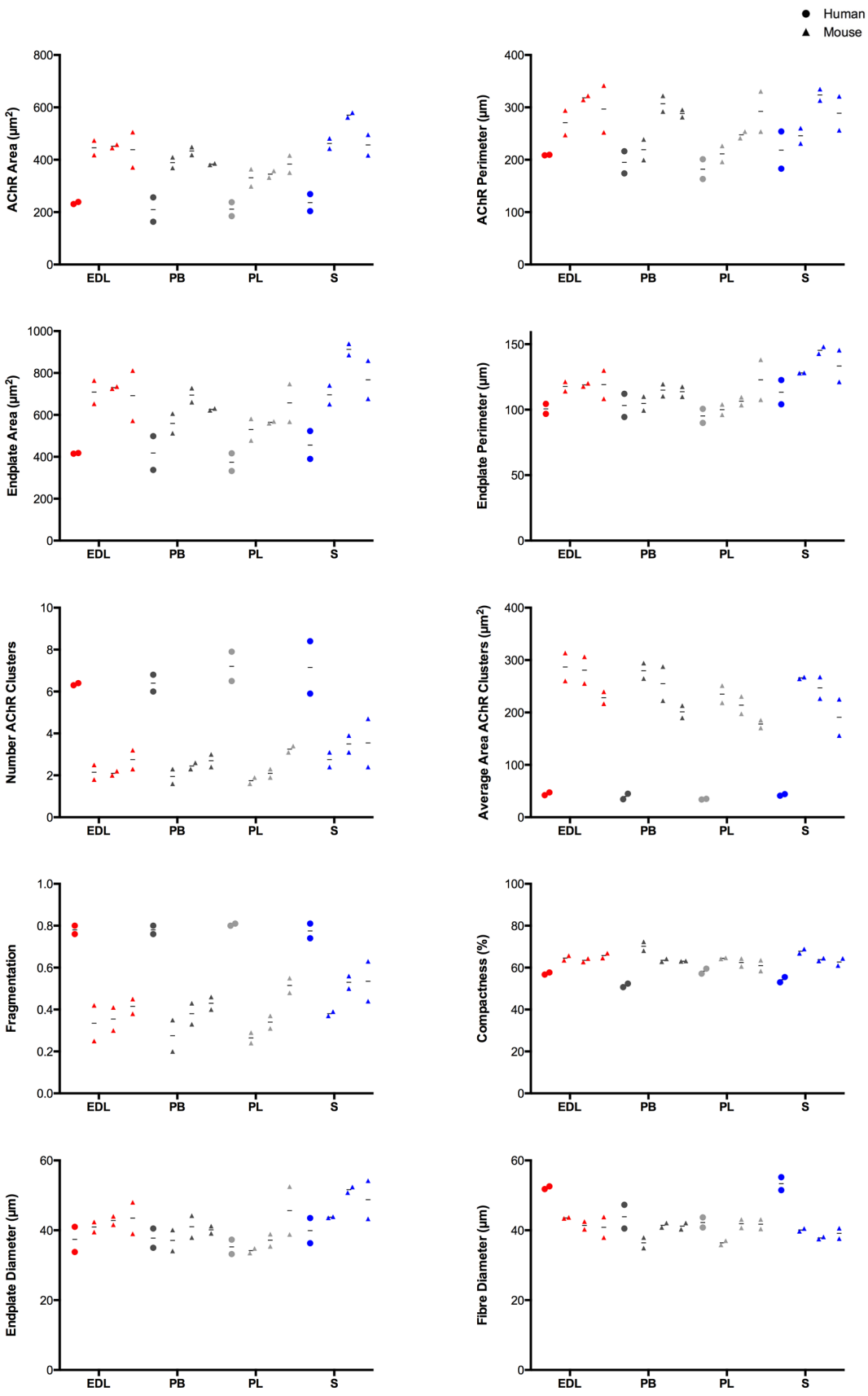

Appendix 13.2 | Influence of side on NMJs, human (See Fig. 4.10 for details)

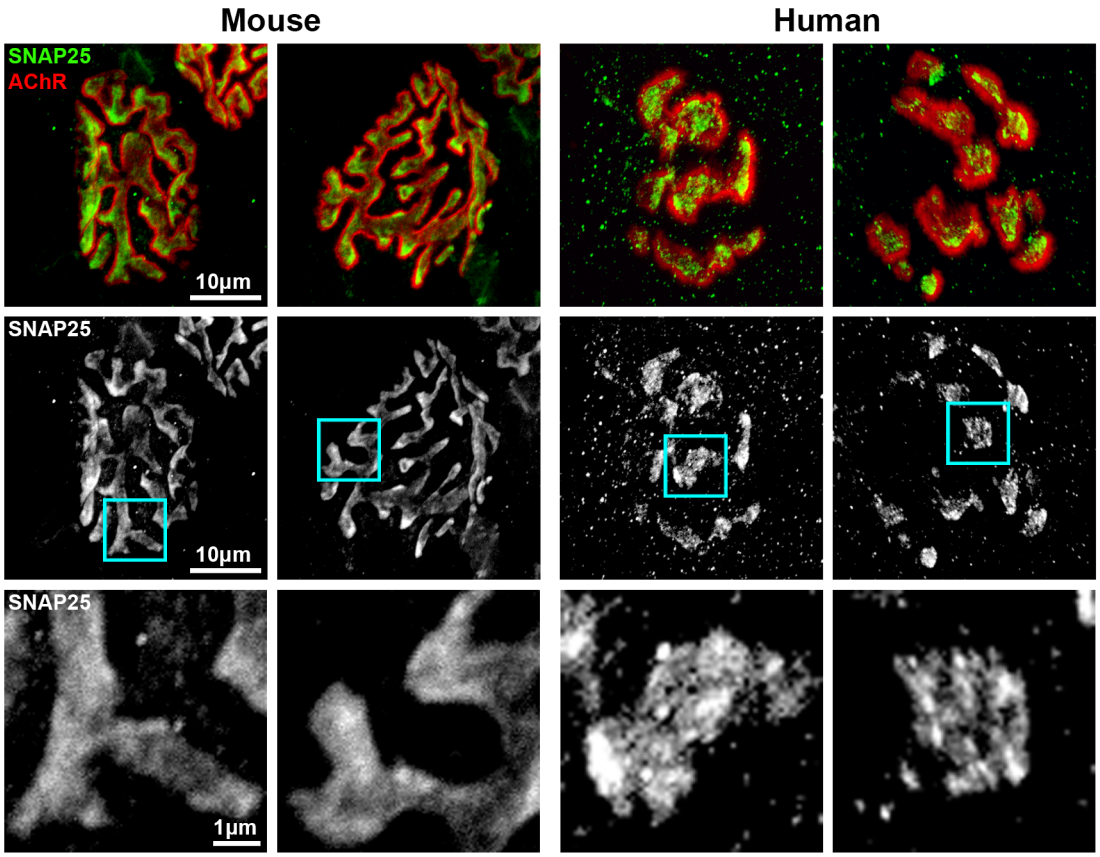

Appendix 14 | SNAP25 distribution at the NMJ
Confocal micrographs of NMJs labeled for the pre-synaptic active zone protein SNAP25 in each species; trial immunohistochemistry prior to super-resolution imaging. Note the heterogeneous labeling in human NMJs (with distinctive 'hot spots' of fluorescence) compared with the homogenous labeling in mouse NMJs. Scale bars = 10µm and 1µm. See also Figure 5.1.

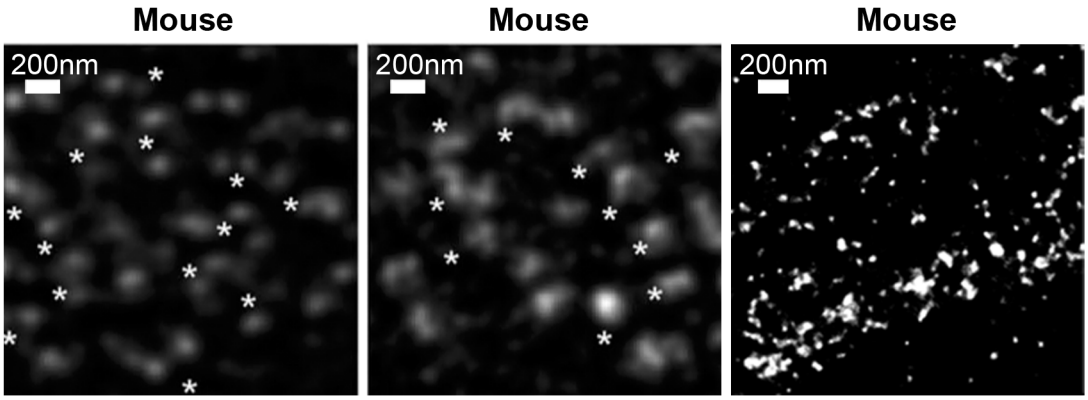

Piccolo (Nishimune et al, 2016) | **Bassoon** (Nishimune et al, 2016) | **SNAP25** (present study)

Appendix 15 | Comparative super-resolution imaging of active zone proteins
The distribution of SNAP25 as revealed by dSTORM imaging (present study) was similar to that of piccolo and bassoon demonstrated previously by STED imaging (Nishimune et al, 2016). Images have been re-sized and re-scaled (from the original article) to allow side-to-side comparison. Note also the slightly better image resolution with dSTORM in the present study. Scale bar = 200nm. (Image of SNAP25 distribution reproduced from Figure 5.2f.)

References

Ackermann F, Waites CL, Garner CC. Presynaptic active zones in invertebrates and vertebrates. *EMBO Rep.* **16**, 923-938 (2015).

Ahmad N, Thomas GN, Gill P, Chan C, Torella, F. Lower limb amputation in England: prevalence, regional variation and relationship with revascularisation, deprivation and risk factors. A retrospective review of hospital data. *J Royal Soc Med.* **107**, 483-489 (2014).

Albuquerque EX, Rash JE, Mayer RF, Satterfield JR. An Electrophysiological and Morphological Study of the Neuromuscular Junction in Patientswith Myasthenia Gravis. *Experimental Neurology.* **51**, 536-563 (1976).

Amorim IS, Mitchell NL, Palmer DN, Sawiak SJ, Mason R, Wishart TM, Gillingwater TH. Molecular neuropathology of the synapse in sheep with CLN5 Batten disease. *Brain and Behavior.* **5**, e00401 (2015).

Angaut-Petit D, Molgo J, Connold AL, Faille L. The levator auris longus muscle of the mouse: a convenient preparation for studies of short- and long-term presynaptic effects of drugs or toxins. *Neurosci. Lett.* **82**, 83-88 (1987).

Anis NA, Robbins N. General and strain-specific age changes at mouse limb neuromuscular junctions. *Neurobiology of Aging.* **8**, 309-318 (1987).

Antoine J-C, Camdessanché J-P. Peripheral nervous system involvement in patients with cancer. *The Lancet Neurology.* **6**, 75-86 (2007).

Antonucci F, Corradini I, Fossati G, Tomasoni R, Menna E, Matteoli M. SNAP-25, a Known Presynaptic Protein with Emerging Postsynaptic Functions. *Front. Synaptic Neurosci.* **8**, 7 (2016).

Aquilonius SM, Arvidsson B, Askmark H, Gillberg PG. Topographical localization of end-plates in cryosections of whole human biceps muscle. *Muscle & Nerve.* **5**, 418 (1982).

Aquilonius SM, Askmark H, Gillberg PG, Nandedkar S, Olsson Y, Stålberg E. Topographical localization of motor endplates in cryosections of whole human muscles. *Muscle & Nerve.* **7**, 287-293 (1984).

Arizono N, Koreto O, Iwai Y, Hidaka T, Takeoka O. Morphometric analysis of human neuromuscular junction in different ages. *Acta. Pathol. Jpn.* **34**, 1243-1249 (1984).

Balice-Gordon RJ, Lichtman JW. In vivo visualization of the growth of pre- and postsynaptic elements of neuromuscular junctions in the mouse. *J. Neurosci.* **10**, 894-908 (1990).

Balice-Gordon RJ, Breedlove SM, Bernstein S, Lichtman JW. Neuromuscular Junctions Shrink and Expand as Muscle Fiber Size Is Manipulated: in viva Observations in the Androgen-Sensitive Bulbocavernosus Muscle of Mice. *The Journal of Neuroscience.* **70**, 2660-2671 (1990).

Balice-Gordon RJ, Lichtman JW. In vivo observations of pre- and postsynaptic changes during the transition from multiple to single innervation at developing neuromuscular junctions. *J. Neurosci.* **13**, 834-855 (1993).

Barker D, Ip MC. Sprouting and Degeneration of Mammalian Motor Axons in Normal and De-afferentated Skeletal Muscle. *Proceedings of the Royal Society of London.* **163**, 538 -554 (1966).

Beeson D, Webster R, Cossins J, Lashley D, Spearman H, Maxwell S, Slater CR, Newsom-Davis J, Palace J, Vincent A. Congenital Myasthenic Syndromes and the Formation of the Neuromuscular Junction. *Ann. N.Y. Acad. Sci.* **1132**, 99-103 (2008).

Behan WMH, Cossar DW, Madden HA, McKay IC. Validation of a simple, rapid, and economical technique for distinguishing type 1 and 2 fibres in fixed and frozen skeletal muscle. *J. Clin. Pathol.* **55**, 375-380 (2002).

Belle M, Godefroy D, Couly G, Malone SA, Collier F, Giacobini P, Chédotal A. Tridimensional Visualization and Analysis of Early Human Development. *Cell.* **169**, 161-173 (2017).

Bjornskov EK, Dekker NP, Norris Jr FH, Stuart ME. End-Plate Morphology in Amyotrophic Lateral Sclerosis. *Arch. Neurol.* **32**, 711-712 (1975).

Blake DJ, Weir A, Newey SE, Davies KE. Function and Genetics of Dystrophin and Dystrophin-Related Proteins in Muscle. *Physiol. Rev.* **82**, 291-329 (2002).

Brooke MH, Kaiser KK. Musle Fiber Types: How Many and What Kind? *Arch. Neurol.* **23**, 369-379 (1970).

Brown R, Dissanayake KN, Skehel PA, Ribchester RR. Endomicroscopy and electromyography of neuromuscular junctions in situ. *Annals of Clinical and Translational Neurology*. **1**, 867-883 (2014).

Bruneteau G, Simonet T, Bauche S, Mandjee N, Malfatti E, Girard E, Tanguy M-L, Behin A, Khiami F, Sariali E, Hell-Remy C, Salachas F, Pradat P-F, Fournier E, Lacomblez L, Koenig J, Romero NB, Fontaine B, Meininger V, Schaeffer L, Hantaï D. Muscle histone deacetylase 4 upregulation in amyotrophic lateral sclerosis: potential role in reinnervation ability and disease progression. *Brain*. **136**, 2359-2368 (2013).

Buller A, Eccles J, Eccles R. Differentiation of fast and slow muscles in the cat hind limb. *J. Physiol*. **150**, 399-416 (1960).

Burgess RW, Cox GA, Seburn KL. Neuromuscular Disease Models and Analysis. In: *Mouse Models for Drug Discovery, Methods in Molecular Biology, Vol. 1438*. Humana Press, New York, pp. 347-393 (2016).

Burghes AHM, Beattie CE. Spinal Muscular Atrophy: Why do low levels of SMN make motor neurons sick? *Nat. Rev. Neurosci.* **10**, 597-609 (2009).

Burkholder TJ, Fingado B, Baron S, Lieber RL. Relationship Between Muscle Fiber Types and Sizes and Muscle Architectural Properties in the Mouse Hindlimb. *Journal of Morphology*. **221**, 177-190 (1994).

Campbell M, Ganetzky B. Extensive morphological divergence and rapid evolution of the larval neuromuscular junction in Drosophila. *PNAS*. **109**, E648-E655 (2012).

Castroflorio T, Farina D, Bottin A, Debernardi C, Bracco P, Merletti R, Anastasi G, Bramanti P. Non-invasive assessment of motor unit anatomy in jaw-elevator muscles. *Journal of Oral Rehabilitation*. **32**, 708-713 (2005).

Chokroverty S, Reyes MG, Rubino FA, Barron KD. Hemiplegic Amyotrophy: Muscle and Motor Point Biopsy Study. *Arch. Neurol*. **33**, 104-110 (1976).

Christensen E. Topography of terminal motor innervation in striated muscles from stillborn infants. Am J Phys Med. **38**, 65-78 (1959).

Clark AW, Bandyopadhyay S, DasGupta BR. The plantar nerves-lumbrical muscles: a useful nerve-muscle preparation for assaying the effects of botulinum neurotoxin. *J. Neurosci. Methods*. **19**, 285-295 (1987).

Coërs C, Woolf AL. *The Innervation of Muscle.* Blackwell, Oxford (1959).

Cornwall J, Stringer MD, Duxson M. Functional morphology of the thoracolumbar transversospinal muscles. *Spine.* **36**, 1053-1061 (2011).

Court FA, Gillingwater TH, Melrose S, Sherman DL, Greenshields KN, Morton AJ, Harris JB, Willison HJ, Ribchester RR. Identity, developmental restriction and reactivity of extralaminar cells capping mammalian neuromuscular junctions. *Journal of Cell Science.* **121**, 3901-3911 (2008).

Couteaux R, Pécot-Dechavassine M. Vésicules synaptiques et poches au niveau des "zones actives" de la jonction neuromusculaire. *C. R. Acad. Sci. Hebd. Seances Acad. Sci. D.* 271, 2346-2349 (1970).

Cox J, Mann M. MaxQuant enables high peptide identification rates, individualized p.p.b.-range mass accuracies and proteome-wide protein quantification. *Nat. Biotechnol.* **26**, 1367-1372 (2008).

Cox J, Neuhauser N, Michalski A, Scheltema RA, Olsen JV, Mann M. Andromeda: A Peptide Search Engine Integrated into the MaxQuant Environment. *J. Proteome Res.* **10**, 1794-1805 (2011).

Crompton RH, Günther M. Humans and other bipeds: the evolution of bipedality. *J. Anat.* **204**, 317-319 (2004).

De Bleecker JL. Organophosphate and carbamate poisoning. In: *Handbook of Clinical Neurology, 3rd Series, Vol. 91, Neuromuscular Junction Disorders*. Elsevier, Amsterdam, pp. 401-432 (2008).

De Vito MA, Malmgren LT, Gacek RR. Three-dimensional Distribution of Neuromuscular Junctions in Human Cricothyroid. *Arch Otolaryngol.* **111**, 110-113 (1985).

Demer LL, Tintut Y. Vascular Calcification: Pathobiology of a Multifaceted Disease. *Circulation.* **117**, 2938-2948 (2008).

Desaki J, Uehara Y. The overall morphology of neuromuscular junctions as revealed by scanning electron microscopy. *J. Neurocytol.* **10**, 101-110 (1981).

Deschenes MR, Hurst TE, Ramser AE, Sherman EG. Presynaptic to Postsynaptic Relationships of the Neuromuscular Junction are Held Constant Across Age and Muscle Fiber Type. *Devel Neurobiol.* **73**, 744-753 (2013).

Dietert SE. The demonstration of different types of muscle fibers in human extraocular muscle by electron microscopyand cholinesterase staining. *Investigative Ophthalmology.* **4**, 51-63 (1965).

Drost G, Stegeman DF, van Engelen BGM, Zwarts MJ. Clinical applications of high-density surface EMG: A systematic review. *Journal of Electromyography and Kinesiology.* **16**, 586-602 (2006).

Duxson MJ, Sheard PW. Formation of New Myotubes Occurs Exclusively at the Multiple Innervation Zones of an Embryonic Large Muscle. *Developmental Dynamics.* **204**, 391-405 (1995).

El-Din Safwat MD, Abdel-Meguid EM. Distribution of terminal nerve entry points to the flexor and extensor groups of forearm muscles: an anatomical study. *Folia Morphol.* **66**, 83-93 (2007).

Elekes K, Kiss T, Fujisawa Y, Hernadi L, Erdelyi L, Muneoka Y. Mytilus inhibitory peptides (MIP) in the central and peripheral nervous system of the pulmonate gastropods, *Lymnaea stagnalis* and *Helix pomatia*: distribution and physiological actions. *Cell Tissue Res.* **302**, 115-134 (2000).

Enck P, Hinninghofen H, Wietek B, Becker HD. Functional Asymmetry of Pelvic Floor Innervation and Its Role in the Pathogenesis of Fecal Incontinence. *Digestion.* **69**, 102-111 (2004).

Enck P, Hinninghofen H, Merletti R, Azpiproz F. The external anal sphincter and the role of surface electromyography. *Neurogastroenterol Motil.* 17, 60-67 (2005).

Engel AG, Santa T. Histiometric analysis of the ultrastructure of the neuromuscular junction in myasthenia gravis and in the myasthenic syndrome. *Annals of the New York Academy of Sciences.* **183**, 46-63 (1971).

Engel AG, MD, Lambert EH, Gomez MR. A New Myasthenic Syndrome with End-Plate Acetylcholinesterase Deficiency, Small Nerve Terminals, and Reduced Acetylcholine Release. *Ann. Neurol.* **1**, 315-330 (1977).

Engel AG. The neuromuscular junction. In: *Myology: Basic and Clinical.* McGraw-Hill, New York, pp. 209-253 (1986).

Engel AG, Fukuoka T, Lang B, Newsom-Davis J, Vincent A, Wray D. Lambert-Eaton Myasthenic Syndrome IgG: Early Morphologic Effects and Immunolocalization at the Motor Endplate. *Annals of the New York Academy of Sciences.* **505**, 333-345 (1987).

Engel AG. The neuromuscular junction. In: *Handbook of Clinical Neurology, 3rd Series, Vol. 91, Neuromuscular Junction Disorders.* Elsevier, Amsterdam, pp. 103-148 (2008).

Engel AG, Shen X-M, Selcen D, Sine SM. Congenital myasthenic syndromes: pathogenesis, diagnosis, and treatment. *Lancet Neurol.* **14**, 420-434 (2015).

Eržen I, Cvetko E, Obreza S, Angaut-Petit D. Fiber Types in the Mouse Levator Auris Longus Muscle: A Convenient Preparation to Study Muscle and Nerve Plasticity. *Journal of Neuroscience Research.* **59**, 692-697 (2000).

Espina V, Wulfkuhle JD, Calvert VS, VanMeter A, Zhou W, Coukos G, Geho DH, Petricoin EF, Liotta LA. Laser-capture microdissection. *Nature Protocols.* **1**, 586-603 (2006).

Everett AW, Edwards SJ, Etherington SJ. Structural basis for the spotted appearance of amphibian neuromuscular junctions stained for synaptic vesicles. *J. Neurocytol.* **31**, 15-25 (2002).

Fahim MA, Holley, JA, Robbins N. Topographic comparison of neuromuscular junctions in mouse slow and fast twitch muscles. *Neuroscience.* **13**, 227-235 (1984).

Falla D, Dall'Alba P, Rainoldi A, Merletti R, Jull G. Location of innervation zones of sternocleidomastoid and scalene muscles – a basis for clinical and research electromyography applications. *Clinical Neurophysiology.* **113**, 57-63 (2002).

Farquharson M, Moran B. *Farquharson's textbook of operative general surgery, 9th Edition.* Hodder Arnold, London (2005).

Fatt P, Katz B. Spontaneous subthreshold activity at motor nerve endings. *J. Physiol.* **117**, 109-128 (1952).

Fearon K, Strasser F, Anker SD, Bosaeus I, Bruera E, Fainsinger RL, Jatoi A, Loprinzi C, MacDonald N, Mantovani G, Davis M, Muscaritoli M, Ottery F, Radbruch L, Ravasco P, Walsh D, Wilcock A, Kaasa S, Baracos VE. Definition and classification of cancer cachexia: an international consensus. *Lancet Oncol.* **12**, 489-495 (2011).

Ferreira T, Rasband WS. ImageJ User Guide – IJ 1.46r (2012). imagej.nih.gov/ij/docs/guide/146-29.html

Fidziańska A. Human Ontogenesis. II. Development of the Human Neuromuscular Junction. *Journal of Neuropathology and Experimental Neurology*. **39**, 606-615 (1980).

Fouquet W, Owald D, Wichmann C, Mertel S, Depner H, Dyba M, Hallermann S, Kittel RJ, Eimer S, Sigrist SJ. Maturation of active zone assembly by *Drosophila* Bruchpilot. *J. Cell Biol.* **186**, 129-145 (2009).

Freije J, Malmgren LT, Gacek RR. Motor End-plate Distribution in the Human Lateral Cricoarytenoid Muscle. *Arch Otolaryngol Head Neck Surg*. **112**, 176-179 (1986).

Freije J, Malmgren LT, Gacek RR. Motor End-plate Distribution in the Human Interarytenoid Muscle. *Arch Otolaryngol Head Neck Surg*. **113**, 63-68 (1987).

Fukunaga H, Engel AG, Osame M, Lambert EH. Paucity and disorganization of presynaptic membrane active zones in the Lambert-Eaton myasthenic syndrome. *Muscle & Nerve*. **5**, 686-697 (1982).

Fukunaga H, Engel AG, Lang B, Newsom-Davis J, Vincent A. Passive transfer of Lambert-Eaton myasthenic syndrome with IgG from man to mouse depletes the presynaptic membrane active zones. *Proc. Natl. Acad. Sci.* **80**, 7636-7640 (1983).

Fukuoka T, Engel AG, Lang B, Newsom-Davis J, Prior C, Wray DW. Lambert-Eaton Myasthenic Syndrome: I. Early Morphological Effects of IgG on the Presynaptic Membrane Active Zones. *Ann. Neurol.* **22**, 193-199 (1987).

Gambino DR, Malmgren LT, Gacek RR. Three-dimensional computer reconstruction of the neuromuscular junction distribution in the human posterior cricoarytenoid muscle. *Laryngoscope*. **95**, 556-560 (1985).

Gambino DR, Malmgren LT, Gacek RR. Age-Related Changes in the Neuromuscular Junctions in the Human Posterior Cricoarytenoid Muscles: A Quantitative Study. *Laryngoscope*. **100**, 262-268 (1990).

Garner CC, Kindler S, Gundelfinger ED. Molecular determinants of presynaptic active zones. *Current Opinion in Neurobiology*. **10**, 321-327 (2000).

Gonzalez-Freire M, de Cabo R, Studenski SA, Ferrucci L. The Neuromuscular Junction: Aging at the Crossroad between Nerves and Muscle. *Frontiers in Aging Neuroscience*. **6**, 208 (2014).

Gonzalez-Freire M, Semba RD, Ubaida-Mohien C, Fabbri E, Scalzo P, Højlund K, Dufresne C, Lyashkov A, Ferrucci L. The Human Skeletal Muscle Proteome Project: a reappraisal of the current literature. *J. Cach. Sarc. Musc.* **8**, 5-18 (2017).

Gramsbergen A, IJkema-Paassen J, Nikkels PGJ, Hadders-Algra M. Regression of polyneural innervation in the human psoas muscle. *Early Human Development.* **49**, 49-61 (1997).

Greene EC. *Anatomy of the Rat.* Hafner Publishing Company, New York and London (1963).

Guénet J-L, Bonhomme F. Wild mice: an ever-increasing contribution to a popular mammalian model. *Trends in Genetics.* **19**, 24-31 (2003).

Guida HL, Zorzetto NL. Morphological and Histochemical Analysis of the Human Vestibular Fold. *Int J Morphol.* **25**, 537-543 (2007).

Guth L. "Trophic" influence of nerve on muscle. *Physiol. Rev.* **48**, 645-687 (1968).

Han J, Pluhackova K, Böckmann RA. The Multifaceted Role of SNARE Proteins in Membrane Fusion. *Front. Physiol.* **8**, 5 (2017).

Happak W, Liu J, Burggasser G, Flowers A, Gruber H, Freilinger G. Human Facial Muscles: Dimensions, Motor Endplate Distribution, and Presence of Muscle Fibres With Multiple Motor Endplates. *The Anatomical Record.* **249**, 276-284 (1997).

Harding BN, Kariya S, Monani UR, Chung WK, Benton M, Yum SW, Tennekoon G, Finkel RS. Spectrum of Neuropathophysiology in Spinal Muscular Atrophy Type I. *J. Neuropathol. Exp. Neurol.* **74**, 15-24 (2015).

Harlow ML, Szule JA, Xu J, Jung JH, Marshall RM, McMahan UJ. Alignment of Synaptic Vesicle Macromolecules with the Macromolecules in Active Zone Material that Direct Vesicle Docking. *PLoS ONE.* **8**, 69410 (2013).

Harriman DGF. A comparison of the fine structure of motor end-plates in Duchenne dystrophy and in human neurogenic diseases. *Journal of the Neurological Sciences.* **28**, 233-247 (1976).

Harris AJ, Duxson MJ, Butler JE, Hodges PW, Taylor JL, Gandevia SC. Muscle fibre and motor unit behavior in the longest human skeletal muscle. *Journal of Neuroscience.* **25**, 8528-8533 (2005).

Harris JB, Ribchester RR. The relationship between end-plate size and transmitter release in normal and dystrophic muscles of the mouse. *J Physiol.* **296**, 245-265 (1979).

Helmprobst F, Frank M, Stigloher C. Presynaptic Architecture of the Larval Zebrafish Neuromuscular Junction. *J. Comp. Neurol.* **523**, 1984-1997 (2015).

Hesselmans LFGM, Jennekens FGI, Kartman J, Wokke JHJ, de Visser M, Klaver-Krol EG, DeBaets M, Spaans F, Veldman H. Secondary changes of the motor endplate in Lambert-Eaton myasthenic syndrome: a quantitative study. *Acta Neuropathol.* **83**, 202-206 (1992).

Hesselmans LFGM, Jennekens FGI, Van Den Oord CJM, Veldman H, Vincent A. Development of Innervation of Skeletal Muscle Fibers in Man: Relation to Acetylcholine Receptors. *The Anatomical Record.* **236**, 553-562 (1993).

Hirst TC, Ribchester RR. Segmentation of the mouse fourth deep lumbrical muscle connectome reveals concentric organisation of motor units. *J Physiol.* **59**, 4859-4875 (2013).

Hogrel JY. Clinical applications of surface electromyography in neuromuscular disorders. *Clinical Neurophysiology.* **35**, 59-71 (2005).

Hopkins WG, Brown MC, Keynes RJ. Postnatal growth of motor nerve terminals in muscles of the mouse. *J Neurocytol.* **14**, 525-540 (1985).

Hou Y, Jayasinghe I, Crossman DJ, Baddeley D, Soeller C. Nanoscale analysis of ryanodine receptor clusters in dyadic couplings of rat cardiac myocytes. *J. Mol. Cell. Cardiol.* **80**, 45-55 (2015).

Huang B, Babcock H, Zhuang X. Breaking the Diffraction Barrier: Super-Resolution Imaging of Cells. *Cell.* **143**, 1047-1058 (2010).

Huang L, Wang MJ. Image thresholding by minimizing the measures of fuzziness. *Pattern Recognition.* **28**, 41-51 (1995).

Hughes CS, Foehr S, Garfield DA, Furlong EE, Steinmetz LM, Krijgsveld J. Ultrasensitive proteome analysis using paramagnetic bead technology. *Mol. Syst. Biol.* **10**, 757 (2014).

Jerusalem F, Engel AG, Gomez MR. Duchenne dystrophy. II. Morphometric study of motor end-plate fine structure. *Brain.* **97**, 123-130 (1974).

Jiang X, Shen S, Cadwell CR, Berens P, Sinz F, Ecker AS, Patel S, Tolias AS. Principles of connectivity among morphologically defined cell types in adult neocortex. *Science.* **350**, aac9462 (2015).

Johnson EA, Montecucco C. Botulism. In: *Handbook of Clinical Neurology, 3rd Series, Vol. 91, Neuromuscular Junction Disorders.* Elsevier, Amsterdam, pp. 333-368 (2008).

Johnson MA, Polgar J, Weightman D, Appleton D. Data on the Distribution of Fibre Types in Thirty-six Human Muscles: An Autopsy Study. *Journal of the Neurological Sciences.* **18**, 111-129 (1973).

Jones RA, Reich CD, Dissanayake KN, Kristmundsdottir F, Findlater GS, Ribchester RR, Simmen MW, Gillingwater TH. NMJ-morph reveals principal components of synaptic morphology influencing structure-function relationships at the neuromuscular junction. *Open Biology.* **6**, 160240 (2016).

Jones RA, Gillingwater TH. NMJ-morph [interactive resource]. University of Edinburgh. Centre for Integrative Physiology. Doi: 10.7488/ds/1490 (2016).

Kariya S, Park G-H, Maeno-Hikichi Y, Leykekhman O, Lutz C, Arkovitz MS, Landmesser LT, Monani UR. Reduced SMN protein impairs maturation of the neuromuscular junctions in mouse models of spinal muscular atrophy. *Human Molecular Genetics.* **17**, 2552–2569 (2008).

Kasthuri N, Hayworth KJ, Berger DR, Schalek RL, Conchello JA, Knowles-Barley S, Lee D, Vázquez-Reina A, Kaynig V, Jones TR, Roberts M, Morgan JL, Tapia TC, Seung HS, Roncal WG, Vogelstein JT, Burns R, Sussman DL, Priebe CE, Pfister H, Lichtman JW. Saturated reconstruction of a volume of neocortex. *Cell.* **162**, 648-61 (2015).

Kay KR, Smith C, Wright AK, Serrano-Pozo A, Pooler AM, Koffie R, Bastin ME, Bak TH, Abrahams S, Kopeikina KJ, McGuone D, Frosch MP, Gillingwater TH, Hyman BT, Spires-Jones TL. Studying synapses in human brain with array tomography and electron microscopy. *Nat. Protoc.* **8**, 1366-1380 (2013).

Khan MAA, Javed AA, Rao DJ, Corner JA, Rosenfield P. Pediatric Traumatic Limb Amputation: The Principles of Management and Optimal Residual Limb Lengths. *World J. Plast. Surg.* **5**, 7-14 (2016).

King MJ, Atwood HL, Govind CK. Structural features of crayfish phasic and tonic neuromuscular terminals. *J. Comp. Neurol.* **372**, 618-626 (1996).

Koelle GB, Friedenwald JS. A Histochemical Method for Localizing Cholinesterase Activity. *Proc Soc Exp Biol Med.* **70**, 617-622 (1949).

Kong J, Anderson JE. Dystrophin is required for organizing large acetylcholine receptor aggregates. *Brain Research.* **839**, 298-304 (1999).

Konig WF, von Leden H. The Peripheral Nervous System of the Human Larynx. Part II: The Thyroarytenoid (Vocalis) Muscle. *Archives of Otolaryngology.* **74**, 153-163 (1961).

Kruger P. Die Innervation der tetanischen und tonischen Fasern der quergestreiften Skelettmuskulatur der Wirbeltiere. Anat. Anz. 97, 169-175 (1949).

Krzanowski WJ. *Principles of Multivariate Analysis: A User's Perspective.* Oxford University Press, Oxford (1988).

Kühne W. Neue untersuchunge über die motorische nervenendigungen. *Z Biol.* **23**, 1-148 (1887).

Kuno M, Turkanis SA, Weakly JN. Correlation between nerve terminal size and transmitter release at the neuromuscular junction of the frog. *J. Physiol.* **213**, 545-556 (1971).

Kupfer C. Motor innervation of extraocular muscle. *J. Physiol.* **153**, 522-526 (1960).

Landini G. Advanced shape analysis with ImageJ. *Proceedings of the Second ImageJ User and Developer Conference*, Luxembourg, 6-7 November (2008).
mecourse.com/landinig/software/software.html

Lapatki BG, Oostenveld R, Van Dijk JP, Jonas IE, Zwarts MJ, Stegeman DF. Topographical Characteristics of Motor Units of the Lower Facial Musculature Revealed by Means of High-Density Surface EMG. *J Neurophysiol.* **95**, 342-354 (2006).

Last RJ. *Anatomy: Regional and Applied, 7th Edition*. Churchill Livingstone, Edinburgh (1984).

Lateva ZC, McGill KC, Johanson ME. The innervation and organization of motor units in a series-fibered human muscle: the brachioradialis. *J Appl Physiol.* **108**, 1530-1541 (2010).

Liu W, Klose A, Forman S, Paris ND, Wei-LaPierre L, Cortés-Lopéz M, Tan A, Flaherty M, Miura P, Dirksen RT, Chakkalakal JV. Loss of adult skeletal muscle stem cells drives age-related neuromuscular junction degeneration. *eLife.* **6**, e26464 (2017).

LoGerfo FW, Coffman JD. Vascular and microvascular disease of the foot in diabetes: Implications for foot care. *The New England Journal of Medicine.* **311**, 1615-1619 (1984).

Lu J, Tapia JC, White OL, Lichtman JW. The Interscutularis Muscle Connectome. *PLoS Biology*. **7**, e1000032 (2009).

Maglione M, Sigrist SJ. Seeing the forest tree by tree: super-resolution light microscopy meets the neurosciences. *Nature Neuroscience.* **16**, 790-797 (2013).

Marques MJ, Conchello JA, Lichtman JW. From Plaque to Pretzel: Fold Formation and Acetylcholine Receptor Loss at the Developing Neuromuscular Junction. *The Journal of Neuroscience.* **20**, 3663-3675 (2000).

Maselli RA, Wollman RL, Leung C, Distad B, Palombi S, Richman DP, Salazar-Grueso EF, Roos RP. Neuromuscular transmission in amyotrophic lateral sclerosis. *Muscle & Nerve.* **16**, 1193-1203 (1993).

Maselli RA, Wollmann R, Roos R. Function and Ultrastructure of the Neuromuscular Junction in Post-Polio Syndrome. *Annals of the New York Academy of Sciences.* **753**, 129-137 (1995).

Masuda T, Miyano H, Sadoyama T. The propagation of motor unit action potential and the location of neuromuscular junction investigated by surface electrode arrays. *Electroencephalography and Clinical Neurophysiology*. **55**, 594-600 (1983a).

Masuda T, Miyano H, Sadoyama T. The distribution of myoneural junctions in the biceps brachii investigated by surface electromyography. *Electroencephalography and Clinical Neurophysiology*. **56**, 597-603 (1983b).

Masuda T, Miyano H, Sadoyama T. The Position of Innervation Zones in the Biceps Brachii Investigated by Surface Electromyography. *Transactions on Biomedical Engineering*. **32**, 36-42 (1985).

Masuda T, Sadoyama T. The propagation of single motor unit action potentials detected by a surface electrode array. *Electroencephalography and Clinical Neurophysiology.* **63**, 590-598 (1986).

Masuda T, Sadoyama T. Skeletal muscles from which the propagation of motor unit action potentials is detectable with a surface electrode array. *Electroencephalography and Clinical Neurophysiology.* **67**, 421-427 (1987).

Masuda T, Sadoyama T. Topographical Map of Innervation Zones Within Single Motor Units Measured with a Grid Surface Electrode. *Transactions on Biomedical Engineering*. **35**, 623-628 (1988).

Masuda T, Sadoyama T. Distribution of Innervation Zones in the Human Biceps Brachii. *Journal of Electromyography and Kinesiology*. **1**, 107-115 (1991).

McArdle JJ, Angaut-Petit D, Mallart A, Bournaud R, Faille L, Brigant JL. Advantages of the triangularis sterni muscle of the mouse for investigations of synaptic phenomena. *J. Neurosci. Methods*. **4**, 109-115 (1981).

McMinn RMH. *Last's Anatomy: Regional and Applied, 9th Edition*. Churchill Livingstone, Edinburgh (1994).

Meinertzhagen IA, Govind CK, Stewart BA, Carter JM, Atwood HL. Regulated Spacing of Synapses and Presynaptic Active Zones at Larval Neuromuscular Junctions in Different Genotypes of the Flies *Drosophila* and *Sarcophaga*. *J. Comp. Neurol*. **393**, 482-492 (1998).

Meinertzhagen IA. Connectome studies on Drosophila: a short perspective on a tiny brain. *J. Neurogen*. **30**, 62-68 (2016).

Mercken EM, Capri M, Carboneau BA, Conte M, Heidler J, Santoro A, Martin-Montalvo A, Gonzalez-Freire M, Khraiwesh H, González-Reyes JA, Moaddel R, Zhang Y, Becker KG, Villalba JM, Mattison JA, Wittig I, Franceschi C, de Cabo R. Conserved and species-specific molecular denominators in mammalian skeletal muscle aging. *npj Aging and Mechanisms of Disease*. **3**, 8 (2017).

Moon JY, Hwang TS, Sim SJ, Chun S, Kim M. Surface Mapping of Motor Points in Biceps Brachii Muscle. *Ann Rehabil Med*. **36**, 187-196 (2012).

Moon M-J. Fine Structural Analysis of the Neuromuscular Junction in the Venomous Organ of the Spider, Agelena limbata (Araneae: Agelenidae). *Korean J. Zool*. **39**, 223-230 (1996).

Morgan JL, Lichtman JW. Why not connectomics? *Nature Methods*. **10**, 494-500 (2013).

Murray LM, Talbot K, Gillingwater TH. Review: neuromuscular synaptic vulnerability in motor neurone disease: amyotrophic lateral sclerosis and spinal muscular atrophy. *Neuropathol Appl Neurobiol*. **36**, 133-56 (2010).

Murray LM, Gillingwater TH, Parson SH. Using mouse cranial muscles to investigate neuromuscular pathology in vivo. *Neuromuscular Disorders*. **20**, 740-743 (2010).

Murray L, Gillingwater, TH, Kothary R. Dissection of the Transversus Abdominis Muscle for Whole-mount Neuromuscular Junction Analysis. *J Vis Exp.* **83**, e51162 (2014).

Nagel A, Engel AG, Lang B, Newsom-Davis J, Fukuoka T. Lambert-Eaton Myasthenic Syndrome IgG Depletes Presynaptic Membrane Active Zone Particles by Antigenic Modulation. *Ann. Neurol.* **24**, 552-558 (1988).

Nagwaney S, Harlow ML, Jung JH, Szule JA, Ress D, Xu J, Marshall RM, McMahan UJ. Macromolecular Connections of Active Zone Material to Docked Synaptic Vesicles and Presynaptic Membrane at Neuromuscular Junctions of Mouse. *J. Comp. Neurol.* **513**, 457-468 (2009).

Newman ZL, Hoagland A, Aghi K, Worden K, Levy SL, Son JH, Lee LP, Isacoff EY. Input-Specific Plasticity and Homeostasis at the Drosophila Larval Neuromuscular Junction. *Neuron.* **93**, 1388-1404 (2017).

Nijhof B, Castells-Nobau A, Wolf L, Scheffer-de Gooyert JM, Monedero I, Torroja L, Coromina L, van der Laak JAWM, Schenck A. A New Fiji-Based Algorithm That Systematically Quantifies Nine Synaptic Parameters Provides Insights into Drosophila NMJ Morphometry. *PLoS Comput. Biol.* **12**, e1004823 (2016).

Nishimune H, Badawi Y, Mori S, Shigemoto K. Dual-color STED microscopy reveals a sandwich structure of Bassoon and Piccolo in active zones of adult and aged mice. *Sci. Rep.* **6**, 27935 (2016).

Nitkin RM, Smith MA, Magill C, Fallon JR, Yao YM, Wallace BG, McMahan UJ. Identification of agrin, a synaptic organizing protein from Torpedo electric organ. *J. Cell Biol.* **105**, 2471-2478 (1987).

Nowak KJ, Davies KE. Duchenne muscular dystrophy and dystrophin: pathogenesis and opportunities for treatment. *EMBO reports.* **5**, 872-876 (2004).

Oda K. Age changes of motor innervation and acetylcholine receptor distribution on human skeletal muscle fibres. *J Neuro Sci.* **66**, 327-338 (1984).

Oda K. The Relationship between Motor Endplate Size and Muscle Fiber Diameter in Different Muscle Groups of the Rat. *Japanese Journal of Physiology.* **35**, 1091-1095 (1985).

Oda K. Motor Innervation and Acetylcholine Receptor Distribution of Human Extraocular Muscle Fibres. *Journal of the Neurological Sciences.* **74**, 125-133 (1986).

Oh SW, Harris JA, Ng L, Winslow B, Cain N, Mihalas S, Wang Q, Lau C, Kuan L, Henry AM, Mortrud MT, Ouellette B, Nguyen TN, Sorensen SA, Slaughterbeck CR, Wakeman W, Li Y, Feng D, Ho A, Nicholas E, Hirokawa KE, Bohn P, Joines KM, Peng H, Hawrylycz MJ, Phillips JW, Hohmann JG, Wohnoutka P, Gerfen CR, Koch C, Bernard A, Dang C, Jones AR, Zeng H. A mesoscale connectome of the mouse brain. *Nature*. **508**, 207-214 (2014).

Parratte B, Tatu L, Vuillier F, Diop M, Monnier G. Intramuscular distribution of nerves in the human triceps surae muscle: anatomical bases for treatment of spastic drop foot with botulinum toxin. *Surg Radiol Anat*. **24**, 91-96 (2002).

Parson SH, Ribchester RR, Davie N, Gandhi NP, Malik RQ, Gillingwater TH, Thomson D. Axotomy-Dependent and Independent Synapse Elimination in Organ Cultures of WldS Mutant Mouse Skeletal Muscle. *J Neurosci Res*. **76**, 64-75 (2004).

Paul AC. Muscle Length Affects the Architecture and Pattern of Innervation Differently in Leg Muscles of Mouse, Guinea Pig, and Rabbit Compared to Those of Human and Monkey Muscles. *The Anatomical Record*. **262**, 301-309 (2001).

Périé S, St Guily JL, Callard P, Sebille A. Innervation of adult human laryngeal muscle fibers. *Journal of Neurological Sciences*. **149**, 81-86 (1997).

Périé S, St Guily JL, Sebille A. Comparison of perinatal multi-innervation in human laryngeal muscle fibers. *Ann. Otol. Rhinol. Laryngol.* **108**, 683-688 (1999).

Peter JB, Barnard RJ, Edgerton VR, Gillespie CA, Stempel KE. Metabolic Profiles of Three Fiber Types of Skeletal Muscle in Guinea Pigs and Rabbits. *Biochemistry*. **11**, 2627-2633 (1972).

Porter JD, Baker RS, Ragusa RJ, Brueckner JK. Extraocular Muscles: Basic and Clinical Aspects of Structure and Function. *Surv. Ophthalmol.* **39**, 451-484 (1995).

Porter JD, Baker RS. Muscles of a different 'color': The unusual properties of the extraocular muscles may predispose or protect them in neurogenic and myogenic disease. *Neurology*. **46**, 30-37 (1996).

Prakash YS, Miller SM, Huang M, Sieck GC. Morphology of diaphragm neuromuscular junctions on different fibre types. *J Neurocytol.* **25**, 88-100 (1996).

Pratt SJP, Shah SB, Ward CW, Inacio MP, Stains JP, Lovering RM. Effects of in vivo injury on the neuromuscular junction in healthy and dystrophic muscles. *J Physiol*. **591**, 559-570 (2013).

Pratt SJP, Valencia AP, Le GK, Shah SB, Lovering RM. Pre- and postsynaptic changes in the neuromuscular junction in dystrophic mice. *Front Physiol.* **6**, 252 (2015).

Pun S, Sigrist M, Santos AF, Ruegg MA, Sanes JR, Jessell TM, Arber S, Caroni P. An Intrinsic Distinction in Neuromuscular Junction Assembly and Maintenancein Different Skeletal Muscles. *Neuron.* **34**, 357–370 (2002).

Qiu J, McQueen J, Bilican B, Dando O, Magnani D, Punovuori K, Selvaraj BT, Livesey M, Haghi G, Heron S, Burr K, Patani R, Rajan R, Sheppard O, Kind PC, Simpson TI, Tybulewicz VLJ, Wyllie DJA, Fisher EMC, Lowell S, Chandran S, Hardingham GE. Evidence for evolutionary divergence of activity-dependent gene expression in developing neurons. *eLife.* **5**, e20337 (2016).

Renier N, Wu Z, Simon DJ, Yang J, Ariel P, Tessier-Lavigne M. iDISCO: A Simple, Rapid Methodto Immunolabel Large Tissue Samples for Volume Imaging. *Cell.* **159**, 1-15 (2014).

Reuveni E, Birney E, Gross CT. The consequence of natural selection on genetic variation in the mouse. *Genomics.* **95**, 196-202 (2010).

Rosen M, Malmgren LT, Gacek RR. Three-dimensional computer reconstruction of the distribution of neuromuscular junctions in the thyroarytenoid muscle. *Ann Oto Rhinol Laryngol.* **92**, 424-429 (1983).

Rossi G, Cortesina G. Multi-motor End-plate Muscle Fibres in the Human Vocalis Muscle. *Nature*. **206**, 629-630 (1965a).

Rossi G, Cortesina G. Morphological Study of the Laryngeal Muscles in Man: Insertions and Courses of the Muscle Fibres, Motor End-Plates and Proprioceptors. *Acta Otolaryngol.* **59**, 575-592 (1965b).

Rowland LP, Shneider NA. Amyotrophic lateral sclerosis. *N. Engl. J. Med.* **344**, 1688-1700 (2001).

Ruskell GL. Spiral nerve endings in human extraocular muscles terminate in motor end plates. *J. Anat.* **139**, 33-43 (1984).

Ruskell GL. Sheathing of muscle fibres at neuromuscular junctions and at extra-junctional loci in human extra-ocular muscles *J. Anat.* **138**, 33-44 (1984).

Sadeh M, Stern LZ. Observations on the Innervation of Human Extraocular Muscles. *Journal of the Neurological Sciences.* **66**, 295-305 (1984).

Saitou K, Masuda T, Michikami D, Kojima R, Okada M. Innervation zones of the upper and lower limb muscles estimated by using multichannel surface EMG. *J Human Ergol.* **29**, 35-52 (2000).

Sanes JR, LIchtman JW. Development of the vertebrate neuromuscular junction. *Annu. Rev. Neurosci.* **22**, 389-442 (1999).

Sanes JR, Lichtman JW. Induction, assembly, maturation and maintenance of a postsynaptic apparatus. *Nature Reviews Neuroscience.* **2**, 791-805 (2001).

Schiaffino S, Reggiani C. Fiber types in mammalian skeletal muscles. *Physiol. Rev.* **91**, 1447-1531 (2011).

Schmitz F. Presynaptic [Ca2+] and GCAPs: aspects on the structure and function of photoreceptor ribbon synapses. *Front. Mol. Neurosci.* **7**, 00003 (2014).

Schnell SA, Staines WA, Wessendorf MW. Reduction of Lipofuscin-like Autofluorescence in Fluorescently Labeled Tissue. *J. Histochem. Cytochem.* **47**, 719-730 (1999).

Sheppert AD, Spirou GA, Berrebi AS, Garnett JD. Three-Dimensional Reconstruction of Immunolabeled Neuromuscular Junctions in the Human Thyroarytenoid Muscle. *Laryngoscope.* **113**, 1973-1976 (2003).

Shi L, Fu AK, Ip NY. Molecular mechanisms underlying maturation and maintenance of the vertebrate neuromuscular junction. *Trends Neurosci.* **35**, 441-453 (2012).

Siksou L, Rostaing P, Lechaire JP, Boudier T, Ohtsuka T, Fejtova A, Kao HT, Greengard P, Gundelfinger ED, Triller A, Marty S. Three-Dimensional Architecture of Presynaptic Terminal Cytomatrix. *J. Neurosci.* **27**, 6868-6877 (2007).

Skipworth RJE, Stewart GD, Ross JA, Guttridge DC, Fearon KCH. The molecular mechanisms of skeletal muscle wasting: Implications for therapy. *Surgeon.* **1**, 273-283 (2006).

Skipworth RJE, Stewart GD, Dejong CHC, Preston T, Fearon KCH. Pathophysiology of cancer cachexia: Much more than host–tumour interaction. *Clinical Nutrition.* **26**, 667-676 (2007).

Slater CR, Lyons PR, Walls TJ, Fawcett PRW, Young C. Structure and function of neuromuscular junctions in the vastus lateralis of man – a motor point biopsy study of two groups of patients. *Brain.* **115**, 451-478 (1992).

Slater CR. Structural determinants of the reliability of synaptic transmission at the vertebrate neuromuscular junction. *J. Neurocytol.* **32**, 505-522 (2003).

Slater CR, Fawcett PRW, Walls TJ, Lyons PR, Bailey SJ, Beeson D, Young C, Gardner-Medwin D. Pre- and post-synaptic abnormalities associated with impaired neuromuscular transmission in a group of patients with 'limb-girdle myasthenia'. *Brain.* **129**, 2061-2076 (2006).

Slater CR. Structural Factors Influencing the Efficacy of Neuromuscular Transmission. *Ann. N.Y. Acad. Sci.* **1132**, 1-12 (2008).

Slater CR The functional organization of motor nerve terminals. *Prog. Neurobiol.* **134**, 55-103 (2015).

Slaughter K, Li H, SokoloffAJ. Neuromuscular Organization of the Superior Longitudinalis Muscle in the Human Tongue. Motor Endplate Morphology and Muscle Fiber Architecture. *Cells Tissues Organs.* **181**, 51-64 (2005).

Sleigh JN, Burgess RW, Gillingwater TH, Cader MZ. Morphological analysis of neuromuscular junction development and degeneration in rodent lumbrical muscles. *J Neurosci Meth.* **227**, 159-165 (2014).

Smit LME, Jennekens FGI, Veldman H, Barth PG. Paucity of secondary synaptic clefts in a case of congenital myasthenia with multiple contractures: ultrastructural morphology of a developmental disorder. *Journal of Neurology, Neurosurgery, and Psychiatry.* **47**, 1091-1097 (1984).

Sommer N, Tackenberg B, Hohfeld R. The immunopathogenesis of myasthenia gravis. In: *Handbook of Clinical Neurology, 3rd Series, Vol. 91, Neuromuscular Junction Disorders.* Elsevier, Amsterdam, pp. 169-212 (2008).

Szule JA, Harlow ML, Jung JH, De-Miguel FF, Marshall RM, McMahan UJ. Regulation of Synaptic Vesicle Docking by Different Classes of Macromolecules in Active Zone Material. *PLoS ONE.* **7**, 33333 (2012).

Titulaer MJ, Lang B, Verschuuren JJGM. Lambert–Eaton myasthenic syndrome: from clinical characteristics to therapeutic strategies. *Lancet Neurol.* **10**, 1098-1107 (2011).

Tokunaga T, Baba S, Tanaka M, Kashiwagi K, Kimura K, Kawazoe T. Two-dimensional configuration of the myoneural junctions of human masticatory muscle detected with matrix electrode. *Journal of Oral Rehabilitation.* **25**, 329-334 (1998).

Tomas J, Fenoll R, Mayayo E, Santafé. Branching pattern of the motor nerve endings in a skeletal muscle of the adult rat. *J Anat.* **168**, 123-135 (1990).

Tooms RE. Acquired Amputations in Children. In: *Atlas of Limb Prosthetics: Surgical, Prosthetic, and Rehabilitation Principles*. American Academy of Orthopedic Surgeons, Rosemont, IL (2002).

Torigoe K, Nakamura T. Fine structure of myomous junctions in the mouse skeletal muscles. *Tissue & Cell.* **19**, 243-250 (1987).

Torri-Tarelli F, Valtorta F, Villa A, Meldolesi J. Functional morphology of the nerve terminal at the frog neuromuscular junction: recent insights using immunocytochemistry. *Progress in Brain Research.* **84**, 83-92 (1990).

Toshifumi K. Location of the Neuromuscular Junction of the Human Masseter Muscle Estimated from the Low Frequency Component of the Surface Electromyogram. *Japanese Journal of Physiology.* **55**, 61-68 (2005).

Tschiriew MS. Sur les terminaisons nerveuses dans les muscle striés. *Arch Physiol Norm Pathol.* **6**, 89-116 (1879).

Tsujihata M, Hazama R, Yoshimura T, Satoh A, Mori M, Nagataki S. The motor end-plate fine structure and ultrastructural localization of acetylcholine receptors in amyotrophic lateral sclerosis. *Muscle & Nerve.* **7**, 243-249 (1984).

Tsujihata M, Kinoshita I, Mori M, Mori K, Shirabe S, Satoh A, Nagataki S. Ultrastructural study of the motor end-plate in botulism and Lambert-Eaton myasthenic syndrome. *Journal of the Neurological Sciences.* **81**, 197-213 (1987).

Tuffery AR. Growth and degeneration of motor end-plates in normal cat hind limb muscles. *J Anat.* **110**, 221-247 (1971).

Valdez G, Tapia JC, Kang H, Clemenson GD, Gage FH, Lichtman JW, Sanes JR. Attenuation of age-related changes in mouse neuromuscular synapses by caloric restriction and exercise. *Proc Nat Acad Sci.* **107**, 14863–14868 (2010).

Van Campenhout A, Hubens G, Fagard K, Molenaers G. Localization of motor nerve branches of the human psoas muscle. *Muscle & Nerve.* **42**, 202-207 (2010).

Vincent A, Cull-Candy SG, Newsom-Davis J, Trautmann A, Molenaar PC, Polak RL. Congenital myasthenia: end-plate acetylcholine receptors and electrophysiology in five cases. *Muscle & Nerve.* **4**, 306-318 (1981).

Vincent A. Unravelling the pathogenesis of myasthenia gravis. *Nature Reviews Immunology.* **2**, 797-804 (2002).

Walrond JP, Reese TS. Structure of Axon Terminals and Active Zones at Synapses on Lizard Twitch and Tonic Muscle Fibers. *The Journal or Neuroscience.* **5**, 1118-1131 (1985).

Watanabe S, Liu Q, Davis MW, Hollopeter G, Thomas N, Jorgensen NB, Jorgensen EM. Ultrafast endocytosis at *Caenorhabditis elegans* neuromuscular junctions. *eLife.* **2**, 00723 (2013).

Watanabe S, Rost BR, Camacho-Pérez M, Davis MW, Söhl-Kielczynski B, Rosenmund C, Jorgensen EM. Ultrafast endocytosis at mouse hippocampal synapses. *Nature.* **504**, 242-247 (2013).

White JG, Southgate E, Thomson JN, Brenner S. The structure of the nervous system of the nematode Caenorhabditis elegans. *Phil. Trans. Royal Soc. London Bio. Sci.* **314**, 1-340 (1986).

Wilhelm BG, Mandad S, Truckenbrodt S, Kröhnert K, Schäfer C, Rammner B, Koo SJ, Claßen GA, Krauss M, Haucke V, Urlaub H, Rizzoli SO. Composition of isolated synaptic boutons reveals the amounts of vesicle trafficking proteins. *Science.* **344**, 1023-1028 (2014).

Wilkinson RS, Teng H. The nerve-muscle synapse of the garter snake. *J. Neurocytol.* **32**, 523-538 (2003).

Willadt S, Nash M, Slater CR. Age-related fragmentation of the motor endplate is not associated with impaired neuromuscular transmission in the mouse diaphragm. *Sci. Rep.* **6**, 24849 (2016).

Wishart TM, Paterson JM, Short DM, Meredith S, Robertson KA, Sutherland C, Cousin MA, Dutia MB, Gillingwater TH. Differential proteomics analysis of synaptic proteins identifies potential cellular targets and protein mediators of synaptic neuroprotection conferred by the slow Wallerian degeneration (Wld^s) gene. *Mol. Cell. Proteomics.* **6**, 1318-1330 (2007).

Wishart TM, Mutsaers CA, Riessland M, Reimer MM, Hunter G, Hannam ML, Eaton SL, Fuller HR, Roche SL, Somers E, Morse R, Young PJ, Lamont DJ, Hammerschmidt M, Joshi A, Hohenstein P, Morris GE, Parson SH, Skehel PA, Becker T, Robinson IM, Becker CG, Wirth B, Gillingwater TH. Dysregulation of ubiquitin homeostasis and β-catenin signaling promote spinal muscular atrophy. *J Clin Invest.* **124**, 1821-1834 (2014).

Wokke JHJ, Jennekens FGI, van den Oord CJM, Veldman H, Smit LME, Leppink GJ. Morphological changes in the human end plate with age. *J Neuro Sci* **95**, 291-310 (1990).

Wood SJ, Slater CR. Safety factor at the neuromuscular junction. *Progress in Neurobiology.* **64**, 393-429 (2001).

Woodley SJ, Duxson MJ, Mercer SR. Preliminary Observations on the Microarchitecture of the Human Abdominal Muscles. *Clinical Anatomy.* **20**, 808-813 (2007).

Wu H, Mei L. Morphological analysis of neuromuscular junctions by immunofluorescent staining of whole-mount mouse diaphragms. *Methods Mol. Biol.* **1018**, 277-285 (2013).

Wu Y, O'Toole ET, Girard M, Ritter B, Messa M, Liu X, McPherson PS, Ferguson SM, De Camilli P. A dynamin 1-, dynamin 3- and clathrin-independent pathway of synaptic vesicle recycling mediated by bulk endocytosis. *eLife.* **3**, 01621 (2014).

Xiong WC, Mei L. Agrin to YAP in Cancer and Neuromuscular Junctions. *Trends Cancer.* **3**, 247-248 (2017).

Yen J, Chang F and Chang S. A New Criterion for Automatic Multilevel Thresholding. *IEEE Transactions on Image Processing*. **4**, 370-378 (1995).

Yoshihara T, Ishii T, Iwata M, Nomoto M. Ultrastructural and Histochemical Study of the Motor End Plates of the Intrinsic Laryngeal Muscles in Amyotrophic Lateral Sclerosis. *Ultrastructural Pathology.* **22**, 121-126 (1998).

Zenker W, Snobl D, Boetschi R. Multifocal innervation and muscle length: A morphological study on the role of myo-myonal junctions, fiber branching and multiple innervation in muscles of different size and shape. *Anat. Embryol.* **182**, 273-283 (1990).

Zhai G, Bellen HJ. The Architecture of the Active Zone in the Presynaptic Nerve Terminal. *Physiology.* **19**, 262-270 (2004).

Zhang Q, Cao YQ, Tsien RW. Quantum dots provide an optical signal specific to full collapse fusion of synaptic vesicles. *PNAS.* **104**, 17843-17848 (2007).

Publications

Jones RA, Harrison C, Eaton SL, Hurtado ML, Graham LC, Alkhammash L, Oladiran OA, Gale A, Lamont DJ, Simpson H, Simmen MW, Soeller C, Wishart TM, Gillingwater TH. Cellular and Molecular Anatomy of the Human Neuromuscular Junction. *Cell Reports*. **21**, 2348-2356 (2017).

Jones RA, Mortimer JW. Anatomy for Surgeons. In: Fisher R, Ahmed K, Dasgupta P (eds) *Introduction to Surgery for Students*. Springer, Cham, pp. 17-29 (2017).

Herranz-Martin S, Chandran J, Lewis K, Mulcahy P, Higginbottom A, Walker C, Martinez-Pena y Valenzuela I, **Jones RA**, Coldicott I, Azzouz M *et al.* Viral delivery of C9orf72 hexanucleotide repeat expansions in mice leads to repeat-length-dependent neuropathology and behavioral deficits. *Disease Models & Mechanisms*. **10**, 859-868 (2017).

Hall EA, Nahorski MS, Murray LM, Shaheen R, Perkins E, Dissanayake KN, Kristaryanto Y, **Jones RA**, Vogt J, Mill P *et al.* PLAA Mutations Cause a Lethal Infantile Epileptic Encephalopathy by Disrupting Ubiquitin-Mediated Endolysosomal Degradation of Synaptic Proteins. *The American Journal of Human Genetics*. **100**, 706-724 (2017).

Jones RA, Reich CD, Dissanayake KN, Kristmundsdottir F, Findlater GS, Ribchester RR, Simmen MW, Gillingwater TH. NMJ-morph reveals principal components of synaptic morphology influencing structure-function relationships at the neuromuscular junction. *Open Biology*. **6**, 160240 (2016).

Ross PD, Guy J, Selfridge J, Kamal B, Bahey N, Tanner KE, Gillingwater TH, **Jones RA**, Loughrey CM, McCarroll CS, Bailey MES, Bird A, Cobb S. Exclusive expression of MeCP2 in the nervous system distinguishes between brain and peripheral Rett syndrome-like phenotypes. *Human Molecular Genetics*. **25**, 4389-4404 (2016).

Powis RA, Karyka E, Boyd P, Côme J, **Jones RA**, Zheng Y, Szunyogova E, Groen EJN, Hunter G, Thomson D, Wishart TM, Becker CG, Parson SH, Martinat C, Azzouz M, Gillingwater TH. Systemic restoration of UBA1 ameliorates disease in spinal muscular atrophy. *JCI Insight*. **1**, 87908 (2016).

Hunter G, Powis RA, **Jones RA**, Groen EJN, Shorrock HK, Lane FM, Zheng Y, Sherman DL, Brophy PJ, Gillingwater TH. Restoration of SMN in Schwann cells reverses myelination defects and improves neuromuscular function in spinal muscular atrophy. *Human Molecular Genetics*. **25**, 2853-2861 (2016).

"What would you think it's worth telling future generations about the life you've lived and the lessons you've learned from it?"

"I should like to say two things, one intellectual and one moral. The intellectual thing I should want to say is this: When you are studying any matter, or considering any philosophy, ask yourself only what are the facts and what is the truth that the facts bear out. Never let yourself be diverted either by what you wish to believe, or by what you think would have beneficent social effects if it were believed. But look only, and solely, at what are the facts. That is the intellectual thing that I should wish to say.

The moral thing I should wish to say… I should say love is wise, hatred is foolish. In this world which is getting more closely and closely interconnected we have to learn to tolerate each other, we have to learn to put up with the fact that some people say things that we don't like. We can only live together in that way and if we are to live together and not die together we must learn a kind of charity and a kind of tolerance which is absolutely vital to the continuation of human life on this planet."

Interview, Face to Face, BBC, 1959

Bertrand Russell
(1872–1970)